Laser shock peening of Ti-6Al-7Nb
evaluation of microstructure, interfacial and biological properties

Shen, Xiaojun

Award date:
2020

Awarding institution:
Coventry University

Laser Shock Peening of Ti-6Al-7Nb: Evaluation of Microstructure, Mechanical, Interfacial and Biological Properties

By

Xiaojun Shen

Award PhD

MARCH 2020

Laser Shock Peening of Ti-6Al-7Nb: Evaluation of Microstructure, Mechanical, Interfacial and Biological Properties

By

Xiaojun Shen

March 2020

A thesis submitted in partial fulfilment of the University`s requirements for the Degree of Doctor of Philosophy

Certificate of Ethical Approval

Applicant:

Xiaojun Shen

Project Title:

Laser shock peening of orthopaedic Ti-6Al-7Nb alloy: Evaluation of mechanical, biomedical properties and internal characteristics

This is to certify that the above named applicant has completed the Coventry University Ethical Approval process and their project has been confirmed and approved as Medium Risk

Date of approval:

17 May 2019

Project Reference Number:

P90450

ABSTRACT

This work comprises of interdisciplinary research on improving the mechanical and biological properties of medical-grade titanium (Ti-6Al-7Nb) alloy for the first-time by using laser shock peening (LSP). Over the years, LSP has been used to enhance the mechanical properties predominantly in the aerospace sector. However, due to the benefits which it could offer, such as enhanced wear, fatigues, hardness, corrosion resistant, just to name a few; it can also be beneficial in the medical sector. Implants failures due to the lack of osseointegration or wear resistance have brought tremendous pain and costs for patients after the primary and often second implant replacement surgeries. In order to avoid such revision surgeries, it is important to extend the service life of the implant to make sure that the implants will not fail until the patients' demise. With that said, this research is focused on both laser shock peening a medical-grade titanium Ti-6Al-7Nb utilised for orthopaedic implants by employing a nanosecond pulse Nd: YAG laser to modify the mechanical properties and enhance bio-compatibility. The process parameters applied were 3J, 5J and 7J at overlaps of 33%, 50% and 67% at 3 mm spot size, 5 Hz pulse repetition rate, a 1064nm wavelength and 20ns pulse duration.

The microstructure examination after laser shock peening showed the average sub-grain size was reduced by 12.5% to 39% for the range of laser energies that were applied. Due to the non-uniform misorientation distributions, heat treatment was conducted to obtain equilibrium and globular microstructure. After heat treatment, the same LSP parameters were applied to the Ti-6Al-7Nb surfaces. The misorientations were dramatically increased after LSP, as evident from the kernel average map (KAM) map. Twinning deformation can be found after the LSP parameter of 7J, 50% for 10 impacts at a spot size of 3 mm.

A range of compressive residual stresses (-42MPa to -512MPa), after LSP were formed at the near-surface region, as characterized by Incremental Hole Drilling (IHD) method. The data was verified for the first-time, by Artificial Neural Network (ANN) technique using a gradient descent learning algorithm. The accuracy of the prediction data are 96.16% and 95.16%. In the case of microhardness, the laser shock peened surfaces were hardened from 14% to 26.5%. The fretting wear in simulated body fluid was conducted using a tribometer to measure the wear behaviour of Ti-6Al-7Nb, before and after LSP. It was found that optimal LSP parameters can improve the wear resistance. What is more, sliding wear behaviour of Ti-6Al-7Nb, subjected

to multiple LSP showed that the wear resistance performance was improved by 44%, after 3 impacts.

The surface morphologies and topographies after LSP were also investigated. The surface roughness was increased after LSP due to the dimpling effect particularly at higher laser energies creating high shock pulse pressure. This influenced the contact angle which was measured with the needle-in method using two different liquids (distilled water, ethylene glycol). Surface-free energy including dispersion and polar components, with subsequent calculation of the work of adhesion were acquired. The results showed that laser energy and overlap were inversely proportional to contact angle but proportional to surface free-energy and work of adhesion. The correlation between laser energy (pressure pulse) and contact angle can be explained by Wenzel's theory, while the relationship between overlap and contact angle is described by the Cassie-Baxter model.

The osteoblast-like MG63 cells were employed to measure the cell viability using MTT assay. The cells were seeded and cultured for 24hrs and 72hrs on the untreated, laser shock peened surfaces and the culture plate as the positive control. The cell morphologies were characterized by fluorescence microscope. The images indicated that the cells can be attached to the surface post LSP, and LSP is not cytotoxic to MG 63 cells. The MTT results show that optimal LSP parameter 5J, 33% and 5J, 50% at the spot size of 3mm can improve cell viability. With considering the wetting properties, the optimal contact angle after LSP is 71.5°

This research has shown that both mechanical strength and biocompatibility can be controlled and improved for orthopaedic Ti-6Al-7Nb alloy. However, it is not necessary that highest LSP induced compressive residual stress yields the best biological response by the material. Although, a compromise between both can render not only stronger, durable and wear resistant next generation implants, but also those that are more biocompatible. The findings of this research can now be adopted to develop the technique to both strengthen and enable medical metallic implants more bio-compatible, which in turn, improves the standard of living of the end-users.

List of Publications

Journal Papers

The work of this PhD project has resulted to the following publications:

1. **X. Shen**, P. Shukla, Philip Swanson, Zhibin An, S. Prabhakaran, David Waugh, Xiangfan Nie, Christopher Mee, Soheil Nakhodchi, Jonathan Lawrence. Altering the wetting properties of orthopaedic titanium alloy (Ti-6Al-7Nb) using laser shock peening. *Journal of Alloys and Compounds*, 15(2019), 327-342. (SCI, IF 4.2,Chapter 11)
2. **X. Shen**, P. Shukla, Deepak Sharma, Ann Zammit, Philip Swanson, Yang Jiao, Jonathan Lawrence. On restructuring the microstructure of Ti-6Al-7Nb alloy before surface engineering. *Materials Characterization*, 169(2020), 110629. (SCI, IF 3.5, Chapter 4)
3. **X. Shen**, P. Shukla, Anand Kumar Subramaniyan, Ann Zammit, Philip Swanson, Jonathan Lawrence, Michael E. Fitzpatrick. Residual stresses induced by laser shock peening in orthopaedic Ti-6Al-7Nb Alloy. *Optics and Laser Technology*, 131(2020), 106446. (SCI, IF 3.2, Chapter 7)
4. **X. Shen**, P Shukla, Subhasisa Nath, Jonathan Lawrence. Improvement in mechanical properties of titanium alloy (Ti-6Al-7Nb) subject to multiple laser shock peening, *Surface & Coating Technology* 327(2017), 101-109 (SCI, IF 2.9, Chapter 9)
5. **X. Shen**, P. Shukla, F. Yao, Subhasisa Nath, Z. An, Jonathan Lawrence. Laser shock peening of orthopaedic Ti-6Al-7Nb: evaluation of topography, wetting characteristics, microstructure and residual stress, *International Journal of Peening Science and Technology*, 1 (2018), 137-154.
6. **X. Shen**, P. Shukla. A review of titanium based orthopaedic implants (Part-I): physical characteristics, problems and the need for surface modification. *International Journal of Peening Science and Technology*, 1(2020), 301-332. (Chapter 2)
7. **X. Shen**, P. Shukla. Laser Shock Peening: A Review of Current State of Technology and its Potential in the Medical Sector (Part-II). Accepted on 20th March 2020. (Chapter 3)

Magazine Article(s)

1. **X. Shen**. Laser shock peening in the medical sector-an overview. The Laser User, 93(2019):18-19.
2. **X**. Shen & Pratik Shukla. Topography & morphology of laser shock peening on Ti-6Al-7Nb. 97 (2020): 18-19.
3. **沈晓骏，**激光冲击强化在医用领域的应用. 工业激光应用，02/03(2019), 12-14.

Journal Papers to be submitted

1. **X. Shen**, Pratik Shukla, Sunita Nayak, Vasanth Gopal, S. Prabhakaran, Amy Sarah Benjamin, S. Kalainathan. Assessment of Wear Characteristics, Microstructure and Cell Viability of Orthopaedic Ti-6Al-7Nb Surface Treated with Laser Shock Peening submitted to Materials Science and Engineering C, under review.

Conference Talks

1. **X. Shen**. 'Wetting Characterise of Ti-6Al-7Nb post Laser Shock Peening', Word Summit on Advance in Science, Engineering and Technology, University of Cambridge, UK, January 4-6,2018;
2. **X. Shen**. 'Wetting Characterise and Cell Response of Ti-6Al-7Nb Orthopaedic Titanium following Laser Shock Peening', 7th International Conference on Laser Peening and Related Phenomena, National University of Singapore, 17-22 June 2018
3. **X. Shen**. Laser shock peening evaluation of Ti-6Al-7Nb alloy: Residual stress, microhardness, and microstructure. 6th Industrial Laser Applications Symposium. Crewe, UK, 2019;

Contribution to Other Publications

1. Yang Jiao, Weifeng He, **Xiaojun Shen**. Enhanced high cycle fatigue resistance of Ti-17 titanium alloy after multiple laser peening without coating [J]. *The International Journal of Advance Manufacturing Technology*, 104(2019): 1333-1343
2. Nath, S., Shukla, P., **Shen, X.,** and Lawrence, J. Effect of laser shock peening on the phase evolution, residual stress and hardness of Hastelloy X superalloys. *Lasers in Engineering*, 39 (2018), 97–112.
3. Ogbekene, Y.F, Shukla, P., Zhang, Y., **Shen, X.**, Prabhakaran, S., Kalainathan, S., Gulia, K., and Lawrence, J. (2018), Enhancement in surface integrity with laser

cleaning and rust removal of grey cast iron automotive brake disc, *International Journal of Peening Science and Technology*, 1(2), 155 - 180.

4. Nath, S., Shukla, P., Behera, A., **Shen, X.**, Lawrence, J. (2019), Evolution of dislocation density and strain hardening behaviour in Hastelloy-X Superalloys following laser shock peening, *International Journal of Peening Science and Technology*, 1(3), 233-257.
5. Yang Z.F, An Z.B, **Shen X.J**, Wang C, Zhou X. Investigation on the effect of microstructure and mechanical properties of laser cladded TC17 titanium alloy following laser shock peening [J]. IOP Conference Series: *Materials Science and Engineering*, 479(2019), 012063
6. Shukla, P, Nath, S. Wang, G, **Shen X**, Lawrence J. Surface property modifications of silicon carbide ceramic following laser shock peening, *Journal of the European Ceramic Society*, 37(2017), 3027-3038.

Acknowledgements

First and foremost, I would like to express my deep and sincere gratitude to my parents and grandparents for their unconditional love, support, encouragement which they have provided for me in my life. Without it, it is impossible to complete my PhD. A special thank needs to be sent to my soul mate and beloved fiancé Lingfeng Zhao for always being there, understanding and supporting my dream. Her endless support, patience, love and encouragement gave me the strength and the determination in pursuing my goal.

I am also thankful to my supervisor, mentor and life friend Prof. Pratik Shukla, for guiding my research direction. He always gave me precious and valuable suggestions, guidance time and support which not only contributes to the research, but also my life throughout the whole duration of this PhD. Also, it would have been impossible for me to undergo the whole journey without him.

During the course of this PhD, I was given valuable advices, ideas and technical guidance from many friends who are acknowledged in the follows according to their contributions to my thesis. I want to thank Dr An Zhibin from Air Force Engineering University China on several occasions which helped me to shape my work better.. I would send my gratitude to Dr Vit Janik (IFTC, Coventry University) for his suggestions and helps in SEM, EBSD analysis. Thanks, Mr Deepak Sharma for his helps with heat treatment. A special thanks also goes to Dr S. Prabhakaran and Prof. S. Kalainathan from VIT University (India), as they were always ready to help during my visit, when TEM sample preparation , operation and analysis was required. Many Thanks to my colleague Dr. Subhasisa Nath for helping me in many ways with my research in general. I would also to like acknowledge Dr Ann Zammit for helping with XRD residuals stress and Dr Anand Kumar Subramaniyan (IIT India) for his kind assistance in conducting the ANN simulations. Herewith, I also send my gratitude to Mr Vasanth from VIT University who provided some good technical assistance with conducting fretting wear experiments. Regarding wetting properties, I need to acknowledge Dr David Waugh in the laser group. I would also thank Dr Sunita and Miss Amy Sarah for assisting me with conducting the cell culture experiments at VIT University during my visit.

I would also like to acknowledge the contributions of Mr Steve Allitt for his valuable advices and providing the training and Dr Phillip Swanson for his valuable time and helps in proofreading journal papers.

Finally, I want to express my sincere gratitude to my Direct of Study Prof. Jonathan Lawrence for his valuable ideas and comments, but also for the questions that prompted me to broaden my studies from various aspects.

Nomenclature and abbreviations

α-TCP	α-Tricalcium Phosphate
$cos\,\theta$	Single-Valued Equilibrium Contact Angle
β_{hkl}	FWHM Full Width Half Maximum
γ_{LG}	Liquid/Gas Interfacial Tensions
γ_L^d	Dispersive Part of Test Liquid
γ_L^p	Polar Part of Test Liquid
γ_S	Solid Free Energy
γ_{SG}	Solid/Gas Interfacial Tensions
γ_{SL}	Interfacial Tension of Solid/Liquid Tension
γ_{SL}	Solid/Liquid Interfacial Tensions
γ_S^d	Dispersive Part
γ_S^p	Polar of the Solid Surface Free Energy
$\gamma_{i,SL}$	Surface Tension of Each Piece Material
$\gamma_{i,SV}$	Surface Energy of Each Piece Material
θ	Diffraction Angle
θ	Poisson`s Ratio
θ_{Ad}	Advance Contact Angle
θ_{Re}	Receding Contact Angle
λ	X-ray Wavelength
σ_y^{dyn}	Dynamic Yield Strength at High Strain
3D	3-dimension
AC	Air Cooling
AC4CH	Aluminium-Silicon-Magnesium Alloy
AFM	Atomic Force Microscopy
Ag	Silver
Ag-PIII	Silver Plasma Immersion Ion Implantation
AHT	Alkali-Heating Treatment
ANN	Artificial Neural Network
ANOVA	Analysis of Variance
Bcc	Body-Centred Cubic

BCP	Biphasic Calcium Phosphates
BMI	Bottom-Mounted Instrumentation
BMSCs	Bone Marrow Mesenchymal Stem Cells
BWRs	Boiled Water Reactors
CA	Contact Angle
CAD	Computer-Aided Design
CaO	Calcium Oxide
CDHA	Calcium-Deficient Hydroxyapatite
CLFA	Co-operation Laser Franco-Allemande-Arcueil Cedx
CLSP	Cryogenic Laser Shock Peening
Co	Cobalt
COF	Friction Coefficients
CP-Ti	Commercial Pure Titanium
Cr	Chromium
CRS	Compressive Residual Stress
D	Crystallite Size
D	The Average Value of Two Indentation diagonals
D	The Diameter of Nozzle (m)
DAPI	4`,6-diamidino-2-phenylindole
DCL	Diamond-like Carbon
DMEM	Dulbecco`s Modified Eagle`s Medium
DP	Dynamic Precipitation
DSA	Dynamic Strain Ageing
E	Elastic Modulus
EBSD	Electron Backscatter Diffraction
ECLSP	Elastic Contact Laser Shock Peening
EDM	Electrics Discharge Machining
EDS	Energy Dispersive X-Ray Spectroscopy
EPRI	Electric Power Research Institute
f	Laser Repetition
F	Loads
FBS	Foetal Bovine Serum
FC	Furnace Cooling
FOD	Foreign Object Damage

FPP	Fine Particle Peening
GEAF	GE Aircraft Engines
GIM	Grain Intercept Method
H	Contact Angle Hysteresis
h	Depth of Wear Scar
Hap	Hydroxyapatite
HCF	High Cycle Fatigue
HCP	Hexagonal Closed-Packed
HEL	Hugonit Elastic Limit
H-P	Hall-Petch
HRLSP	High Repetition Laser Shock Peening
HV	Vicker Hardness
I	Power Intensity (Gw/cm^2s)
ICUs	Intensive Care Units
IHD	Incremental Hole Drilling
IPF	Inverse Polar Figure
J	Energy of Each Pulsed Laser
K	Shape Factor
KAM	Kernel Misorientation Map
LCF	Low Cycle Fatigue
LLNL	Lawrence Livermore National Laboratory
LPE	Laser Pulse Energy
LSP	Laser Shock Peening
LSPT	LSP Technology
LSPwC	Laser Shock Peening without Coating
LSPWP	Laser Shockwave Planishing
MAPE	Mean Absolute Percentage Error
MELISA	Memory Lymphocyte Immunostimulation Assay
MIC	Metal Improvement Company
MTT	Methyl-tetrazolium Assay
N	Nitrogen
Nb	Niobium
ND	Normal Direction
NHS	National Heathy Service

OHA	Oxyhydroxyapatite
OLP	Overlap Percentage
P	Peak Wave Pressure (GPa)
P_i	Predicted Values
PIII	Plasma Immersion Ion Implantation
PIII-Ag+N	Ag/N Dual Ions Co-implantation
PIII-Ag-N	Ag Ions prior to N Implantation
PIII-N-Ag	N priors to Ag Ions Implantation
Pw	Laser Power
PWRs	Pressurized Water Reactor
Q	Volume of Gas Flow Rate (m^3m^{-1})
R	Radius of the Counterpart
RD	Rolling Direction
Sa	Arithmetic Mean Height
SBF	Simulated Body Fluid
SE	Strain Energy
SEAD	Selected Area Electron Diffraction
SEM	Scanning Electron Microscopy
SFE	Surface Free Energy
SH	Surface Hardness
SMA	Shape Memory Alloy
SP	Shot Peening
SPD	Severe Plastic Deformation
SS	Stress Shielding
SSC	Stress Corrosion Cracking
T	Gas Temperature (K)
TC4	Ti-6Al-4V
TD	Transverse Direction
TEM	Transmission Electron Microscopy
THA	Total Hip Arthroplasty
THR	Total Hip Revision
T_i	Experimental Values
Ti	Titanium
T	Tensile Strength

TTCP	Tetra-Calcium Phosphate
T_β	Beta Transus Temperature
UNSM	Ultrasonic Nanocrystalline Surface Modification
USDM	Uniform Stress Deformation Model
V	Vanadium
V	Velocity of Plasma (ms^{-1})
V	Wear Volume Loss
W_a	Work of Adhesion
W-H	Williamson-Hall
WLI	White-light Interferometer
WLSP	Warm Laser Shock Peening
WQ	Water Quench
XRD	X-ray Diffraction
YS	Yield Strength
Z	The Impedance of Shock Wave (g/m^2s)
Zr	Zirconium

List of Figures

Chapter-1

Chapter-2

Chapter-3

Chapter-4

Chapter-5

Chapter-6

Chapter-7

Chapter-8

Chapter-9

Chapter-10

Chapter-11

Chapter-12

List of Tables

No Tables

Chapter-9

Chapter-10

No Tables

Chapter-11

Chapter-12

Contents

PART-1 BACKGROUND AND INTRODUCTION

CHAPTER 1 Introduction

There is a significant demand for artificial implants, due to an ageing population.. In this Chapter, firstly introduce huge quantity demanded of artificial implants due to the decrease of human health, addressing the necessity for employing an implant. The human orthopaedic health data and the need for artificial implants and was discussed. Then the objective and the structure of the research are given.

1.1 Background

Orthopaedic implants play an important role in enhancing the quality of life for patients. The orthopaedic implant is a medical device designed and manufactured to support a damaged joint or to replace a fractured part of the bone. Specifically, orthopaedic implants are able to relieve issues the joints and bones inside the human body when the original "human parts" are damaged, worn and unable to function on their own. They are subject to replacement due to various reasons, namely, scoliosis, chronic pain, spinal stenosis, osteoarthritis and bone fractures. For example, rods, screws, pins and plates are used to anchor fractured bones while the bones are in the self-healing stage. [1].

The orthopaedic implants are made from alloys of different kinds of materials such as traditional materials (gold, silver, aluminium, iron steel, copper, etc.), stainless steel, titanium alloys and magnesium. For now, the traditional orthopaedic materials were no longer employed as their mechanical properties and releasing toxic ion when the implants are degraded inside the human body [2]. Nowadays, most of the materials employed for medical replacements are stainless [3] and titanium alloys [4]. Since the 1900s, the application of orthopaedic devices made from stainless steel has been continued to to-date. Especially, one of the most used stainless types is 316L stainless. Due to its capability of anti-corrosion, mechanical properties and cheap cost, it has been widely employed to replace the tissue in clinical surgeries or assist in stabilizing as a biological structure, such as dental implants, spinal rods, orthopaedic fracture plates and joint replacement etc.[5].

However, due to the complex human body environment, the Stainless steel will be subject to the electrochemical mechanism. Once the metallic implants start to be corroded, the metal ion will be released from the surface materials into to human body thereby causing ion toxic. In

comparison to stainless steel, Ti and its alloys exhibit better performance in corrosion[6]. This is because Cl-rich body environment could react with stainless thereby causing corrosion, Thus, since 1962, titanium alloys have continuously received substantial attention.

1.1.1 The need for orthopaedic implants

If the need to have an orthopaedic implant is a thought that comes to mind for the end-user when it becomes an absolute requirement. The use of prosthetic implants for replacing and restoring tissues is continuously increased. This is because that approximately 90% of the world population over the age of 40 are suffering from the degenerative diseases that are caused by the absence of normal biological self-healing ability or excessive and pre-longed loading [7-9]. For instance, for musculoskeletal conditions, such as arthritis, (disorders of the joints, bones and muscles) affect around 10 million people across the UK and cost around £5 billion to the National Health Service (NHS) programme in the U.K.to treat new and existing patients [10, 11].

Besides that, breaking bones is also the main reason why one would require an artificial implant. The braking of bones occurs through fractures which are often very painful for patients. There are various types of bone fractures, including complete, incomplete, simple and complex type of failures that a bone may undergo. A total of over 1 million bone fractures are reported each year in the UK, around 21% of fractures occurred as a result of road traffic accidents[12]. Bone fractures may happen at any time during people`s life. However, Children and elderly people tend to sustain the most fractures. In the childhood age group, the broken forearm is the most common fracture, and fractures occurred in boys are more than girls have. Moreover, adolescents tend to be the most active age group that may increase the risk of fracture, and their bones are more fragile during the adolescence period of rapid. In addition, the increased incidence of falls and the decreased bone density caused by Osteoporosis indicated that the possibility of bone fractures and their recovery time naturally increases with age[13] in elder age group.

What is more, a hip fracture is the most common for elderly people, occupying over 4,000 hospital beds in any day each year and costs the NHS roughly a £1 billion per annual [14]. Moreover, the age and frailty of hip fracture patients mean that nearly a third of people die within a year of the injury due to different reasons, namely; osteoarthritis, as reported by National Joint Research (NJR) [14]. There are 2055687 procedures between 2003 to 2015.

The number of percentages of primary surgery is shown in Table 1.1. This include 875,585 knee replacements; 800,686 total hip replacements; 17,300 shoulder replacements; 3,185 ankle replacements, and 1,639 elbow replacements. What is more, 146,220 of the 1,698,395 surgeries had a revision surgery, due to the complicated human physical environment.

Table 1.1 shows the statistics of primaries (first) and revisions surgeries in the UK [14].

BODY PARTS	KNEES	HIPS	SHOULDERS	ANKLES	ELBOWS	Total
Primary	875,585	800,686	17,300	3,185	1,639	1698395
Revision	54,287	89,023	2,045	358	507	146220

The need for implant products is not only for the initial replacement surgeries, but also, also for the revision procedure due to the implant failure. For example, total hip revision (THR) is one of the highest numbers of surgeries in the UK. There are many reasons for a revision surgery. The reason why the THR is painful is that it has been placed in the human body for a period. However, the components have started to loosen or wear as the implants moved a little in the bone. Some bone loss and damage will be occurred after such type of loosening. Thus, a revision surgery is needed for dealing with the bone loss and stop the further complication caused by implants failure. Moreover, repeated occasions will lead to the dislocation of the implant thereby THRs is needed.

In summary, the global market for orthopaedic implant products in 2016 was $40.20 billion according to BIS Research [15]. The industry sees annual growth of 6.1% compared with last year, which means the market is predicted to about $ 61 billion by 2023. Therefore, the need for implant products is significant and the quality of implant products should be strictly controlled and supervised for the health of people all over the world.

1.1.2 Reasons for Failures in Orthopaedic implants

As we mentioned in Table 1.1, there are nearly 150 thousand procedures done in 2016 [14]. Since there are many reasons for failures for orthopaedic implants as shown in Figure 1.1, the primary reasons for the revision are as follow aseptic loosening (5,073 surgeries); pain (4,078); wear (3,548 surgeries); and infection (2,889 surgeries). It can be seen that aseptic loosening is the most reason, followed by pain (26%), wear (22%) and infection (19%)

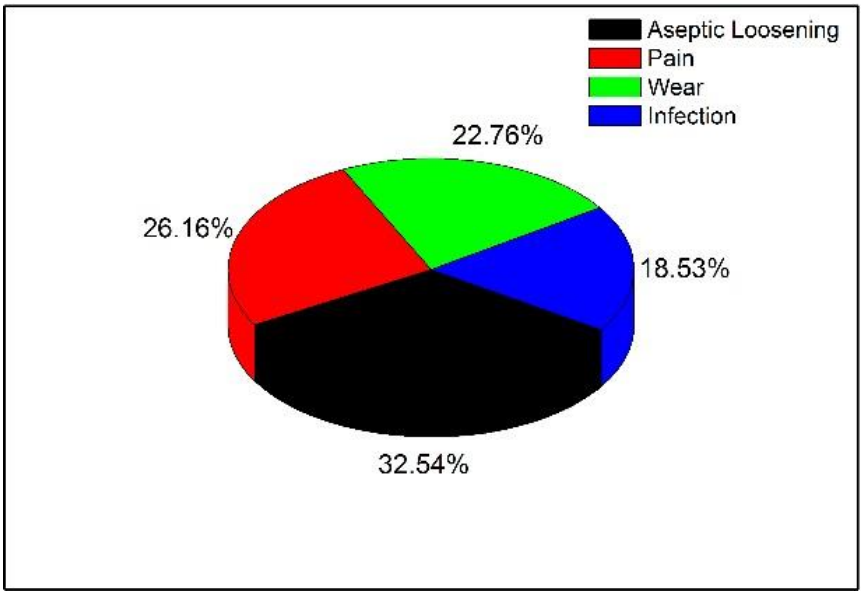

Figure 1.1 The main reason for revision procedures: aseptic loosening; pain; wear and infection.

1.1.2.1 Loosening of Implants

Implants loosening is a mode of failure resulting from implant movement or migration in the bone or cement according to Havelin *et al.* [16]. In 1993, implant loosening accounted for 64% among the revision procedures from 1987 to 1990 in Norway. Also, Malchau *et al*. [17], found that 79% of secondary surgeries were caused by implant loosening in Sweden from 1987 to 1990. Additionally, a report by the national joint research, UK (2016), stated that implant loosening was still the highest failure reason corresponding to 32.6%. Stress shielding was one of the reasons that results in implant loosening. Stress shielding refers to the osteopenia as a result of the removal of typical stresses from the bone by an implant. According to Wolff`s law, bones will remodel responded to the loads where it is placed. Thus, if the loading decreases on a recovering bone, the bone will be weaker and the bone density is less as there are no stimulus for continued remodelling which is required to maintain bone mass [18-21].

Shown in Figure 1.2, when the artificial femoral and Proximal Femur were implanted in the body, it shared the load from the body instead of the bone. In a healthy body environment, the load should be born by bone, otherwise, the upper femoral subjected to reduced stress could cause a loss of bone mass (osteopenia) through the biological process called “resorption”. In the contact, in the lower femoral, the bone is overloaded which causes dense skeleton.

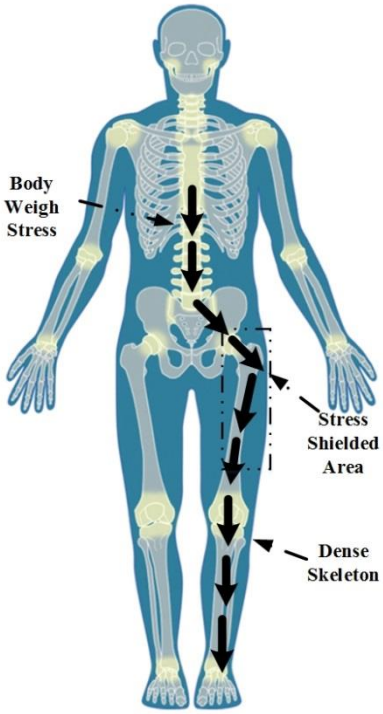

Figure 1.2 A schematic diagram illustrating stress shielding.

A bone will remodel itself to become stronger to resist the load acting upon it. In order to investigate the schematic of this remodelling, many researchers have worked on calculating the stresses in the bone. Especially, with Finite Element Analysis, conducted by Joshi *et al*.[22], explored a hypothesis that a total hip prosthesis can be developed to substantially reduce stress shielding through re-design. Weinans *et al.* [23] also came up with a definition of stress shielding that it works like a change in strain energy (SE) in each element of the implanted bone relative to a reference value of SE in the contacting bone and SS is for stress shielding as shown in Equation 1-1:

$$SS = \frac{SE(Treated) - SE(Reference)}{SE(Reference)} \quad (1\text{-}1)$$

1.1.2.2 Implant Infection Caused by Bacteria

As we may be surprised that even it was under aseptic conditions such as Intensive Care Units (ICUs), there would still be around 5000 to 50000 microparticles, broadcasted daily from each physician to patients[24]. In addition, although the wounds were clean when procedures were finished, the number of pathogenic bacteria such as staphylococci still can be recovered to around 90%[25]. Therefore, bacteria were able to find their pave into the human body despite

the strict environment. Thus, minor contamination areas of pre-inserted medical devices may be regarded as infectious.

Typically, the main sources of bacteria causing implant infections are from the physician and the skin of the patients themselves near the wound during implant insertion. Thereafter, bacteria migrated through incision channels to the surface of implants inside the patients' body, spreading towards the *vivo* environment during the hematogenesis [26].

The bacteria adhesion is the first and foremost step during implants infections caused by bacteria. The bacteria become adhered and immobile to the implant which provides surfaces for biofilm formation, bacterial attachment and proliferation. In the surfaces of inserted medical devices, the adherent bacteria generate a protective polymeric, extracellular substance, protecting these bacteria from being eradicated. Without it, bacteria could float around the body.

Although a wide variety of bacteria can lead to implant infections, majority cases are infected by a small group of species. As mentioned above, Staphylococci, prominently account for nearly 70% of orthopaedic implant infections. Moreover, Pseudomonas aeruginosa accounts for another 8% of infections [27]. Thus, it warrants the development of a new type of sophisticated anti-bacterial orthopaedic implants.

1.1.2.3 Wear of Implant Material

Wear is also another critical challenge for medical devices such as hip, knee and medial proximal tibia. It can cause loss of mass from the implanted materials, which leads to critical degradation of the function of orthopaedic prostheses. For instance, wear debris generated from Polyethylene acetabular components could lead to osteolysis in THA (Total Hip Arthroplasty). Zhu *et al*. [28] pointed out that the osteolysis caused by wear debris can result in loosening between the femoral head and proximal femur. Additionally, John *et al*.[29], conducted a 12-years of research, investigating the relationship between wear and osteolysis. They have found that there is no correlation between the amount of polyethylene wear and osteolysis volume.

In a titanium alloy such as Ti-6Al-4V, Vanadium (V) is found to be a toxic element to the human body. When the stable coating TiO_2 layer on the TC4 is worn out due to wear behaviour, the V ion will be released into the *vivo* environment, leading to ion toxicity [30, 31].

The wear properties of biomedical materials play a significant role when choosing a suitable prothesis. What is more, adhesive wear, fatigue wear and abrasive wear, also have a great influence in analysing the degradation of medical prostheses. Decreasing wear of medical devices was always an important research topic to study for many researchers.

1.2 Research Aims and objects

1.2.1 Project aims

The extended titanium made orthopaedic implants can help patients decrease the risk of undergoing the removal surgeries, which costs great money, pain and time for thousands of end-users (patients). The aim of this thesis is to improve the mechanical and biological performances of Ti-6Al-7Nb alloy using laser shock peening, thereby, extending the service life of orthopaedic implants. To accomplish this aim, different essential experimental approaches were used.

1.2.2 Project objective

To investigate both mechanical and biological response of vanadium free titanium alloy (Ti-6-Al-7Nb) suitable for biological implants. The specific objects of this thesis are as follow:

- To conduct a broad range of parametric sweep of laser shock peening on a bio-grade titanium alloy (Ti-6Al-7Nb alloy);
- To conduct a microstructural, morphological and crystallographic analysis of the laser shock peened Ti-6Al-7Nb and form a relationship with process parameters.
- To investigate the effect of laser shock peening on the residual stresses with multiple techniques, measure mechanical properties, namely: hardness, reciprocating and fretting wear subject to laser shock peening of Ti-6Al-7Nb.
- To investigate the surface topography after LSP, and determine the effect of laser shock peening on the wetting characteristics of Ti-6Al-7Nb alloy.
- To investigate the effect of LSP on cell viability in Ti-6Al-7Nb alloy.

1.3 The research programme and structure

The research presented in this thesis consists of both analytical and experimental parts. A schematic illustration of the thesis` outline is shown in Figure 1.3

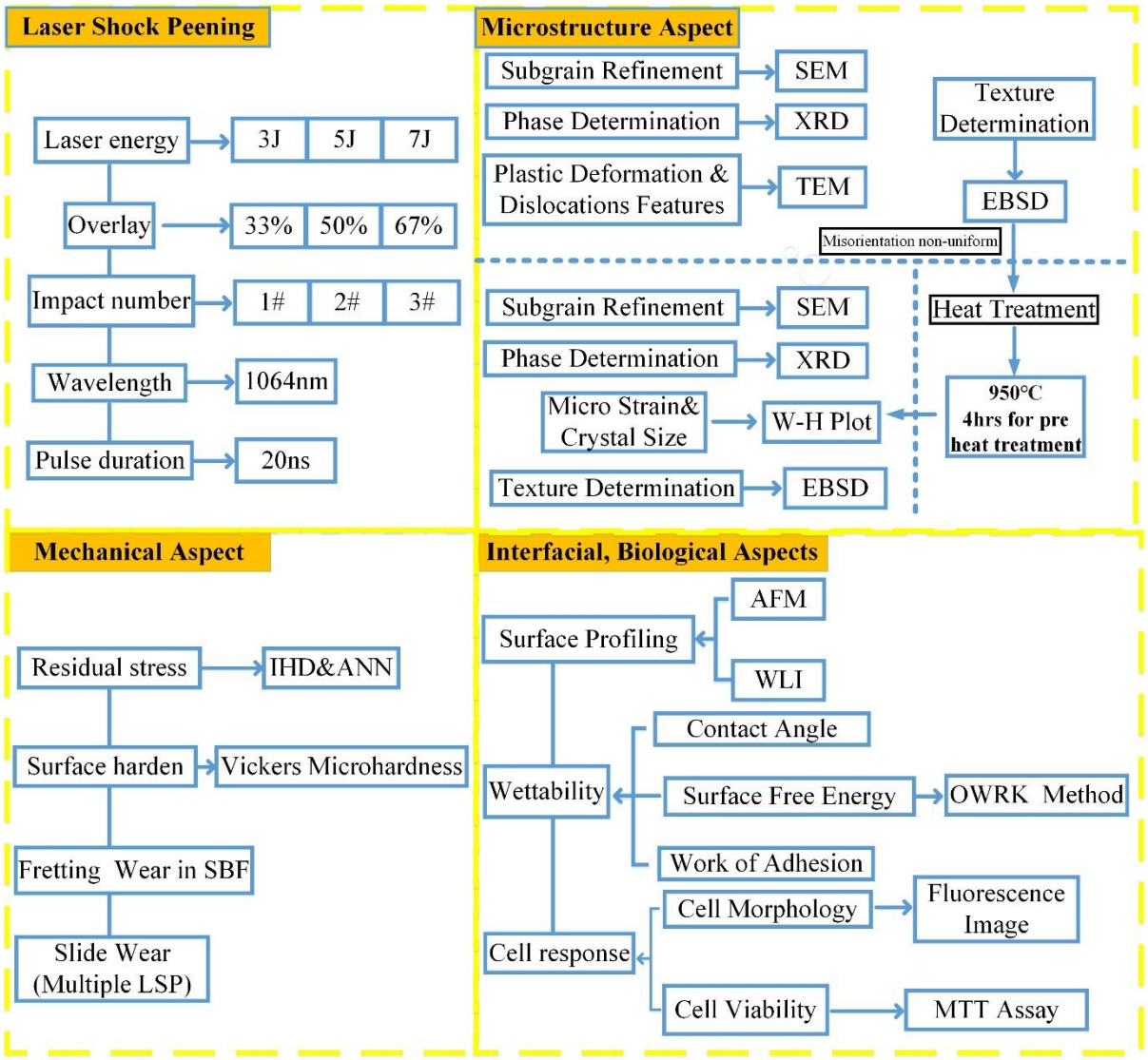

Figure 1.3 Thesis outline

Part 1

The research outline is given in Chapter 1 including research background (section 1.1), research aims and objects

In Chapter 2 and 3, the literature review is presented. Titanium and its alloy including mechanical properties, biocompatibility, corrosion behaviour and wear are described in chapter 2 section 2.1. To improve the above properties of titanium, surface modification methods are also reviewed in Chapter 3 section 3.2. Specifically, laser shock peening is introduced in section 3.3, and its application in Aerospace, Automotive and Nuclear reactor are reviewed. Section 3.4 discusses the medical application for laser shock peening.

Part 2

Chapter 4 characterized the microstructure of Ti-6Al-7Nb alloy subject to laser shock peening using SEM, EBSD and TEM

In Chapter 5, in order to acquire uniform globular α phase, heat treatment was carried out.

Chapter 6 analysed the microstructure of Ti-6Al-7Nb alloy subject to LSP after heat treatment.

Part 3

In Chapter 7 residual stress field are determined with multiple techniques, namely incremental hole drilling, X-ray diffraction and artificial neural network.

Chapter 8 gave and analyzed the mechanical experimental data including microhardness, and fretting wear. r

Chapter 9 investigate the effects of multiple LSP on the mechanical properties including microhardness, microstructure and sliding wear

Part 4

Chapter 10 examined the surface topography after LSP through AFM and white light interferometer

In Chapter 11, the wettability of Ti-6Al-7Nb alloy before and after LSP was studied by the sessile drop method. Additionally, the surface free energy and adhesion work were calculated in the following sub-section. Also, to analyze the results, the 3D surface profiling was provided.

In Chapter 12, biological properties experiments are given. Cell viability test was carried out.

1.4 Summary

As introduced in this chapter, the huge quantity demanded of artificial implants was introduced, addressing the necessity for employing an implant. In addition, the artificial implant failure reasons and human orthopaedic health data were discussed. The key challenges for the patients and medical engineers would be how to extend the service life of the artificial implant with a efficient technique to meet the requirement of the end-user. Therefore, LSP is proposed to improve the both mechanical and biological properties of a medical-grade titanium alloy (Ti-6Al-7Nb). As Ti-6Al-7Nb alloy has never been process by LSP, the premium LSP processing parameters would be another key scientific challenge. Lastly, the project aims and objective, and the structure of the research are also presented.

CHAPTER 2 State-of-the-Art in Titanium Alloys and Their Surface Modifications as Used for Medical Applications

This chapter reviews existing literature on basic titanium properties, applications and surface modifications. The use of titanium as biomaterials are widely common due to the excellent mechanical, easy of manufacturing and biocompatible properties. It majorly reviews titanium and its alloy employed as orthopaedic implants. The basic mechanical properties, biocompatibility, wear and corrosion resistance of Ti-based biomaterial are also summarized. Furthermore, it is necessary for implants to comprise of necessary mechanical properties and physical characteristics to enable implants to maintain their strength and for a significant period of time by surface modifications. Therefore, such comprehensive surface modification techniques for titanium alloys are briefly discussed. The biocompatible properties of titanium implants were enhanced by surface roughening or coating biocompatible materials. Such techniques not only satisfy the end-users but also improve the standard of living conditions. This work illustrates the current trend of titanium-based alloys and surface modification techniques, which contributes to the end-user to understand the pros and cons of titanium made implants.

2.1 Introduction

2.1.1 State-of-the-Art in titanium alloys and other metallic as used for medical Applications

It is in the early 1940s that Titanium alloys were introduced in the medical areas such as the Bothe *et al* [32] and Okabe *et al* [33], investigated the reaction of bone to metallic implants. Titanium and its alloys have been widely used in orthopaedic implantations due to its excellent biocompatibility and mechanical properties [34]. A great variety of implants for many different designs are now made from titanium in either its pure or its alloyed forms.

2.1.2 Mechanical properties of titanium and its alloys for orthopaedic applications

Metallic materials, which under concern for fabricating medical devices were mainly considered from mechanical properties namely, tensile strength, hardness, modulus and elongation. The elastic modulus mismatch between implantation devices and bones also causes "stress shield" phenomenon. Since the 1960s, such as titanium alloy, stainless steel and Co-Cr

alloys have been widely employed in the medical area. However, metallic based implants possess much higher Young's Modulus than human bones which will cause stress shielding which has been discussion in Chapter 1. Thus, the design and manufacturing orthopaedic materials should possess an equal modulus to the bone for bearing loads. Figure 2.1 illustrates the elastic modulus of titanium and its alloys compared with bones, Cr-Co alloy and 316l SS[35]. As we know that the bone modulus varies from 4 GPa to 30 GPa differentiating from the bearing type of bone and direction of measurements [36]. However, both the modulus of Cr-Co alloy and stainless steel are greatly higher than load bones. This will lead to a stress shielding effect, thereby, causing the implant to loosen. Compared to 316L stainless steel (210 GPa) and Cr-Co alloy (240GPa), the titanium alloys possess a lower modulus varying from 55 GPa to 120 GPa. Thus, among those implant metallic materials, titanium alloys are selected for most medical applications due to its high strength and low modulus.

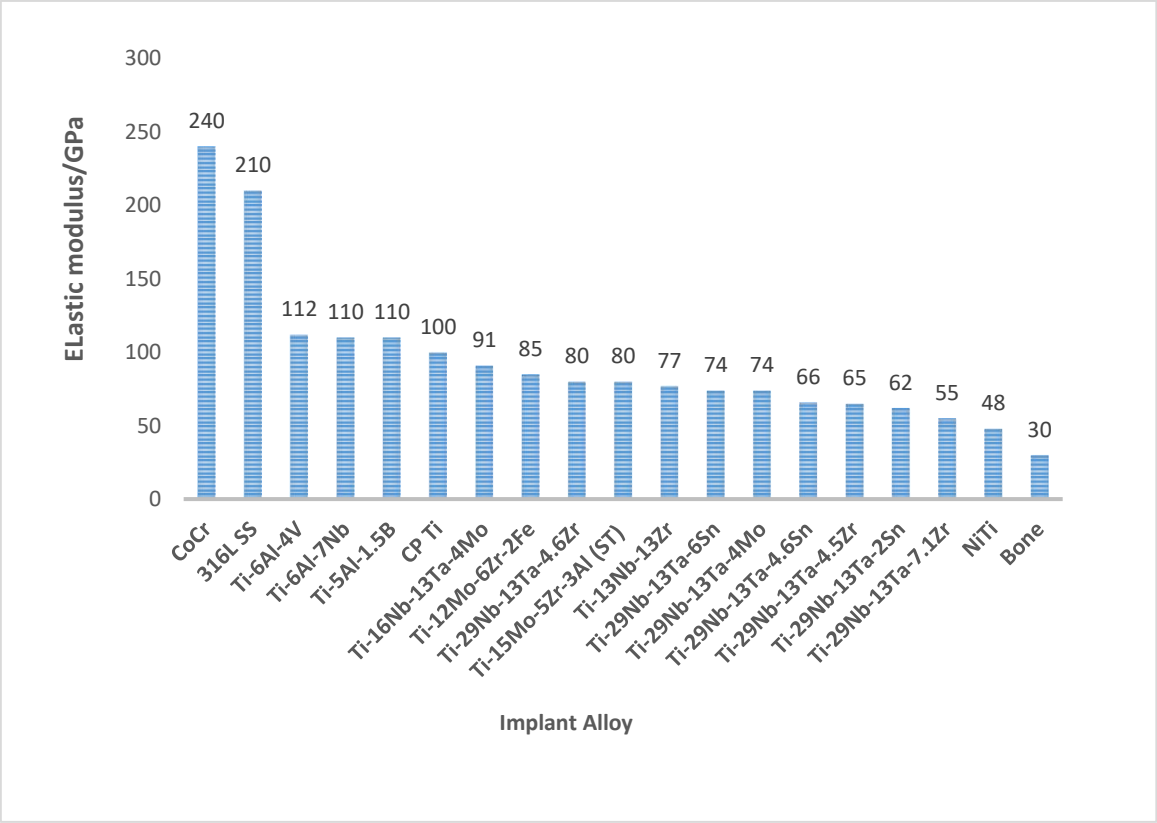

Figure 2.1 The elasticity modulus of titanium alloys are compared with bones, Cr-Co alloy and 316l SS.

Although the elastic modulus Ti-6Al-4V (TC4 or Ti64) alloy is half than that of stainless steels or Cr-Co alloy, the modulus of Ti64 is still high (100 GPa) compared to bone modulus (30 GPa). Phase α and phase α/β titanium alloys were the first generations to reduce the elastic

modulus of orthopaedic implants from the 1950s to 1990s [7]. The mismatch between bones and implants could lead to the stress shield effect, causing the fracture of the remodelled bone. For example, a femoral stem made by titanium alloy with high elastic module bears considerable part of body loading, which shields the necessary stress to maintain the density, strength and health structure for recovering. In order to balance the mismatch, Song *et al.* [37], found that adding elements Nb, Zr, Mo, and Ta into titanium alloy can decrease the elastic modulus of bcc Ti without weakening the strength. According to Since the 1990s to date, researchers focused on the β type titanium alloys that process closer elastic modulus to bones and excellent cold workability, high strength. Ti-13Nb-13Zr [38], Ti-12Mo-6Zr-2Fe [39], Ti-15MO-5Zr-3AL [40], Ti-29Nb-13Ta-4.6Zr [41] and Ti-35Nb-7Zr-5Ta [42] alloy are all the second generation orthopaedic titanium that modulus vary from 55 GPa to 84 GPa. Ti-35Nb-7Zr-5Ta (TNZT) elastic modulus ranks the lowest places amongst theses β titanium alloys at 55 GPa. From a mechanical point of view, the strength of β type titanium alloys can be improved by cold working according to Young's modulus law. Therefore, β type titanium alloys are receiving more attention for research.

Additionally, when orthopaedic implants are undergoing repeat daily body action, they are naturally affected by cyclic loading. For the long term, this can lead to changes in plastic deformation of small zones of the stress of concentration. The response of the material to repeated cyclic loading is determined by the fatigue strength of the material. Factors such as strength, materials, shape, loading type determine the long-term success of the implant subjected to cyclic loading [43]. Amongst these factors, if the strength of metallic materials is not enough to support the repeated cyclic loads or object impacts, patients will not need to undergo another revision surgery, due to the fracture of orthopaedic implants. Although fatigue is so critical properties among biomaterials, the standard fatigue test methods have not been established as simulating actual implantation and loading condition is too expensive and difficult. 'Standard' fatigue measurement consists of bending, tension(compression), and rotating bending/flexural are normally used to characterize the mechanical properties of materials, candidates before implantations.

Table 2.1 Mechanical properties of titanium alloys [44-46].

	Titanium	YS (MPa)	TS (MPa)	E (GPa)	$T_\beta(^0C)$	Hardness

α	High purity Ti (99.98% Ti)	140	235	100-145	882	100
	CP-Ti grade 1(0.2Fe-0.18O)	120	170-310	>210	-	120
	CP-Ti grade 4 (0.5Fe-0.4O)	260	480-655	>550	100-120	260
	Alloy grade 6 (Ti-5Al-2.5Sn)	827	861	109	1040	300
Near α	Ti-6-2-4-2-S(Ti-6Al-2.7Sn-4Zr-2Mo-0.1Si)	990	1010	114	995	340
	TIMETAL 1100(Ti-6Al-5Zr-0.5Mo-0.25Si)	900-950	1010-1058	112	1010	-
	TIMETAL 685	850-910	990-1020	120	1020	-
α+β	Ti-6-4 (Ti-6Al-4V)	800-1100	900-1200	110-140	995	300-400
	Ti-6-6-2(Ti-6Al-6V-2Sn)	950-1050	1000-1100	110-117	945	300-400
	Ti-6-2-4-6(Ti-6Al-2Sn-4Zr-6Mo)	1000-1100	1100-1200	114	940	300-400
	Ti-17 (Ti-5Al-2Sn-2Zr-4Mo-4Cr)	1050	1100-1250	112	890	400
Near β	SP 700 (Ti-4.5Al-3V-2Mo-2Fe)	900	960	110	900	300-500
	Beta III(Ti-11.5Mo-6Zr-4.5Sn)	800-1200	900-1300	83-103	760	250-450
	Beta C(Ti-3Al-8V-6Cr-4Mo-4Zr)	800-1200	900-1300	86-115	795	300-450
	Ti-10-2-3(Ti-10V-2Fe-3Al)	1000-1200	1000-1400	110	800	300-470
	Ti-15-3(Ti-15V-3Cr-3Al-3Sn)	800-1000	800-1100	80-100	760	300-450

YS: Yield strength; TS: Tensile strength; E: Elastic modulus: T_β: Beta transus temperature

Nonetheless, titanium and its alloys process excellent mechanical performance, required by the aforementioned tests, which are summarized in Table 2.1.The Mechanical properties (especially fatigue resistance)of titanium alloys are mainly determined by microstructures that are formed during thermal and manufacturing processes. Titanium has two allotropic forms. One of them is a hexagonal close-packed crystal structure (HCP, α phase,) at room temperature [47, 48]. This structure is stable at temperatures up to 873^0C, above which, α phase transferred to a body-centred cubic structure (β-phase body-centred cubic (bcc)) [49]. Intermediate amounts of alloying additions allow both alpha and beta phase stability at room temperature. Using this principle, two-phase alloys have been developed with superior mechanical properties; an example of this is Ti-6Al-4V. This alloy contains, mostly, α+β titanium, due to its balanced strength and toughness and it is the first registered titanium alloy (ASTM standard F136). In terms of β-alloy, although, its elastic modulus value is comparative smaller than that of α+β titanium, the fatigue resistance of β-titanium is lower under the same fatigue testing condition. For instance, Under RBF (R=-1/60 Hz), the fatigue limit of Ti-35Nb-7Zr-5Ta is 265 MPa, which is much lower than that of TC4 (610 MPa) at the same testing condition [7].

However, although β-titanium alloy has comparably poor performance in smooth fatigue resistance, the behaviour of orthopaedic implants are more closely associated with notch fatigue behaviour in vivo conditions. For example, hip stems and femoral normally coated which induced stress concentration sites. Thus, regarding notch fatigue behaviour, β titanium alloy has a comparative better performance than TC4.

2.1.3 Biocompatibility of orthopaedic titanium alloys and osseointegration

Biocompatibility denotes the capability to contact with a living system without producing an adverse effect [50]. The reasons why titanium is considered as biocompatible is attributed to the outstanding corrosion resistance in body environment, bio-inertness, capacity for osseointegration and high fatigue strength. Once titanium is inserted into the human body, a serious of reactions with proteins, cells and body fluid will happen in the biological microenvironment (Figure 2.2).

Osseointegration refers to the formation of an interface between implant surface and bones. More specifically, Branemark [51], stated that a direct functional and structural connection between the surface of a load-carrying implant and ordered living bone. According to this, it has been used to describe the interaction of implants and bones. Thus we should know, what

has happened after the replacement of the implant. Once the implant is inserted in *vivo*, within 10^{-9}s, water molecules layer is formed on the implant surface, which benefits the the adsorption of proteins and cells. Onwards, within 30s to hours, proteins cover the surface of water molecules layers. Those proteins are from tissue fluid and blood near the insertion site and the ones later come from cellular activity. After the proteins adsorption, from few hours to days, cells adsorption occurs on the adsorbed protein layers, thereby, starting cellular adhesion, migration and differentiation [52-55]. Degree of the interaction of the above stages is influenced by the implant surface topography and chemical composition, which determines the healing effects of orthopaedic implants. There is no evidence shown that the implant materials have a completely no-adverse effect. Compared to Co-Cr alloys and the stainless steel, titanium and its alloys have a better performance in osseointegration as a stable TiO_2 layer is formed on the surface of titanium alloys, which also contributes to the biocompatibility.

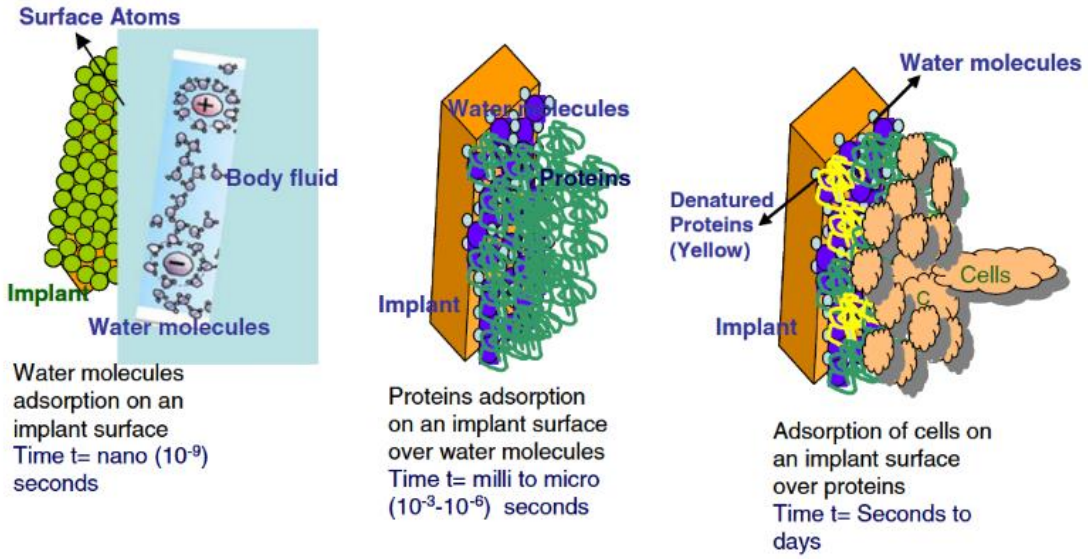

Figure 2.2 The evolution of interaction between human bone with implants at different time intervals [7].

2.1.4 Corrosion behaviour of orthopaedic titanium alloy

Orthopaedic implants made from titanium and its alloys all undergo corrosion as they are contacting body fluid after being inserted in the human body. Additionally, the body environment is corrosive due to the chloride ions and proteins, thereby, causing different kinds of chemical reaction on the implant surface. The metallic elements are oxidized to ionic forms and hydroxide ions are reduced by the dissolved oxygen, finally leading to the corrosion process [56].

The human body fluid is a complex environment, including amino acids, proteins, organic compounds etc. Thus, corrosion would take place after the implant was replaced in the body. This gives rise the need for surface modification techniques to avoid and pre-long the onset of corrosion. Such a technique could be in the form of plastic burnishing, shot peening, or laser-based peening technique.

Compared to stainless steel, titanium and its alloys have immunity to both pitting corrosion and stress corrosion cracking in chloride solution. The reason why titanium has such excellent performance in corrosion resistance can contribute to the formation of a very chemically stable, highly adherent, and continuous protective oxide film (TiO_2 film) on the titanium surface [57-59]. The passive TiO_2 film is formed spontaneously in nature and remain stable, which separates Ti from the outside environment avoiding the further oxidation. Normally, the thickness of the TiO_2 film is around 10-20nm [60] would affect the oxide stability. As stated previously, in section 2.1.2, the TiO_2 can provide favourable osseointegration. The passive films prevent further transport of metallic ions or electrons across the film. For instance, Ti64 has been widely used in the medical area. However, element Al and V are toxic to the human body. Once the film covered the metal surface is broken, Al and V ion will be released into the body fluid as metal ions, causing Alzheimer's and neuropathy disease [61]. Thus, the films must be compact, and possess an atomic structure, thereby, limiting the transportation of ions across the films from the body fluid.

In terms of corrosion, the biggest weakness of titanium appears to be crevice corrosion in industry, while for medical applications, it is not the main concern. Liang et. al. [62], examined the crevice corrosion behaviour of Ti-6AL-4V , and commercial pure titanium (CP Ti) and Ti-Ni Shape memory alloy (SMA) in Ringer's fluids at the potential of 400 mV. In terms of temperature, the crevice corrosion of all three titanium alloys have a positive correlation with that. Among these three alloys, the crevice corrosion resistance of Ti64 is better than that of CP Ti and SMA Ti-Ni.

The majority of the medical implants are exposed to low-frequency loads which leads to the corrosion fatigue. For example, the fatigue corrosion may occurred in the total hip implant due to the daily walking as it can result in a cyclic loading with the frequency of 1Hz. Yu *et al* [63], studied the corrosion behaviour of Ti-6Al-4V alloy post multiple surface treatments under a cyclic loading condition at 1.25Hz. They found that surface treatment such as heat-treatment

and nitrogen ion implantation can enhance the fatigue corrosion resistance, through refining prior-β grains.

Fretting corrosion is another typical amongst load-bearing orthopaedic implants. In the hip implant, it often occurs at the interfaces between the bone and the stem, stem and cement, and on the interface of modular connection between implant components. As discussed above, cyclic loading can not only lead to fatigue corrosion but also fretting corrosion because of the small motion (1-100 μm) between implants parts. What is more, surface roughness is another factor affecting fretting corrosion of titanium. For that case, Sivakumar *et al* [64], investigated the effect of roughness from 43nm, 116nm,177nm and 474 nm on fretting corrosion of commercial pure titanium in Ringer's solution for the medical application. The anodic polarization and EIS results showed that the sample with Ra 43nm exhibits the best corrosion resistance performance as the formation of less defective and impermeable TiO_2 layer. In addition, fretting corrosion phenomenon is also found in a joint between titanium and nitinol. Fretting corrosion behaviour of nitinol spinal rods with TC4 was investigated in simulated body fluid by Lukina *et. al*. [59]. Their study reveals that nitinol spinal rods with TC4 screw are vulnerable to fretting corrosion.

2.1.5 Wear in titanium alloy

As we know the biomaterials shouldn't be cytotoxic which is caused by increasing ion content in the human body from the metallic implant. That disease is called metallosis which is a side effect from replacements, such as metal-on-metal hip implants, made from different metals [65, 66]. The metal particle will be released into human blood from the metal implants when the two metals wear against each other.

Wear is a vitally critical problem in any joint application, and it contributes 13.6% of all implants failure reasons [14]. Wear is inevitable that it appears in the joint of artificial implants as a result of the mixed lubrication regime. When the implant is working, tremendous microscopic particles are cut into the body fluid due to cutting motions during the movement of the joint. Some of cutting particles are left inside the tissues, thereby, maybe leading to foreign body reaction such as the activations of macrophages and foreign body giant cells [67]. A revision surgeon not only means money-cost and time-consuming but also extremely pains for patients. Thus, the wear resistance of titanium plays a very important role in manufacturing orthopaedic implants.

Due to the low hardness, titanium and its alloys have comparatively poor tribological properties and fretting fatigue resistance, which has normally been presented with a high coefficient of friction, severe adhesive wear and low abrasion resistance. Titanium has a tendency that it moves or slides to gall, thereby, seizing, when titanium is rubbing between itself or other materials. The movement of these two bodies may cause to more intensity wear because adhesion couplings are created and the surface oxide layer becomes unstable, especially third bodies show up, Figure 2.3 [68]. Due to these drawbacks, 10%-20% of joints which consist of titanium-made head and polymer cup need to be replaced with 15 to 20 years [18]. More, aseptic Loosen (50.1%, 1st) and wear (13.6%, 3rd) are the main two failure reason for implant devices according to NHS annual reports [14]. Due to the human body activity, the wear debris are rubbed off the implant to the surrounding human body tissue, leading to bone resorption, which will finally result in aseptic loosening which is 32.54%. Amongst the aseptic loosened of femoral heads made by 316l SS, Co-Cr-Mo system alloy and Ti-6Al-4V EI, titanium alloy possess the highest average wear 74.3% against high molecular weight polyethylene acetabular component [69]. That drives us to explore another surface modification technique, such as shot peening, surface coating, laser shock peening, blast cleaning, or laser polishing. However, in order to improve the wear resistance of titanium alloys, a technique that enhances the mechanical property and gives better structural integrity is more favourable in this instance. Thus, laser shock peening would be more suitable as it induces a deep level of compressive stresses in comparison to their techniques mentioned.

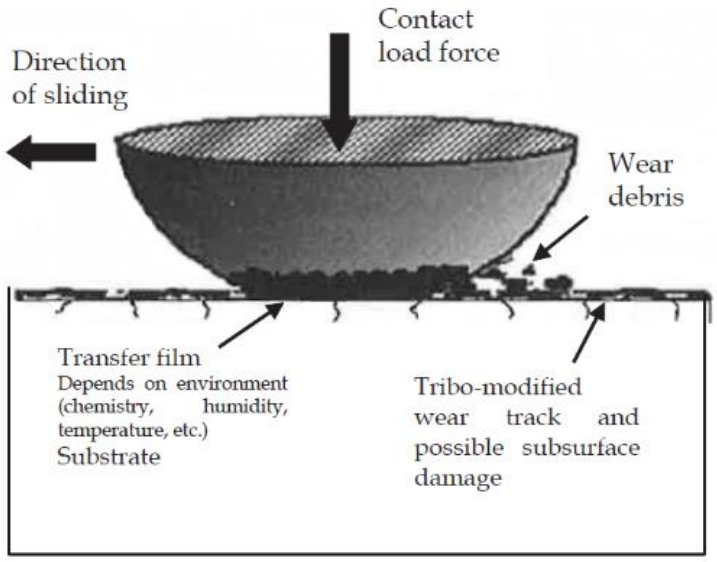

Figure 2.3 A schematic diagram illustrating the sliding tribology with a ball pin [68].

2.2 Titanium alloys for medical applications

2.2.1 Dental application

Titanium alloys are widely used for manufacturing dental implants and orthopaedic prostheses. This cost around more than 1000 tones in manufacturing titanium devices over the world every year [70]. Before titanium and its alloys, stainless steel and cobalt-chromium were employed as dental implant materials. However, the low success-implanting rate and poor osseointegrative performance limit their further applications in manufacturing dental prosthesis. For now, endosseous dental implant applications specifically require titanium alloys. This is because they possess excellent corrosion resistance, high strength-to-weight ratio and outstanding osseointegration. Therefore, titanium and its alloys have a long history in clinical applications for both dental and orthopaedic implants dating back to 1965 [71]. Since the 1980s, with the development of the computer-aided design (CAD), dentistry devices namely dental bridges, crowns, screw, abutment, and over-dentures are manufactured by titanium alloys.

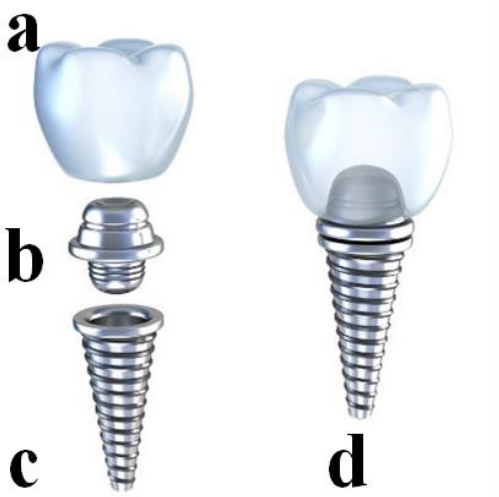

Figure 2.4 Dentistry devices: (d) includes dental implant abutment (b), the porcelain crown (a) and the titanium prost (c) [72].

As shown in Figure 2.4, in the bottom, it is a titanium screw with a longitude of 8-16 mm which is implanted into a prepared dental alveolus in the jaw and acts as a replacement root for the missing tooth. In the top, a special attachment component called the abutment is used to fit the

top of the implant, thereby, forming the external connection with a dental crown or dental bridges.

In titanium dental implanting surgeries, there is a 9 out 10 success rate and the service life of the components could last 30 years or more due to its strong and durable properties. However, some patients are allergic to titanium that exhibit in the form of urticaria, mucosa, atopic dermatitis, pain and necrosis.[73] Therefore, it is necessary to undergo a Memory Lymphocyte Immunostimulation Assay (MELISA) test to diagnose a number of different metal allergies.

2.2.2 Hip joint implants and other applications

CP Ti and Ti-6Al-4V alloy is a good choice around the world for orthopaedic joint replacements, namely, total knee replacement and total hip replacements (Shown in Figure 2.5 and Figure 2.6).

Figure 2.5 Digital image displaying a prosthetic hip implant [74].

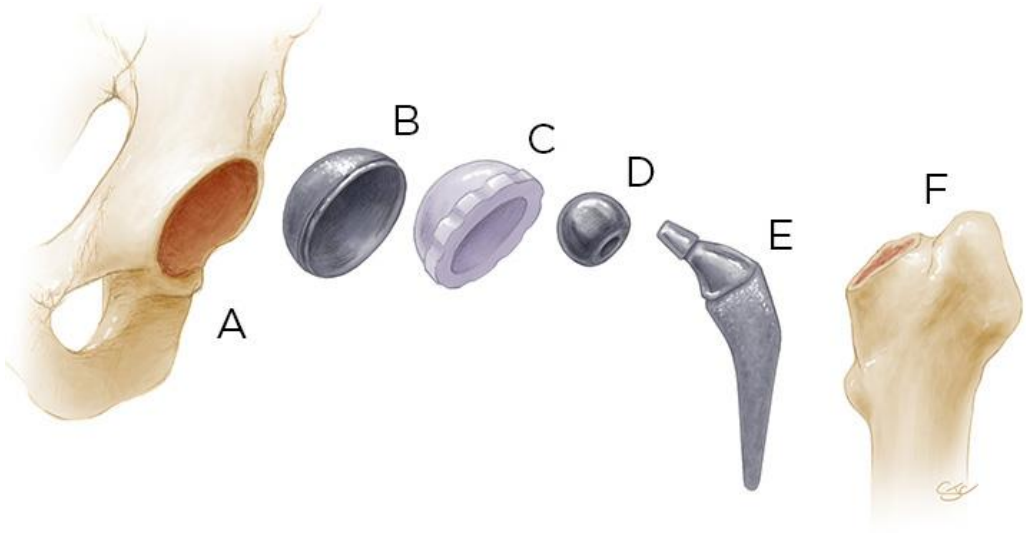

Figure 2.6 Components of hip replacement surgery: the acetabulum in (a), or socket of the ball-and-socket joint, is reamed to receive the cup in (b) and the liner in (c). The ball (d) is placed on the stem (e) which is then inserted into a hollowed-out femur in (f), or thigh bone liner ball are made of titanium alloys [75].

Hip joint replacement surgery is the most common clinical surgery over the world for most patients. Hip implant components are made of plastic (polyethylene), metal, ceramic or a combination of the materials. A hip joint implant can be divided into four categories according to the connection between socket and ball. They are: ceramic-on-plastic; metal-on-plastic; metal-on-metal, ceramic-on-metal and ceramic-on-ceramic. In a metal hip joint system, structural components such as acetabulum, the socket of the ball-and-socket joints are normally made of titanium alloys. Although the metal-on-metal system presented a very low wear rate in the laboratory experiment, the bearing surface using titanium alloys is no longer suitable for long-term replacement as there is the record that patients require the revision surgeries due to metal-on-metal system. For now, the combination of ceramic and plastic with titanium is more popular than just metal hip systems. What is more, titanium alloys are also involved in manufacturing shoulder and elbow joint replacements. Bone plates, screws, staples, cables and mesh manufactured by titanium and its alloys facilitate fixation and support broken bones.

Not limited to orthopaedic applications, titanium alloys are not only involved in clinical instruments namely forceps, laser electrodes and dental drills but also be used in neurosurgical

applications including acrylic, cranial plates and mesh. What is more, it has been 3-D printed manufacturing rib cages for use by children and elder people.

2.3 Review on surface modifications for titanium and its alloys

As surface properties decide the long-term performance of medical devices, various surface modifications are needed prior to implants stabilization [76]. There are many reasons to perform the surface modification of implants before implantations, which are summarized in Table 2.2.

Liu *et al* [77]summarized the main surface modification methods of titanium alloys are in Table 2.3. In this section, those methods will be reviewed, along with the recent research evaluating the use of the surface modification of titanium alloys in orthopaedic application, as well as future perspectives. The goal is to improve biocompatibility, corrosion and wear resistance of titanium alloys.

Table 2.2 Reasons for surface modification of Ti and its alloys.

Surface modification effect	Reasons
Mechanical purpose	Improve the fatigue life
	Increase the hardness for wear resistance
	Improve adhesion in bonding
Biological purpose	Increase the osseointegration
	Introduce a passive layer to prevent toxic ion being released into the body
	Clean surface material and improve bacterial resistance

Table 2.3 A summary of main surface modification of titanium alloys [76, 77].

Surface modification methods	Modified layers	Objective
Mechanical methods: Machining,	The smooth or rough surface formed by the subtraction process	Produce specific surface topographies; clean and roughen surface improve adhesion in bonding

grinding Polishing blasting		
Chemical methods Alkaline treatment Acidic treatment Hydrogen peroxide treatment	<10 nm of the surface oxide layer ~1 μm of sodium titanate gel ~5nm of dense inner oxide and porous outer layer	Remove oxide scales and contamination Improve biocompatibility, bioactivity or bone conductivity
Anodic oxidation	~10 nm to 40μm of TiO_2 layer, adsorption and incorporation of electrolyte anions	Produce specific surface topographies; improved corrosion resistance; improve biocompatibility, bioactivity or bone conductivity
Sol-gel	~ 10μm of thin film, such as calcium phosphate, TiO_2 and silica	Improve biocompatibility, bioactivity or bone conductivity
Biochemical methods	Modification through silanizaed titania photochemistry, sel-assembled monolayers, protein-resistance etc	Induce specific cell and tissue response by means of surface-immobilized peptides, proteins, or growth factors
Physical methods Thermal spray Flame spray HVOF DGUN	30~200 μm of coatings, such as titanium, HA, calcium silicate, Al_2O_3, ZrO_2, TiO_2	Improve wear resistance, corrosion resistance and biological properties
PVD (Physical Vapour deposition) Evaporation Ion plating	~1 μm of TiN, TiC, TiCN, diamond and diamond-like carbon thin film	Improve wear resistance, corrosion resistance and blood compatibility

sputtering		
Ion implantation and deposition Beam-line ion implantation PIII	~10 nm of surface modified layer and/ or ~1 μm of thin film	Modify surface composition; improve wear, corrosion resistance, and biocompatibility
Glow discharge plasma treatment	~ 1nm to ~ 100 nm of surface modified layer	Clean sterilize, oxide, nitride surface removed the native oxide layer

2.3.1 Mechanical methods for surface topography modification

Mechanical methods including grinding, polishing, machining have been wildly used for acquiring a rough or a smooth surface through shaping or removal of the material's surface. The purpose of the mechanical way is to acquire specific surface topographies and roughness which contributes to the adhesion within a body environment. Alternatively, cleaning-off surface contamination is another option. In terms of metallic materials, machining changed deformations and the surface structure, as well as the increased surface hardness. Generally, mechanical methods result in a rough structure. Increased surface roughness is considered more beneficial to cell adhesion, proliferation and differentiation, which are important factors of osseointegration. Among those methods, sand-blasting has been one of the most used techniques. The usual abrasive particles of the blasting media are silicon carbide, alumina, hydroxyapatite and β-Tricalcium phosphate and biphasic calcium phosphates (BCP) [78]. Sand-Blasting is the process that impact of a jet of abrasive particles against the surface by compressed air which may lead to surface contamination and local inflammatory reactions of surrounding tissues as a result of the dissolution of abrasive particles into the body environments [79]. Fini *et al* [80], pointed out that rougher surface exhibited better bone response after the implantation in the *vivo* environment.

2.3.2 Acide and alkali treatments

Acid treatment is in general employed to wipe out the oxide and contamination for achieving desirable clean and equilibrium surface finishes. TiO_2 consists of the main oxide layered of titanium alloys as titanium can easily react with O_2. To remove the oxide layer before further coating, 10~30vol% nitric acid and 1~3 vol% in distilled water involve the standard solution

for acid-pretreatment of titanium and its alloys. Hydrofluoric acid is able to react with TiO_2 rapidly, forming soluble titanium fluorides and hydrogen. A ratio of 10 to 1 of mixed hydrofluoric acid and nitric acid can be employed for decreasing the formation of free hydrogen to prevent embrittlement surface layers caused by the inclusion of hydrogen [81]. Normally, a thin oxide layer is formed by acid etching with a depth under 10 nm. More than that, its growing speed is much slower than that of untreated, from 3-6nm within 400-day period [82].

Alkali-Heating Treatment (AHT) is a surface modification technique of immersing titanium alloy in alkali solution (KOH or NaOH). After AHT, bioactive porous layers on the material surfaces was formed, followed by heating treatment to dehydrate and transform the amorphous structure into porous crystalline [83]. Kim et al [84] started by immersing in a 5~10 ml[85] KOH or NaOH for 24 hrs, then rinsed in distilled water and ultrasonic cleaning. Onwards, dried in the oven and the carried on the thermal treatment that heating the material at the temperature of 600-800 C° for 1h. The heating treatment is required to be performed at a low pressure of 10^{-4} to 10^{-5} bar to avoid titanium oxidation at high temperature. After the thermal treatment, the porous sample is soaked in simulated body fluid (SBF) for 4 weeks, onwards bioactive bone-like apatite is formed on the surface of the titanium. This processing can also be described by the following chemical formulations:

$$TiO_2+NaOH \rightarrow HTiO_3^-+Na^+$$

$$Ti+3OH^- \rightarrow Ti(OH)^+_3+4e^-$$

$$Ti(OH)_3^+ + e^- \rightarrow TiO_2\ H_2O + 1/2\ H_2\uparrow$$

$$Ti(OH)_3^+ + OH^- \leftrightarrow Ti(OH)_4$$

Hydroxyl attack on the hydrated TiO_2 generates negatively charged hydrates on the surfaces:

$$TiO_2*H_2O+OH^- \leftrightarrow HTiO_3^-*nH_2O$$

An alkalinic titanate hydrogel layer is formed as the negatively charged substances combine with the alkali ions in the solution. Onward, when it is heating, the hydrogel layer is dehydrated and become thicker, finally forming a crystalline alkali titanate or stable amorphous layer.

2.3.3 Osseointegration enrichment by ion implantation

Ion implantation (Figure 2.7) is a process that ions of a material are accelerated in an electric field and impacted to the solid surface to modify its physical characteristics[86]. There are various kinds of ions can be used to bombarded into substrate materials such as oxygen, nitrogen, carbon. Two common types of ions implantation methods are well known which are conventional beam line ion implantation and Plasma immersion ion implantation (PIII).

Additionally, Silver plasma immersion ion implantation (Ag-PIII) technique is used for implanted into Ti implant to enrich the osseointegration of acid-etched sand and blasted medical implants. What is more, Nitrogen (N) dual ions are also implanted with Silver (Ag). Ti-6Al-4V with an aluminium oxide-blasted surface was treated by Ag-PIII by Jorg et al, measuring the biocompatibility in vitro environment, and antibacterial effects. Ag-PIII gave a promising present for antibacterial functionalization of titanium from the results.

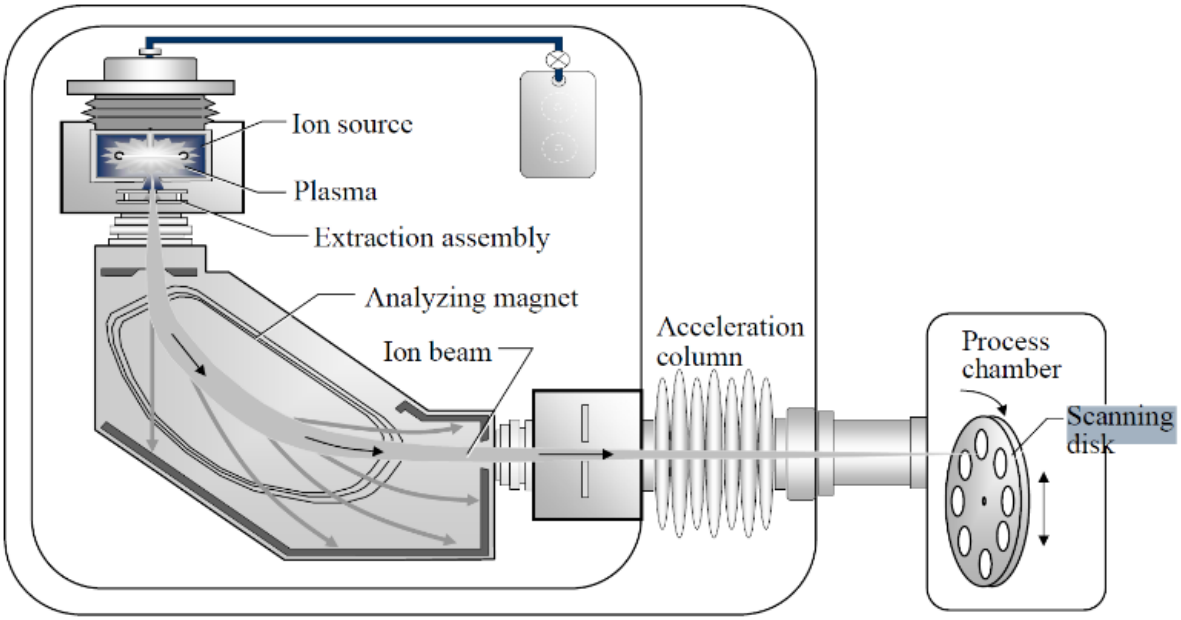

Figure 2.7 A schematic diagram showing the process of ion implantation. [87].

There are PIII-Ag-N (Ag ions prior to N implantation), PII-N-Ag (N priors to Ag ions implantation) and PII-Ag+N (Ag/N dual ions co-implantations). Li *et al*. [88] employed SEM, and XPS to compare the effect of antibacterial activity, corrosion resistance of titanium subject to PIII-Ag+N, PIII-Ag-N and PIII-N-Ag. The results showed the PIII-Ag+N is the most efficient process to achieve high antibacterial activity and corrosion resistance.

PIII-Zn+Mg were also employed to improve the ossoeintegration. PIII-Zn+Mg modified titanium implants were inserted as femurs into rabbit for 4 and 12 weeks by Yu *et al*.[89]. Micro-CT, push-out test and histological analysis indicates that PIII-Zn+Mg implant presents better capacities for enriching bone formation, thereby enhancing sustained biomechanical stability.

2.3.4 Plasma spray

Plasma spray is a thermal spray coating process to form a high-quality coating layer by a combination of high energy heat source, high temperature, an inert spraying medium, usually argon, and high particle velocities [90, 91]. The schematic diagram is shown in Figure 2.8.

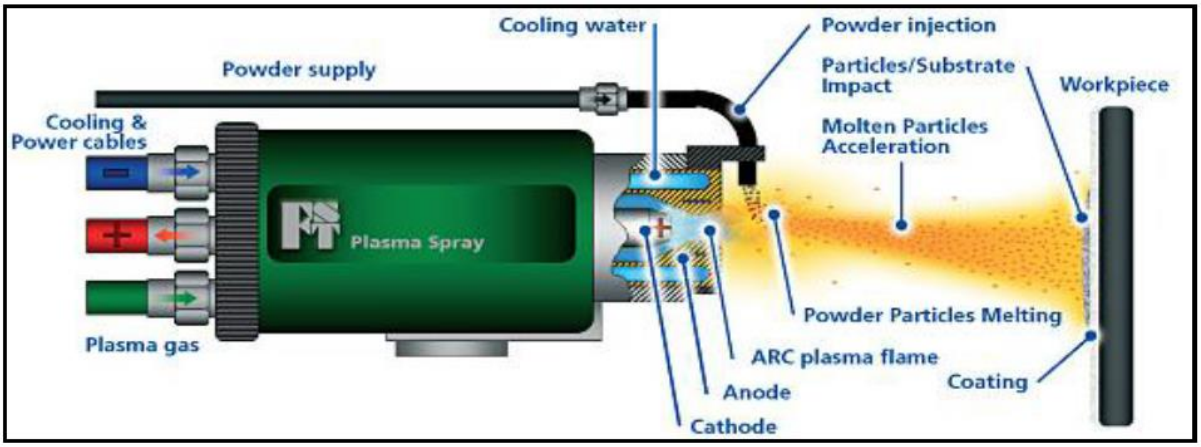

Figure 2.8 A schematic diagram showing the process of plasma spray. [91].

Plasma spraying is one kind of thermal spraying techniques. It has been widely used in industrial gas turbines, automotive, aerospace, medical, biomedical and electronics. Among those fields, currently, DC plasma arc devices are the most used in the commercial market. The plasma gun comprises a tungsten cathode and a copper anode which are cooled by water. Plasma gas, such as Ar, He, H_2 and N_2, flow around the cathode and through the anode. The anode is manufactured as a constricting nozzle and ionized[92]. During the spraying processing, the powder material is melted by using an electrical arc in the plasma plume, sprayed onto the substrate surface. In the jet, the density, velocity and energy of plasma are very high, which are very significant to the formation of coatings. Additionally, the temperature is another critical factor which is controlled by parameters of the plasma torch and the type of plasma gas. It is very impressive that the core region area temperature can reach a stable and extremely high value of 15726.9℃. Under that temperature, nearly no metal materials can “survive”, being turning into plasma gas. The equation 2-1 describes the relation in gas volume, the nozzle diameter and plasma beam intensity by Matejka *et al* [93]:

$$v = A\frac{Q_0}{d^2}\frac{T}{M} \qquad (2\text{-}1)$$

where V is the velocity of plasma(ms^{-1}); Q is the volume of gas flow rate (m^3s^{-1}); A is a constant value; d is the diameter of nozzle (m) ;T is gas temperature (K) and M is the molecular weight of gas Plasma has its advantage over other surface modification techniques. The advantage is that it can spray the materials at a very high melting temperature. What is more, a broader powder particle size range, typically 5-100 μm, and a variety of coating materials to meet different needs can be coated onto the substrate surface. The sprayed coating possess a rough surface which contributes to the adhesion of bone cells. Therefore, in terms of titanium, Ti_2O_2 Al_2O_3 and ZrO_2, are normally sprayed onto the titanium surface due to their excellent wear and corrosion resistance. Utu *et al* [94], deposited Al_2O_3+TiO_3 coatings on the commercial titanium using plasma spray. SEM, XRD and sliding wear test were employed and the results witness the improvement of wear resistance properties due to the increased surface coating hardness. However, such Al_2O_3 and TiO_3 can be used as the bond surface material between body and titanium. Thus, some more biocompatible materials need to be coated on the implant titanium alloy which is the focus of the next section.

2.3.4.1 Plasma sprayed Hydroxyapatite Coating on Titanium Alloy

In order to improve the osseointegration of the implant, Hydroxyapatite (Hap) coating is coated onto the implant surface to enhance the osseointegration. HAp ($Ca_{10}(PO_4)_6(OH)_2$) is a mineral form of calcium apatite. It is a calcium phosphate which is very similar to human bones in composition. The Ca/P ratio is 1.67 which is identical to human bones and about 70% of the mineral fraction of bone has an HA-like structure. In addition, Hap is very stable under human body conditions such as pH, temperature, and body fluids. Previous work [95], indicated that implants with an HA surface coating form a strong connection between the implants and the bone tissue in short-time.

However, one of the disadvantages of HA is that the mechanical properties are relatively weak. Focusing on the mechanical properties of HA coating, many researchers have contributed plenty of works. Specifically, in vivo and *vitro* study, Thian *et al.* presented the mechanical properties and morphology of HA/Ti-6Al-4V composition immersed by SBF solution for 2 weeks. The secondary phase namely Cao, TCP and TTCP, and were all found after immersion. The strength and modulus were found to decrease after immersing 4-6 weeks. What is more, Chu et al [96] conducted a *vivo* experiment of HA/Ti composite with New Zealand rabbits. The results demonstrated that there was excellent biocompatibility of HA/Ti after implant

integration with bones. HA/TiO_2 coating on porous titanium (Ti) was investigated as well. Chen *et al* [97] found that the data of protein adsorption and cellular shows the composite lay allows more adsorption of serum protein. This enhances the osseointegration of titanium made implants.

In order to improve the compressive strength, Zhang *et al* [98] studied the compressive strength of porous HA/Ti composites made by spark plasma sintering (SPS). They found that with 5 ~ 30 wt% HA content, the composite possessed high compressive strength (86 - 388 MPa) and low elastic modulus (8.2 ~ 15.8 GPa). In terms of corrosion resistance, Singh e*t al* [99, 100] acquired a better corrosion performance of titanium with HA-SiO_2 coating on the AISI 304 steel and Ti-6Al-4V titanium compared with uncoated. In addition, the corrosion behaviour and mechanical properties of HA coating on Ti-13Nb-13Zr composite was also investigated by He *et al* [101], Composite with 10% of HA exhibited outstanding corrosion resistance in SBF.

Another problem for HA coating is the poor bonding strength between the substrate and plasma sprayed HA coatings. Kweh *et al* [102], found that, in vitro, the mechanical properties of the bonding coatings deteriorate with the increasing immersion time in SBF. The reason for this was due to the mismatch of the thermal expansion of titanium (8.4~8.8) $\times 10^{-6}K^{-1}$) and HA ($13.3\times 10^{-6}K^{-1}$). Thus, residual stress is generated and it is found to be the reason for the low bonding strength.

Resorption and degradability of HA coatings are another two important concerns in body environment. This leads to the disintegration of the coating, resulting in loss of the bonding strength and implant fixation. During the spraying, the temperature of the core plasma torch could reach extremely high. When the HA powder particles experience the high flame temperature, thermal decomposition happens. This might lead to the different crystal structure formations of substances, such asα-tricalcium phosphate(α-TCP), Calcium oxide (CaO), oxyhydroxyapatite (OHA), β-tricalcium phosphate, calcium-deficient hydroxyapatite (CDHA) and tetra-calcium phosphate (TTCP). The thermal effects on Hydroxyapatite are listed in Table 2.4.

Table 2.4 Thermal effects on Hydroxyapatite.

Temperature	Reactions

25-600℃	Evaporation of absorbed water
600-800℃	Decarbonation Dehydroxylation of HA forming partially
800-900℃	Dehydroxylated(OHA) or completely dehydroxylated oxyapatite (OA)
1050-1400℃	HA decomposes to form β-TCP and TTCP
<1120℃	β-TCP is stable
1120-1470℃	β-TCP is converted to α-TCP
1550℃	Melting temperature of HA
1630℃	Melting temperature of TTCP, leaving behind CaO
1730℃	Melting of TCP

It has been reported that these amorphous and metastable compounds are more soluble than crystalline HA [103]. These dissolved phases have shown good performance in proteins and cell attachments, which benefit the implant fixation, promoting bone remodelling. However, the dissolution of the amorphous and metastable compounds in HA coating is undesirable as it leads to the decreasing of the mechanical bonding strength. Therefore, from long term prospect, high pure crystallinity Hydroxyapatite is more preferred in plasma spraying industry.

2.3.5 Laser surface texturing

Laser surface texturing, also known as laser texturing, laser structuring or laser patterning, is a laser-based surface modification technique deployed for changing the material properties namely tribology, wettability and biocompatibility. As shown in Figure 2.9, a nanosecond/ picosecond pulsed laser was fired to irradiate the target material surface with a particular spot size and overlap. The pulsed laser induced concentrating energy exceeds to the material`s ablation threshold thereby removing the surface material selectively. What is more, the textural processing time is mainly determined by the laser system parameters (output power, laser spot size), the target material, and the desired surface finishing level.

According to the pulse width, lasers can be classified into microsecond laser, nanosecond laser, femtosecond laser and picosecond laser. The early LST was carried out with long pulse lasers namely nanosecond excimer laser, nanosecond Nd:YAG laser and picosecond laser. More recently, with the development of ultrafast laser, shorter pulse laser like picosecond laser starts to emerge in surface texturing. Both surface texture processing was performed via laser ablation. But the interaction with the target materials differs between nanosecond and

femtosecond scale. Specifically, heat diffusion from ultrafast laser to lattice is hindered as the pulse duration is much shorted than longer pulsing laser, which results in less recrystallized burr around the crater and the heating affected zone (HAZ), higher precision.

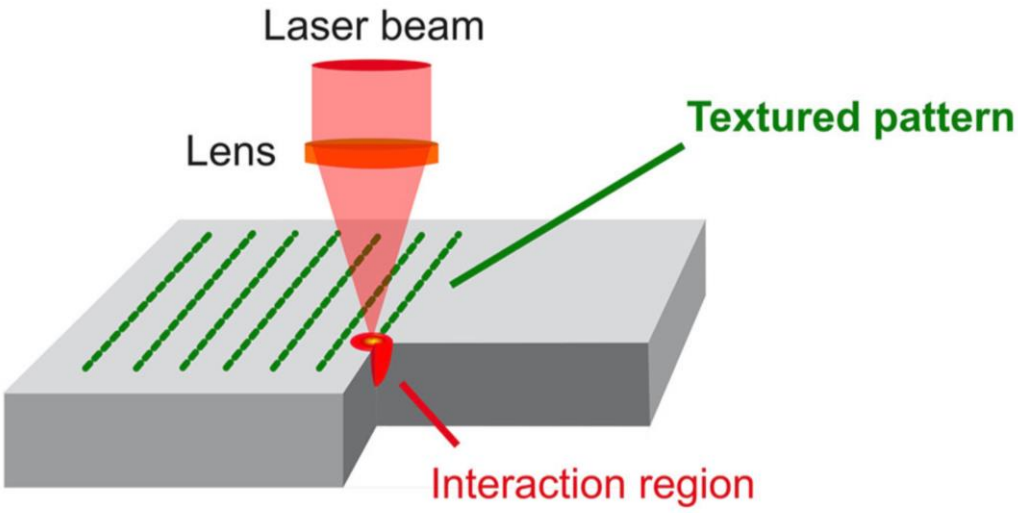

Figure 2.9 showing the schematic of Laser Surface Texturing [104].

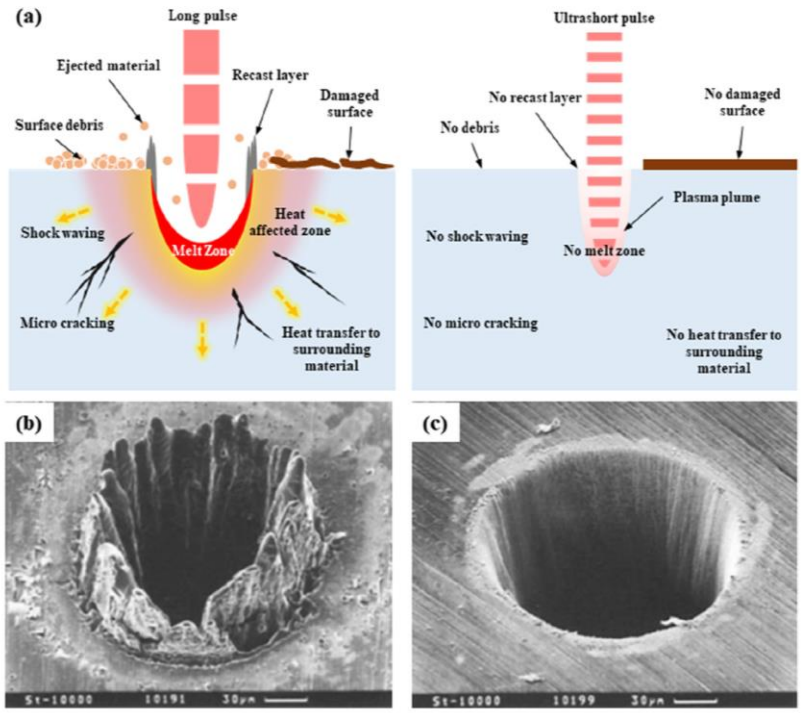

Figure 2.10 comparing the Laser ablation craters between nanosecond laser and femtosecond laser [105].

With the relative movement between the stationary laser beam and the target material surface, typical patterns such as dimples, grooves and ripples can be formed. Such patterns will not increase the surface roughness of the target material but also change the wetting properties thereby improving the osseointegration between the implant and the bone. More than that, when target material is polymers, the laser beam breaks the chemical bonds in the polymer surface chemistry, onwards leading to the formation of functional group. For example, Polyether-ether-ketone (PEEK) possess excellent mechanical and chemical properties but poor adhesive properties. But, this can be enhanced by laser surface treatment with wavelength of 355nm from the work by Rivero *et al* [106]. Therefore, they [107] also transferred the wettability of the Polytetrafluoroethylene (PTFE) surface into superhydrophobic with a CO_2 laser, which enables PTFE surface became self-cleaning. The work suggested that the CO_2 laser facilitated the process of large-scale superhydrophobic surfaces. What is more, the self-cleaning performance can also be achieved by LST in metallic materials (e.g., stainless steels, aluminium, nickel alloys) and ceramics.

LST can also improve the tribological characteristics, namely wear rates, lubrication, and load capacity, wear rates. From the work by Chen *et al*.[108], the load-bearing capacity is proportional to the texture rate. And the load-bearing capacity increases linearly with the increase of texture depth. Regarding the effects of LST on the lubrication, Li *el al.*[109] investigated the lubrication behaviours of $Ga_{76}In_{24}$ (LM) in steel/steel contact. They found that LM`s anti-friction and anti-wear abilities were improved by laser textured surface. In addition, by a nanosecond laser, Kummel *et al* [110] enhanced the wear resistance, decrease the friction in Ti-6Al-4V alloy by a factor of 160 compared to the un-textured sample. Therefore, at the early beginning, engineers deployed LST in improving the adhesion of mechanical seals that are subjected to high pressure and friction by texturing their surface with a dimple pattern. The laser textured patterns were proved to significantly enhance the tribological properties of mechanical seals as dimples retain lubricants, improving the seal's durability, and dramatically reduce the friction from the harsh working environment.

It should note that the main purpose of LST in medical application is facilitating the cellular activity in the implant surface. During the process of bone remodeling, the textured patterns lodge the adhesive and provide additional anchoring surface for cell adhesion. At the micrometre scale, Raimbault *et al.* [111] used focused femtosecond laser to form various orientation grooves (e.g. perpendicular or parallel to LIPPS). The result shows that the cells

settled down and spread following these micro-structures. Additionally, Xu *et al* [112] seeded human bone marrow-derived mesenchymal stem cells (hBMSCs) on the Ti-6Al-4V surface before and after LST, And the results showed that laser textured patterns improved the cell attachment, proliferation, osteogenic differentiation.

2.4 Summary

In this work, the huge quantity demanded of artificial implants was introduced, addressing the necessity for employing an implant. Then, the artificial implant failure reasons and human orthopaedic health data were discussed.

- Literatures based on the basic properties of titanium and its alloys, including mechanical properties, biocompatibility, corrosion and wear resistance witness the reason why titanium alloys have been widely employed in oral and orthopaedic applications.
- Implants surface modification methods such as mechanical, acid/alkali treatments; ion implantation and plasma spray were briefly discussed. The osseointegration of the implants can be improved by roughening surfaces using grinding technique or chemical etching methods or coating a biocompatible layer (HA) using plasma spray, laser surface texturing *etc*.

CHAPTER 3 Laser Shock Peening: A Review of Current State of Technology and its Potential in the Medical Sector

This chapter reviews laser shock-based techniques and their applications, followed by the discussion of laser shock peening surface treatment deployable for biomedical applications. Although there are various benefits of titanium alloys, all of the clinical requirements cannot be met. Thus, it is necessary to apply surface modification on the titanium implants to promote the biological, physio-chemical and mechanical properties. Amongst these techniques, laser shock peening was considered as a promising technique to improve mechanical and biological properties for implants, maintaining their strength for a significant period of time. Therefore, basic LSP theory is introducing at the beginning followed by laser shock-based techniques including High Repetition Laser Shock Peening (HRLSP), Laser Shock Peening without Coating (LSPwC), Warm Laser Shock Peening (WLSP) and Cryogenic Laser Shock Peening (CLSP). Furthermore, its applications in aerospace, automotive and nuclear reactor are reviewed. Finally, the potentiality of LSP in the medical sector by evaluating titanium performance fatigue, corrosion, wear resistance, wettability and biocompatibility.

3.1 Introduction

Improvement of material properties by modifying material surface has always been a purpose of industry. Laser shock Peening is a useful modification technique which has been widely applied to Aviation and manufacturing for improving mechanical properties namely fatigue, wear, corrosion resistance etc. LSP is mainly a technique to modify the metallic surface using short-pulse (nanosecond), high peak power density (GW/cm^2) laser beam, rapidly vaporizing the absorbing layer to generate high-pressure plasma [113]. If the shock-waves are high enough that the peak pressure exceeds the Hugoniot Elastic Limit (HEL), of the metal material, undergoing plastic deformation, even a nanocrystalline layer. After the shock-wave, the plastically deformed metal surface was left in a layer of compressive residual stress, extending from the surface to depths up to 2mm, which can greatly improve the mechanical properties. The schematic diagram of LSP is shown in Figure 3.1

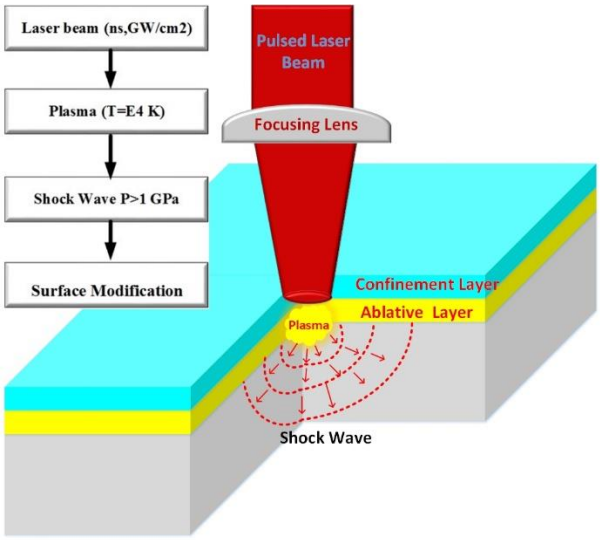

Figure 3.1 The schematic diagram showing Laser Shock Peening.

The history of LSP can be dated back to late 1960s and early 1970s in the USA. It is a cold process for metal that work hardens metallic material with controlled pressure and minimal heat input *via* a pulsed laser to generate shock-waves [reference]. From 1968 to 1980, the initial LSP experiment was carried out and designed at the Battelle Institute (Columbus, OH, USA), where researchers employed LSP to improve the fatigue properties of steel alloys and aluminium [114]. Meanwhile, theoretically, Fabbro et.al. [115] built a one-dimensional longitudinal expansion model for calculating the shock wave pressure. Besides that, Meyers [116] studied on the dynamic load behaviour of plastically deformed metallic materials and reported on the mechanism of enhanced materials. Additionally, furthers experiments were carried out in laboratories including Co-operation Laser Franco-Allemande-Arcueil Cedx (CLFA) [117], and Metal Improvement Company (MIC) [118]. However, these LSP experiments were initially limited as the highly cost of a laser system and process arrangement to practice LSP.

In 1974, the first patent of LSP application was registered in the U.S. by Industrial Materials Limited [119]. In the following two decades, more patents based on LSP were registered by such as Battelle Development Corporation and General Electric Company. With 20-years development, in the 1990s, the process has become a possible technique in the industry as the reliable powerful Q-Switched Nd: glass laser system was developed. In 2001, based on the cooperation with Lawrence Livermore National Laboratory (LLNL), Metal Improvement Company (MIC) developed a high throughput production system with a unique high power

laser system [120]. Since the first generation LSP system, 3 more LSP have been built in Livermore CA and Earby. With this equipment, over 12,000 aero-engine fan blades and blade hubs are peened for hundreds of wide body and small corporates jets. In 2003, LSP Technologies (LSPT) who dedicate to commercialize LSP, helped U.S. force solve fatigue problem on B-1 bomber [121]. Additionally, in 2010 F-22 program, Hill Engineering Ltd. [122] employed laser shock peening to repair the F-22 wing-attach lugs which are designed to carry wing loads shown in Figure 3.2. Nowadays, numerous researchers from China, America, UK, Spain, Japan and India are still investigating laser shock peening in numerical simulation, material interaction mechanism, and LSP optimization.

Figure 3.2 Strengthening of the wing-attach lugs of F-22 with LSP [122].

This chapter reviews the basic laser shock peening theory, laser-shock based techniques including HRLSP, LSPwC, WLSP and CLSP and their applications in different sectors. Furthermore, laser shock peening surface treatment deployable for biomedical applications is discussed.

3.2 Overview of laser shock peening and its Basic Theory

In terms of the generations of shock pressure during LSP, it is the main power to improve the mechanical properties and refine the surface microstructure of materials. Thus, in order to generate enough high shock-waves, an absorptive layer is glued on the target material surface. The absorbent coating is also a sacrificial layer. This can not only form plasma shock-waves, but also prevents material melting and ablation due to laser radiation. Absorbent coatings can

be vinyl tape, aluminium foil, copper tape and even the black marker pen painting (for ceramic LSP). It is found that the transformation of laser energy into shock pressure is almost 100%, while of Aluminum it is only 80% as stated by Hong et al [123]. What is more, they also found that, with the same absorptive overlay under different confining media, the transformation rate (laser intensity to plasma generation) varied greatly. The details rate are listed as following: Perspex (192%); Silicon rubber (121%); Pb Glass(40%),; K9 Glass (24%) and Quartz Glass (20%). Temping water is normally used as a confining overlay to prevent plasma shock-waves expanding away off the target surfaces. Theoretically, the generated plasma shock-waves should be higher than the dynamic yield strength (σ_y^{dyn}) so that plastic deformation can occur, thereby, affecting the microstructure and properties of target materials. Hugonoit Elastic Limit (HEL) is explained as the limit of elastic response and the onset of failure under dynamic uniaxial strain loading calculated by Equation 3-1.

$$\mathrm{HEL} = \frac{1-\theta}{1-2\theta}\sigma_y^{dyn} \tag{3-1}$$

Where θ is the Poisson`s ratio and σ_y^{dyn}dynamic yield strength at high strain. There are many presented shock-wave calculation models. It can be calculated using the following Equations (3-2 to 3-8):

$$\mathrm{P} = \mathrm{A}\left(\frac{\alpha}{2\alpha+3}\right)^{1/2} Z^{1/2} I^{1/2} \tag{3-2}$$

$$\mathrm{P(GPa)} = 0.01\left(\frac{\alpha}{2\alpha+3}\right)^{1/2} Z^{1/2} I^{1/2} \tag{3-3}$$

$$\mathrm{P(GPa)} = 1.02 I^{1/2} \tag{3-4}$$

$$\mathrm{P(GPa)} = 0.25(IMA)^{1/2} \tag{3-5}$$

$$\mathrm{P} = 5.47\left(\frac{\alpha}{2\alpha+3}\right)^{1/2} I^{1/2} \tag{3-6}$$

$$\mathrm{P(kbar)} = \mathrm{B} I^{1/2} \tag{3-7}$$

$$\mathrm{P} = (AZI)^{1/2} \tag{3-8}$$

In 1990, Fabrro [115], presented a model which predicts accurate results, shock-wave can be interpreted with Equation 3-9 to 3-10:

$$P(GPa) = 0.01\sqrt{\frac{\alpha}{2\alpha+3}}\sqrt{Z(\frac{gr}{cm^2})}\sqrt{I(\frac{GW}{cm^2})} \quad (3\text{-}9)$$

$$\frac{2}{Z} = \frac{1}{Zs} + \frac{1}{Zw} \quad (3\text{-}10)$$

$$I = J/\tau A \quad (3\text{-}11)$$

$$z = \rho U \quad (3\text{-}12)$$

Where P is the peak wave pressure, Z(g/cm^2s) is the impedance of shock-wave, I (Gw/cm^2) is power intensity, J is the energy of each pulsed laser. α is a constant which is related to the efficiency of laser absorption by materials (normally, α is 0.1). Zw and Zs are the impedance, defined by density and shock velocity in water and materials respectively. Overall, the plastic deformation is critical to the plasma shock-waves, which should exceed the HEL of the target material.

3.3 Overview of Laser-Shock Based Peening Techniques

Under laser shock peening, there are many different sub-processing methods that use the fundamental laser-plasma driven shock-wave to be induced into the material. All these processes involve multiple parameters and a wide range of experimental conditions. These conditions are: high repetition laser shock peening (HRLSP) [124]; ultra-short pulse laser shock peening with femtosecond lasers and short pulse laser shock peening with both ps and ns regime; laser shock peening without coating (LSPwC) [125]; warm laser shock peening (WLSP)[126] and cryogenic laser shock peening (CLSP) [127] and dry-tape laser peening and obviously standard laser shock peening with water (as previously discussed). HRLSP, LSPwC, WLSP and CLSP will be separately discussed in the following sub-section.

3.3.1 High Repetition Laser Shock Peening

Owing to the cost of low repetition rate high power lasers, Caralapatti [124, 128] propose to use high repetition laser for LSP (HRLSP). Normally, the low repetition laser for LSP varies from 1HZ to 100Hz, while of HRLSP laser could reach to 10kHz. Apparently, due to its high repetition, HRLSP with lower energy pulses could be more effective to deal with the tiny specimen as applying high energy laser may have physical damage to small samples. One more benefit of HRLSP is the high processing speed compared to traditional LSP. This means dealing the same amounts of specimens, HRLSP faster than standard LSP, thereby, having the

potential to save economical cost. Figure 3.3 is the comparison of the low and high repetition rate of laser pulses.

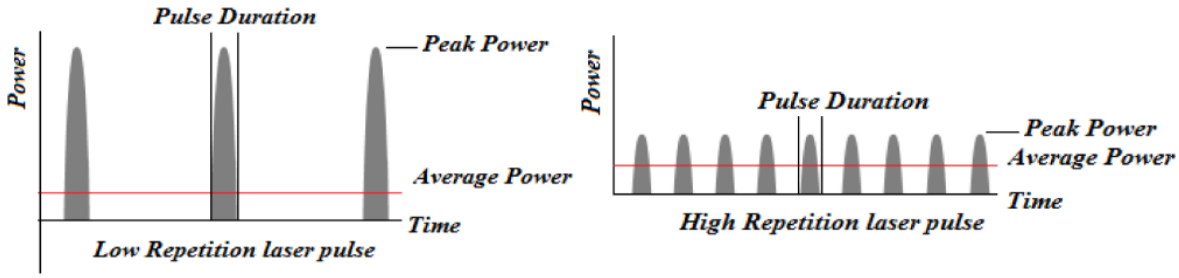

Figure 3.3 Comparison of low and high repetition rate laser pulses [129]

Each pulse energy can be explained by Equation 3-13:

$$J = Pw/f \tag{3-13}$$

Where Pw is laser power and f is the laser repetition; J is the energy of each pulse. It can be seen that J has revised the linear relationship with laser repetition when laser power is fixed. By increasing pulses number, pulse energy will decrease. However, according to the equation, when laser power is fixed, the energy of each pulse in high repetition is not large enough for driving surface material to work harden and create plastic deformation. Therefore, HLSP is more suitable for low mechanical strength, shallow residual stresses, and small size metallic materials such as aluminium and magnesium alloys. The comparison of LSP and HSLP showed in Table 3.1

Table 3.1 The comparison of standard LSP and HLSP [129].

	HRLSP	LSP
Cost of laser	Medium	Expensive
Laser processing speed	Fast	Medium
Increasing hardness		Better performance due to CRS
Wear reduction		Better performance due to CRS
Corrosion control	Better due to smaller spot size	
Peening Precise	High	Medium

3.3.2 Laser Shock Peening Without coating (LSPwC)

In 1995, Mukai [130] proposed a method, namely; Laser Shock peening without Coating (LSPwC), as shown in Figure 3.4, as an application of copper vapor lasers. Since that, it has been performed on various metallic materials especially in strengthening nuclear reactor part as an alternative to LSP. Compared to conventional LSP, the absorptive layer is removed which does not need any samples preparations. But it also has same capability of LSP. It has been proved to enhance the resistance against fatigue and stress corrosion cracking (SCC) types of failures.

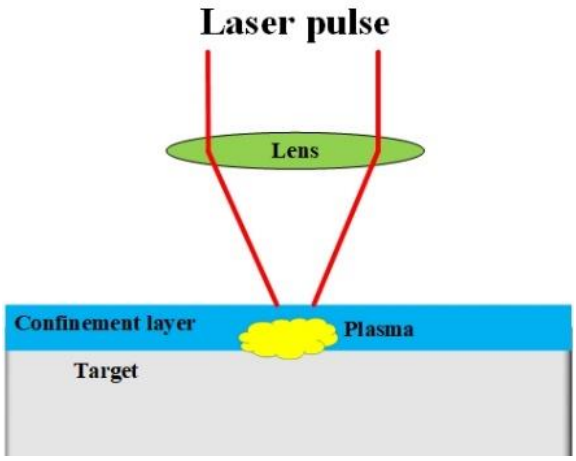

Figure 3.4 The schematic image of Laser Shock Peening without Coating.

In terms of compressive residual stress (CRS), Trdan *et al.* [131] applied a nanosecond laser with a wavelength of λ=1064 nm on 6082-T651 aluminium to investigate the effect of LSPwC on mechanical properties. Compressive residual stress on the top was significantly increased from -20MPa to -407MPa with laser parameter of 900 pulses/cm^2. A similar increase in microhardness can also be witnessed. In Nickel alloy, Kulkarni *et al*. [132], examined the effects of low energy LSPwC on Nickel-200 alloy. Compared to unpeened sample (-32.6MPa), the residual stress reached to -323MPa. Recently, Prabhakaran *et al*. [133], found that LSPwC is an effective method to solve Stress corrosion Crack (SCC) in austenitic stainless steel. A considerable amount increase was formed in the pitting corrosion resistance after LSPwC. With different laser energy (1600 pulses/cm^2, 2500 pulses/cm^2, 3900 pulses/cm^2), surface CRS after LSPwC treatment can vary from 320MPa to 550MPa. Literatures regarding LSPwC-induced CRS on different alloys are given in Figure 3.5

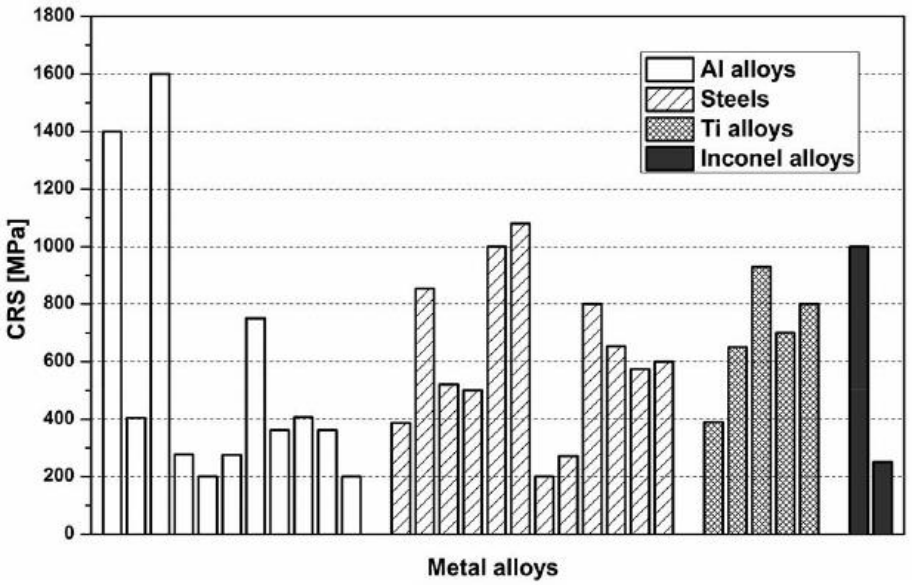

Figure 3.5 CRS on Aluminium, steels, Titanium, and Inconel alloys after LSPwC by [134].

With the formation of CRS, it would effectively contain the crack initiation if metallic materials possess stable compressive residual stress on the surfaces, thereby prolonging the fatigue lives of engineering parts. Reported by Sano *et al*. [135], Figure 3.6 discussed the comparison of S/N behaviour of stainless steel SUS316L and Ti-6Al-4V titanium alloy prior to and after LSPwC. It is noted that fatigue strength of FH (full heat treatment:1373K, 3600s in vacuum) and SR (stress relieving: 1173K, 3600s) SUS316L with LSPwC were 300MPa and 340 MPa at 10^8 cycles, which were 1.7 times and 1.4 times than that of unpeened. In Ti-6Al-4V alloy, fatigue strength with LSPwC was around 2.2 times than that of unpeened at the 10^4-10^5 cycles. What is more, fatigue strength enhancement was also found in the aluminium-silicon-magnesium alloy (AC4CH) with LSPwC [136]. For example, with LSPwC is 150 to160MPa, while that of as-received sample is 130 at 10^7 cycles.

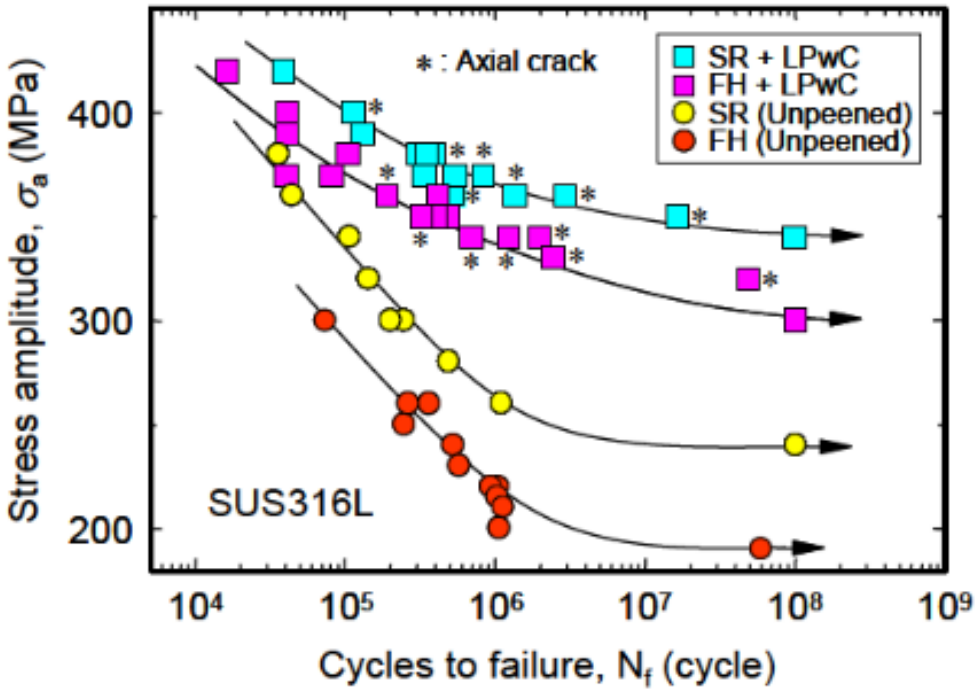

(a)

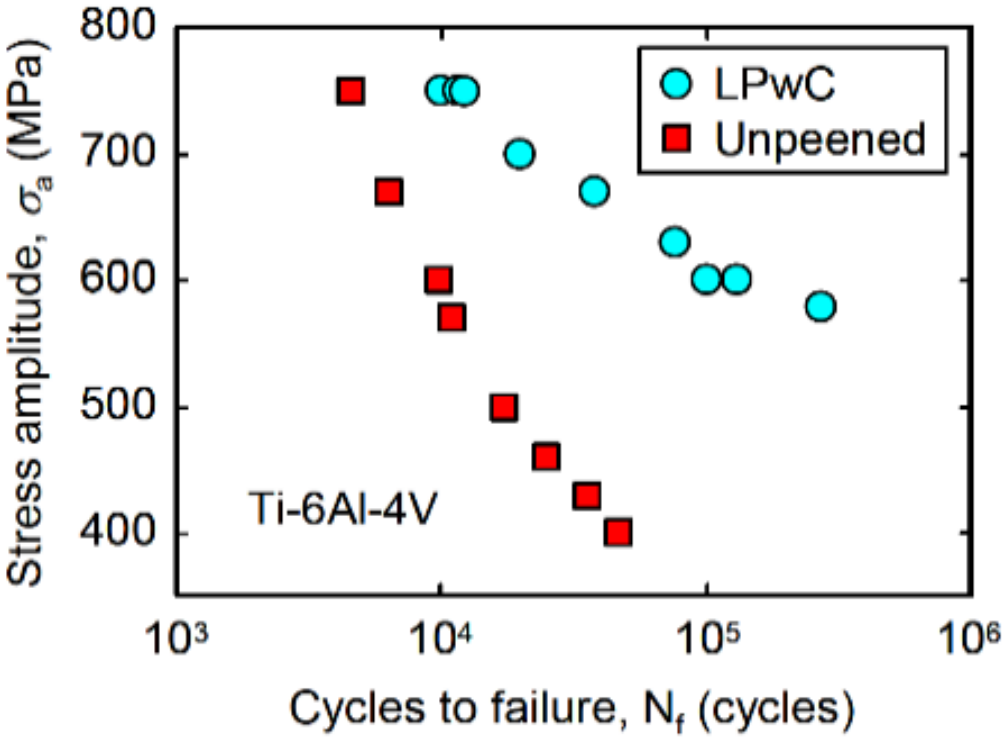

(b)

Figure 3.6 Fatigue test result before and after LSPwC showing rotary bending results of SUS316L in (a) and (b) the push and pull Ti-6AL-4V [135].

Various LSPwC applications for improving mechanical properties can also be found in Inconel alloy 718 [125], austenitic stainless AISI 321 [137], and welded Al6061-T6 alloy [138] . Overall the main characteristics of LSPwC are as follows :

1. LSPwC does not utilize any protective coatings which protect the target materials from being damaged due to laser irradiation;
2. Employs frequency-doubled and Q-switched Nd: YAG laser;
3. Laser pulses can be delivered through a flexible optical fibre;
4. Peening environment can be immersed in the water without the restrictions of transmitting length;
5. Without coatings, less apparatus is required and no reactive force against laser irradiation when LSPwC is carried on.

3.3.3 Warm Laser Shock Peening

It is well known that CRS is a key factor to improve the mechanical properties of target materials. However, there is a major challenge for LSP that CRS layer could easily relax under thermal heating process or a mechanical loading as well as the hardened layer. Three main reasons can be attributed to residual stress relaxation which are: 1) tensile or compressive overloading, 2) thermal cycling and 3) cyclic loading near or above the endurance limit. Therefore, in 2009, Cheng *et al* [139], proposed Warm Laser Shock Peening (WLSP) to tackle the residual stress relaxation problem. The schematic diagram is shown in Figure 3.7. Compared with traditional LSP, most peening procedures are the same except that the target material is heated up to a certain degree during the process. It is one of the most significant factors during the peening process. As temperature could affect the residual stress relaxation and microstructure rearrangement, it is important to choose a suitable processing temperature for WLSP.

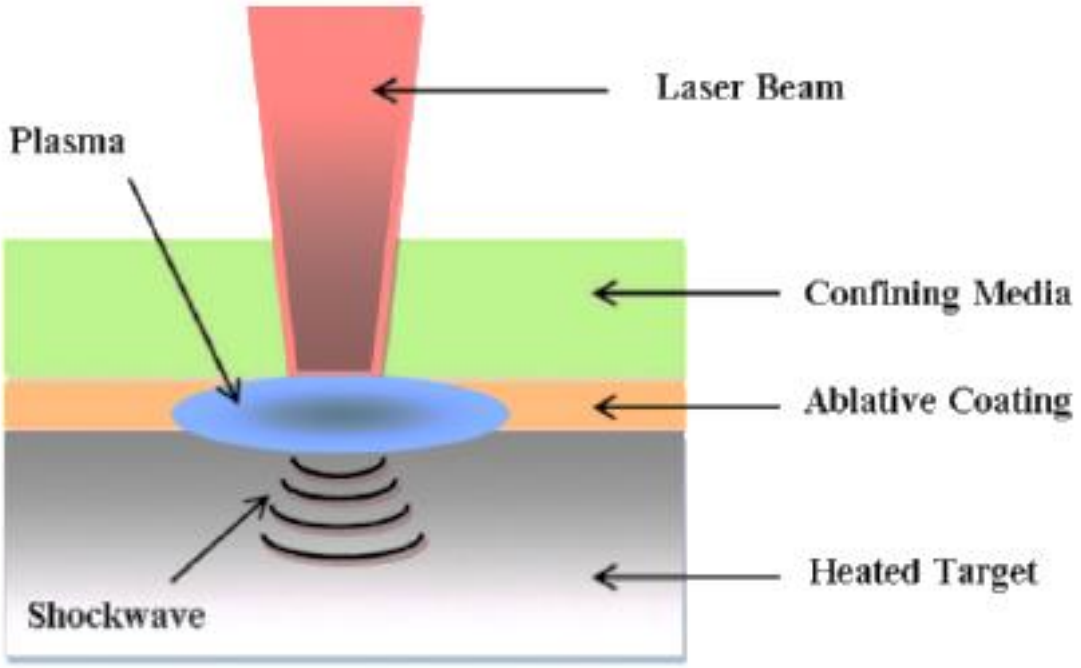

Figure 3.7 Schematic diagram of WLSP[139].

WLSP could lead to better microstructure refinement and mechanical properties, namely residual stress, microhardness, fatigue life compared to the microstructures and properties generated by standard LSP. These improvements can be attributed to the reasons of dynamic strain ageing (DSP occurring at a temperature between 150C° and 300C°) and dynamic precipitation (DP) which both contribute to the stability of microstructure. The dislocation multiplication through the interaction between mobile dislocations and diffused solute atoms is promoted by DSP. It will result in more uniform and highly dense dislocation structures [126]. What is more, DP is a thermal-mechanical precipitation effect which can lead to the nucleation of precipitates during the deformation process.

Since it was deployed, WLSP has been applied to treat various metallic materials. Meng *et al* [140], examined the effect of fatigue life of Ti-6Al-4V alloy subject to WLSP. At 400 MPa, the fatigue life of 300°C, the WLSPed was 1.68 times that of room temperature standard LSP treated sample. Additionally, the initial release rate of CRS of WSLP is also 22.7% lower than traditional LSP. Tensile property by WLSP is also investigated by Lu *et al* [141] in copper. Ultimate tensile strength of WLSP exhibits the highest value of 389MPa, while that of room temperature LSP is 368MPa. In stainless steel, Ye [142], compared the fatigue behaviour in AISI 4140 with WLSP and SLSP. Comparing LSP improves the bending fatigue by surface hardening and the introduction of CRS, DSA and DP in WLSP result in the stable dislocation

structure by locking mobile dislocations, thereby, receiving a superior fatigue performance than LSP.

3.3.3 Cryogenic Laser Shock Peening

It has been extensively reported that standard LSP can induce stable compressive residual stress and beneficial microstructure characteristics. However, due to the harsh service environment of the metallic materials such as aero and auto engines, compressive residual stress will release under alternating load or high temperature. Meanwhile, plastic deformation at low temperature will further increase the microhardness.

Therefore, in 2010, Ye and his group [127], proposed to carry out laser shock peening in the cryogenic temperature which is called Cryogenic Laser Shock Peening (CLSP). The cryogenic temperature is acquired by using liquid nitrogen which normally is under -136℃ [143]. The schematic image of CLSP is shown in Figure 3.8. Compared to standard laser shock peening in the room temperature, the volume shrinkage effect of CLSP will further strengthen mechanical properties, by delaying the relaxation of compressive residual stress and generating more inner microstructural characteristics. What is more, severe plastic deformation induced nano-crystalline material exhibit low ductility performance, but high strength. This is can be attributed to the low dislocation accumulation capacity of the nanograins [144]. With the CLSP, both high strength and ductility can be acquired through cryogenic ultra-high strain deformations [145].

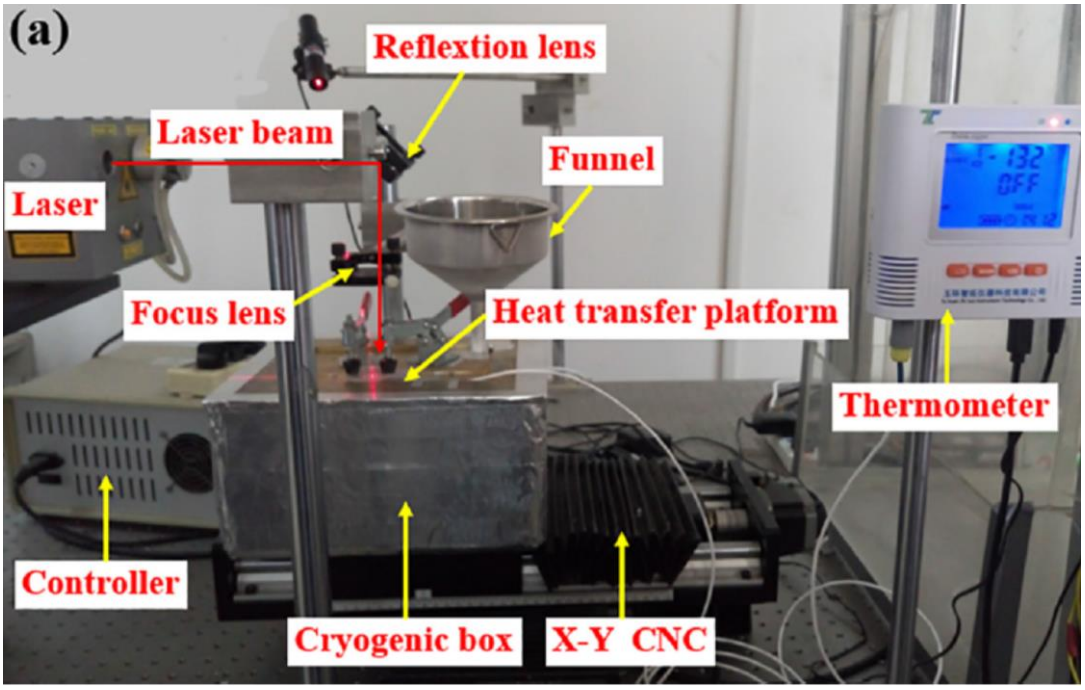

Figure 3.8 A schematic image of cryogenic laser shock peening system [146].

In terms of mechanical aspect, Li *et al* [147], studied the effect of CLSP on the tensile properties of 2024-T351 aluminium alloy. In comparison to standard LSP, the tensile and yield strength after CLSP were increased from 352 to 409 MPa and 462 to 506 MPa respectively. What is more, Zhou *et al* [143], compared the fatigue properties of 2024-T351 aluminium alloy subject to CLSP and standard LSP. The fatigue life of CLSP was 28077 cycles. This was 19.3% higher than that of standard LSP. Tribological studies were also carried out to evaluating the effect of CLSP on the wear resistance of 40CrNiMo structural steel [148]. The results showed that the mass loss after CLSP was the lowest compared to the untreated and standard LSP which in turn improves the high-temperature wear resistance.

With respect to the microstructural aspect, Ye *et al* [145], reported that nanograins were formed in the top surface embed with highly dense nano-twins after CLSP in the copper(Figure 3.9). Li *et al* [149], explained the strengthening twin formation mechanism of CP-Ti after CLSP. The cryogenic temperature is not only a key factor for increasing the dislocation density. This contributes to the formation for mechanical twins, but also supress the dynamic recovery and annihiliation of the dislocation structures.

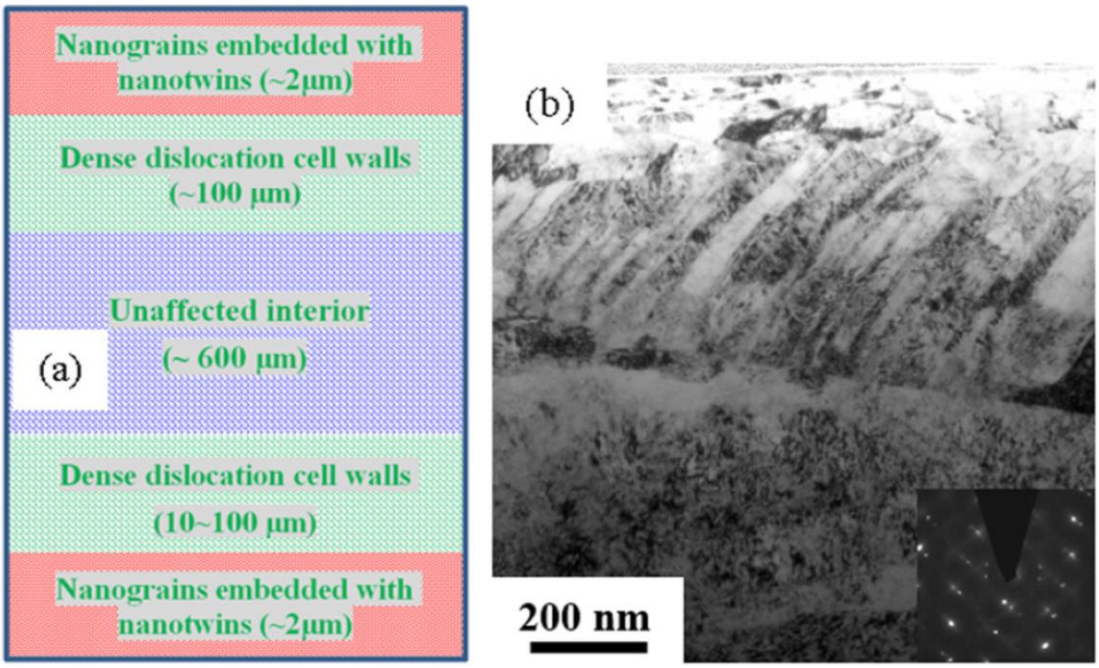

Figure 3.9 A schematic showing the cross-sectional microstructural of copper after CLSP in (a) and The TEM image along the cross-depth with features of dislocations, nanotwins and nanograins in (b) [145].

3.4 Review on Laser shock peening Application in non-medical sectors

3.4.1 Aerospace

Since Laser shock Peening was invented, it has been continuously applied in the aviation industry. Manufacturers such as Rolls-Royce, General Electric Company (GE), Airbus, Boeing and Lockheed Martin etc. have all employed LSP as an effective metallic surface improvement method to repair their aircraft components. One of the most important applications was the High Cycle Fatigue (HCF) Science and Technology Program. In 1991, the USA air force started the program to resolve the problem of the Foreign Object Damage (FOD) with LSP. The damage caused by high cycle fatigue failure was around $400 million per year [150]. GE Aircraft Engines (GEAE) took LSP to improve the durability of F101 fan blade to FOD shown in Figure 3.10b [151]. The blades were notched up to 0.25 inches in order to simulate the FOD circumstance. Shown in Figure 3.10a, they were treated by LSP and SP (shot peening) onwards subjecting to fatigue examination. The results showed that the tolerance of a damaged F101 fan blade decreased from 70Ksi to 20Ksi. But the LSPned help the damaged blades to maintain at round 70Ksi The durability of target metallic materials were improved by LSP that all data meet the service demand. From 1997-2004, GEA has produced more than 50,000 LSP airfoil for US Air Force (USAF) for applications such as stage 1 fan blades in various aero-engines such as F110-GE-100, F110-GE -129 turbofans, F101-GE-102 [152].

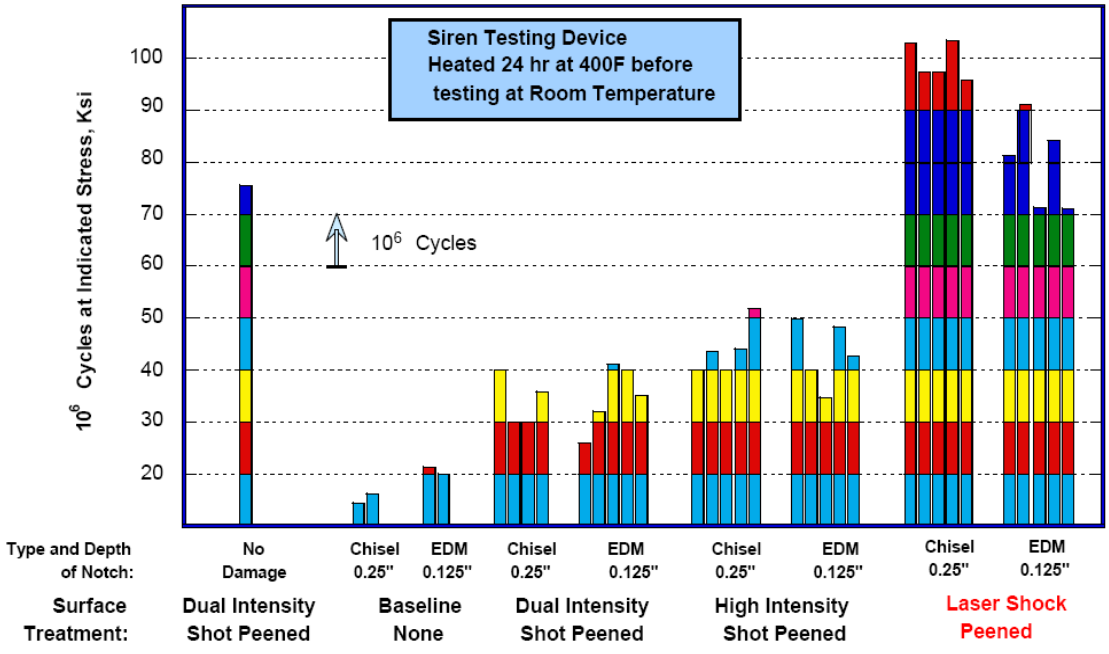

(a)

(b)

Figure 3.10 LSP for F101 first-stage fan blade Damage tolerance in (a) and (b) F101 first-stage fan blade [151].

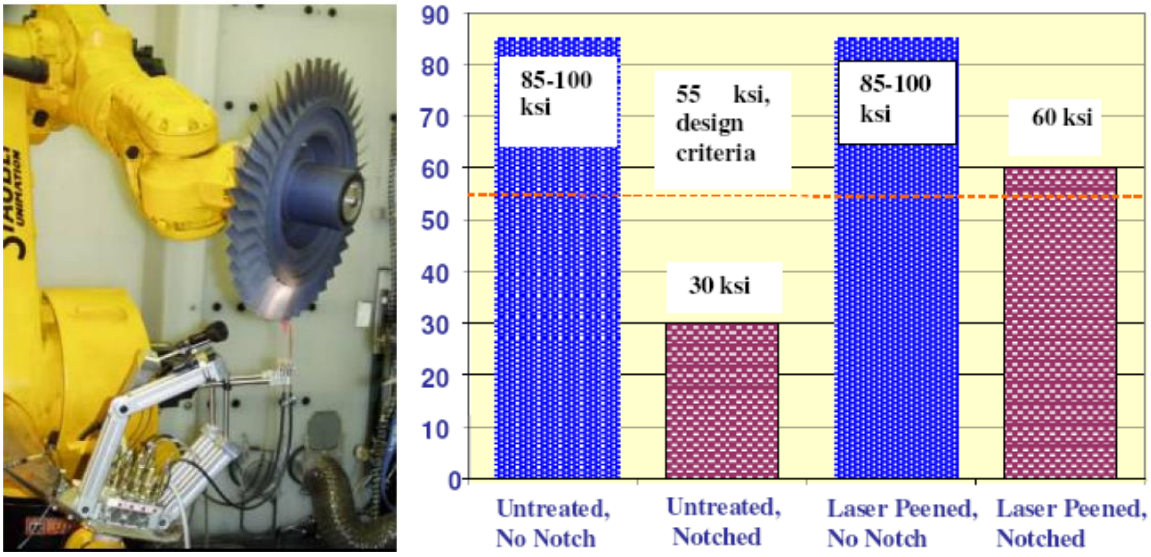

(a) (b)

Figure 3.11 LSP for F119 fort-stage titanium blisc in (a) RapidCoater^{TM} system for processing an F119 Integrally Bladed Rotor, and b) F119 fourth-stage titanium blisk [153]

In 2003, Laser Shock Peening (LSPT) company employed LSP on the F119 forth-stage Integrally Bladed Rotor (IBR) shown in Figure 3.11. LSP improved the Fatigue strength of notched IBR airfoil higher than the 55Ksi design criteria [100]. What is more, Rolls-Royce used LSP on the aero-engines to Trent 60 turbine blades to improve the fatigue resistance.

Since then, Trent 500, -800, -1000 and XWB engines were also enhanced by LSP [154]. Recently, Lockheed Martin, Boeing, USAF and Hill Engineering worked together to support laser shock peening treatment for the structure repairing of F-22 wing-attach lugs which bear wing loads into the fuselage (shown in Figure 3.12). A stable CRS layer was introduced by LSP to enhance the resistance of crack initiation and slows fatigue crack growth [122].

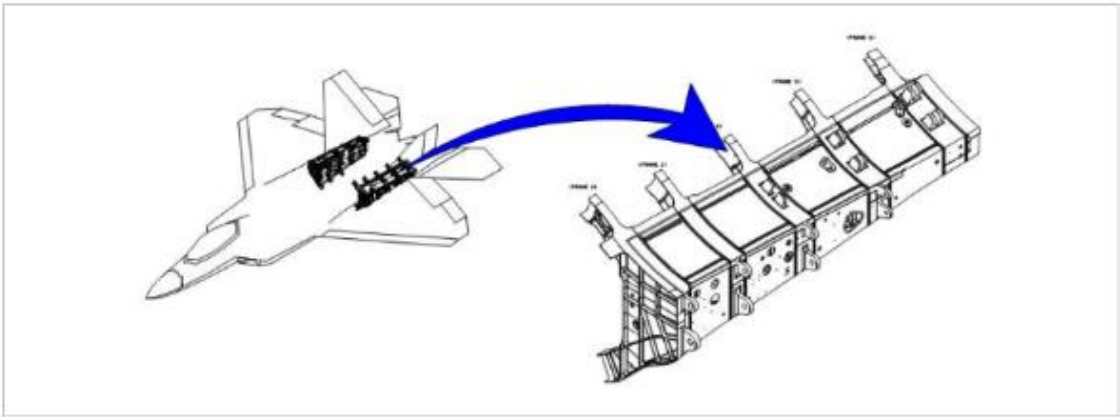

Figure 3.12 Illustration of F-22 structure showing wing-attach lugs where laser shock peening was applied [102].

3.4.2 Automotive

In the same way, LSP can be applied in the automotive area through improving the material performance of auto components, namely; rotating engine parts, transmission gears, crankshafts and valves. Raja Ramanna Centre co-operated with Tata Motors Ltd undertook a project to laser shock peen as an alternative to existing SP practice for automotive components [155]. The leaf spring manufactured by SAE 9260 spring steel was enhanced in a three-point bending fatigue test, with a comparative low laser energy system. Improved fatigue resistance of LSPned automotive components would benefit the designing components with fewer quantity materials which decreases the weight of automotive parts, thereby, increasing fuel efficiency.

What is more, valve springs in automotive also has been strengthened by LSPT Ltd [156]. The vales spring normally is used to allow air or fuel into the combustion chamber and seal the camber to expel the combustion gases out of the chamber. High rapid acceleration rates and repeated number of cycles may lead to the failure of Valves springs. But, the peened springs are able to withstand higher stress level. This allows the valves to have longer remain open for

a longer duration. This also allows more air into the engine chamber translating to more horsepower. This is because residual stress is engineered into the exterior of the wire shown in Figure 3.13, improving the fatigue resistance.

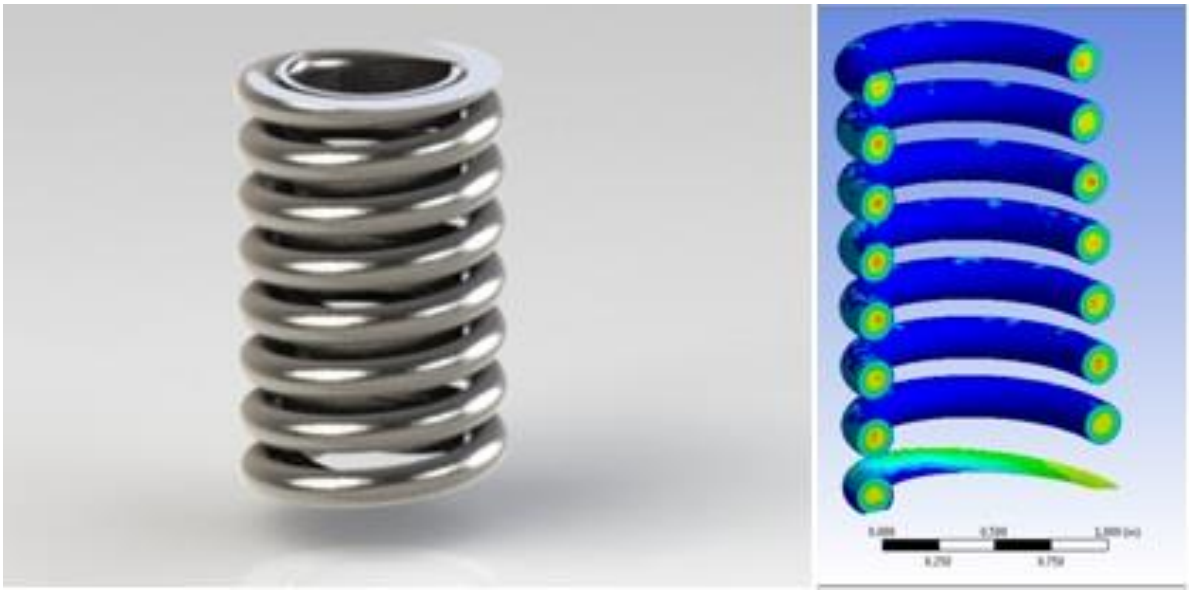

(a) (b)

Figure 3.13 Valve springs (a) and cross-halves FE Mode after LSP(b)[156]

3.4.3. Nuclear Reactor

More than aeroengine and automotive components, nuclear reactor has always been a critical application for laser shock peening. Due to Stress Corrosion Cracking (SCC) in the welded components, the aged nuclear reactor would face the problem of nuclear leakage. Therefore, Toshiba Ltd [157], began its research on laser shock peening in the mid-1990s. Onwards, Toshiba developed a laser peening system for reactor bottom part of BWRs (Boiled Water Reactors, shown in Figure 3.14). To begin with, the laser irradiation position was controlled by an elaborate system of alignment and tracking optic. Then, in 2002, the laser peening system was able to deliver of 10mW laser pulses through 50m optical fibres.

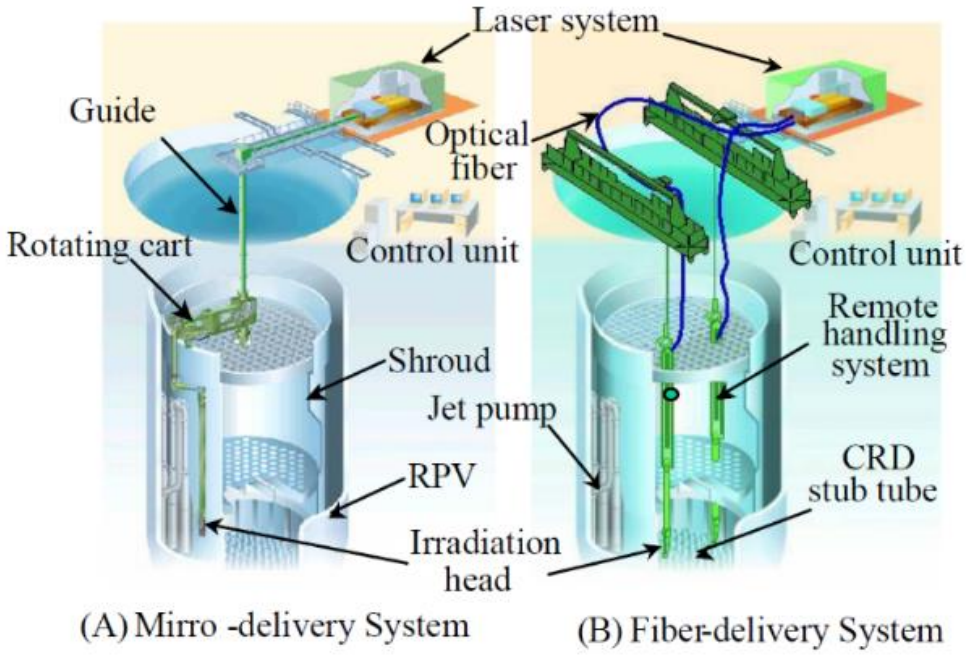

(a)

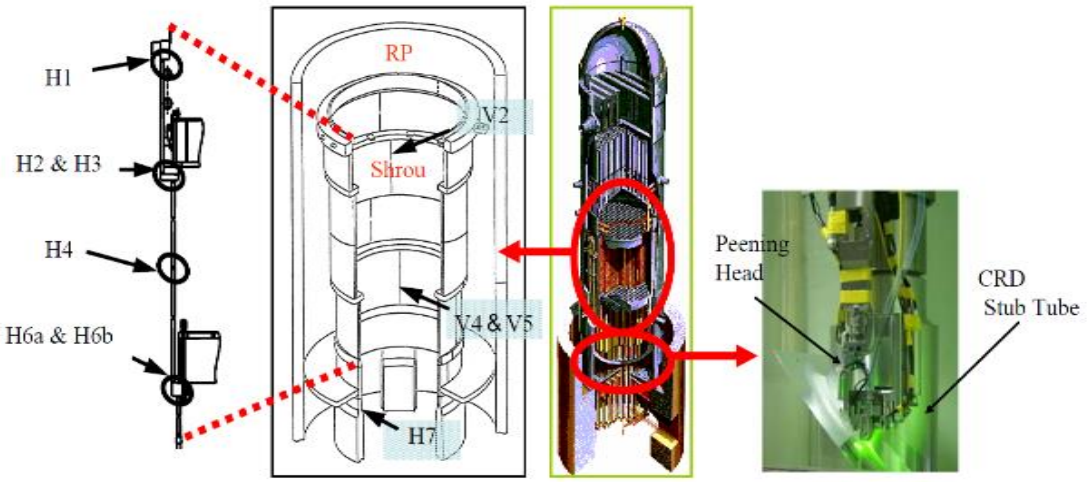

(b)

Figure 3.14 Underwater laser peening system for BWRs (a) and applications for Japanese BWRs (b)[158].

Moreover, since 2004, Toshiba also has developed another system (shown in Figure 15) for Bottom-Mounted Instrumentation (BMI) nozzles and other nozzles in PWRs (Pressurized Water Reactor) [158]. In this system, laser pulses are transmitted through twin optical fibres which peen separate positions in parallel. Peening work has been accomplished on the inner surface, the outer surface of J-groove welds on the BMI nozzles, dissimilar metal welds of the

primary water inlet nozzles. All operations were successfully accomplished which shows the reliability and applicability of LSP.

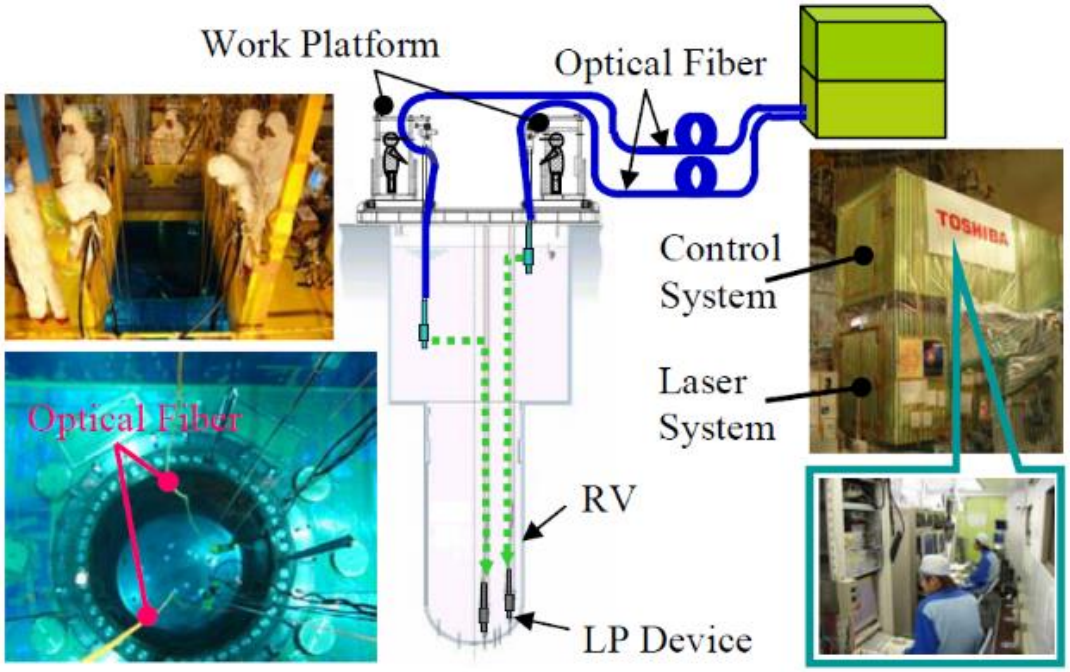

Figure 3.15 Under Laser Shock Peening system for PWRS [158].

It should be noted that, since the LSP is conducted underwater, the sacrificial overlay is usually removed. Therefore, underwater laser peening is actually laser shock peening without coating (LSPwC) as shown in Figure 3.16. When a nanoseconds laser pulses focus on the target material immersing in the water, the target surface absorbs the laser energy and evaporates immediately through the ablative interaction. The vapor is confined by the water, and instantaneously ionized by inverse-bremsstrahlung to form plasma, onwards absorbing laser energy and generating a plasma shock-wave. The shock-wave far exceeds the yield strength of the metals, thereby, a compressive stress layer was formed on the material surface.

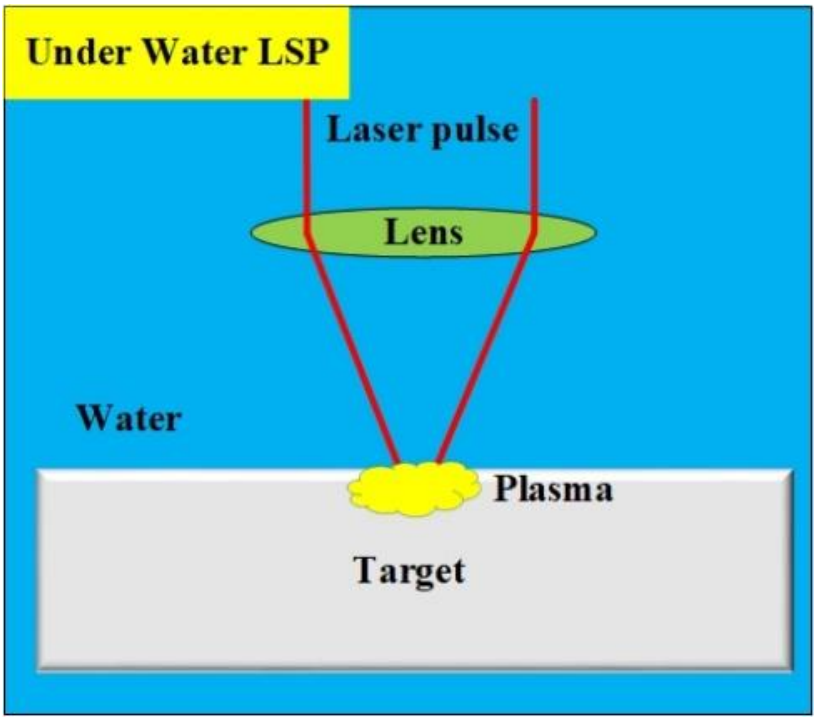

Figure 3.16 A diagram of Underwater Laser Shock Peening.

By 2009, Toshiba successfully manufactured eighty nuclear power plants. Electric Power Research Institute (EPRI) of U.S started to co-operate with Toshiba. In the U.S., Lawrence Livermore National Laboratory (LLNL) investigated the effect of laser shock peening on UNS NO6022 alloy, which is used for the outer layer on the spent-fuel nuclear waste container. The compressive residual stress of 4.3mm was formed by LSP to improves the fatigue resistance and effectively stop the stress cracking corrosion [159]. Additionally, supported by U.S. Department of Energy, Vasudevan *et.al* from University of Cincinnati [160], investigated the effect of LSP to establish parameters that enhanced the fatigue properties and the resistance of stress corrosion cracking (SCC) of Nickel alloys 600/690. These two materials are currently applied in manufacturing nuclear steam generator tubing, and the candidates for GEN IV reactors.

3.5 An overview of laser shock peening applicable to the medical sector

3.5.1 Residual stress and fatigue

Induction of compressive residual stress is the primary goal of LSP and is one of the important factors that the process introduces to the metallic materials. Normally, a compressive residual stress layer induced by LSP is able to reach a depth x5 that of shot peening. The compressive residual stress layer has many benefits for metal components. One of these benefits is that it

can decrease the risk of metal fracture. Kashaev *et. al* [161], investigated the effects of LSP on initiation and propagation of fatigue crack of aluminium alloy AA2024 with a thickness of 2 mm. The authors observed a significant decrease in the fatigue crack propagation (FCP) rates due to the compressive residual stress. Additionally, LSP is also used to solve the cracks, fracture problem of nickel-based alloyed components. Wang *et. al* [113], reported that the fatigue life of K403 nickel alloy samples were improved by 244% subjected to 3 impacts LSP. The crack fracture morphology showed that it took more energy for the fatigue crack to propagate. Therefore, LSP can effectively reduce the risk of cracks in metallic materials such as Aluminium, Nickel alloy etc. What is more, Foreign Object Damage (FOD) was also solved by LSP [162]. According to USA Air Force reports, Damage to an F101 blade results in the less of fatigue strength to 20 KSI that is only half of the design requirements. The toleration limitation of peened blades was improved to 75-100 KSI, presenting an acceptable fatigue strength, thereby, saving millions of dollars in blade replacement. The above applications are limited in the manufacturing industry and the aviation industry. Nowadays, researchers have started to use LSP to improve the fatigue life of medical implants. Mannava *et. al.* [163], designed a flexible prototype rod with a flat section made by TC4 which was laser peened. They found that the magnitude of the in-plane compressive residual stress was increased to -300 MPa to - 350 MPa. Additionally, an increase in the fatigue load ratio was observed. In order to investigate the residual stress distribution of TC4 hip replacement, Correa *et.al*. [164], built a 3-D hip model in Abaqus to simulate the initiated cracks when the implant failure.

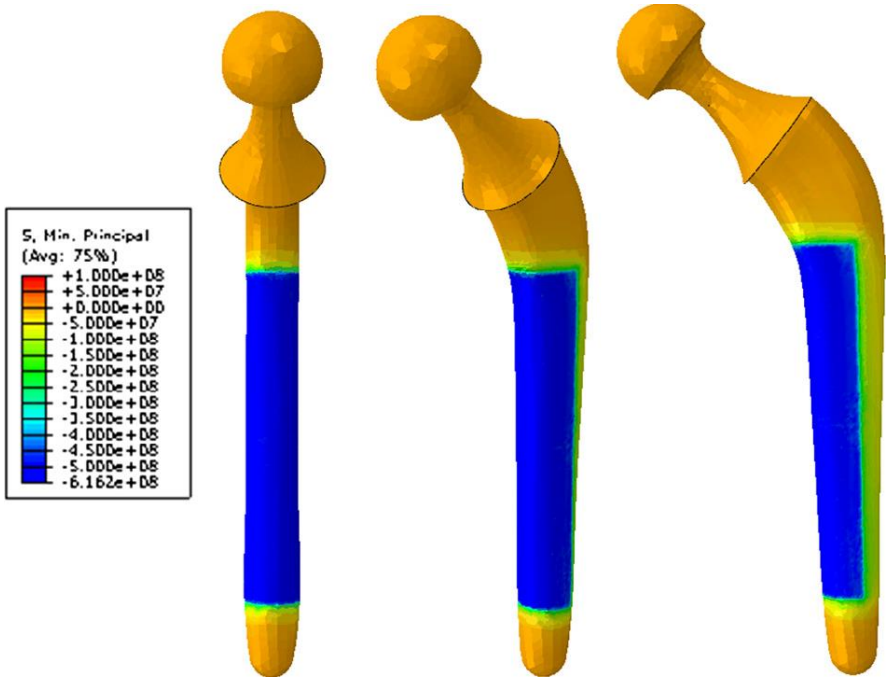

(a)

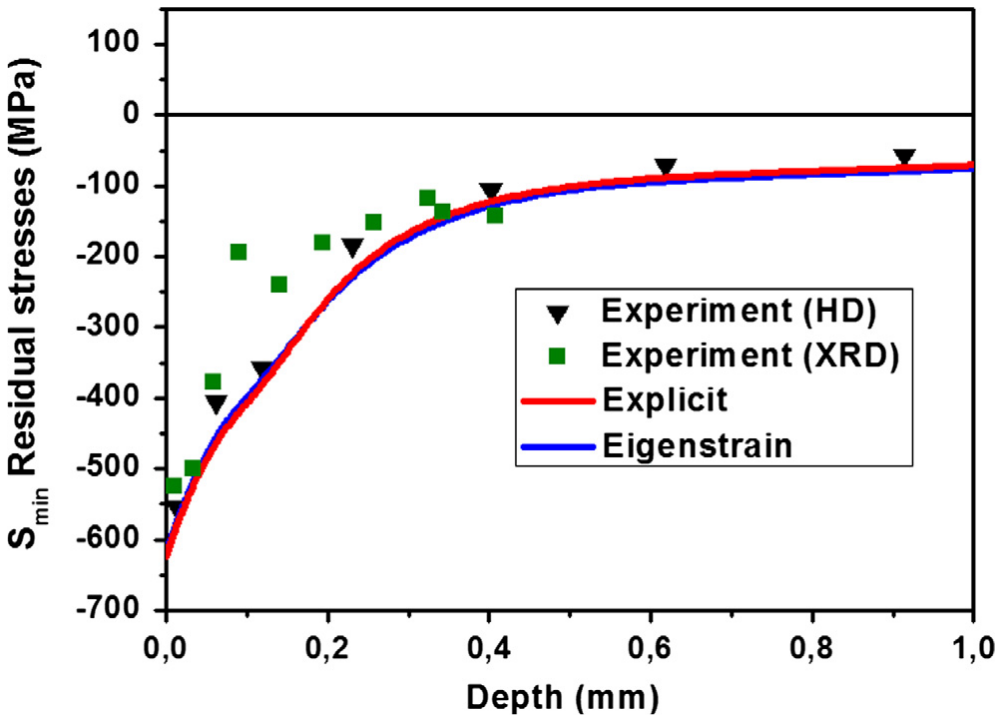

(b)

Figure 3.17 Induced residual stress in simulated hip replacement in (a); and (b) the obtained residual stress of experiment and simulation [164].

The simulated and experimental residual stress distribution in cross-sections are shown in Figure 3.17. It the first that residual stress induced by LSP in total hip replacement was simulated with the Finite Element Method using Abaqus. Due to LSP, compressive residual stress of 600MPa was formed in the surface from both simulated model and residual stress experiments. Therefore, researchers are favouring the use of LSP to diminish the surface tensile stress and introducing compressive residual stress to prolong the fatigue life of medical metals.

3.5.2 Corrosion

Magnesium has excellent biocompatibility which has been widely used for fabrication of medical devices. Additionally, magnesium implants can greatly reduce stress shielding effects as the density of magnesium and elastic modulus was very close to human bones (density:1.74-2g/cm^3 vs 1.8-2.1g/cm^3; Elastic modulus:42-45 GPa *vs* 40-57 GPa), compared to other traditional metallic materials such as stainless steel and titanium alloys. However, due to the rapid corrosion, aggressively, magnesium corrodes in physiological and enriched Cl^- ions solutions [165]. What is more, hydrogen gas pockets were generated adjacent to the implants

while Mg alloy was corroding. Therefore, magnesium was greatly limited by its poor anti-corrosion capability in its further application in orthopaedic implants.

Therefore, many researchers are dedicated to improving the anti-corrosion of magnesium. Especially, some of them made great progress. Guo *et. al.* [166], explore the process capability of laser shock peening to control the corrosion of Magnesium-Calcium implants by tailoring the surface integrity. More specifically, some of the parameters such as overlapping laser pulses during peening have a great influence during the experiments. Thus, Caralapati *et. al.* [128], investigated the effect of high overlap with lower power density laser shock peening (HLSP), which is close to traditional LSP, on the commercial purity of Mg in simulated body solutions (Hank's solution, Chemical composition is shown in Table 3.2). The result showed that the corrosion rate of peened samples was at least six times lower than the unpeened samples and 66% overlap 1 scan presented the least corrosion.

Table 3.2 A table showing Chemical composition of Hank's solution.

Composition	NaCl	KCl	$MgSO_4$	$CaCl_2H_2O$	Na_2HPO_4	$NaHCO_3$	KH_2PO_4	D-Glucose
Hank's	8	0.4	0.09767	0.185	0.04788	0.35	0.06	1.0

What is more, as we know that Laser Shock Peening introduces Compressive Residual Stress (CRS) into the surface layer of metallic materials through high power density laser beam impacting the metallic surface. The CRS not only improves the fatigue lives of implant components but also contributes to the resistance to Stress Corrosion Cracking (SCC). For example, Caralapatti [124], found that HLSP with laser intensity of 2.1 GW/cm^2 can form maximum compressive residual stress of 48 MPa at the depth of 28 μm. By changing different parameters such as power, overlap and impact number, LSP can introduce deeper compressive residual stresses RS layers, which enhances resistance to micro-crack expansion, stopping the crack from its start.

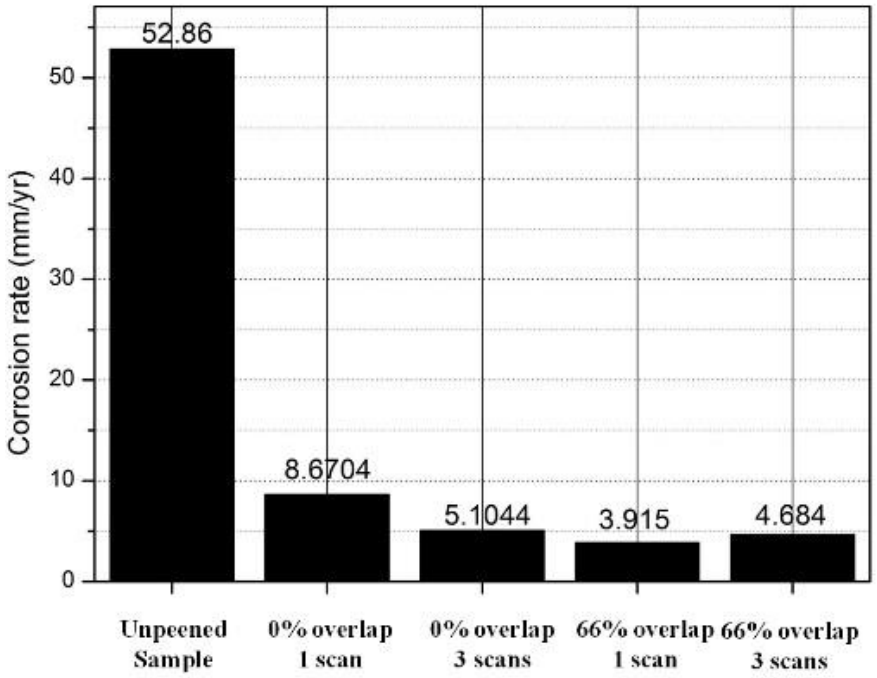

Figure 3.18 Corrosion rate of Pure Mg after 72 hours of immersion in Hank's solution [10].

Figure 3.18 showed the corrosion rate of Pure Mg after 72hs immersion in Hank's solution, it can be seen that, unpeened samples is ranked highest position of corrosion rate, while 66% overlap, 1 scan is the lowest among these samples. Interestingly, the corrosion rate decrease with scan numbers when it is 0% overlap, while, with high laser pulse repetition rate, the overlap higher, thus, increases with scan numbers and reduces the rate of corrosion due to higher magnitudes of compressive residual stress. Moreover, in dynamic conditions after 72h, the corrosion rate difference between unpeened and peened samples was extremely high (52.86 mm/yr *vs* 3.92 mm/yr). Therefore, LSP helps implants endure longer services time and reduce reduces the risk of failure caused by corrosion.

3.5.3 Wear

More than corrosion resistance, the capability of anti-wear is still a problem faced by magnesium that limits the application in the medical sector. Guo *et al* [167], employed LSP to improve the wear resistance pf magnesium alloy ZK60. With LSP, the wear rate decreased by 17.6 in maximum in comparison to the untreated. What is more, a dry sliding wear experiment was carried out by Ge *et al* [168], with various laser energies of 6.5J, 8.5J and 10.5 J to evaluate the wear behaviour of Mg-3Al-1Zn alloy. The wear rates before and after LSP was given in Figure 3.19a. The wear rate was decreased with increasing laser energy. It can be seen from the worn images (Figure 3.20) that the wear for all samples are all identified as abrasive wear.

From Figure 3.20, the width of grooves for the laser shock peened was more narrow and shallow compared to that of the untreated.

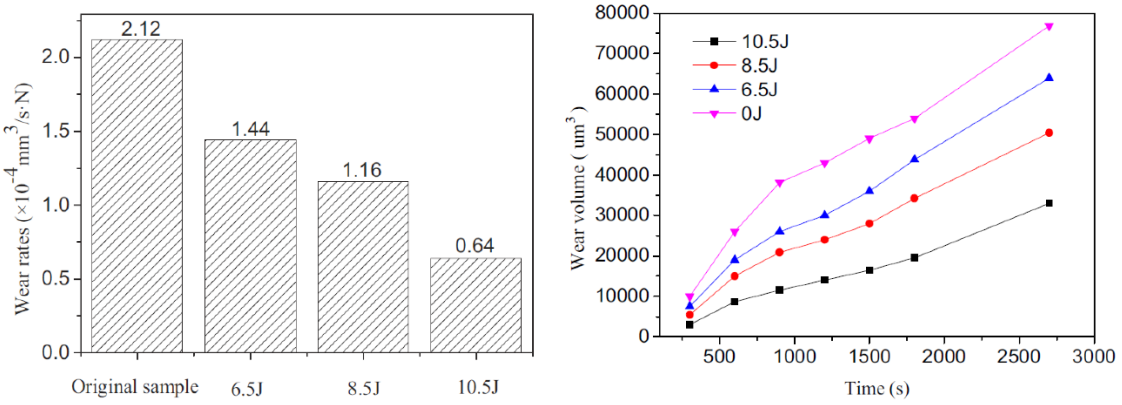

(a) (b)

Figure 3.19 Wear rates (a) and wear volume (b)prior to and after LSP at 6.5J 8.5J and 10.5J [168].

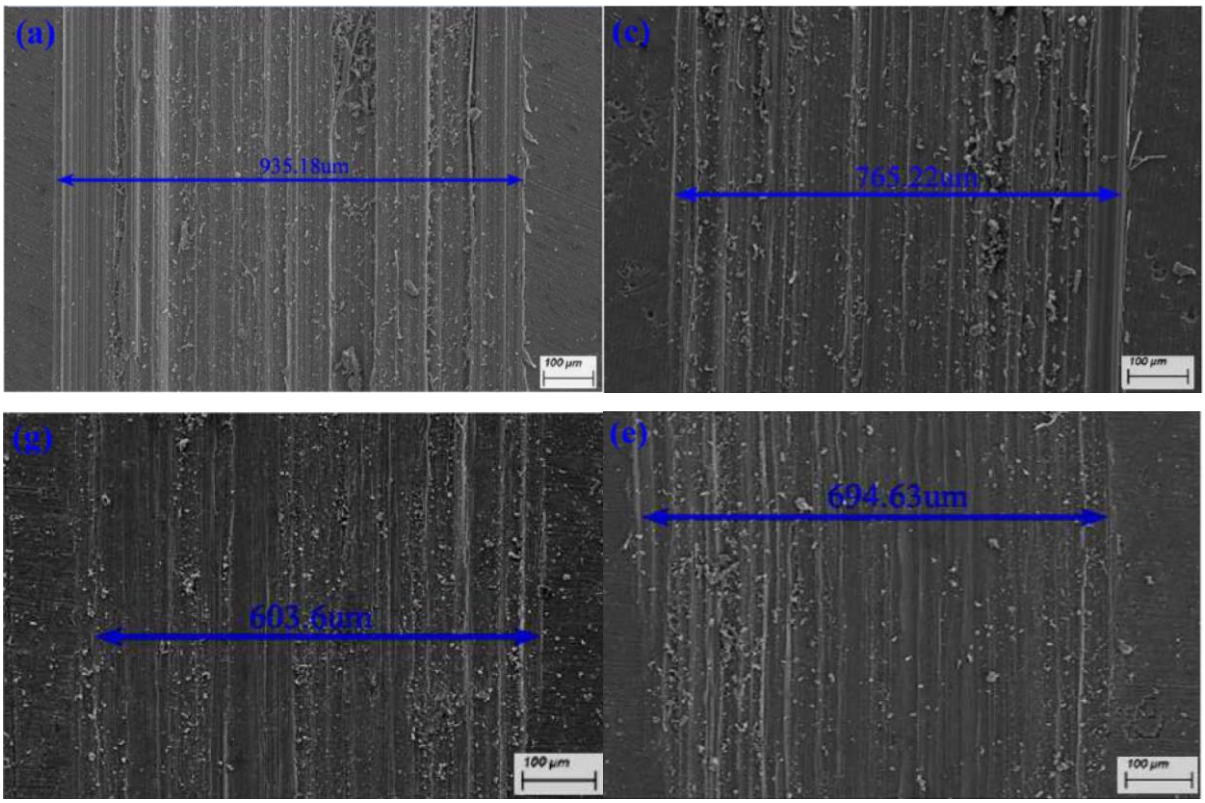

Figure 3.20 SEM images of worn surfaces in (a) untreated; (c) treated with 6.5J;(e) at 8.5J and (g)treated at 10.5J with 3mm spot size 5 Hz and 15 ns pulse duration [168].

In addition, optimal LSP parameters should be chosen for improving wear resistance purposes. Trdan *et al* [169], investigated the tribological behaviour of Aluminium alloy with 3 different

LSP. The results illustrated that the friction coefficient and wear rate were reduced by optimal LSP parameters. However, except the optimal parameters, the rest of the LSP parameters samples exhibited the wear resistance performance maybe even worse than that of untreated. Therefore, by applying a suitable LSP parameter it is quite important for improving the anti-wear performance in the metallic materials.

3.5.4 Wettability

Wetting characteristic is often a research focus for surface modification technology and bio-compatibility. Normally, as a surface modification method, laser shock peening increases the surface roughness of the target material surface by increasing the overlap, thereby, leading to a high contact angle, causing hydrophobicity or low wettability. For instance, according to recent researches, Caralapatti et al. [124], investigated the effect of high repetition laser shock peening on the wettability of pure Magnesium. It was found that the surface of peened Magnesium samples were increased in microhardness from 46HV to 62HV and 74HV. The contact angle was increased to 81.3°. What is more, Prabhakaran et. al. [133], also acquired a similar conclusion, when they used LSP was applied to austenitic stainless steel. They presented that the contact angle of unpeened samples was 34.24° and the surface roughness was also increased by LSP. The unpeened austenitic stainless steel was hydrophilic in nature. But, after 1 impact, the contact angle was increased to 95.75°, thereby, becoming hydrophobic after laser shock peening. Therefore, we realize that surface roughness (morphology) is not the only factor that affects the contact angle of peened samples. Actually, wettability is determined by surface-free energy and surface morphology.

Two equation models are usually employed to investigate the wetting characteristics of solid surface, which is Wenzel model and Cassie-Baxter model [170], shown in Figure 3.21. As it can be seen in Fig 21a, if the valleys of the coarse surface are filled by liquid such as water, thereby, Wenzel's model was more suitable. However, if fluid just stuck on the surface of the top of the protrusions, leaving, the underneath space air. In this condition, shown in Figure 3.21b, Cassie-Baxter model was used to describe the contact angle.

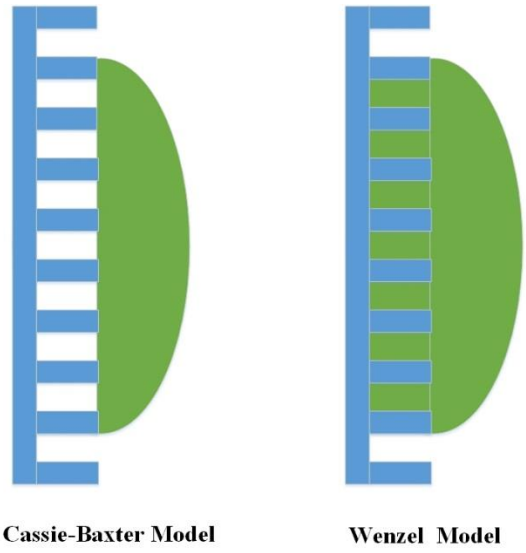

(a) (b)

Figure 3.21 Schematic diagrams of Cassie-Baxter Model in (a); and (b) the Wenzel Model.

In terms of LSP, due to its high laser energy applied with high-pressure plasma is driven shock waves, the surface-free energy was greatly altered. The oxygen concentration is presented on the surface. Specifically, both the hydroxyl group and the oxide layer are very important factors. Hydroxyl group was presented on the ionically bonded surface like oxides, it can greatly reduce the acid and the base components, thereby, increasing the contact angle for polar liquids such as water.

Additionally, due to the ablation of laser shock peening, the contaminations such as dirt is removed which contributed to improving the surface-free energy. This was because the contaminations have low surface-free energy. High surface-free energy can contribute to the biological properties of implants. It is said that a contact angle of 70° is considered to be ideal for cell attachment and better bonding with osteoblast cells, which is key for cell adhesion. When implants are serving inside the human body, they are undergoing different interactions such as cells, proteins adhesion.

3.5.4 Biocompatibility

What is more important, osseointegration is also influence by surface wettability of the implants. However, there is a clear gap in knowledge of the effect of laser shock peeing on cell adhesion and osteointegration of medical metals. Therefore, it is very important to investigate the biological effect of laser shock peening of medical metal materials. At present, the

published literature specifically in the area of evaluating cell behaviour subject to surfaces treated by LSP is still scarce. A study on *vitro* cell culture demonstrated that LSP did not compromise the cytotoxicity of AZ321B in *vitro* [171] and still provided good strength to the part. Creating Groove architecture on the titanium surfaces using LSP can enhance the osseointegration of an implant with the host tissue [172]. Osteoblast cell adhesion and differentiation on Ti-6Al-4V implant were also improved due to the modified surface morphology by LSP. Like other mesenchymal-derived cells, osteoblasts is one of the most crucial cells during the recovery stage after the implantation surgery for the end-user. They need anchorages to survive, proliferate, and differentiate which LSP modified surfaces can provide and that too with induced beneficial residual stresses that enhance the functional properties at the same time.

3.6 Summary

This chapter entails a review on LSP literatures including theory, techniques, applications and especially the medical sector. In this work, the conclusions were drawn as follows:

- Recent research on high repetition laser shock peening, laser shock peening without coating, warm laser shock peening, cryogenic laser shock peening illustrate that LSP is not only constrained in inducing compressive residual but also marching to a widen research area such as surface nano-crystallization, corrosion and wear resistance.
- For now, LSP is still mainly applied in the aerospace industry especially in extending the fatigue life of aero-engine metallic materials namely titanium alloys and nickel alloys. With respect to applications in automotive and nuclear industries, more research findings are still needed.
- Despite the fact that the biological evaluations on LSP are still lack of data, LSP is still considered a promising surface modification technique to be employed in the medical sector as its enhancement on fatigue, corrosion, wear resistance associated with specific surface topography that contributes the implant osseointegration. Applying LSP on the implants will, in turn, benefits the end-user by extending service time and relieving pain from revision surgery

PART 2 Microstructure Characteristics

CHAPTER-4 Effects of Laser Shock Peening on the Microstructure of Ti-6Al-7Nb Alloy

This chapter focuses on laser shock peening conducted by a Q-switched, nanosecond, Nd: YAG laser with 3J, 5J, 7J and at the overlap of 33%, 50% and 67% on the as-received Ti-6Al-7Nb alloy. The cross-sectional microstructure prior to and after LSP was characterized by Scanning Electron Microscopy (SEM), Electron Backscatter Diffraction (EBSD). What is more, the phases before and after LSP were also determined by X-ray diffractions. Thereafter, Transmission Electron Microscopy (TEM) was employed to evaluate the dislocation features after LSP as a primary strengthening mechanism.

4.1 Introduction

Titanium and its alloys have been receiving attention for decades due to its excellent properties: namely; low density of around 4.5 g/cm^3, high corrosion resistance and critical bio-compatibility. Therefore, they were employed in manufacturing components in the automotive, aerospace, biomedical industries. Due to various failure reasons such as medical implants fracture or the need for increasing the serves lifetime of implants, the titanium components were pre-treated by means of surface modifications, namely: shot peening and laser shock peening to make it more deployable for the aforementioned applications. Near-surface compressive residual stresses and work-hardening induced by LSP benefitted the mechanical properties of metallic components. Guo et al. [173] post-processed the additive manufactured Ti-6Al-4V alloy with LSP, and typical deformation-induced microstructures, namely: high density dislocations, dislocation tangles, and mechanical twins were observed along the cross-section leading to improvement of yield strength and ultimate tensile strength. Li *et al* [174], examined the vibration fatigue behaviour and its microstructural response in laser shock peened TC6 alloy. The vibration fatigue life was dramatically increased by 105% in comparison to that of as-received after being subject to LSP. Compressive residual stress, microhardness were increased post LSP. It was found that large amounts of dislocations were accumulated near the twin boundaries which decrease the crack propagation time, thereby, prolonging vibrational fatigue life. According to the Hall-Petch (H-P) equation, the microstructural grain-sizes are inverse proportional to the metal strength. The plastic deformations induce large crystal defects, namely: dislocation features and deformation twins, forming refined grains.

Therefore, LSP induced microstructural refinement benefits the metallic mechanical properties, and in this chapter, the microstructure of the as-received prior to and after LSP were characterized by SEM, EBSD, and TEM.

4.1.1 Titanium alloys and its crystallography

Titanium mainly has two crystallographic forms which are hexagonal close-packed crystal structure (Figure 4.1 (a)) known as the α-phase at room temperature and body centred cubic crystal structure (Figure 4.1b) called β-phases at high temperature. In pure titanium, the α-phase transforms to β-phase when the temperature is raised above 882.5℃ which is called β transus temperature. It is the lowest equilibrium temperature that the titanium consists of 100% β-phase [175]. By alloying elements, titanium atoms are determined into two forms. The β-transus temperature is influenced by additional elements. Elements such as O, C, Al, and Ca that increase the β transus temperature are referred as α-phase stabilizers. However, it should be noted that elements such as N, O, and C lead to contaminations as microscopic hardening was in the alloy which in turn drimente the ductility of the alloys. Elements like Nb, V, and Mo that decrease the β transus temperature are known as β stabilizers which allows the beta phase to exist at ambient temperature. As mentioned in Chapter 2, there are three main microstructure forms in titanium and its alloys, namely; lamellar, equiaxed and bimodal structures. The mechanical properties such as hardness, ductility and tensile property of a titanium alloy are influenced by the above microstructural structures.

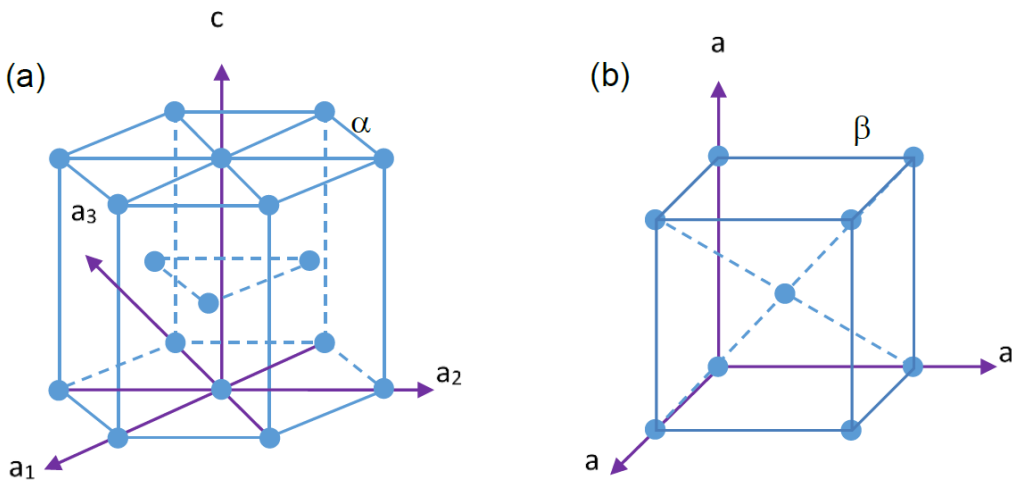

Figure 4.1 Hexagonal close pack structure and centred body cubic structure [176].

A typical tensile stress vs strain curve of Ti-6Al-4V alloy is presented in Figure 4.2. In turn, this material has a similar set of mechanical properties as that used for this work (Ti-6-Al-7Nb). The curve generally demonstrated that as the stress initially increased with increasing strain; work-hardening behaviour was evident, till the peak strain was reached. After reaching the peak (ultimate tensile strength (UTS)), the stress starts to decrease with the strain, exhibiting flow softening behaviour. Yield of this material occurred at tensile stress of 960MPa, thus plastic deformation begun to take place thereafter reaching UTS of 1034 MPa, necking at 800 MPa and fracture at 500MPa.

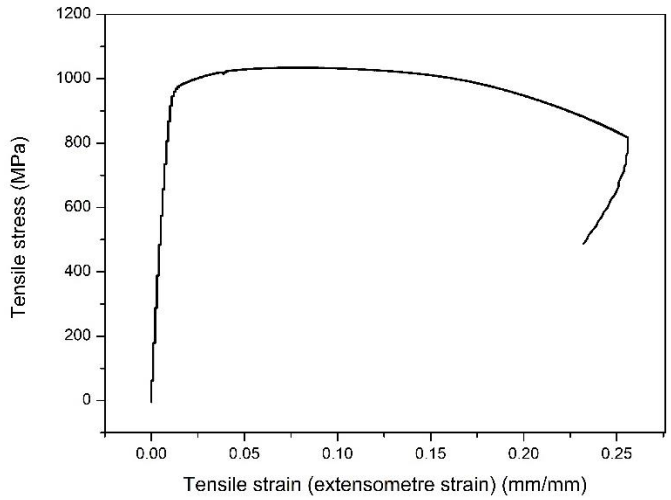

Figure 4.2 the map showing the typical strain vs stress curve of Ti-6Al-4V alloy.

4.1.2 Ti-6Al-7Nb alloy

Ti-6Al-7Nb alloy was developed for clinical and surgical devices with properties mostly identical to Ti-6Al-4V in 1977 at Gebruder Sulzer in Winterthur, Switzerland, substituting Niobium for Vanadium as the beta stabilizing element. It has been widely employed in the medical applications, especially for manufacturing orthopaedic applications, such as fracture fixation plates, intramedullary rods and nails, total hip replacement systems. The titanium alloys employed for the experiment was Ti-6Al-7Nb (ASTM F1295 Rev 11) Table 4.1.

Table 4.1 The chemical composition of Ti-6Al-7Nb alloy.

Element	Al	Nb	Ta	Fe	N	O	C	H	Ti
Wt%	6.1	6.88	0.5	0.19	0.008	0.166	0.04	0.002	BAL

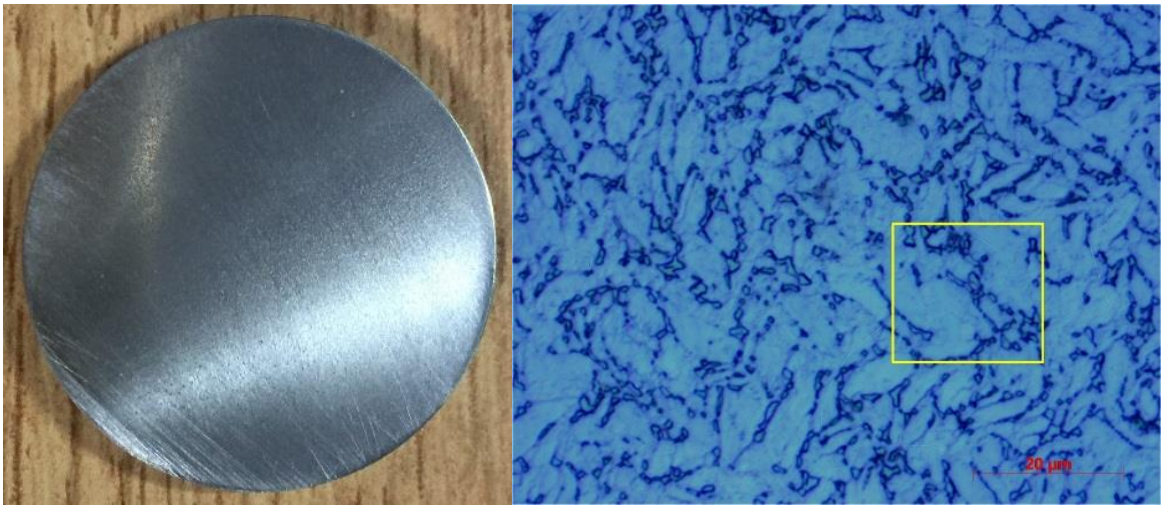

Figure 4.3 The metallographic image of as-received Ti-6Al-7Nb.

It is widely used in the prosthetic implant to relieve patient pain. The Ti-6Al-7Nb titanium alloy belongs to the group of α/β alloys. It is seen that the cross-sectional microstructure consists of globular and acicular α-grains within the β-transformed matrix, shown in Figure 4.3. Regards to the titanium etching methods, due to the toxic and environmental hazards of hydrofluoric acid, Phosphoric acid method was employed for SEM observation samples in this study. The dimensions for SEM and metallographic samples are 10mm × 10mm. These were wet-abraded with 2000 grit SiC abrasive paper and cleaned ultrasonically in deionized water, washed with acetone and dried at room temperature. Thereafter, the surface etching acid etching was carried out by immersion of 100ml beaker in 30ml concentrated phosphoric acid at 80℃ for 20mins in the fume hood.

4.2 Experimental procedures

4.2.1 Laser shock peening parameters for microstructure determination

The LSP experiments were conducted by a Q-Switched Nd: YAG laser (YS120-R200A, Tyrida, Xi`an, China), using a wavelength of 1064nm and 20ns pulse width. The pulse energy applied was 3J, 5J, and 7J, with overlapping of 33%, 50%, and 67%. The experimental and theoretical laser shock peened (LSPned) samples are shown in the optical images in Figure 4.4. The laser spot size was 3 mm. Thus, the power densities were 2.13 Gw/cm^2, 3.54 Gw/cm^2, 4.95Gw/cm^2, as detailed in Table 4.2. The water layer with thickness of 7 mm was used as the confinement layer as it can greatly enhance the mechanical properties via the material deformation. Regarding the confinement layer thickness, Takata *et al* [177]found that the maximum impact

force subject to LSP exhibited in the range of 3-5mm at the power density of 3 GW/cm^2. Additionally, if the water layer is thicker than 6mm, a secondary shock induced by cavitation bubble will be achieved when the power density is higher than 2.5 GW/cm^2 [178]. The absorbent/ablative layer was black vinyl tape with thickness of 2 mm. Figure 4.4 (a) presents (a) a schematic diagram of the process and (b), the comparison of experimental and theoretical LSPned samples, and the as-received Ti-6Al-7Nb titanium bar.

Table 4.2 Parameters employed for the Laser Shock Peening Ti-6Al-7Nb.

Parameters	**Value**
Pulse energy (J)	3, 5, 7,
Laser wavelength (nm)	1064
Spot diameter (mm)	3
Number of laser impacts	1
Overlapping rate (%)	33%, 50%, 67%
Pulse duration (ns)	20ns
Radiance Density (W.mm^2.Sr.µm)	0.46 @ 3J 0.77 @ 5J 1.09 @ 7J

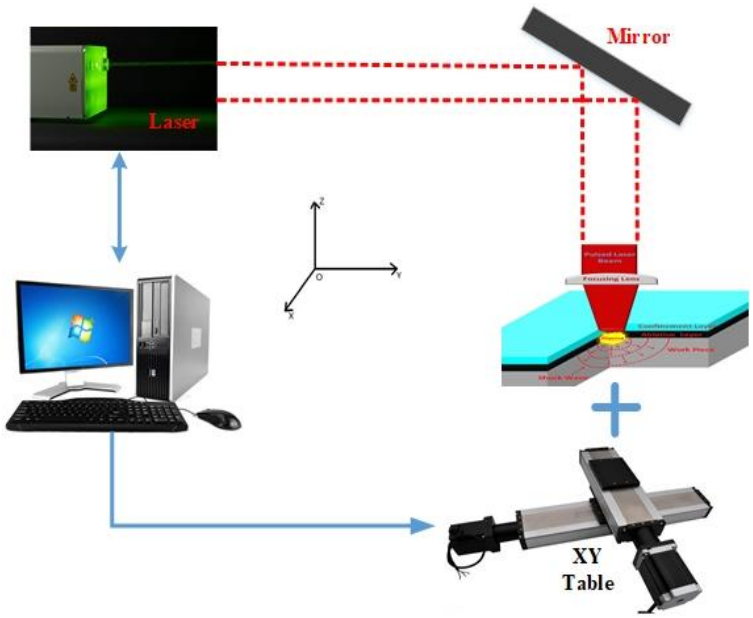

(a)

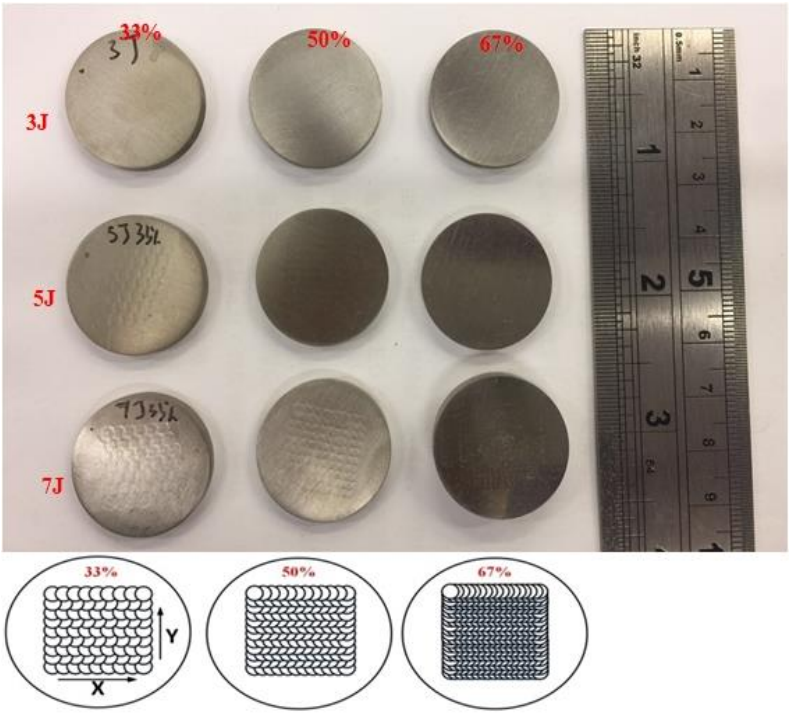

(b)

Figure 4.4 A schematic diagram of the Laser Shock Peening process in (a) the laser shock peened surfaces and the schematics of the laser shock peening strategy in (b).

4.2.2 Electron Microscopy

4.2.2.1 Scanning Electron Microscopy and texture determination with Electron Backscatter Diffraction

The samples were mechanically polished and examined under SEM (VP500 Zesis, Germany) with an EBSD (Electron Back Scatter Diffraction) for Microstructure evaluation at 5kV. The Ti-6Al-7Nb samples were cut into ø 25mm x 8mm, grinded from 300 to 2000 grit with SiC abrasive paper in stages until the material comprised of Sa (Arithmetic mean height) 0.16 µm surface finish, onwards polished from 9 µm to 1 µm using colloidal-silica suspension. The polished samples were immersed in the Koll's reagent for 15 seconds.

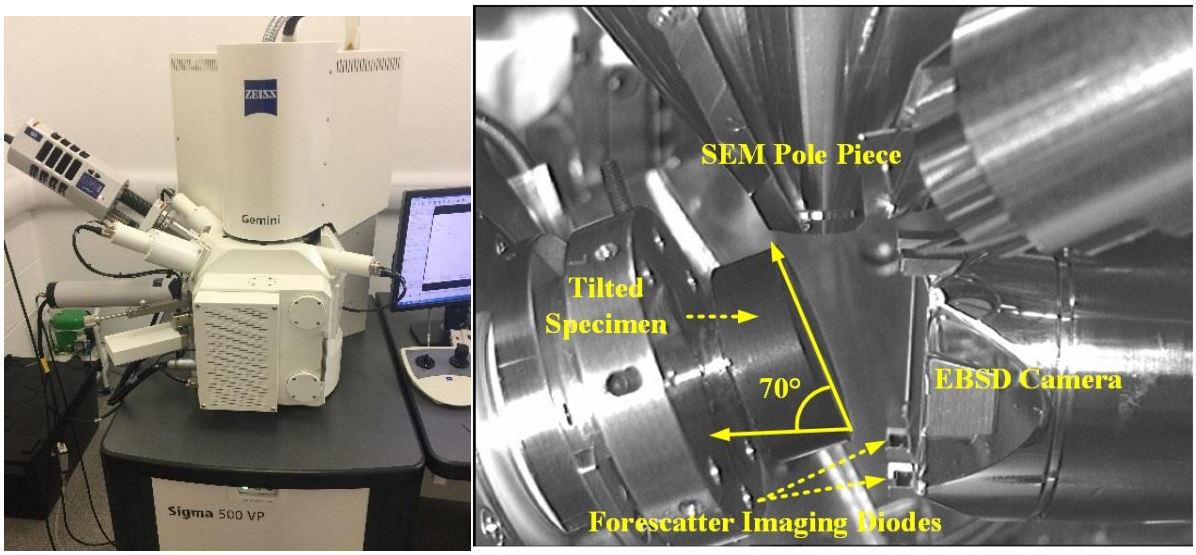

Figure 4.5 image set up for EBSD data.

Microstructure characterizations were examined by EBSD. The etched SEM samples were employed to re-polishing for 12 hours with vibratory polishing to mirror-finished surfaces of titanium sample, set-up and tilted at 70° inside SEM chamber as shown in Figure 4.5. The EBSD analysis was conducted with Oxford detector equipped with an AZtec EBSD system.

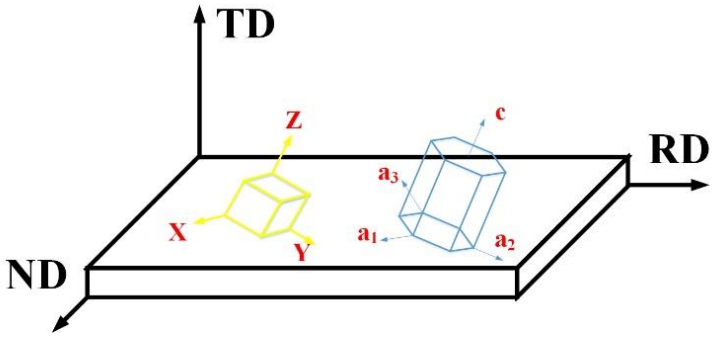

Figure 4.6 Sample co-ordinates and crystal co-ordinate (cubic and hexagonal crystal structure).

In order to characterize the crystal orientations, specimen coordinate system and crystal system was employed. The specimen coordinate system is specified by the direction of the external shape of the specimen. There are three directions in the specimen system, namely: Normal direction (ND), Transverse direction (TD) and Rolling direction (RD) representing the rolling, transverse and normal direction for rolled products (Figure 4.6). In the specimen co-ordinate, one axis is specified while the other two are arbitrarily determined. The ideal orientation nomenclature (hkl)[uvw] (crystal coordinate system) is employed to specify the crystal directions. According to the crystal symmetry, the crystal coordinate is represented with 3

digitals or 4 digitals. For example, for orthogonal symmetry (cubic, tetragonal or orthorhombic), axis [001], [100], [010] were employed. For hexagonal closed packed crystal structure, the axis used are, namely: [0001], [0100], [1000].

4.2.2.2 Transmission Electron Microscopy

The microstructure of the material was observed under a TEM transmission electron microscope (Fei Tecanai G2, shown in Figure 4.7). The cross-section TEM samples were prepared as follows: to make its thickness less than 100μm, both sides of the samples were ground and polished by means of mechanical lapping. Afterward, the vertical sections were etched for 15min at -25℃ with a polishing reagent that consisted of 300ml of CH_3OH, 175ml of C_4H_9OH and 30ml of $HCLO_4$. The TEM foils were prepared by a combination of single and twin-jet electropolishing. The TEM observation was carried out at the accelerate voltage of 200Kv.

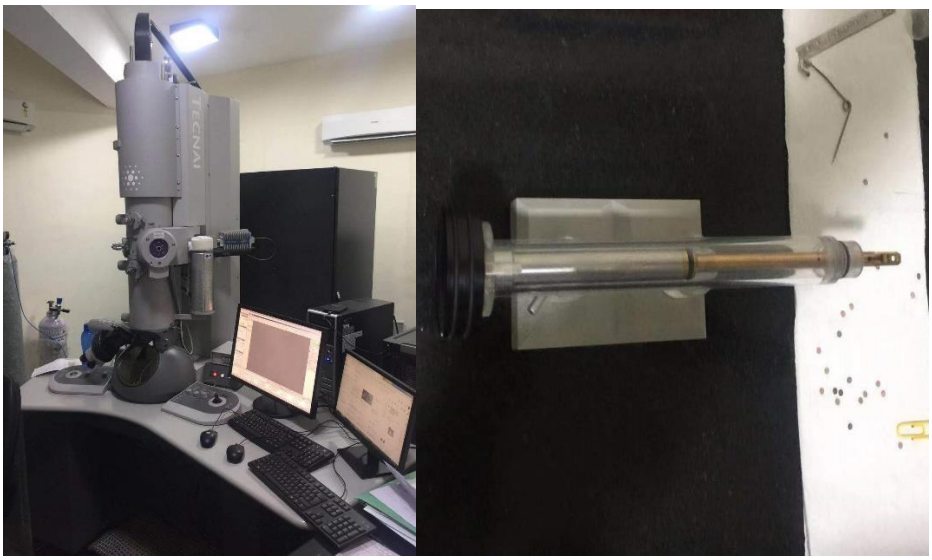

Figure 4.7 Fei Tecanai G2 Transmission Electron Microscopy and Single tilt TEM sample Holder deployed for the analysis at Vellore Institution of Technology (VIT University).

4.2.3 X-ray Diffraction for phase determination

The phase evolution analysis of Ti-6Al-7Nb alloy was conducted *via* X-ray diffraction (XRD) equipment (PANalytical, Netherlands) as shown in Figure 4.8, with Cu-Kα radiation (wavelength: 0.15418nm) with PRS X-beam detector at a working voltage of 40kV and current of 35mA. The diffraction data were collected over a 2θ range of 10° to 90°.

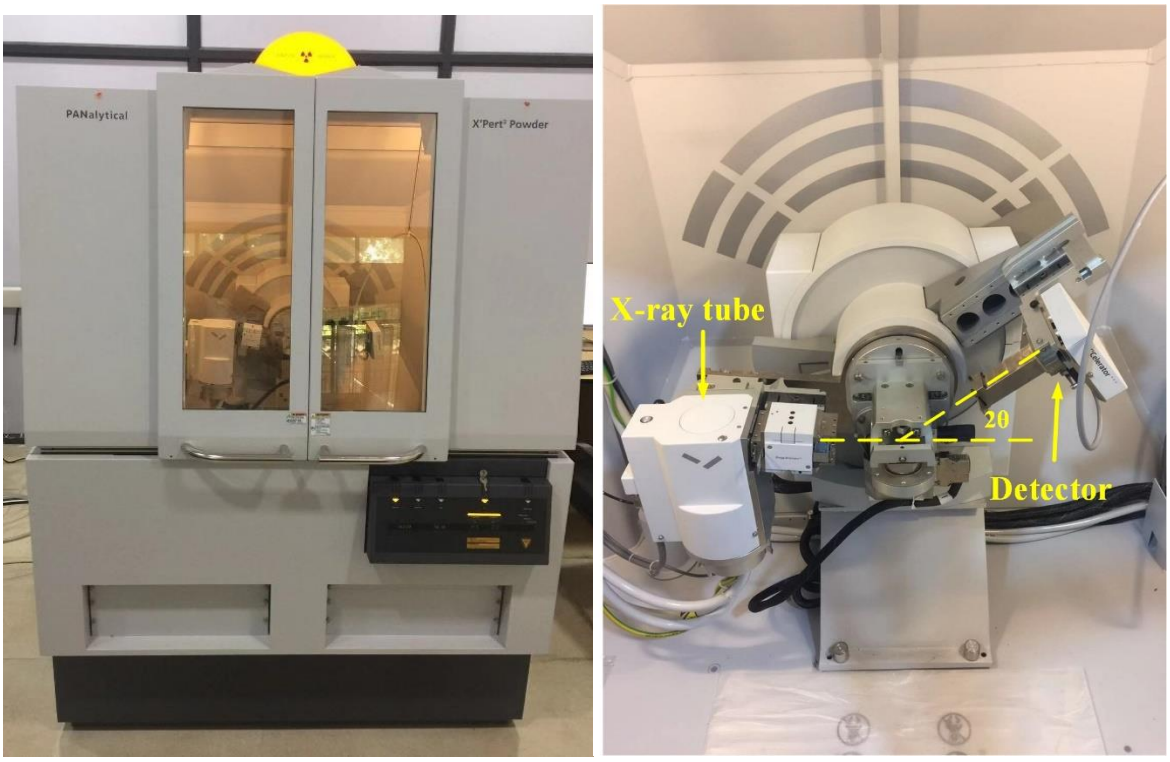

Figure 4.8 PANalytical advance powder XRD instrument.

4.3 Microstructure characterization of as-received and laser shock peened Ti-6Al-7Nb alloy

4.3.1 As-received Surface and cross-sectional microstructural characterizations

The grain refinement has a significant relationship with the mechanical properties of the metal alloy [179]. In this section, SEM was used to evaluate the microstructure of Ti-6Al-7Nb alloy. The surface microstructure at lower and higher magnification is shown in Figure 4.9. The surface microstructure of as-received Ti-6Al-7Nb alloy consists of globular and acicular α and retained β grains. The acicular and globular α distribute non-uniformly. Smaller α grains surround around large coarse α grain, and between them, retained β grains are distributed randomly. What is more, the size of α-grains varies from several micrometres to tens of micrometres due to the hot rolling process applied previously. Observing at high magnifications, we can clearly see the sub-grains are inside the coarse grains and the sub-grain boundaries are somewhat sharp. Cross-sectional microstructures are given in Figure 4.10, as mentioned above (hot rolling), the grains are elongated along rolling direction. Figure 4.10 shows that, the grains also distribute randomly and non-uniformly. At higher magnification, we also can see sub-grains and sub-grains boundaries. With the grain intercept method, the as-received sub-grain size was 266.5 nm.

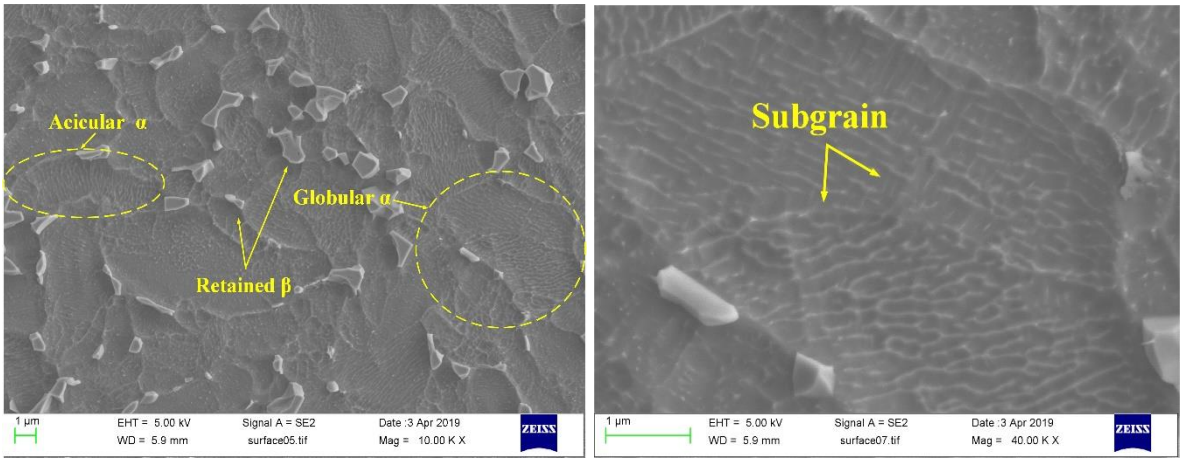

Figure 4.9 SEM images showing surface microstructure of Ti-6Al-7Nb at magnifications of, X 20K, X 40K.

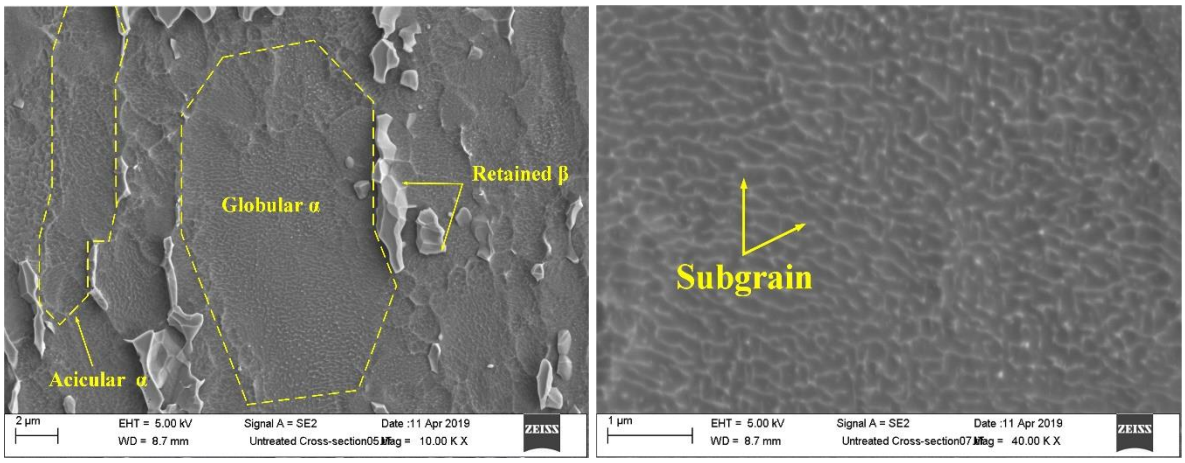

Figure 4.10 SEM images showing the cross-section microstructure of Ti-6Al-7Nb at magnifications of x 20K and x 40Kmagnification.

4.3.1.1 Texture determined by Electron Backscatter Diffraction (EBSD)

EBSD is superior at being able to determine the texture orientation due to the crystallographic orientation contrast in the inverse pole figure maps, and indicate the adjacent crystal misorientation. Figure 4.11 shows the local misorientation map (KAM) and band contrast image of as-received Ti-6Al-7Nb alloy. The as-received bar has been thermo-mechanically processed *via* hot rolling, followed by annealing at 700℃ for 1 hour for the purpose of residual stress relaxation. In Figures 4.11b, it can be seen that, due to the hot rolling, grains along the rolling direction were somewhat elongated. Additionally, some coarse grains were refined into many small grains, where the adjacent grain misorientation was comparatively higher than that

of the prior coarse grains. It is the thermo-mechanical process of hot rolling that facilitates the crystallographic misorientation in the as-received microstructure.

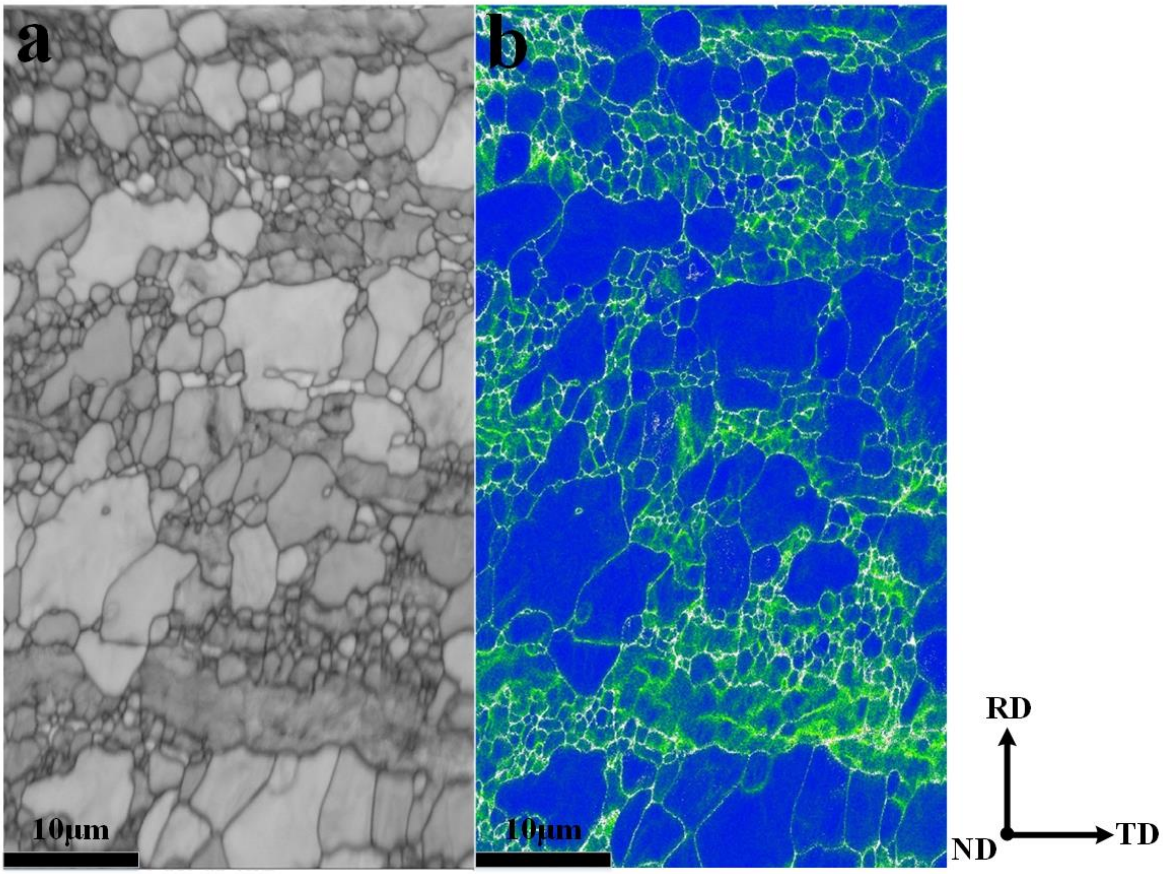

Figure 4.11 The cross-section microstructure of as-revived Ti-6Al-7Nb alloy.

4.3.2 The Cross-sectional microstructure of Laser Shock Peened Ti-6Al-7Nb

Figure 4.12 shows the microstructure of Ti-6Al-7Nb alloy after LSP. At the magnification of X 10K, among all LSP parameters, we did not see that the grains are refined after LSP. All microstructures are similar to the as-received.

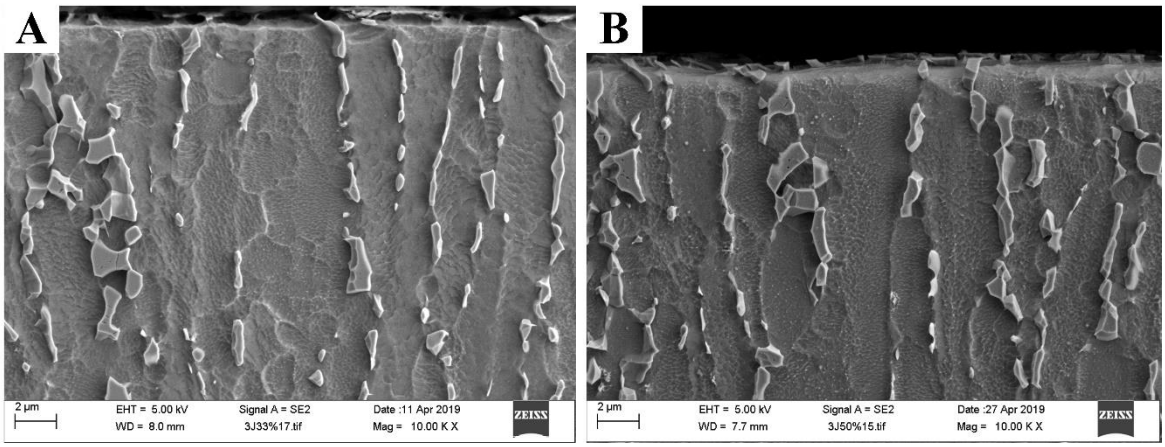

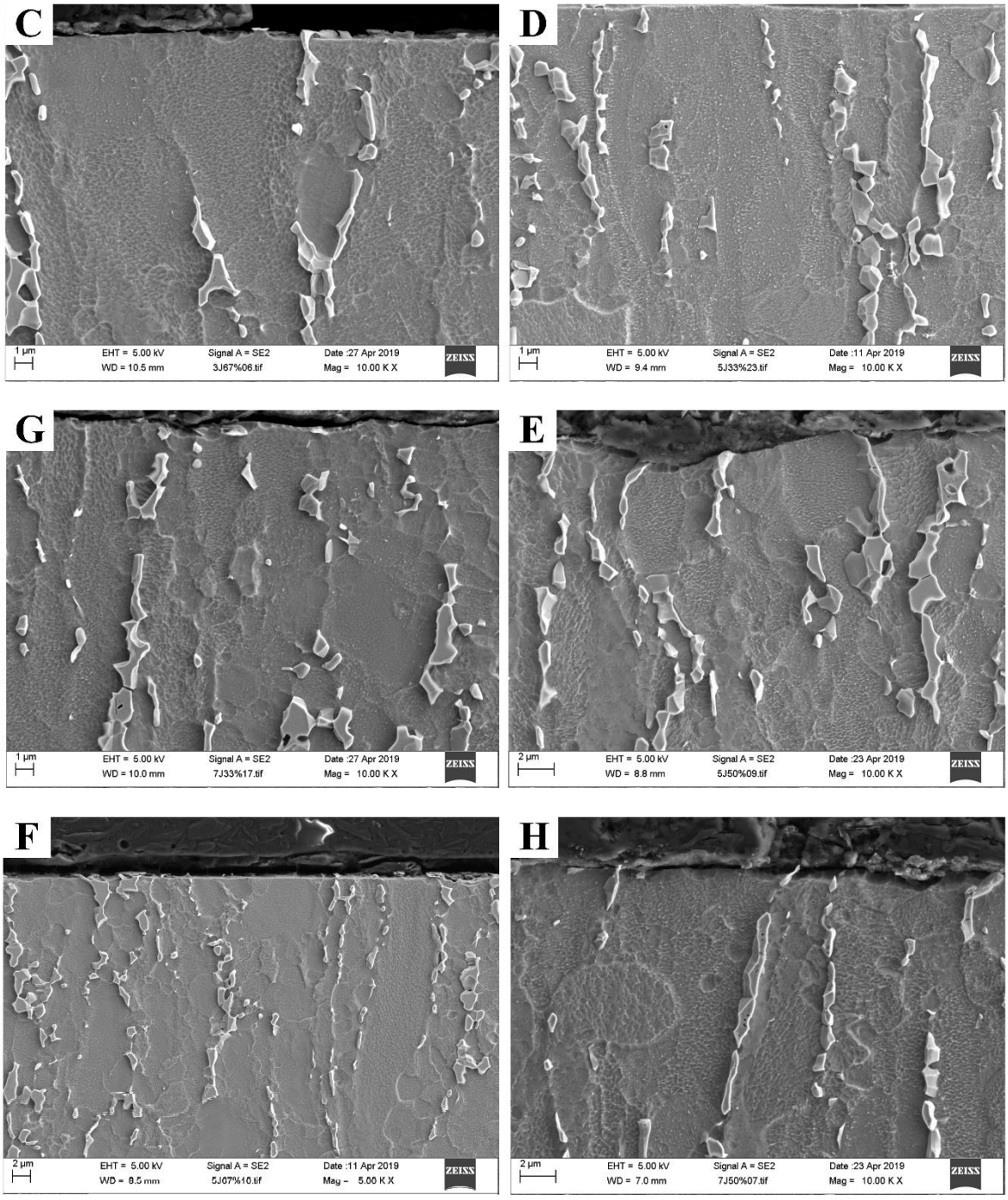
C
1 µm
EHT = 5.00 kV
WD = 10.5 mm
Signal A = SE2
3J67%06.tif
Date :27 Apr 2019
Mag = 10.00 K X
ZEISS
D
1 µm
EHT = 5.00 kV
WD = 9.4 mm
Signal A = SE2
5J33%23.tif
Date :11 Apr 2019
Mag = 10.00 K X
ZEISS
G
1 µm
EHT = 5.00 kV
WD = 10.0 mm
Signal A = SE2
7J33%17.tif
Date :27 Apr 2019
Mag = 10.00 K X
ZEISS
E
2 µm
EHT = 5.00 kV
WD = 8.8 mm
Signal A = SE2
5J50%09.tif
Date :23 Apr 2019
Mag = 10.00 K X
ZEISS
F
2 µm
EHT = 5.00 kV
WD = 8.5 mm
Signal A = SE2
5J67%10.tif
Date :11 Apr 2019
Mag = 5.00 K X
ZEISS
H
2 µm
EHT = 5.00 kV
WD = 7.0 mm
Signal A = SE2
7J50%07.tif
Date :23 Apr 2019
Mag = 10.00 K X
ZEISS

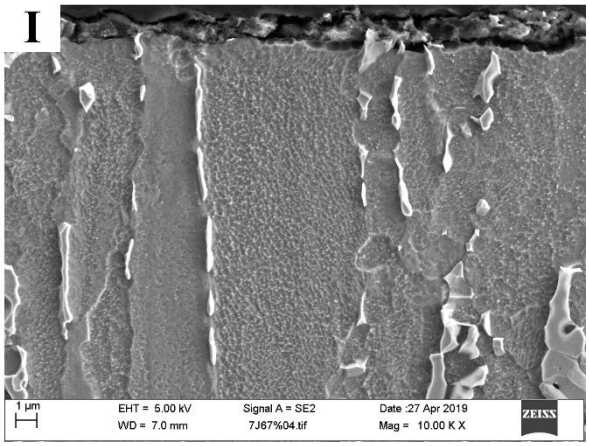

Figure 4.12 SEM images showing the cross-section microstructure of Ti-6Al-7Nb post to laser shock peening at parameters of (a) 3J33%, (b) 3J50%, (c) 3J67%, (d) 5J33%, (e)5J50%, (f) 5J67%, (g) 7J33%, (h) 7J50%, (i)7J67% .

Therefore, increasing the magnifications to 40Kx, inside coarse grains, the sub-grains are clearly observed (Figure 4.13). With GIM, the average sub-grain sizes are given in Table 4.3

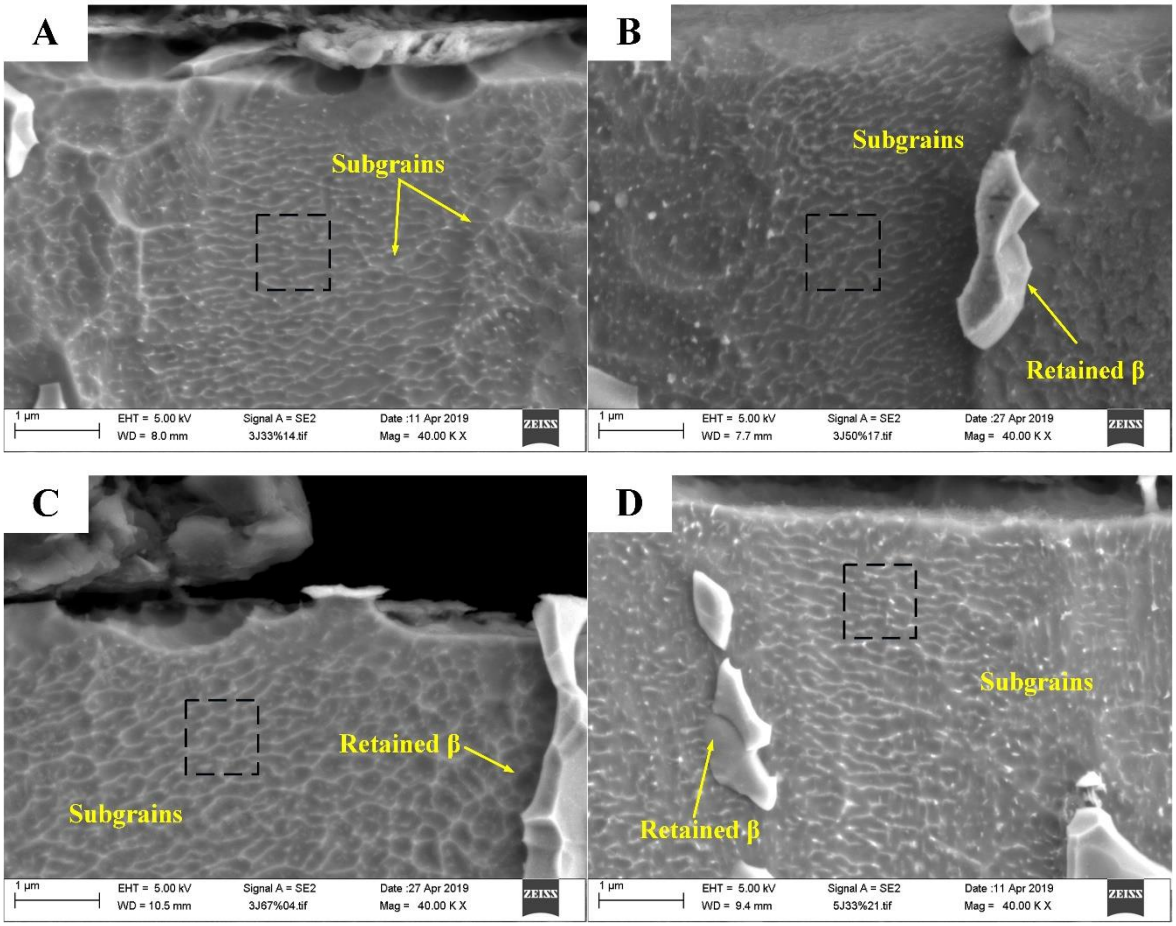

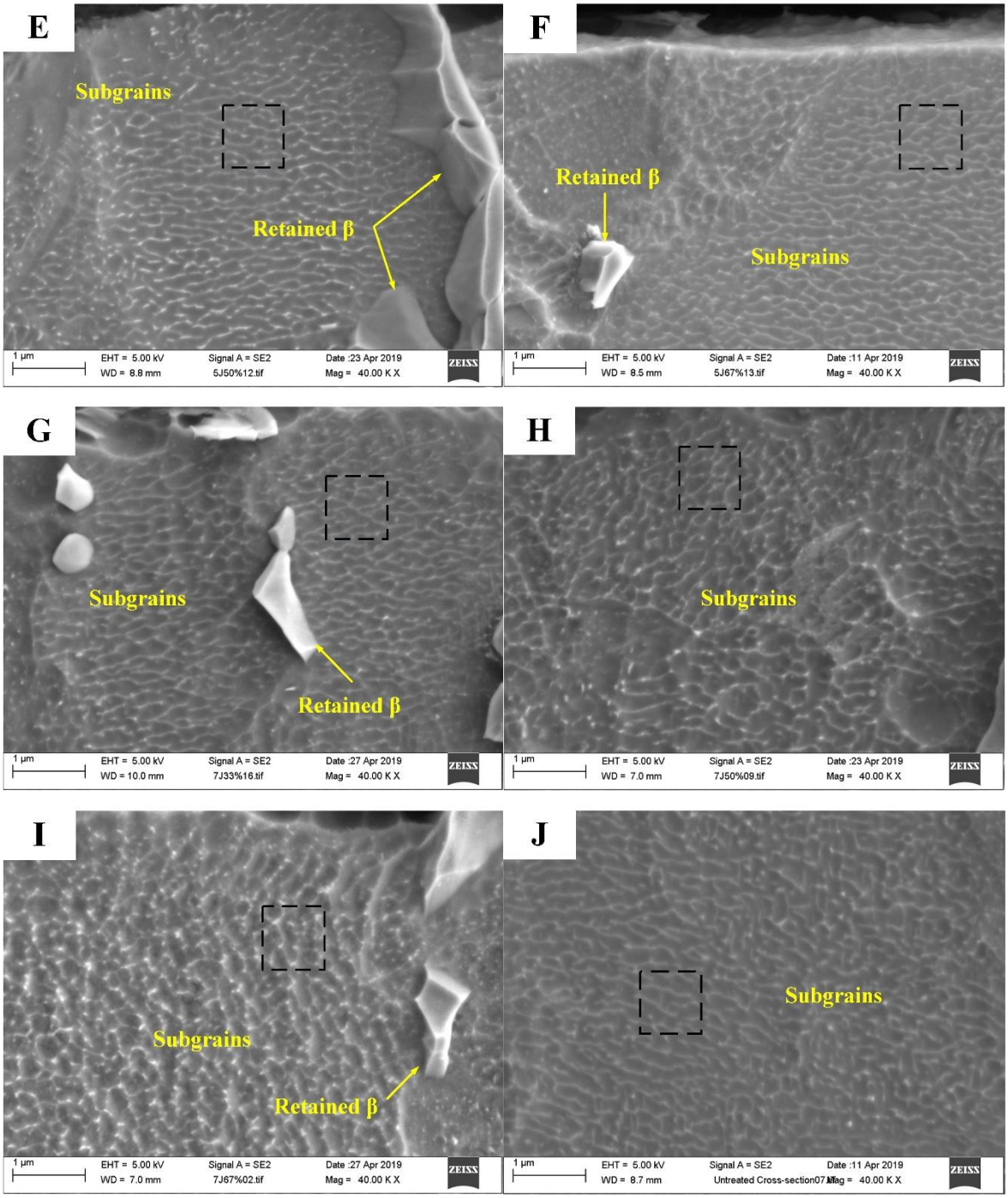

Figure 4.13 SEM images (at 40Kx magnifications) showing the sub-grains before and after laser shock peening at parameters of (a) 3J33%, (b) 3J50%, (c) 3J67%, (d) 5J33%, (e)5J50%, (f) 5J67%, (g) 7J33%, (h) 7J50%, (i)7J67%, (j) untreated.

Table 4.3 Average sub-grain size (nm) after laser shock peening calculated by the grain intercept method.

33%	50%	67%

3J	**266.39**	**251.5**	**222.76**
5J	**265**	**240.7**	**215.6**
7J	**217.62**	**194.2**	**168**

4.3.3 Phase determination by X-ray diffraction

The LSP induced high pressure shock wave can result in plastic deformation and even grain refinement. In order to investigate the effect of laser shock processing on the microstructure of Ti-6Al-7Nb, XRD method was conducted to measure the different diffraction patterns. Therefore, the XRD patterns of laser shock peened samples (2θ from 10° to 90°) were shown in Figure 4.14. It can be seen that the main phase of Ti-6Al-7Nb alloy are still peaks of α (100); α(002); α(101); α(102); α(110) and α(103), α(200), α(201) and β(002). There are not any new peaks after LSP. This indicates that there are no phase transformation and no new crystalline phases generated.

The peaks broadening and shifting can be found in the magnified peaks images. This is due to changes in lattice strain and crystallite size caused by high-strain plastic deformation. In the peak of α (100), we find that the peak was broadened with increasing the energy (if we keep overlapping the same). It is reported that if peaks shift toward higher 2 theta angles, it is compressive residuals stress. However. we did not see such a trend about the peak shifting relating the residual stress. Therefore, the broadening is the domain factor for examine lattice strain and crystallite size.

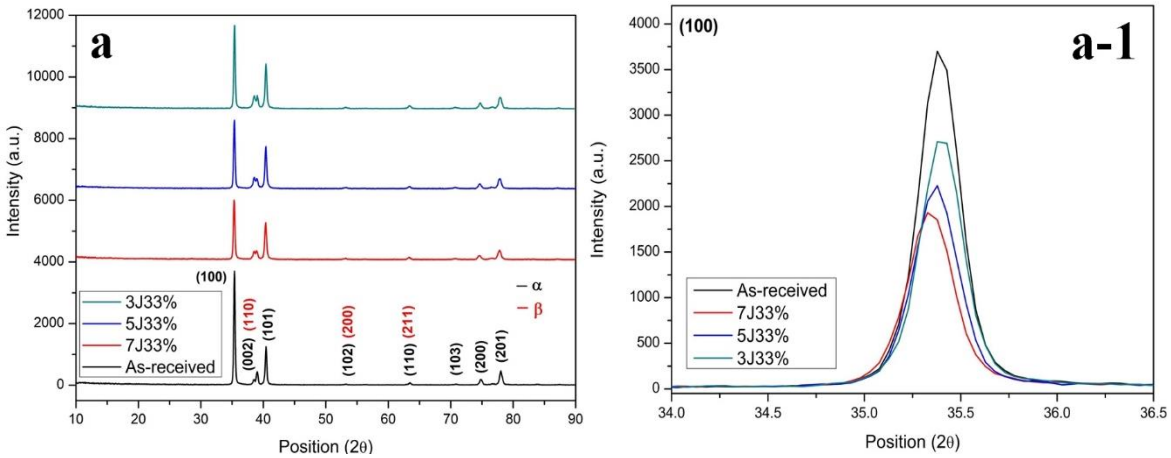

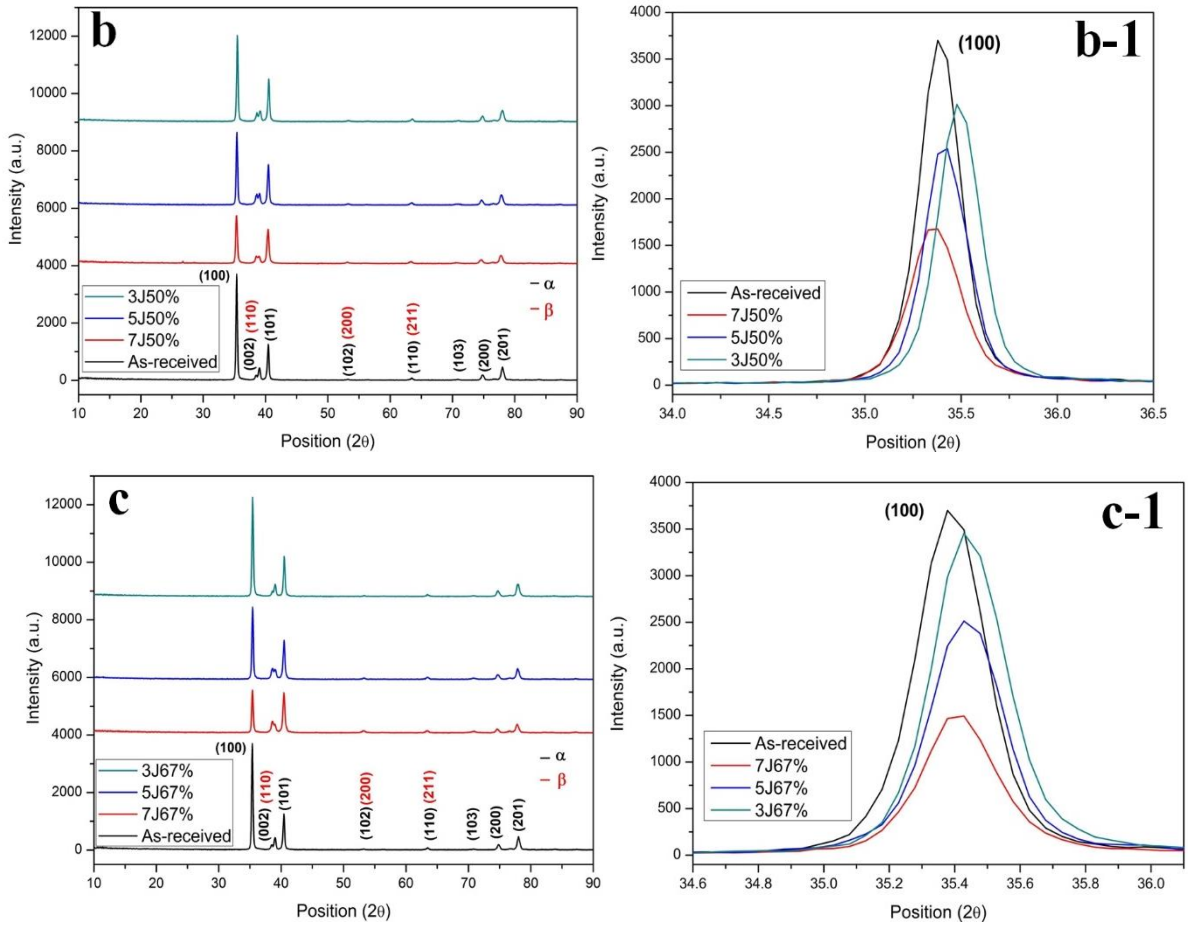

Figure 4.14 X-ray diffraction patterns and magnified α (100) peak of Ti-6Al-7Nb alloy in (a) at 33%; (b) at 50%, (c) at 67% laser peening over-laps.

4.3.4 Transmission Electron Microscopy observation of dislocations at grain boundaries after Laser Shock peening on the as-received

The microstructure at the top surface of LSPned Ti-6Al-7Nb alloy was characterized by using TEM shown in Figure 4.15 and 4.16. Literatures have reported that LSP could lead to surface and near-surface microstructure deformation movements, especially high-density dislocations[180, 181]. At the top surface, there are many dislocations features including dislocation tangles, dislocation walls, dislocation cells, and dislocation pile-ups. In Figure 4.15 (a) to (d), dislocation lines, dislocations walls are accumulated near the grain interfaces as the impeding of the grain boundary. With increasing the density of dislocations, the dislocation tangles will transform into dislocation walls (Figure 4.15(e)) Furthermore, these will further form new sub-grain boundaries, and the sub-grains were even refined into nano-size which we call this phenomenon as “Laser Shock Peening Nano-crystallization ”[182]. It has been shown that the higher the density of the sub-grains, the higher the yield stress of material due to the increased sub-grain boundary. In Figure 4.15 (f) and (g), more dislocations move towards the

subgrain or grain boundaries, and unable to pass the boundary, thereby a process of 'pile-up' occurs at the grain boundary. The grain boundary strengthening theory has a great influence on the yield strength, as described by Hall-Petch relationship as shown in Equation 4-1:

$$\sigma_y = \sigma_0 + \frac{k_y}{\sqrt{d}} \tag{4-1}$$

Where d is grain size, σ_y is the yield stress, σ_0 is the material constant for the starting stress and k_y is the material strengthening coefficient. This H-P relationship indicates that the smaller the grain size, the higher the applied stress needed to propagate dislocations through the material. Therefore, that is an important factor in the microstructural aspect that LSP can benefit the fatigue resistance of the metallic materials.

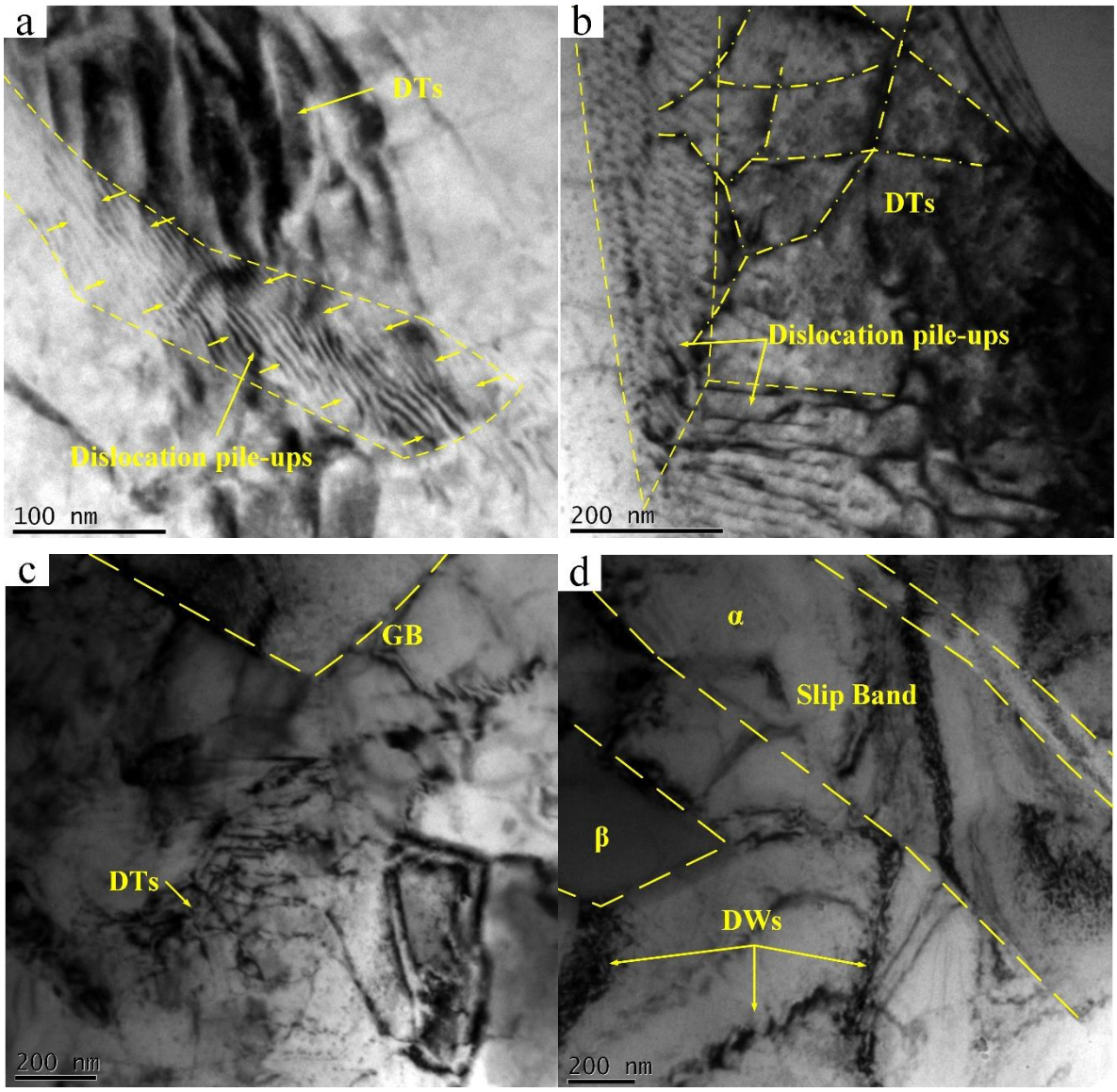

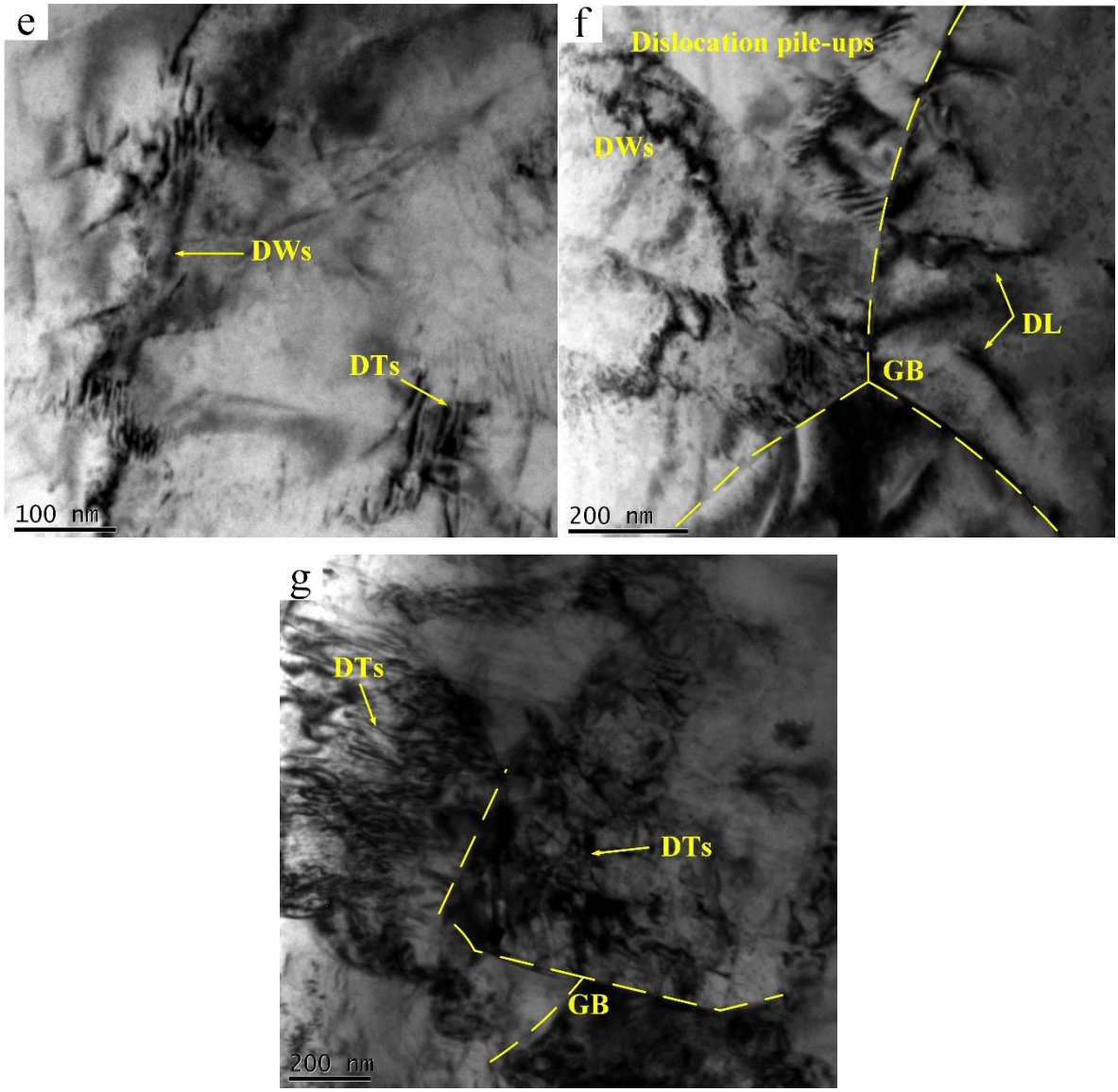

Figure 4.15 TEM images showing dislocations features including dislocations walls, cells, tangles in laser shock peened Ti-6Al-7Nb alloy.

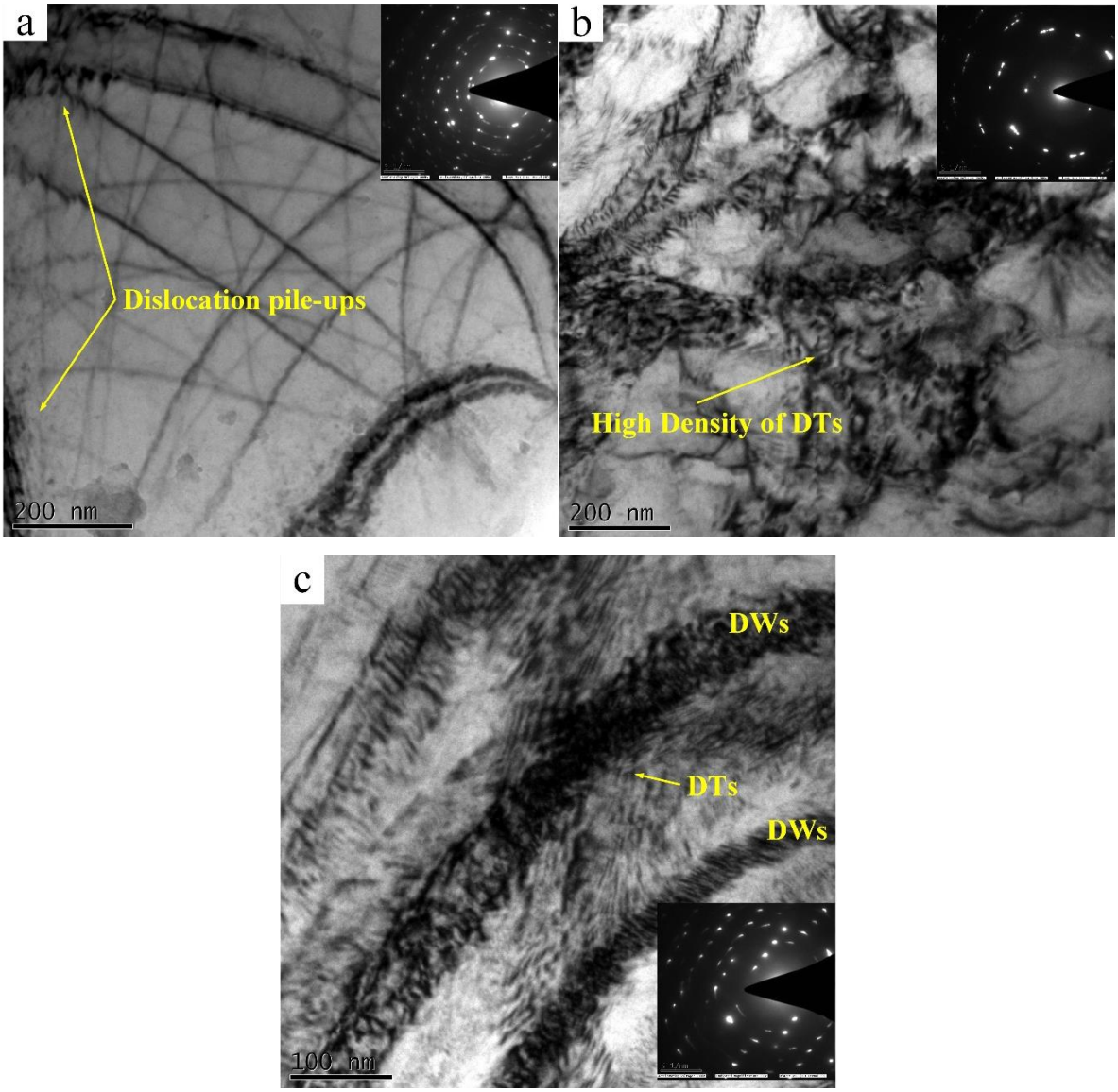

Figure 4.16 The TEM images showing the microstructure of laser shock peened Ti-6Al-7Nb at the top surface(a) and sub-surface(b-c) corresponding selected area electron diffraction separately.

Figure 4.16 (a-c) with the selected area electron diffraction (SEAD) was taken from top surface to the inner substrates. It can be seen from Figure 4.16 (a) the SEAD pattern in the image was ring-shaped which indicated that the original sub-grains have been refined and the orientation distributed randomly. In Figure 4.16 (b), there a great of high intensity dislocations forming dislocations tangles and dislocations wall. However, the corresponding SEAD image presents the arc-shaped diffraction pattern which means the sub-grain refinement has not been completed yet. A similar trend can also be found in Figure 4.16 (c) corresponding SEAD image.

There is some matrix in the SEAD. This may due to the large coarse grain that is still not refined by LSP which is also can be seen in the IPF map from EBSD observations.

4.4 Summary

The following conclusions were drawn from laser shock peening treatment of bio-grade Ti-6Al-7Nb alloy with 3J, 5J and 7J at the overlap of 33%, 50% and 67% with a spot-size of 3mm, 20ns pulse duration and a frequency of 5 Hz in this chapter.

- The cross-sectional microstructure prior to and after LSP was characterized by SEM. At the low magnification, the SEM images reveal that the average α and β grains did not see any refinements. At the high magnification, the average sub-grain sizes are refined to the range 168nm to 265nm, while that of as-received was 266nm.
- From the Kernal average map, the high misorientations angles localized in the smaller grains while that of the coarse grains are much higher.
- The phase of Ti-6Al-7Nb alloy was determined by XRD. There was no new phase formed after LSP. The peak was broadened with increasing the energy when the overlap was kept consistent.
- Dislocation tangles, dislocation walls, dislocation cells and dislocation pile-up were observed using TEM. According to Hall-Petch theory, these deformation features benefits the mechanical properties of Ti-6Al-7Nb alloy.

CHAPTER 5 Globularization *via* Heat Treatment of Ti-6Al-7Nb alloy

This Chapter focuses on the effect of heat treatment processes on the microstructure of medical-grade Ti-6Al-7Nb alloy, with an objective to acquire a globular microstructure suitable for subsequent surface treatment such as Laser shock Peeing (LSP). All heat treatments were carried out using a high temperature furnace in the ambient environment. The titanium alloy samples initially received solution treatment at various temperatures between 800℃ to 1100℃ for a range of times followed by subsequent cooling rates ranging from furnace cool to water quench. A number of the samples were then subject to ageing at 800℃ for either 2hrs or 4hrs. The microstructure revealed that alpha (α) martensite was formed on cooling after solution treatment from 980℃ which is typical of bi-modal microstructure. What is more, air cooling and furnace cooling for 2hrs and 4hrs were also conducted after solution treatment at 900℃ and 950℃. A globular microstructure was formed with furnace cooling from both temperatures. Further adjacent grain crystallographic misorientation was characterized by EBSD.

5.1 Introduction

The alloy under investigation in this work is Titanium Ti-6Al-7Nb, this being a two phase material, consisting of alpha (α) + beta (β) phases. The α hexagonal close-packed (HCP) phase being stabilised by the aluminium constituent whilst the body centred cubic (BCC) β phase is stabilised by the niobium alloying addition [183-185]. In 1977, at Gebruder Sulzer, Switzerland, Ti-6Al-7Nb was initially developed for surgical implants, aimed at replacing Ti-6Al-4V alloy as vanadium is cytotoxic once it is released into the human body. The replacement of alloying addition 4V by 7Nb leads to higher corrosion resistance and better biocompatibility. Thus, Ti-6Al-7Nb alloy has been employed for manufacturing joint prostheses especially for hip implants [186].

Laser Shock Peening (LSP) is an advanced surface modification technique primarily utilised for improving mechanical properties such as wear [187], corrosion[188], and fatigue resistance[189-192]. Now, LSP is receiving increasing interest as a technique for improving the surface characteristics of alloys for clinical applications requiring high levels of biocompatibility.

In the study which was previously published by the same authors [193], it was demonstrated that the wear resistance of Ti-6Al-7Nb alloy was improved after multiple LSP, due to surface hardness enhancement. The wettability of the Ti-6Al-7Nb alloy could be controlled and altered by laser spot footprint overlap and laser energy of the LSP process. However, the mechanisms of material deformation following laser shock peening are not clear since the as-received material is in hot rolled condition, During the hot rolling thermal process, dislocations are formed, adjacent grain crystallographic misorientations are increased, even coarse grains could be refined to a smaller level. Therefore, it is difficult to determine the effect of LSP on dislocation movement and grain refinement of such a hot rolled alloy. Consequently, it is necessary to modify the morphology of the phases within the microstructure of the as-received material to be able to analyze clearly the deformation mechanism when the material is subjected to LSP.

However, the mechanisms of material deformation and misorientation distribution following LSP are not clear. In order to investigate the changes in the microstructure after LSP, a uniform misorientation microstructure is needed as original untreated samples. This is because the as-received material is in hot/cold rolled condition. Residual stresses are caused during the processing of hot/cold rolling. Therefore, annealing is normally employed to release the thermal-compressive residuals stresses. However, annealing may not change the effects of hot rolling on the dislocation density and adjacent grain crystallographic misorientations. Additionally, after hot rolling, coarse grains could have been refined to a smaller level. Therefore, it is difficult to determine the effect of LSP on dislocation movements and grain refinement of such a hot rolled alloy. Consequently, it is necessary to modify the morphology of the phases within the microstructure of the as-received material to be able to analyse clearly the deformation mechanism when the material is treated by LSP.

It is recommended by Kohn and Ducheyne *et al* [194] that an equiaxed microstructure is ideal for the medical application of α+β titanium alloys. The transformation into an equiaxed microstructure can be obtained via a non-complex heat-treatment process. Among previously published work, solution treatment at 955°C (below β transus) and 1055°C (above β transus) on Ti-6Al-7Nb was conducted by Sercomb *et al* [195] to investigate the mechanical properties and microstructural morphology of Ti-6Al-7Nb components manufactured by selective laser melting. After solution treatment in the β-phase field, it was found that a homogeneous structure was formed was formed. On the other hand, solution treatment in the α+β field did

not completely change the as-received microstructure which consists of an α martensitic structure in a metastable β matrix. What is more, the cooling rate after solution treatment is another important factor in phase transformation in Ti-6Al-7Nb. In a study conducted by Dabrowski *et al* [196], following solution treatment in the α+β field at 970℃, Ti-6Al-7Nb was cooled down at a continuous cooling rate ranging between 0.05 and 25℃/s. Results showed that the α phase volume fraction increased with the decreasing cooling rate. What is more, heat treatment also plays an important role in improving the mechanical properties of titanium alloys. With the processing such as solution, annealing, and aging, the α+β titanium alloy can not only be strengthened but also be reduced the residual stresses formed during the manufacturing. A combination mechanical property of machinability, ductility, dimensional and structural stability also can be produced. For α and near-α titanium alloy, for example, Ti-8Al-1Mo-1V. solution and aging treatment normally is used to achieve higher strengths. Regarding the β titanium, annealing has been mostly employed for residual stress relieving. And in α+β titanium, the microstructures are manipulated below the β transus temperature by solution treatment for hardening and stress relieve.

For α+β titanium such as Ti-6Al-7Nb, there are three typical microstructures, namely: lamellar [197], equiaxed [198] and bimodal[199] Various work has been published on heat treatments designed to generate these three fundamental microstructures and ascertain corresponding relationships with attained mechanical properties. Geetha *et al* [200], attempted to generate an equiaxed microstructure in three β titanium alloys (Ti-13Nb-13Zr, Ti-20Nb-13Zr and Ti-20Nb-20Zr) by hot rolling in α+β field with initial hot-rolled microstructure. Sabban *et al* [201], focused on generating a bimodal microstructure to enhance the ductility and toughness of additively manufactured Ti-6Al-4V alloy from the as manufactured lamellar microstructure, by thermal cycling between 875℃ and 975℃. Globularization is known as the transformation of a lamellar microstructure into a globular microstructure, the process can be performed via either static or dynamic thermal (thermo-mechanical) treatments. Xu *et al* [202], investigated the mechanism of static globularization in Ti-17 titanium using heat treatment at 820℃. What is more, the dynamic globularization of Ti-17 alloy had also been quantitatively analysed under the conditions of hot compression over a temperature range of 780℃-860℃ [203].

The aims of this investigation is to develop a thermal processing methodology to generate a globular microstructure in Ti-6Al-7Nb alloy to facilitate understanding of the microstructure deformation mechanism after subjecting the material to surface modifications such as

mechanical shot peening or laser shock peening. The microstructures were characterised with Optical Microscopy (OM), Scanning Electron Microscopy (SEM) and Electron Back Scattered Diffraction (EBSD). The obtained results will not only supplement existing knowledge concerning phase transformation microstructures in Ti-6Al-7Nb but also be useful for further two phase (α+β) titanium microstructural engineering

5.2 Experimental procedures

The as-received Ti-6Al-7Nb alloy was supplied from Aircraftmaterial co., Ltd in the form of 1 inch diameter bar. The as-received bar was cut into 3mm thickness disks and placed into a well-calibrated tube furnace (PTF; Lenton co., Ltd, UK) for the heat treatment experiment at various temperatures as listed in Table 5.1. The whole heat treatment experiment was carried out in the ambient atmosphere.

Table 5.1 Heat treatment conditions applied to Ti-6Al-7Nb alloy in this work.

Sample No	Solution treatment Temperature (℃)	Time (hrs)	Cooling method	Ageing temperature (℃)	Ageing time (hrs)	Cooling method
1-1	800	0.5	WQ			
1-2	800	0.5	WQ	800	2	AC
1-3	800	0.5	WQ	800	4	AC
2-1	900	0.5	WQ			
2-2	900	0.5	WQ	800	2	AC
2-3	900	0.5	WQ	800	4	AC
2-4	900	2	AC			
2-5	900	2	FC			
3-1	950	2	AC			
3-2	950	2	FC			
3-3	950	4	AC			
3-4	950	4	FC			
4-1	980	0.5	WQ			
5-1	1000	0.5	WQ			

5-2	1000	0.5	WQ	800	2	AC
5-3	1000	0.5	WQ	800	4	AC
6-4	1040	0.5	WQ			
7-1	1100	0.5	WQ			
7-2	1100	0.5	WQ	800	2	AC
7-3	1100	0.5	WQ	800	4	AC

Note: WQ: water quench; AC: air cooling; FC: Furnace cooling.

After heat treatment samples were ground by SiC papers from grit 320 to 2400, then following by 9 microns to 1 micron polishing procedures. For optical microscopy and SEM, vibratory polisher with 0.02 micron colloidal suspension was employed for final polishing. Thereafter, the samples were immersed in Kroll`s regent for 20 seconds for etching. The etched samples were re-polished in the vibratory polisher for 12 hours for subsequent EBSD analysis. For the KAM maps (Kernel Misorientation Map) generated, the crystallographic misorientation angles which are higher than 5° were set with a lime colour whilst those misorientation angles lower than 5° was presented with a blue colour.

5.3 Result and discussions

5.3.1 Heat treatment at 800℃, 900℃, 1000℃ and 1100℃

According to heat treatment conditions proposed by Gallego *et al* [204], the as-received samples were separately subject to solution treatment at 800℃, 900℃, 1000℃ and 1100℃, followed by 2 hours or 4-hour ageing at 800℃. The OM microstructures generated are shown in Figure 5.1. Corresponding to a solution treatment at 800℃, the microstructures were still consisting of primary α and secondary α and retained β which are similar to the as-received microstructure. In terms of microstructure, the differences between samples subject to differing conditions after solution treatment at 800℃ are quite un-resolved. Increasing the solution temperature to 900℃, the primary alpha grain starts to nucleate, subsequently facilitating the formation of course alpha grains. Solution temperature at 1000℃ starts to reveal poorly resolved α martensite, and some large rectangular alpha grains. With post solution treatment ageing for 2 hours or 4 hours, the martensitic alpha phase becomes more acicular, and rectangular α grains were reduced in size. With a solution treatment temperature at 1100℃, compared to the microstructure obtained after solution treatment at 1000℃, the rectangular α is larger and martensite α phase is clearer. Ageing after between 2 to 4 hours, the rectangular alpha grains are longer evident, all having transformed into acicular α martensite.

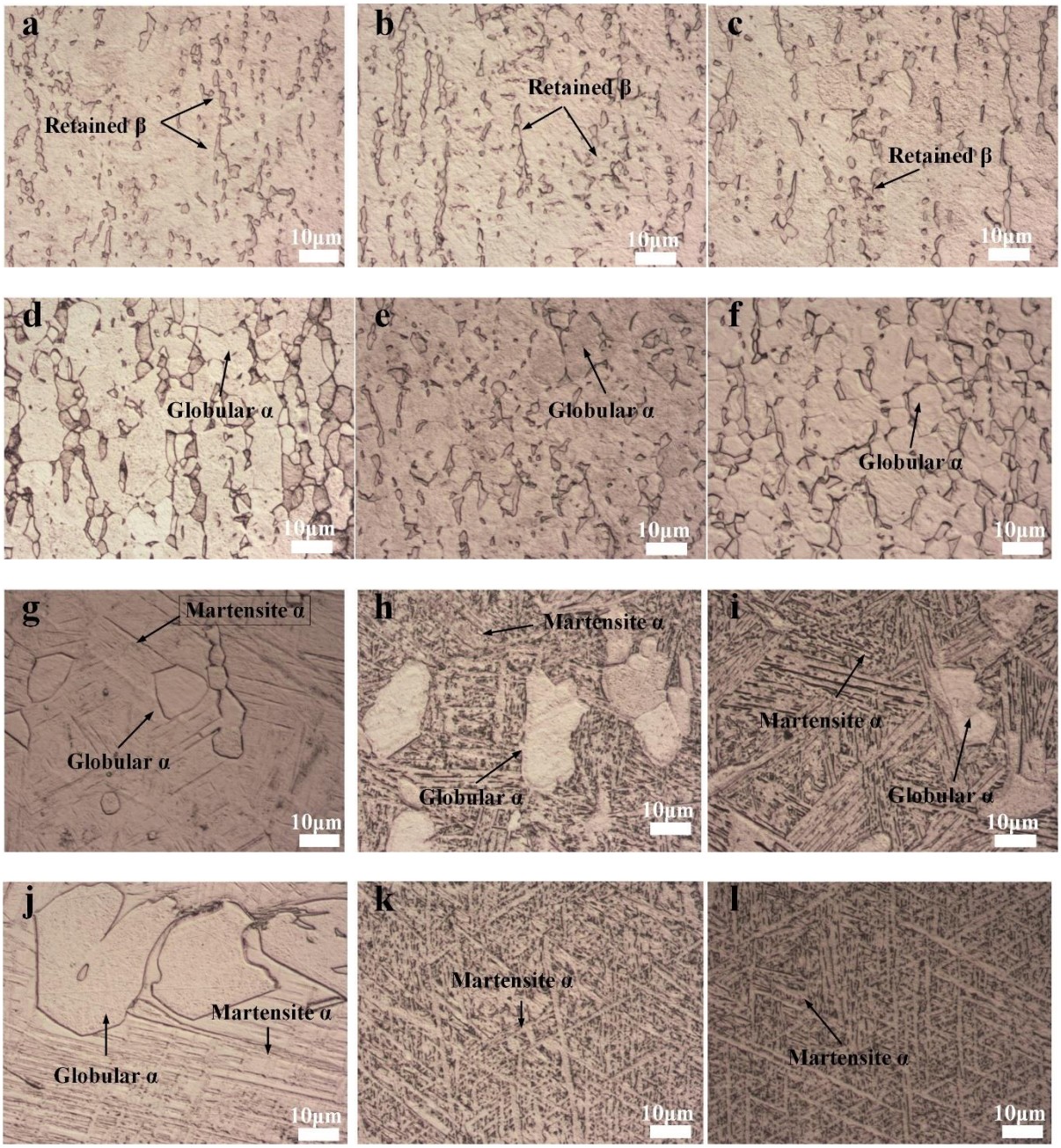

Figure 5.1 Optical images of the cross-sectional microstructure of Ti-6Al-7Nb at various temperature conditions in (a) 1-1; (b) 1-2; (c) 1-3; (d) 2-1; (e) 2-2; (f)2-3; (g) 5-1; (h) 5-2; (i) 5-3; (j) 7-1; (k) 7-2; and (l)7-3.

5.3.2 Solution treatment at 980℃ and 1040℃

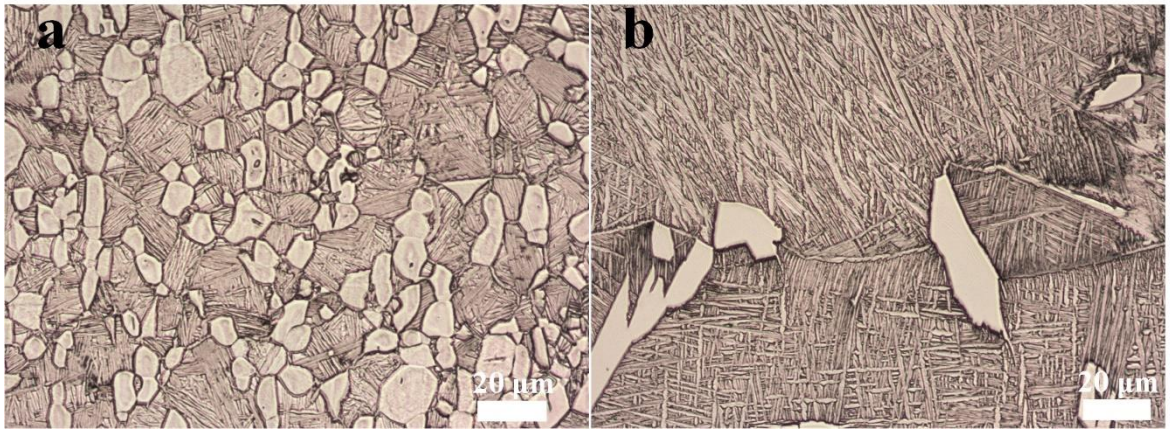

Figure 5.2 Optical microscopy images showing the microstructure of Ti-6Al-7Nb alloy subject to the solution treatment at 980℃ in (a) and 1040℃ in (b) for half-hour then water quenched.

Based on the above OM microstructure images are shown previously in Figure 5.2 and with a knowledge of the Ti-6Al-7Nb β transus temperature (around 1020℃), half an hour solution treatments at 980℃ and 1040℃ were performed. In Figure 5.2b, the microstructure attained after solution treatment at 1040℃ and water quenching consists of martensite α phase and rectangle α phase. Additionally, in Figure 5.2a, the microstructure after 980℃ solution is a typical bio-modal microstructure that has both equiaxed primary alpha in a lamellar α+β matrix. In light of the results from solution treatment at 900℃ and this bimodal microstructure, it is suggested that the temperature for solution treatment should be around 900-980℃ with various cooling methods or developing a uniform globular phase microstructure.

5.3.3The effect of cooling on the microstructure of Ti-6Al-7Nb alloy at 900℃ and 950℃

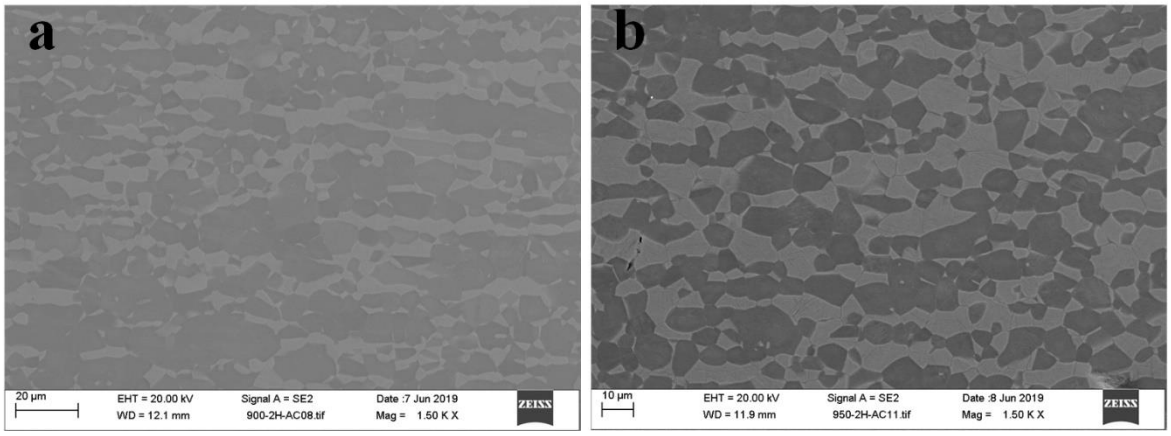

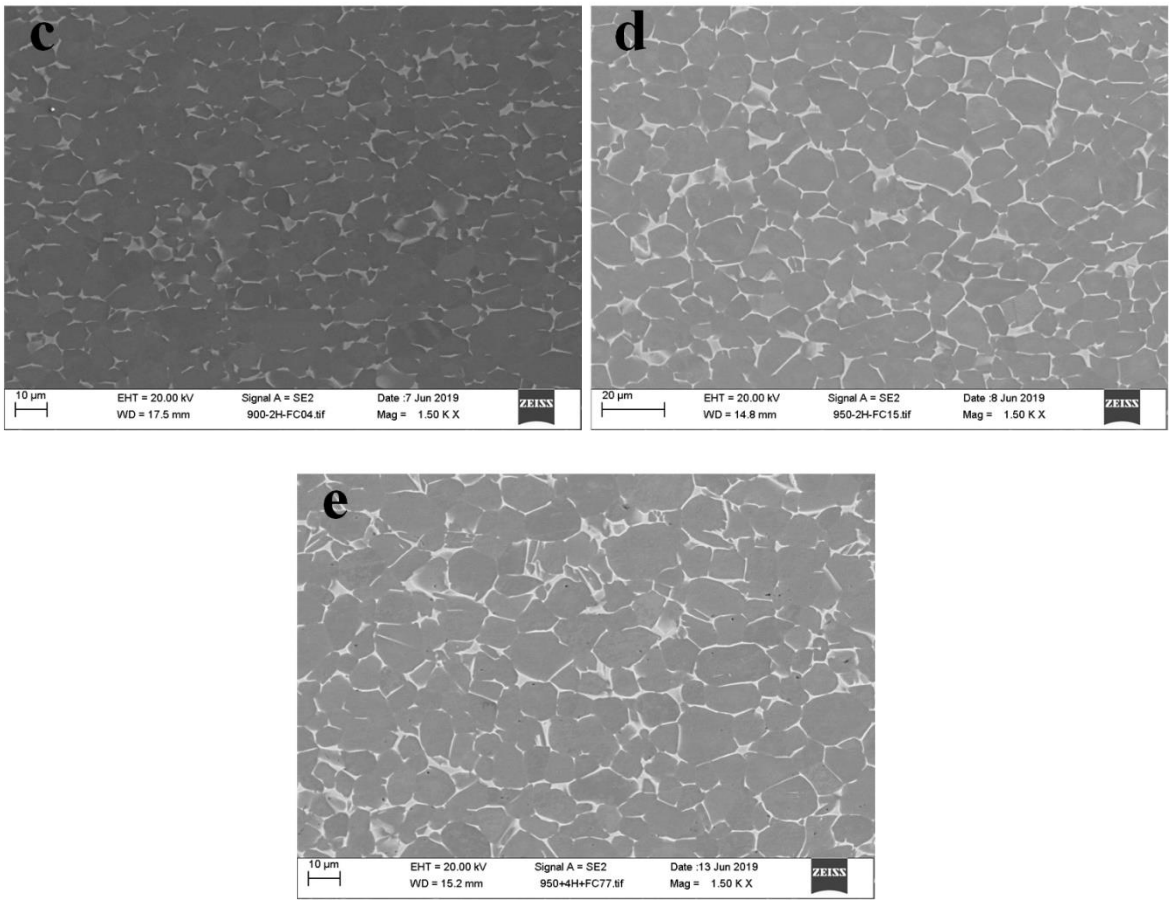

Figure 5.3 SEM images showing the microstructure of Ti-6Al-7Nb alloy subject to solution treatment at 900℃ and 950℃ with air cooling and furnace cooling at: (a) 2-4; (b) 3-1; (c) 2-5; (d) 3-2 and (e) 3-4.

In Figures 5.3a, and 5.3b, it can be seen that the microstructure consists of globular primary α, secondary (α) and retained β. In the EBSD images, shown in Figure 5.4a, the black retained area actually consists of acicular alpha grains. This is due to the high cooling rate facilitated by air cooling. In comparison to that, among the furnace cooling samples, the microstructures are similar. It consists of globular primary α, secondary α and retained β adjacent to the α grain boundaries.

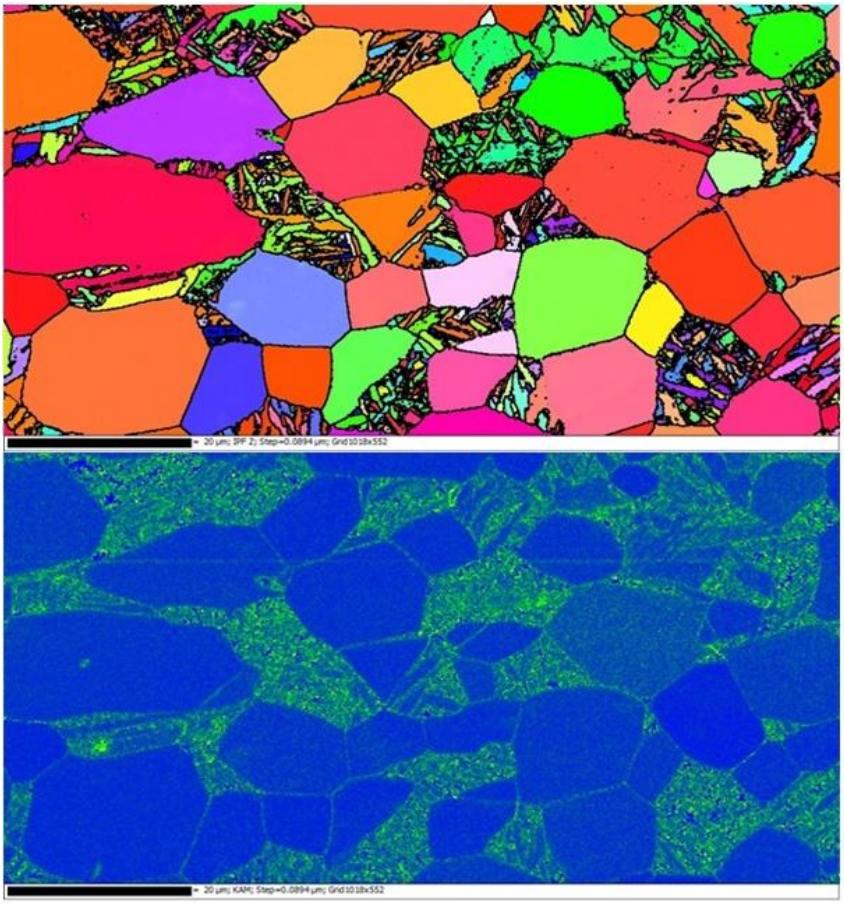
a
IPF Z
0001
$\bar{1}2\bar{1}0$
$01\bar{1}0$
KAM
TD
ND
RD

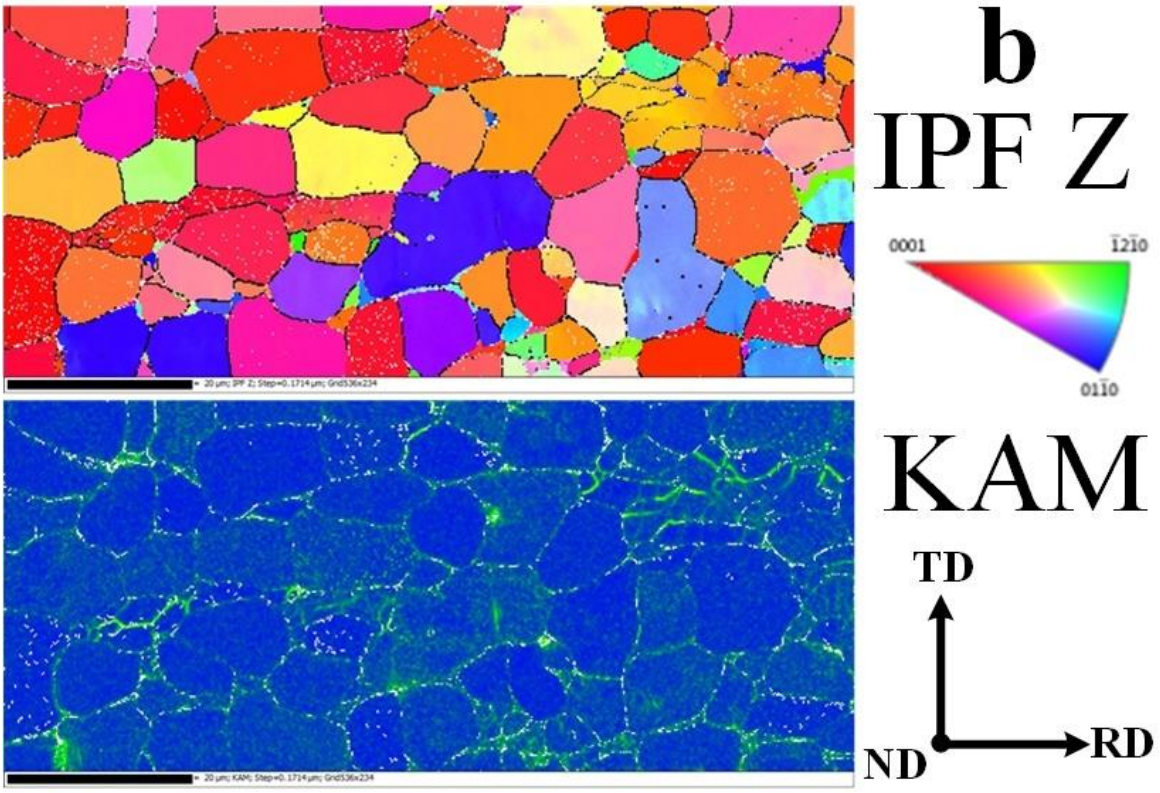
b
IPF Z
0001
$\bar{1}2\bar{1}0$
$01\bar{1}0$
KAM
TD
ND
RD

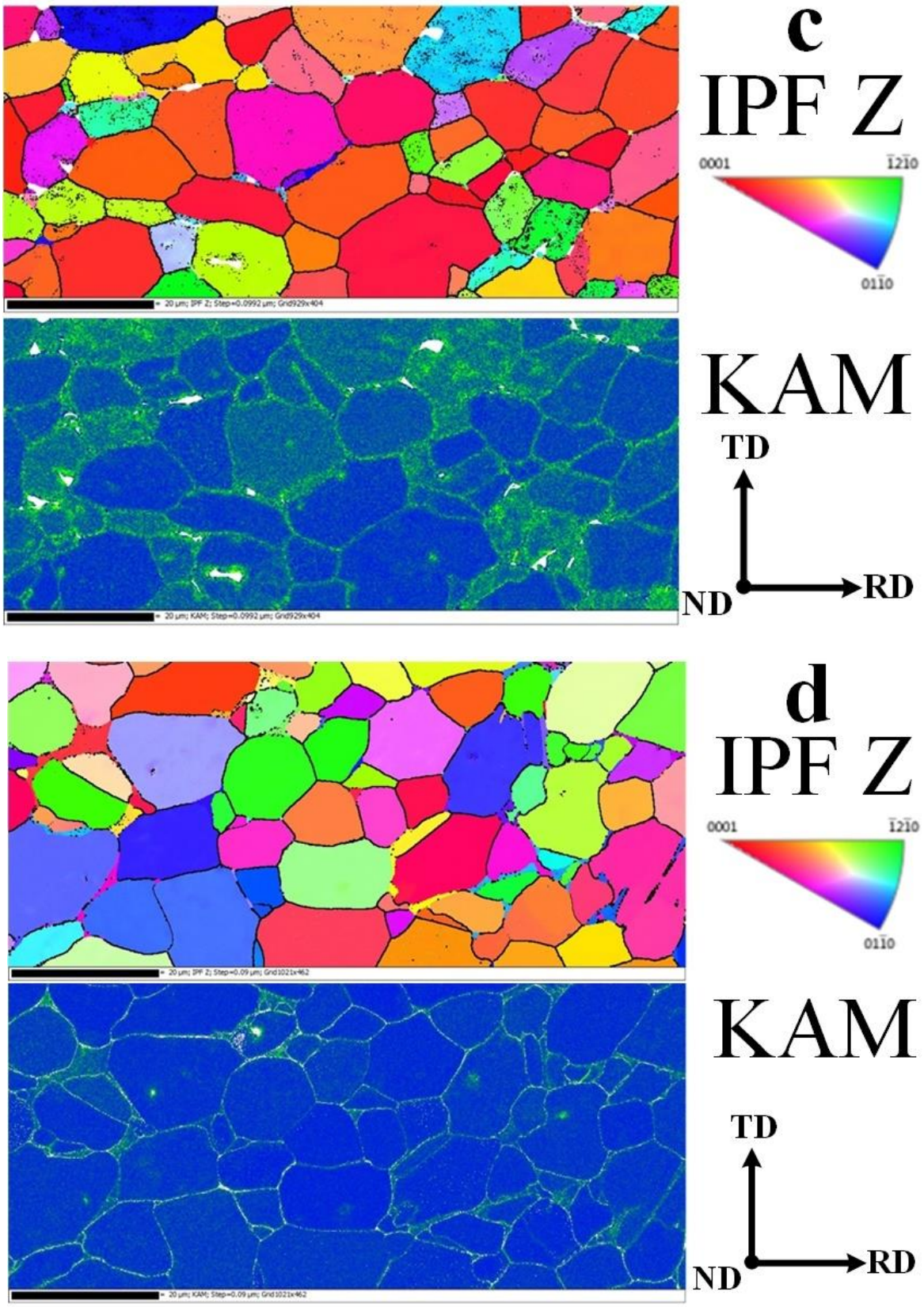

Figure 5.4 EBSD images showing inverse pole figure (IPF) Z-map, the colouration in the IPF Z map being related to crystallographic texture (preferred orientation), misorientation

distribution (KAM) and corresponding inverse pole figure of Ti-6Al-7Nb alloy in (a) 3-3; (b) 2-5; (c) 3-2 and (d) 3-4.

As mentioned previously, LSP facilitates an increase in the local crystallographic misorientations inside the grains, thereby, forming a new grain boundary if the pressure from the LSP sourced shock is high enough to drive dislocation movement. In Figure 5.4b, the higher misorientations (>5°) are mainly located near the grain boundaries. However, the grains are notably non-uniform, this may due to the solution treatment temperature (900℃) is not high enough. In Figure 5.4c, the grain size appears more uniform than that generated under the conditions of 900℃ for 2hours with furnace cooling (sample 2.5). However, from the KAM image, the misorientations are shown to be much higher even inside the grains. This indicates that 2 hours of solution treatment at 950℃ is insufficient. Therefore, an increase in the solution treatment time to 4 hours. In Figure 5.4d, from both IPF-Z contrast and KAM, it can clearly be observed that the microstructure is uniform and the misorientation is the lowest amongst all four samples.

5.4. Summary

The aim of this study was to develop an optimised thermal processing route to generate globular microstructure in Ti-6Al-7Nb alloy to facilitate LSP, examining its effects on microstructure deformation. The conclusions are made as follows:

- Furnace cooling post solution treatment at either 900 ℃ and 950℃ leads to a globular microstructure of Ti-6Al-7Nb alloy.
- Longer thermal preservation time at the same temperature decreases the local sub-grain misorientation. Meanwhile, with the same thermal preservation time, higher temperature will lead to greater extents of misorientation in the microstructure.
- The bi-modal microstructure can be acquired in Ti-6Al-7Nb alloy with a thermal solution at 980℃ for half hour, the alloy starting to reveal the presence of α martensite.
- For solution treatment temperatures at of 1000℃, 1040℃, and 1100℃, the primary α keeps reducing while α martensite continues to expand.

CHAPTER 6 Microstructural Effects of Laser Shock Peening Post Heat Treated Ti-6Al-7Nb Alloy

In this Chapter, the same LSP parameters were applied (to previous chapters) on the heat-treated Ti-6Al-7Nb with uniform globular alpha and beta-phase microstructure. The cross-sectional microstructure prior to and after LSP was characterized by SEM. Local misorientations and Crystal orientations were determined by EBSD using Kernal Average Map (KAM) and Inverse Polo Figure Z contrast map. What is more, the phases were examined by X-ray Diffractions, and the crystal average sizes and lattice strain before and after LSP were calculated using the Williamson- Hall plot.

6.1 Introduction

In the previous chapter, heat treatment was applied to the as-received microstructure in order to remove the effect of hot rolling on the misorientations and non-uniform microstructure. The heat treated Ti-6Al-7Nb alloy was laser shock peened again with the parameters mentioned in Chapter 4.

LSP utilises high energy density, short laser pulse to cause local plastic deformation in the metallic materials. The strain-rate during the processing is estimated to reach the level of ~10^{6}/s. In such strain-rate, microstructural features, namely; twinning, slip system, grain refinement (nano-crystallization) and dislocations were observed in the materials. For instance, In the commercially pure titanium with uniform equiaxed microstructure, the average grains were refined to the size of less than 50nm after LSP through multi-directional mechanical twin intersection and interactions between longitudinal mechanical twins and transverse dislocations wall [205]. By contrast to LSPned CP Ti, it was reported by Lainé *et al* [206], that the nano-scale deformation twinning was limited in the surface grains, and absent at deeper depths which was unexpected in Ti-6Al-4V alloy. Therefore, as a substitute, it is necessary to investigate the material response to LSP in Ti-6Al-7Nb alloy.

Many characterization methods such as SEM, TEM, XRD, and EBSD were employed to determine the LSPned microstructure. EBSD is used to reveal the detailed microstructural features and deformations characteristics such as the orientation of crystal lattice, grain, and adjacent grain crystallographic misorientation. Gill *et al* [207] investigated the local plastic deformation and surface hardening effect induced by LSP in Inconel alloy using EBSD based

misorientations and grain orientation spread analysis. It was found that low angle misorientations (<15°) was increased due to the extensive plastic deformation induced by LSP at the near-surface. Similarly, Lu *et al* [208], applied multiple LSP on the AISI 304 stainless steel and found that the frequency of 60° misorientation is increased from 9% to 46% after LSP. What is more, twining is also an important feature during the plastic deformation after LSP. Mao *et al* [209], reported that {10-12} twin variants were presented in individual parent grains after LSP in magnesium. Additionally, two types of {10-12} twining were observed in pure titanium by Xu *et al* [210]. In this chapter, SEM was used to characterise the microstructure of heated Ti-6Al-7Nb. Knernal Average Map (KAM) were employed to analysis the adjacent grain crystallographic misorientation. Furthermore, phase determination was carried out using X-ray Diffraction, and the micro-strain and crystal average size were calculated by the Williamson- Hall plot. This chapter mainly focuses on the effects of local misorientation, twining deformation, microstructure refinement in the initial globular and uniform microstructure post LSP.

6.2 Surface and cross-sectional microstructural characterizations of untreated Ti-6Al-7Nb alloy post heat treament

6.2.1 Microstructural characterizations by Scanning Electron Microscope

After heat treatment, the microstructure becomes more uniform in the rolling direction, Figure 6.1. The domain phase is α while β-phase was still distributed between α grains. Increasing the magnification at 80Kx, sub-grains are clearly observed. The size can be calculated with the IGM method, and it is 279 nm.

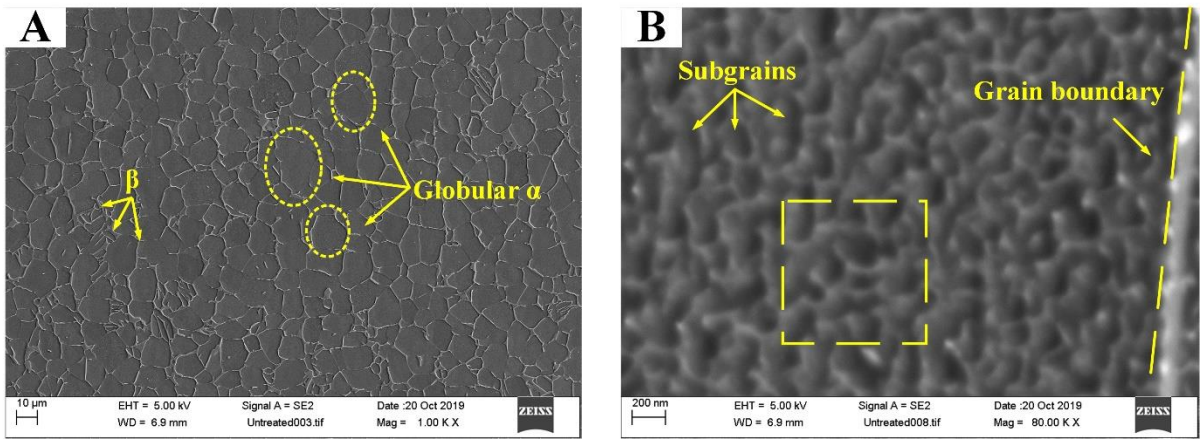

Figure 6.1 SEM images showing the cross-section microstructure of untreated Ti-6Al-7Nb after heat treatment.

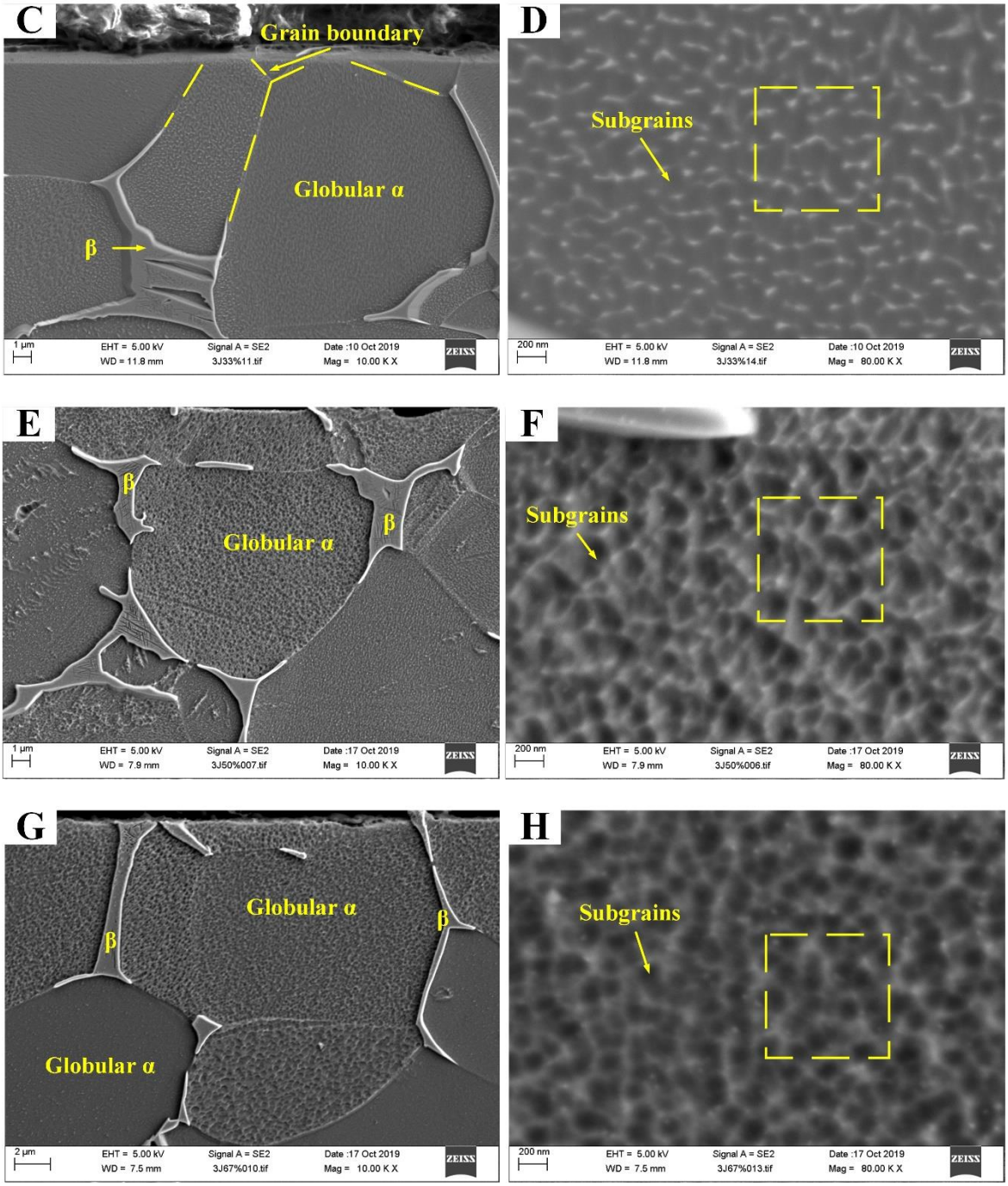
C
Grain boundary
Globular α
β
1 µm
EHT = 5.00 kV
WD = 11.8 mm
Signal A = SE2
3J33%11.tif
Date :10 Oct 2019
Mag = 10.00 K X
D
Subgrains
200 nm
EHT = 5.00 kV
WD = 11.8 mm
Signal A = SE2
3J33%14.tif
Date :10 Oct 2019
Mag = 80.00 K X
E
β
Globular α
β
1 µm
EHT = 5.00 kV
WD = 7.9 mm
Signal A = SE2
3J50%007.tif
Date :17 Oct 2019
Mag = 10.00 K X
F
Subgrains
200 nm
EHT = 5.00 kV
WD = 7.9 mm
Signal A = SE2
3J50%006.tif
Date :17 Oct 2019
Mag = 80.00 K X
G
Globular α
β
β
Globular α
2 µm
EHT = 5.00 kV
WD = 7.5 mm
Signal A = SE2
3J67%010.tif
Date :17 Oct 2019
Mag = 10.00 K X
H
Subgrains
200 nm
EHT = 5.00 kV
WD = 7.5 mm
Signal A = SE2
3J67%013.tif
Date :17 Oct 2019
Mag = 80.00 K X

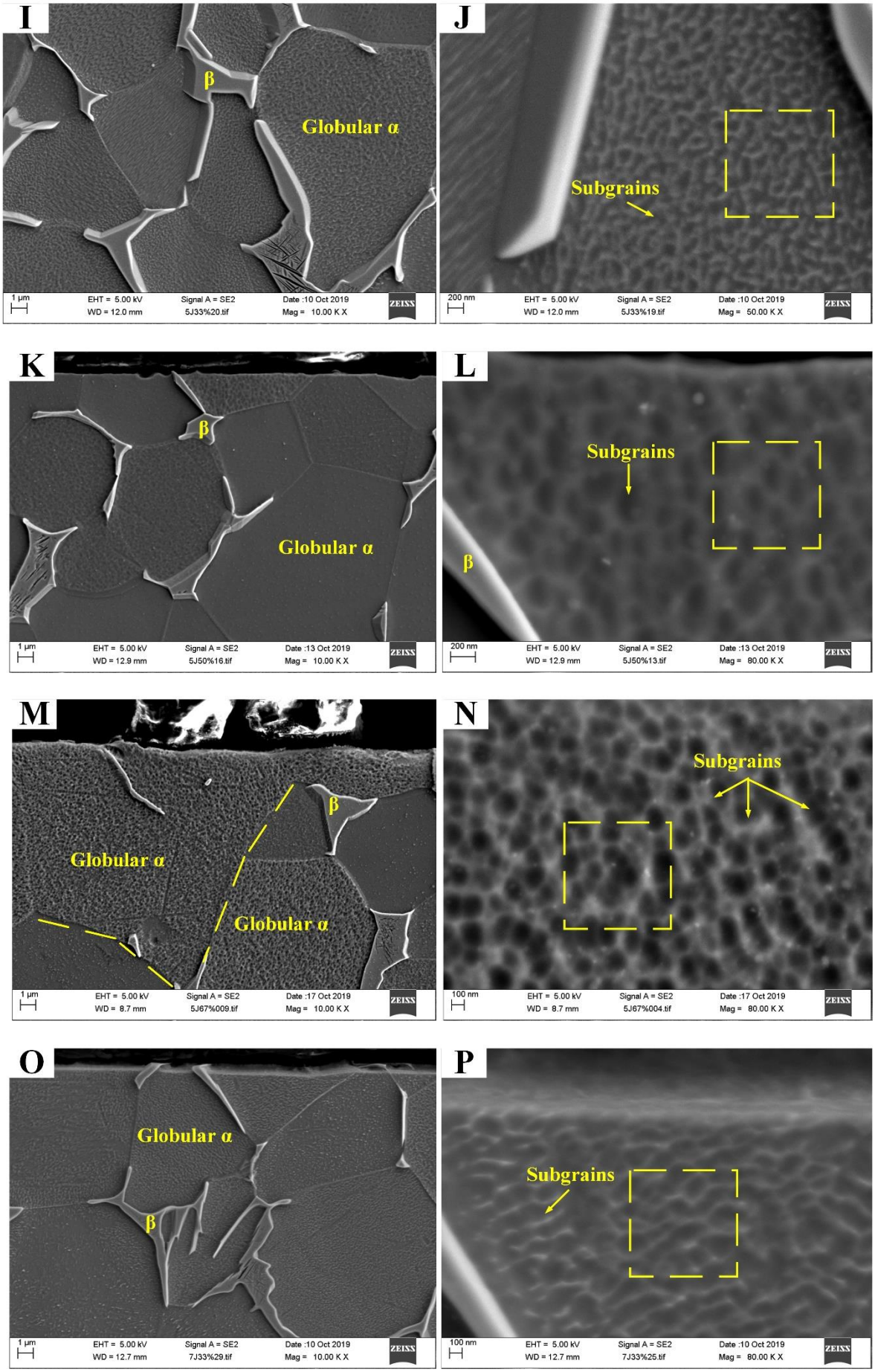
I
β
Globular α
1 µm
EHT = 5.00 kV
WD = 12.0 mm
Signal A = SE2
5J33%20.tif
Date :10 Oct 2019
Mag = 10.00 K X
ZEISS
J
Subgrains
200 nm
EHT = 5.00 kV
WD = 12.0 mm
Signal A = SE2
5J33%19.tif
Date :10 Oct 2019
Mag = 50.00 K X
ZEISS
K
β
Globular α
1 µm
EHT = 5.00 kV
WD = 12.9 mm
Signal A = SE2
5J50%16.tif
Date :13 Oct 2019
Mag = 10.00 K X
ZEISS
L
Subgrains
β
200 nm
EHT = 5.00 kV
WD = 12.9 mm
Signal A = SE2
5J50%13.tif
Date :13 Oct 2019
Mag = 80.00 K X
ZEISS
M
β
Globular α
Globular α
1 µm
EHT = 5.00 kV
WD = 8.7 mm
Signal A = SE2
5J67%009.tif
Date :17 Oct 2019
Mag = 10.00 K X
ZEISS
N
Subgrains
100 nm
EHT = 5.00 kV
WD = 8.7 mm
Signal A = SE2
5J67%004.tif
Date :17 Oct 2019
Mag = 80.00 K X
ZEISS
O
Globular α
β
1 µm
EHT = 5.00 kV
WD = 12.7 mm
Signal A = SE2
7J33%29.tif
Date :10 Oct 2019
Mag = 10.00 K X
ZEISS
P
Subgrains
100 nm
EHT = 5.00 kV
WD = 12.7 mm
Signal A = SE2
7J33%25.tif
Date :10 Oct 2019
Mag = 80.00 K X
ZEISS

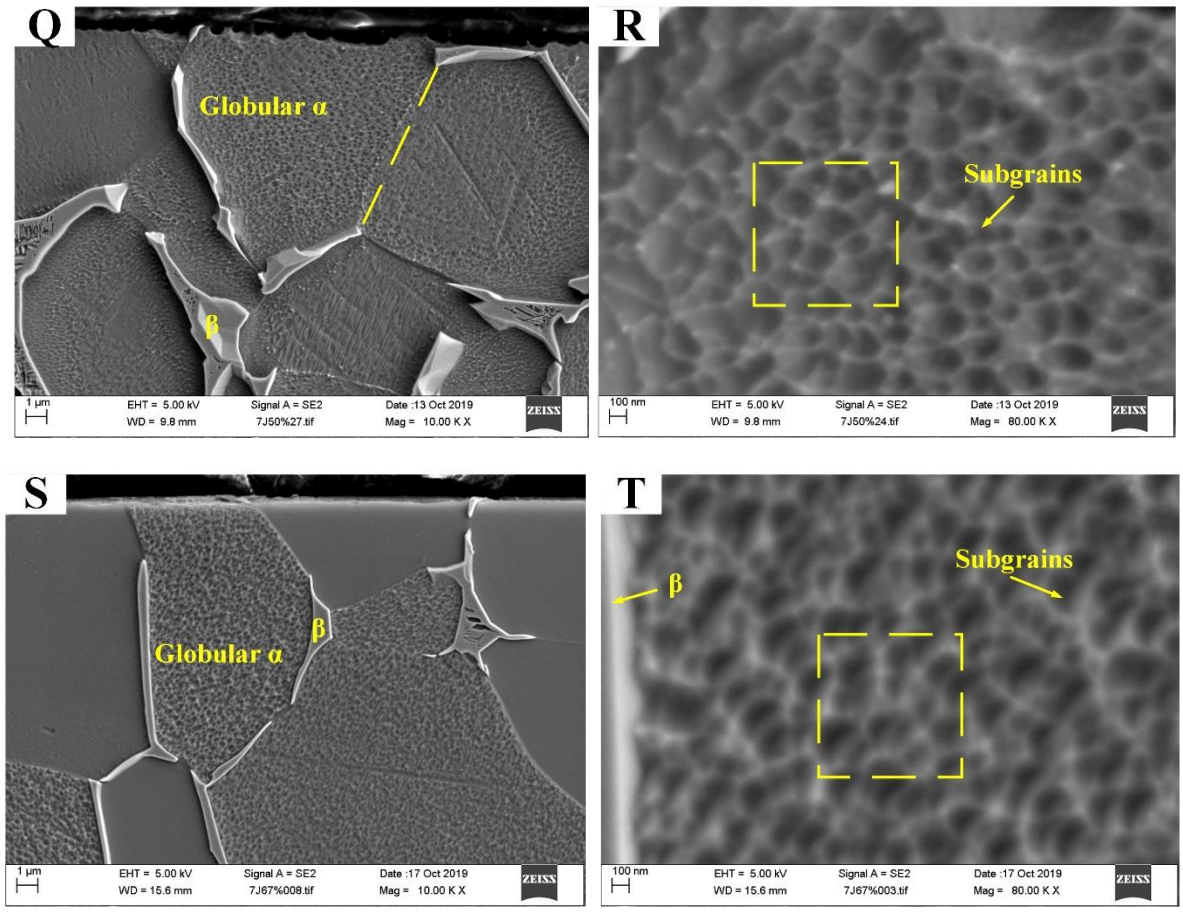

Figure 6.2 SEM images showing the lase shock peened cross-section microstructure of Ti-6Al-7N alloy after heat treatment in (C, D) at 3J, 33%, (E, F) at 3J, 50%, (G, H) at 3J, 67%, (I, J) at 5J, 33%, (K, L) at 5J, 50%, (M, N) at 5J, 67%, (O, P) at 7J, 33%, (Q, R) at 7J, 50%, (S, T) at 7J, 67%.

After LSP, any signs regarding the grain refinement were not observed (Figure 6.2). The microstructure still consists of α and β-phase. Upon, increasing the magnifications, the average sub-grain size is given in Table 6.1. The results indicated that overlap has limited influence on sub-grain refinement when the laser energies are 3J and 5J. However, in the laser energy of 7J, the sub-grain size is obviously refined from 263.7nm (7J, 33%) to 205.5nm (7J, 67%). Also, a similar phenomenon was found when the overlap was the same. It can be seen that the decreased rate of 67% overlap is the highest among the three.

Table 6.1 Average sub-grain size (nm) after LSP calculated by grain intercept method.

	33%	50%	67%
3J	**331.6.**	**296.6**	**303.6**

5J	**261.2**	**261.7**	**256.7**
7J	**263.7**	**222.6**	**205.5**

6.2.2 Texture determination by EBSD

Figure 6.3 and Figure 6.4 present the grain (HCP and cubic) adjacent crystal misorientation prior to and after LSP. In the untreated KAM map, the high misorientation is localized in the grain boundary. The average HCP and cubic local misorientation are 0.52° and 1.04° separately, shown in Table 6.2.

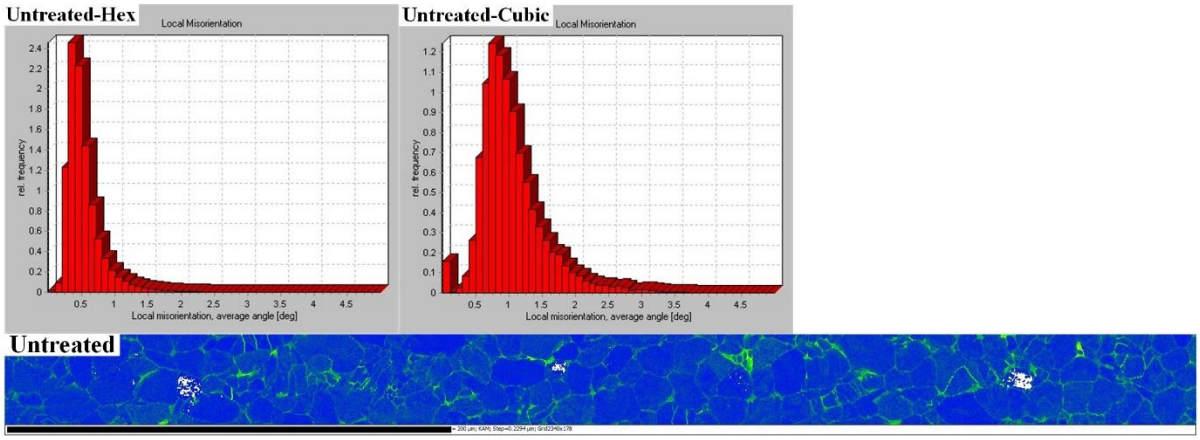

Figure 6.3 KAM map, HCP and Cubic local misorientation distribution of untreated.

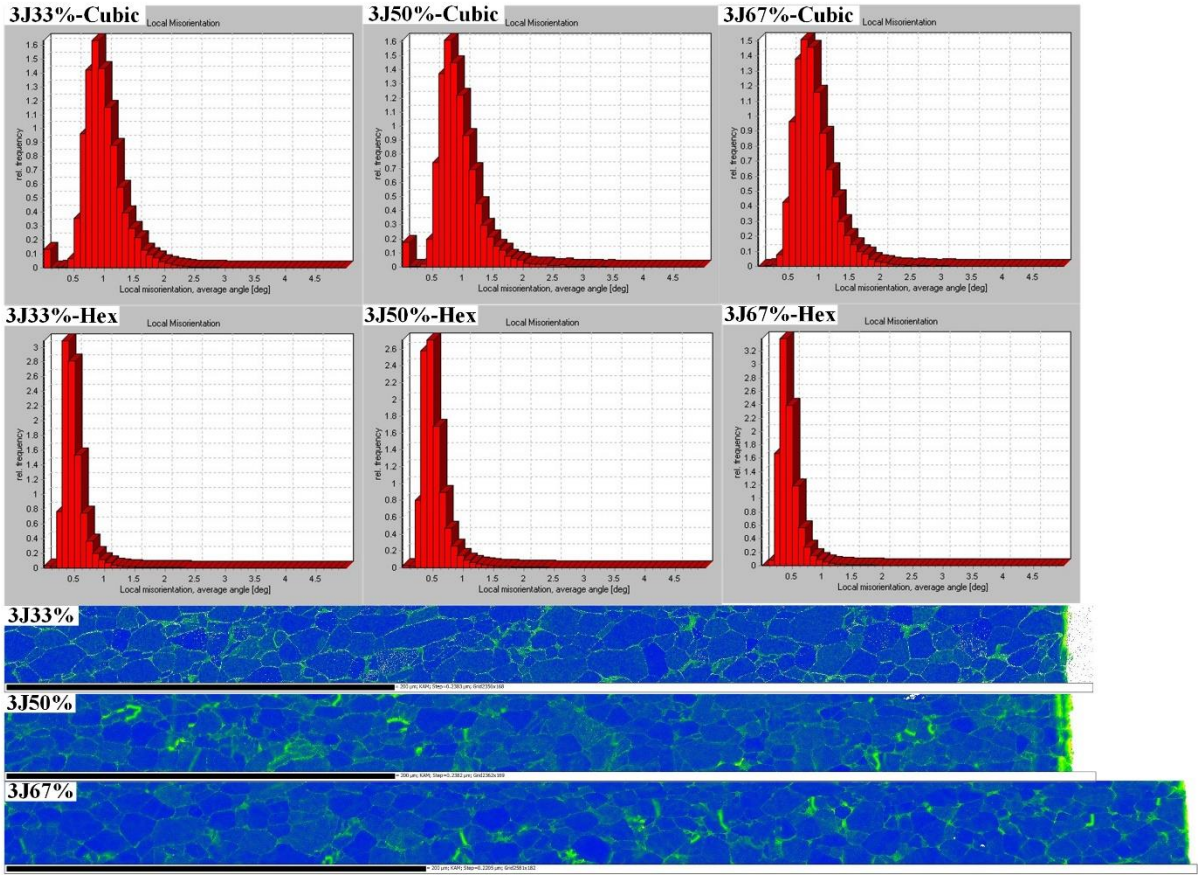

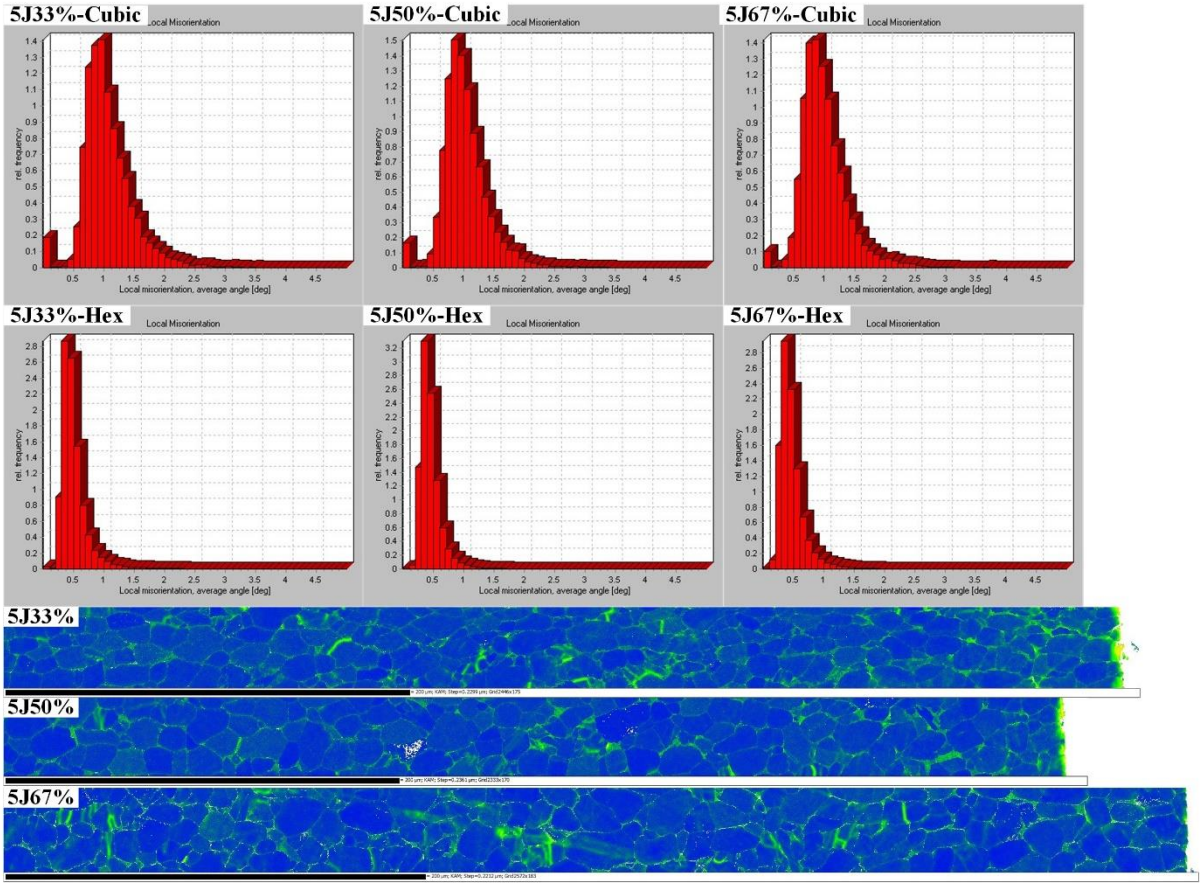
5J33%-Cubic
5J50%-Cubic
5J67%-Cubic
5J33%-Hex
5J50%-Hex
5J67%-Hex
Local Misorientation
rel. frequency
Local misorientation, average angle [deg]
5J33%
5J50%
5J67%

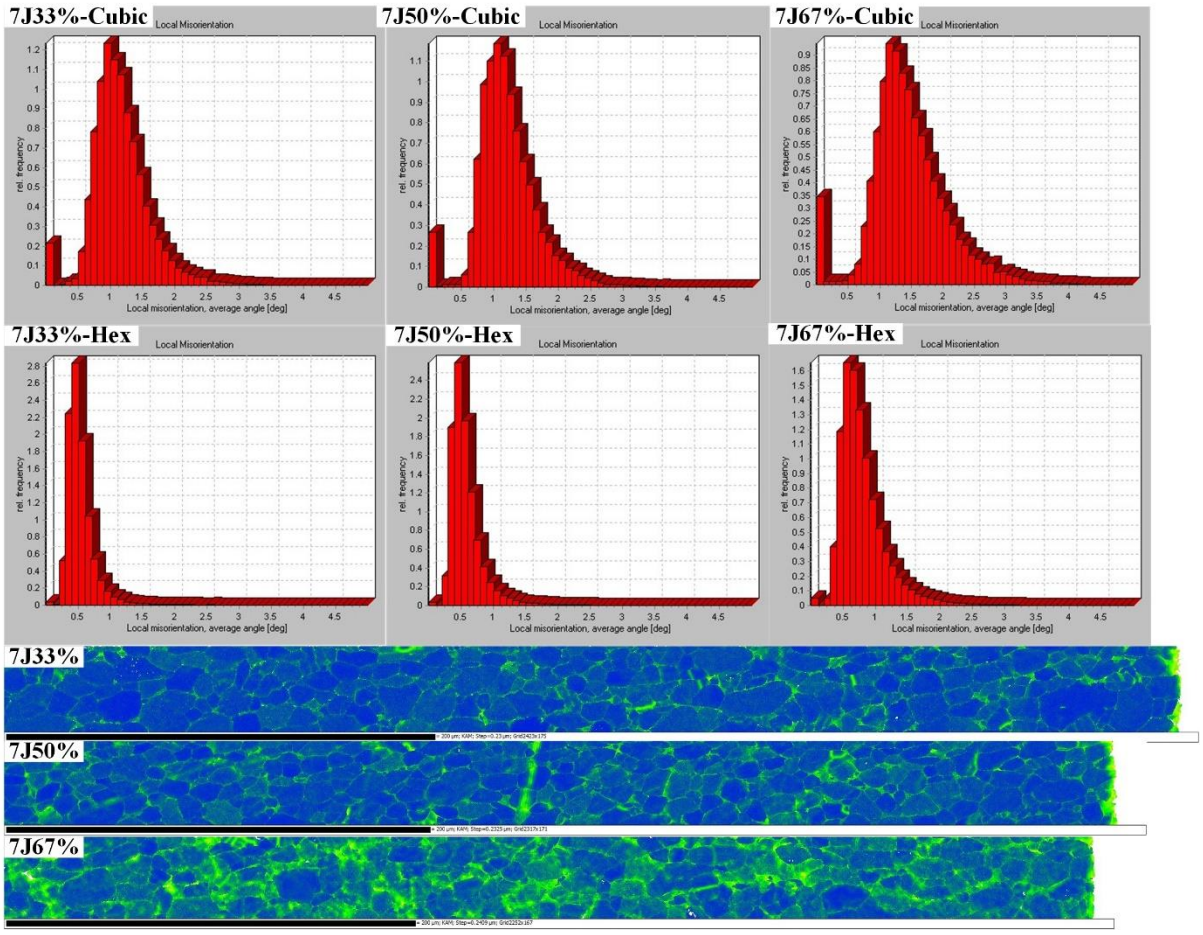
7J33%-Cubic
7J50%-Cubic
7J67%-Cubic
7J33%-Hex
7J50%-Hex
7J67%-Hex
Local Misorientation
rel. frequency
Local misorientation, average angle [deg]
7J33%
7J50%
7J67%

Figure 6.4 KAM map, HCP and cubic local misorientation of the laser shock peened.

Table 6.2 The weighted average value for HCP/Cubic grains (Unit: °).

Untreated:0.52/1.04	33%	50%	67%
3J	0.49/0.96	0.5/0.93	0.44/0.9
5J	0.5/1.06	0.45/1.02	0.46/0.98
7J	0.52/1.05	0.57/1.19	0.79/1.48

It is well known that in bulk crystal material, defects such as dislocations and grain boundaries facilitate in strengthening the material. Such grain boundaries include low-angle, high-angle boundaries. Polyakova *et al.* [211] examined the relationship between the misorientation of boundaries and the mechanical properties of Ti-6Al-7Nb alloy subject to equal-channel angular pressing (ECAP). The results showed the ultimate tensile strength was improve to 1210Mpa as the density of high-angle boundaries was increased. After LSP, it was evident from the KAM maps of 7J, 50% and 7J, 67% that the local misorientation angles of grains vary to each other. This means the strain distribution is non-uniform amongst the grains. Regarding hcp local misorientation, it can be seen that the KAM map did not receive huge changes when the laser energy is lower than 7J. In comparison to the misorientation of untreated, misorientations of 3J (33%-67%), 5J (33% - 67%) and 7J, 33% are comparatively lower which is not expected. When it comes to 7J, 50% and 7J, 67% overlap, the weighted average misorientations of LSPned are higher than that of untreated that due to enough shock wave generated by the laser energy pulse. With respect to cubic grains, apart from 7J group, the misorientations of samples that subjected to lower LSP parameters (3J and 5J), were not increased compared to that of the untreated (1.04). In the 7J group, 7J, 33% is comparatively, close to the untreated. On the other hand, 7J, 50%, and 7J, 67% are separately increased to 1.19 and 1.48. Therefore, with respect to cubic grains, the affected LSP parameters are 7J, 50% and 7J, 67%.

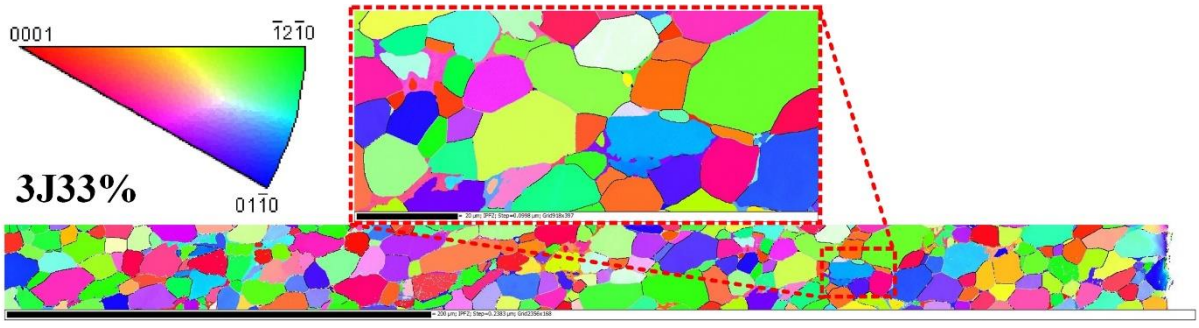

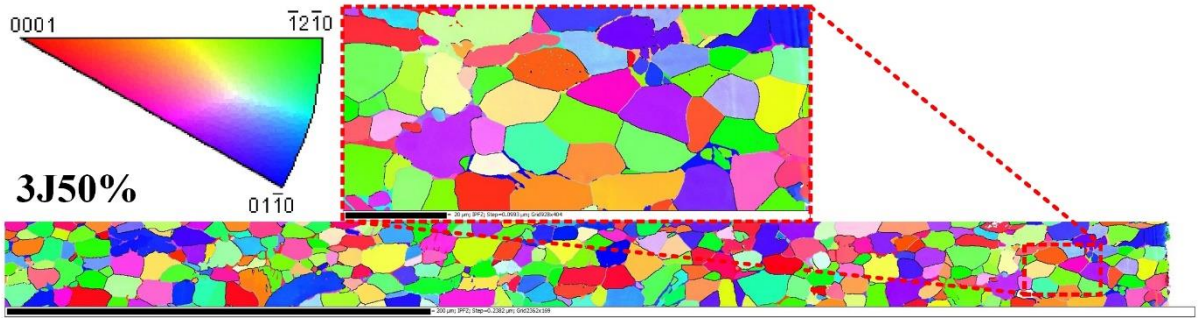
0001
$\bar{1}2\bar{1}0$
3J50%
$01\bar{1}0$

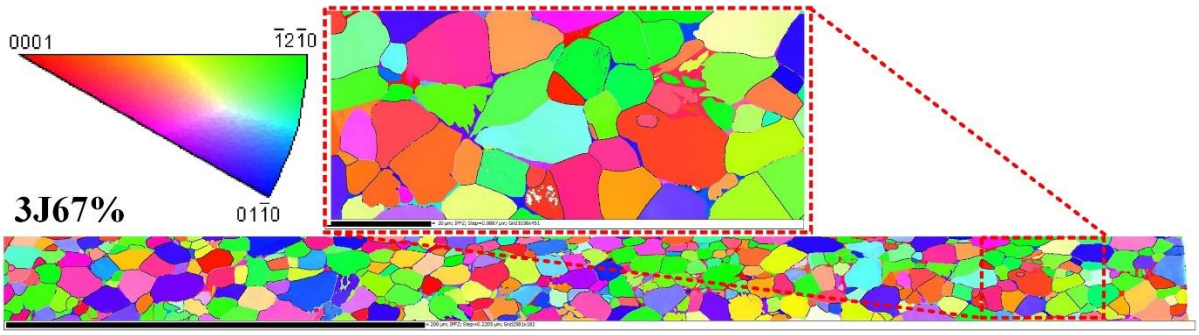
0001
$\bar{1}2\bar{1}0$
3J67%
$01\bar{1}0$

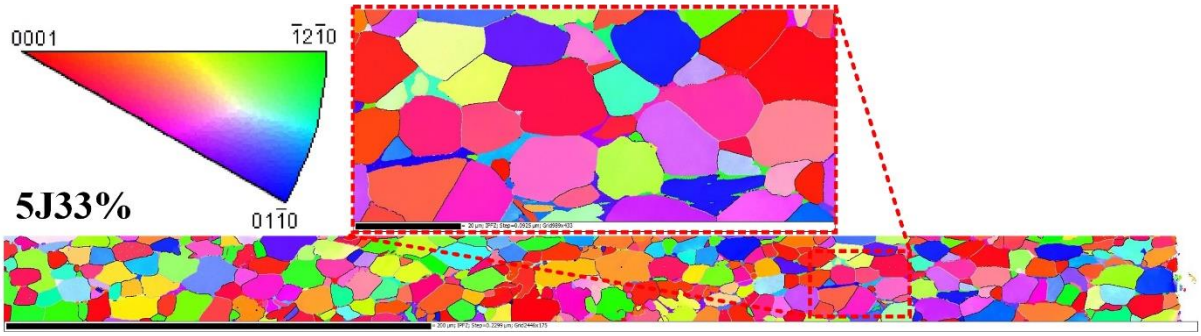
0001
$\bar{1}2\bar{1}0$
5J33%
$01\bar{1}0$

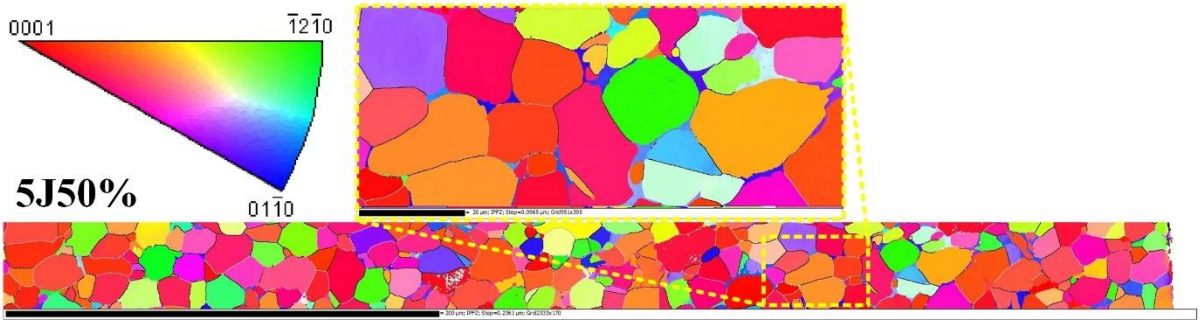
0001
$\bar{1}2\bar{1}0$
5J50%
$01\bar{1}0$

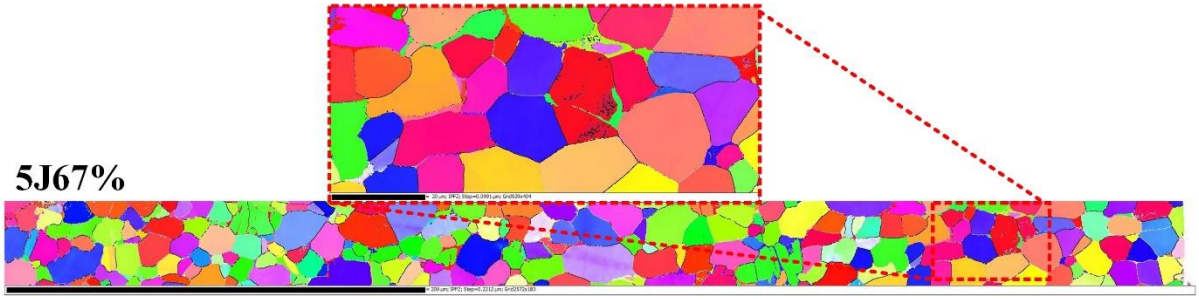
5J67%

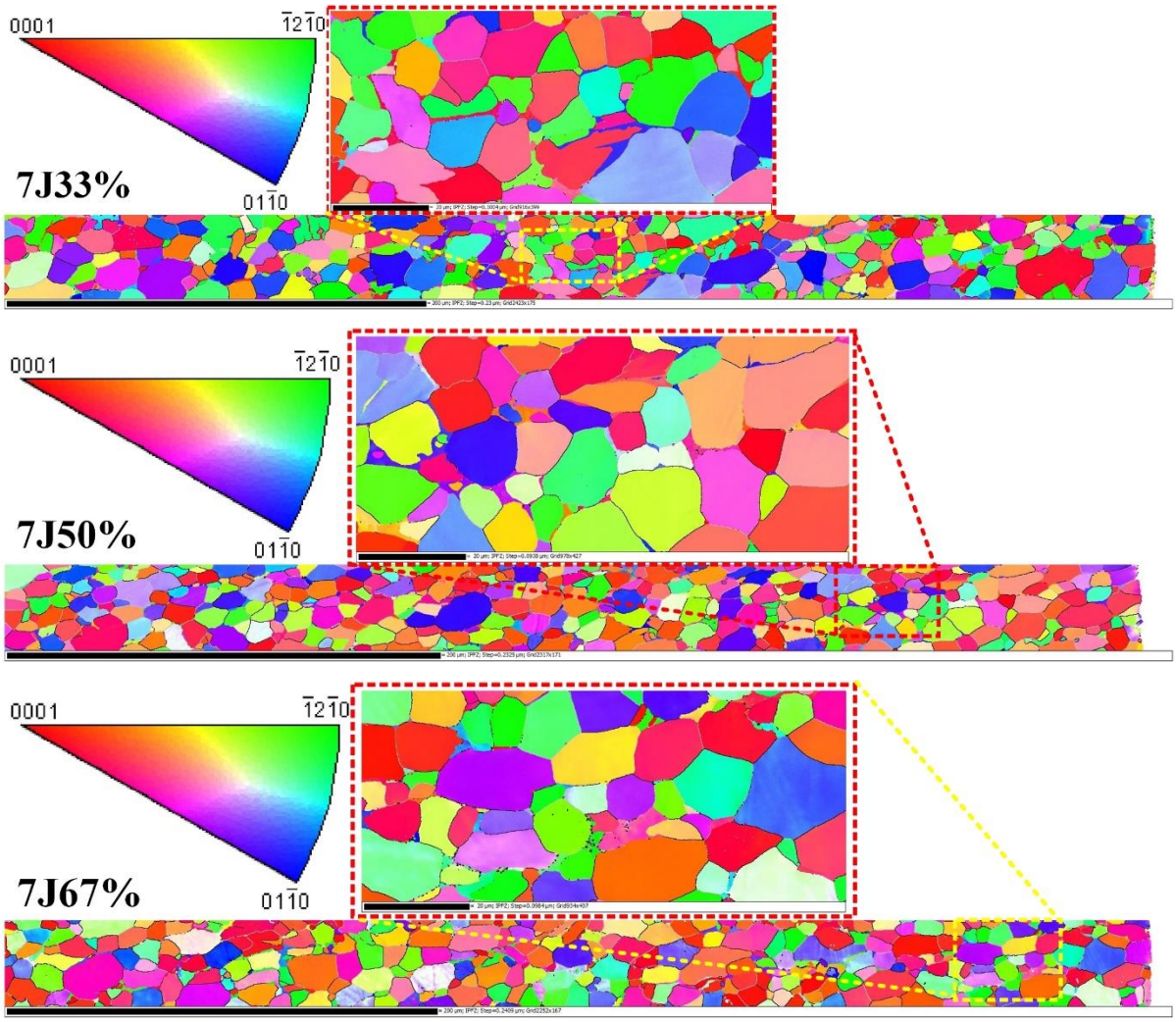

Figure 6.5 IPF Z contrast map showing the texture of LSPned Ti-6Al-7Nb alloy.

EBSD is an excellent tool to examine the location of deformation twinning with the crystallographic orientation contrast in inverse pole figures. Figure 6.5 presents the inverse pole figure colouring of Ti-6Al-7Nb alloy after LSP. However, after 9 different LSP parameters processing, there is no deformation twinning happened in the magnified IPF Z map. These results are consistent with the works of Laine *et al* [206]. Laine *et al.* employed a 1054nm, pulse duration of 10ns laser to process Ti-6Al-4V alloy with initial globular microstructure. The laser power density is estimated at around 5GW/cm^{-2}. The EBSD results did not exhibit any signs of twinning deformations in LSPned Ti-6Al-4V alloy. But they observed a layer of high local misorientation at the top surface of LSPned Ti-6A-4V as well as we can see such a high local misorientation layer is formed in LSPned Ti-6Al-7Nb alloy. In addition, Bisht *et al* [212] processed cp-Ti with initial globular microstructure using femtosecond laser shock-waves. The cross-section IPF map showed that no typical deformations such as transition bands, shear bands, mechanical twins, etc. were observed, even at the top surface subject to shock-

waves. Also, local misorientation angles of grains were increased according to the KAM map. By examining the misorientation distribution, the conventional twin systems information including angle/axis misorientation can also be found.

As shown above, there are no obvious twining deformations that happened after such LSP parameters. To account for the twining deformation in Ti-6Al-7Nb alloy with uniform globular microstructure, 10 impacts of LSP with the same parameters setting of 7J, 50% were carried out on Ti-6Al-7Nb along the ND direction. The KAM map and image quality map of 7J50% 10impacts were presented in Figure 6.6. It was observed that the local misorientation gradient layer was formed along with the LSP directions. The maximum of local misorientation was not at the top surface rather than in the depth around 200-400 μm. As local misorientation is proportional to strains inside or amongst grains, it is why the maximum residuals stress is not at the top surface in the cross-sectional residual stress curves plotted by incremental hole drilling data. The maximum residual stress value is at the sub-surface, where the local misorientations are saturated. Onwards, we can see a decent trend in the ND direction. Figure 6.7 is an IPF map at the depth around 300μm. Under the extensive shock-wave, macroscopic twinning deformation can be seen inside the globular hcp grains. As reported by McCabe et al [213], there are three twining system in Ti which are {10-12}<10-1-1>(tensile twin), {11-21}<11-2-6>(tensile twin), {11-2-2}<11-2-3>(compressive twin). As the twinning in {10-12}, shear is the lowest, it is the most common twining mode in the HCP system. Therefore, we can see {10-12} inside parent grain after of 10 impacts LSP. What is more, {11-21} twining can also be seen. But there are no signs of {11-2-2} twining after LSP.

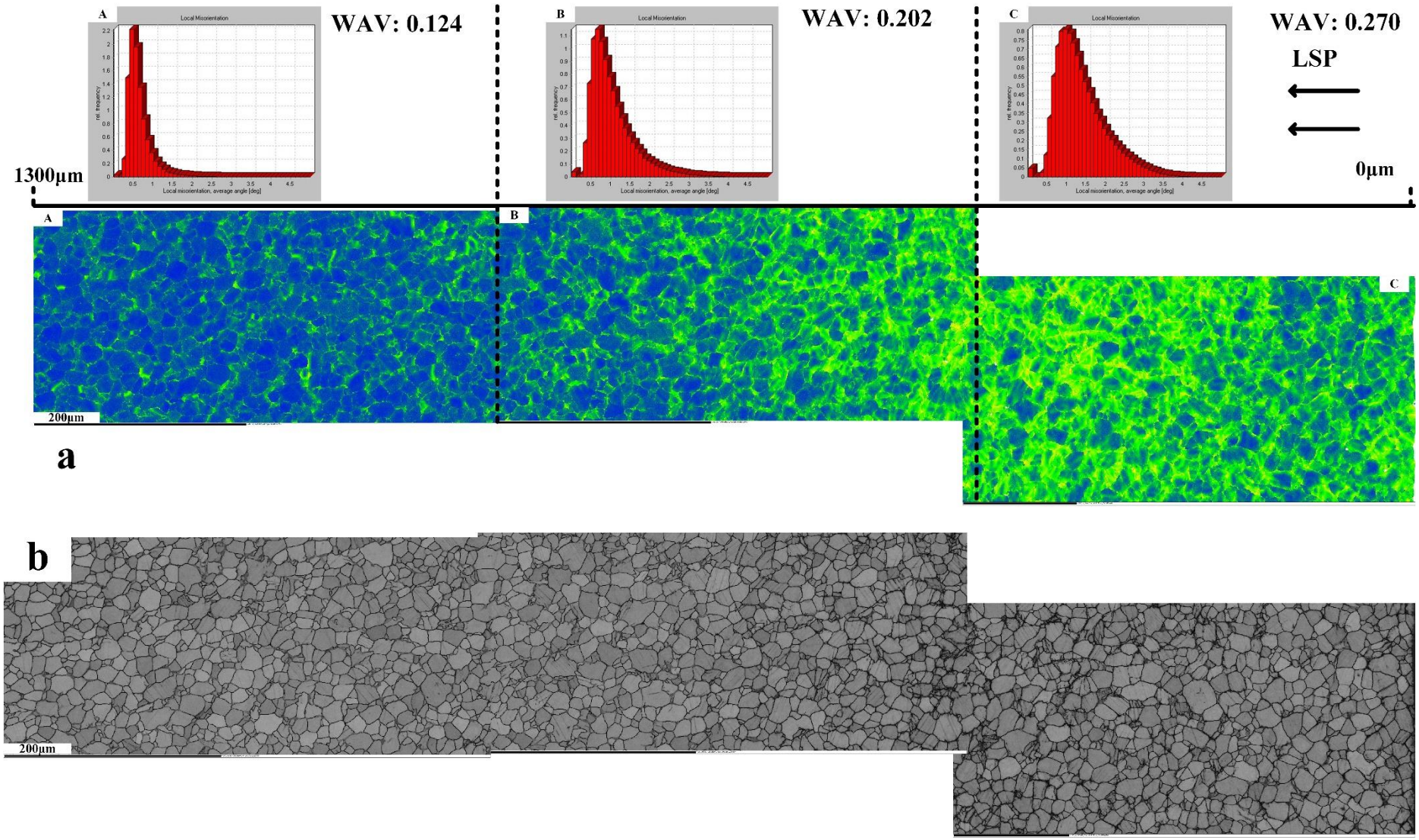
A
Local Misorientation
WAV: 0.124
B
Local Misorientation
WAV: 0.202
C
Local Misorientation
WAV: 0.270
LSP
1300μm
0μm
A
B
C
200μm
a
b
200μm

Figure 6.6 EBSD analysis of 7J at 50% overlap with 10 impacts of LSP where (a) is kernel average misorientation (KAM) map of Laser shock peened ; and (b) is the image quality map

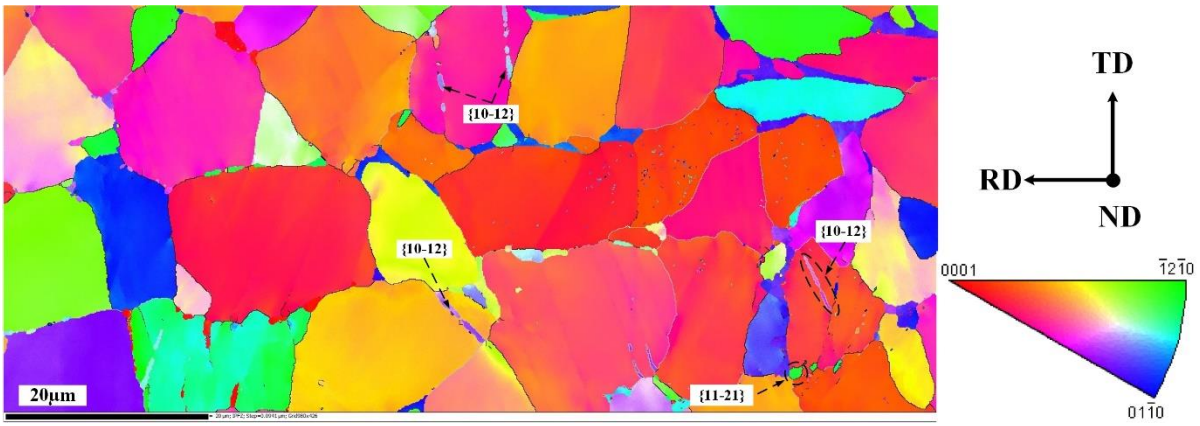

Figure 6.7 IPF map showing 10 impacts laser shock peened with twining in {10-12} and {11-21}.

6.3 Phase characterization using X-ray diffraction

The phase after heat treatment is also characterized by X-ray diffraction. In Figure 6.8, X-ray patterns and magnified α (100) peaks of LSPned area are presented by keeping laser energy the same. In all patterns, there are still no new phases generated. However, peak broadening and peak shifting are more obvious than the ones before heat treatment. According to the work from [214], the broadening is due to the grain refinement in the sub-micron domain and the presence of high-level micro-strain. It is interesting that shifting degrees in 5J groups are less than ones in 3J and 7J groups. This may be related to the lattice strain inside crystallites and more detailed information will be calculated by Williamson-Hull equation in the next section.

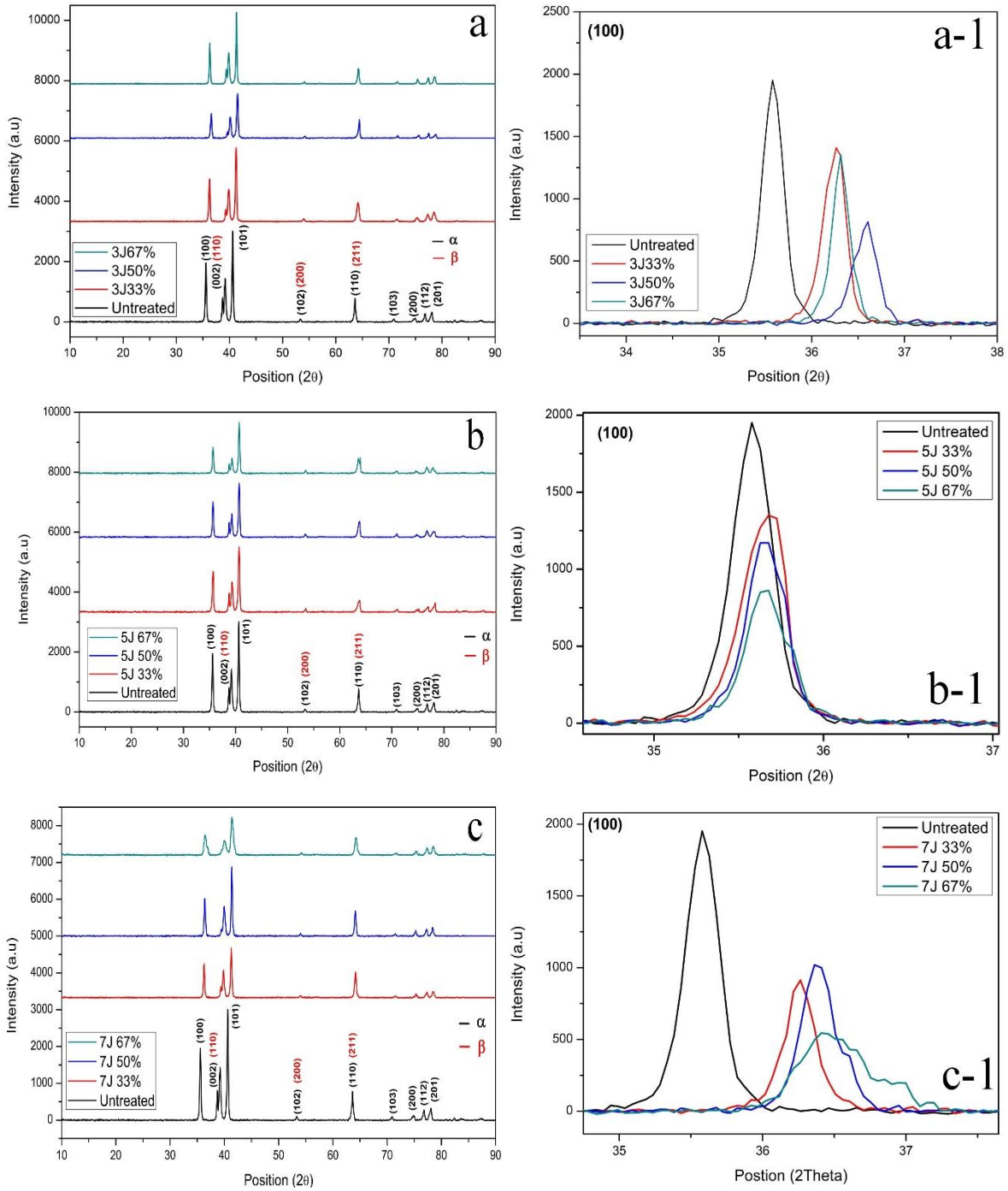

Figure 6.8 XRD patterns and magnified α (100) after laser: A, 3J; B) 5J; C) 7J.

6.4 Determination the crystal size and micro-strain using Williamson- Hall plot

The Williamson- Hall method for the Uniform Stress Deformation Model (USDM) considering the anisotropic nature of the strain was used for the determination of the micro-strain developed in the crystal lattice following LSP. The equation used to calculate the micro-strain is presented in Equation (6-1):

$$\beta_{hkl} \cos \theta_{hkl} = \frac{K\lambda}{D} + 4\varepsilon \sin \theta_{hkl} \quad (6\text{-}1)$$

Where, θ is the diffraction angle; β_{hkl} is the full width half maximum (FWHM), K is the shape-factor; D is the crystallite size (or domain size) and λ is the X-ray wavelength. The suffix, hkl, refers to a crystallographic plane.

From the slope and intercept of the plot between $\beta_{hkl} \cos \theta_{hkl}$ and $4\varepsilon \sin \theta_{hkl}$, The lattice deformation stress, σ and the crystallite size, D, were measured respectively and acted as important input parameters to Equation (6-1)(illustrated in Figure 6.9).

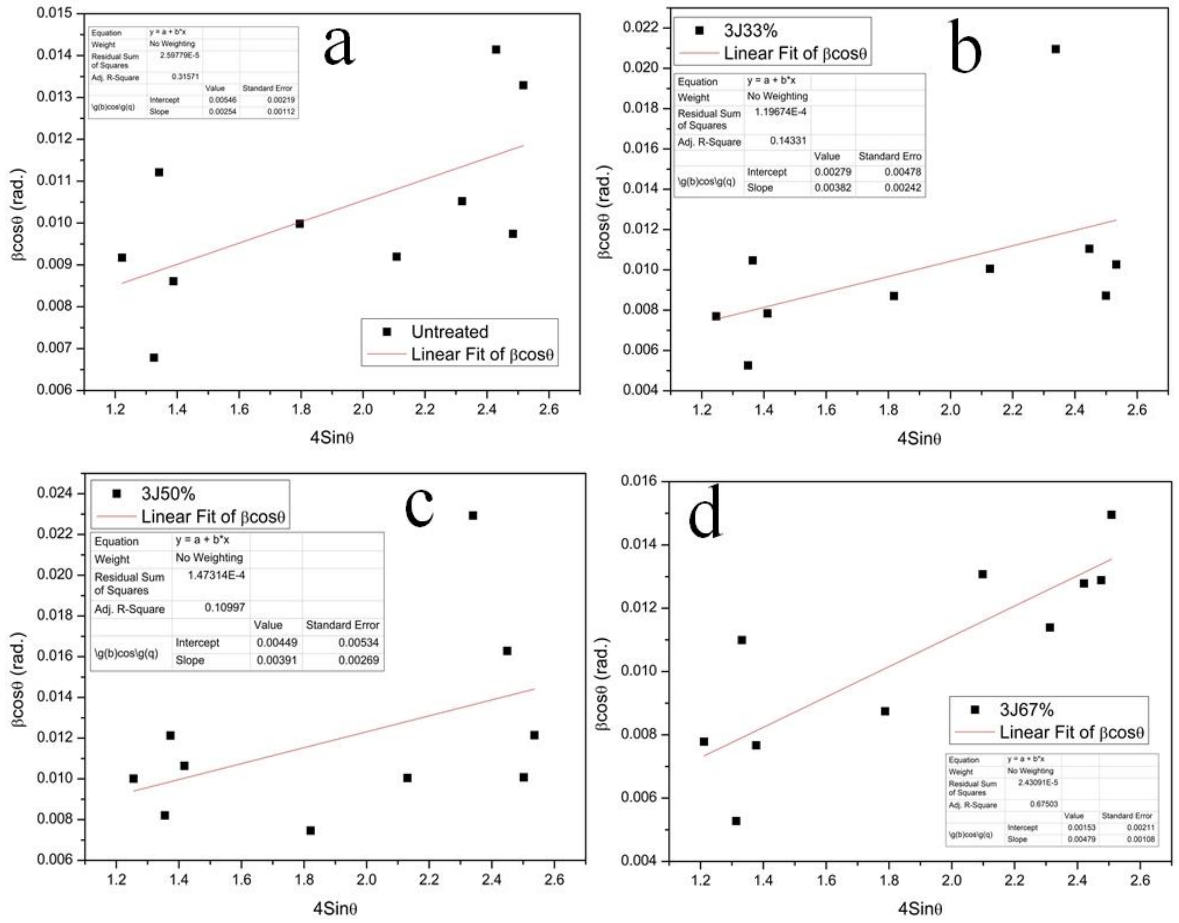

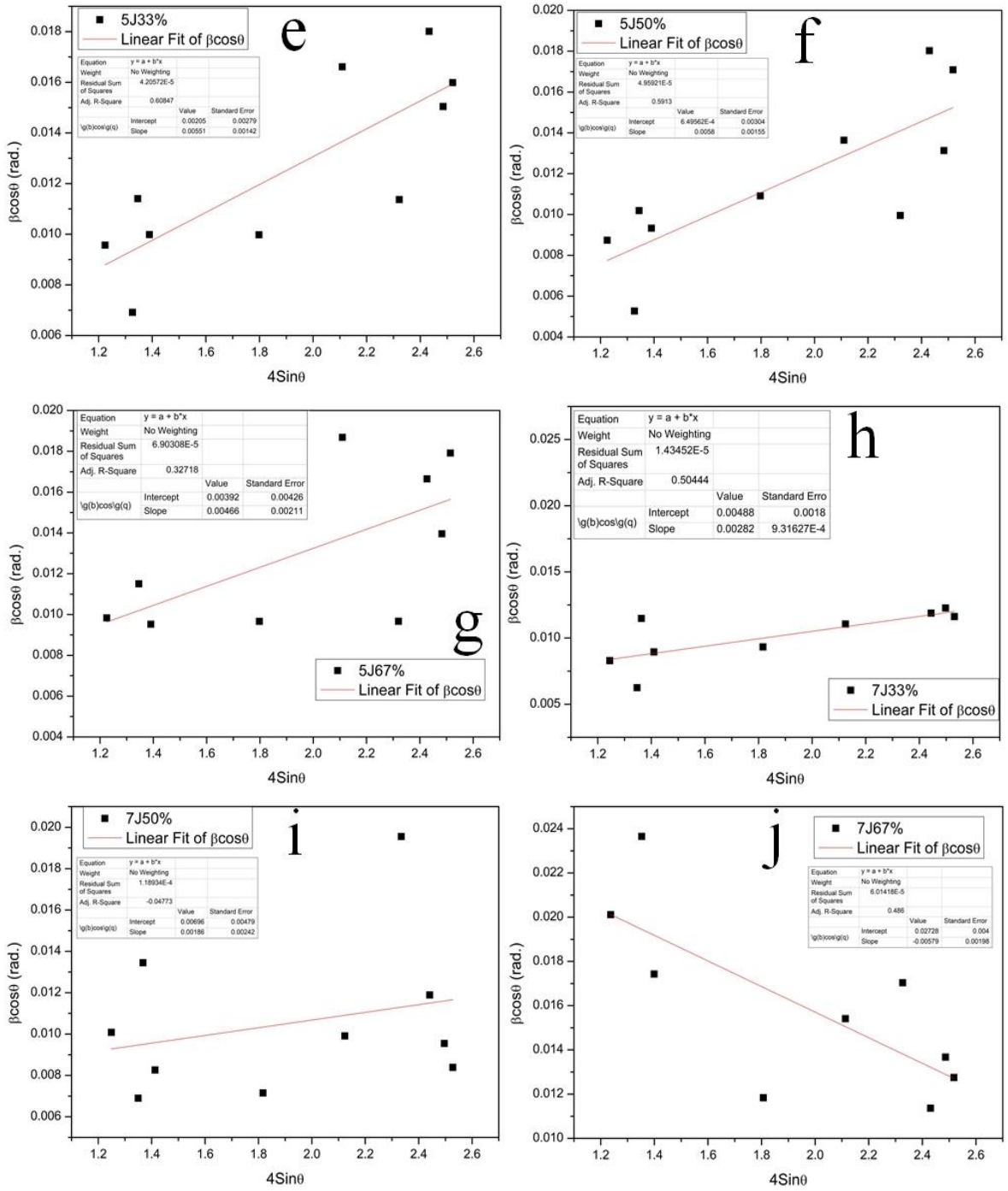

Figure 6.9 Plot of βcosθ *vs* 4sinθ of Ti-6Al-7Nb alloy before (a) and after LSP at (b)3J, 33%, (c) at 3J, 50%, (d) at 3J, 67%, (e) at 5J, 33%, (f) at 5J, 50%, (g) at 5J, 67%, (h) at 7J, 33%, (i) at 7J, 50%, (j) at 7J, 67%.

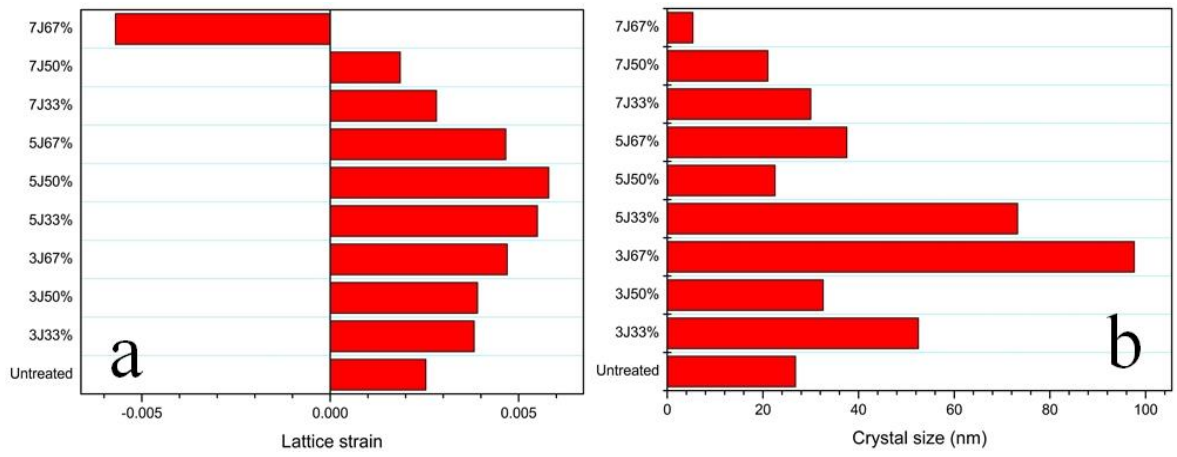

Figure 6.10 Plotted map showing the lattice strain (a) and crystallite size (b) by Williamson-Hall method for Ti-6Al-7Nb alloys.

It has been reported that a positive slope in the W-H plot indicates the presence of tensile strain. At the same time, a negative slope of the fitted line indicates the compressive strain present in the crystal lattice and absence of any slope in the W-H plot implies that the sample is strain-free [215] In the LSPend and untreated samples (Figure 6.10), only the slope of 7J, 67% overlap was negative, while the rests are all positive. That means the lattice strain in the 7J, 67% overlap was compressive, and others are all tensile. The purpose of LSP is usually to introduce compressive residual stress. However, in this case, we can see that if the power density is not high enough, the lattice strain after treatment is still tensile. With the increasing pressure to drive microstructure to deform, the tensile lattice strain keeps on increasing till and peaks at 5J, 50% overlap, onwards it begins to decrease and finally transfers to compressive (at 7J, 67%). From plotting the lattice strain, it indicates that the reason why the shifting in 5J groups is much less than 3J and 7J is that inner tensile lattice strains are highest among the three groups. What is more, in terms of crystal size, we did not see an obvious trend when the laser energy was lower than 7J. In the 7J group, the crystallite size was decreased dramatically compared to the one that was untreated and the refinement of 7J, 67% crystal size is the largest (around 5nm).

6.5 Summary

This chapter focuses on an experimental investigation of post heat treatment microstructures of Ti-6Al-7Nb alloy before and after LSP. The conclusions were drawn as follows:

- Compared to the sub-grains of untreated of 279nm, the average sub-grains were reduced to a range of 222 nm to 205 nm by LSP parameters of 7J, 50% and 7J, 67%

overlap. The rest of LSP parameters have limited or even no influence on the sub-grains refinement

- The HCP and Cubic low angle misorientation of Ti-6Al-7Nb alloy subject to 7J50% and 7J, 67% were increased from 0.52/1.04 to 0.57/1.19 and 0.79/1.48 separately. If LSP parameters are under 7J, there are no effects on the changing of misorientations.
- The saturated local misorientation was located in the depth of 200 to 400 μm rather than the top surface. Twin {10-12} and {11-21} can be found in the sub-surface after 10 LSP impacts. In XRD patterns results, the peaks of all laser shock peened samples were broadened and shifted toward high diffraction angles.
- Calculated by Williamson-hull plot, the micro-strain of 7J, 67% was compressive while the rest LSPned parameters are tensile. In addition, crystal average size received refinement when LSP parameters are 7J, 67%, 7J, 50% 7J, 33% overlay

PART 3 MECHANICAL ASPECTS

CHAPTER-7 Residual Stresses induced by Laser Shock Peening in Orthopaedic Ti-6Al-7Nb Alloy

Prolonged usage can lead to fatigue failures in prosthetic implants. This is an emerging concern for the prosthesis designer and as well as for end-users. Laser shock peening (LSP) can emloyed used to improve the life of prostheses by introducing compressive surface stress that delays or arrests the initiation of cracks. We report measurements of residual stresses induced by laser shock peening (LSP) in a medical-grade Ti-6Al-7Nb alloy. In this chapter, the LSP introduced residual stress field was characterized by using Incremental Hole Drilling (IHD) with predictive modelling using an Artificial Neural Network (ANN). The Ti-6Al-7Nb samples were processed by a pulsed Nd: YAG laser with laser energy of 3J, 5J, and 7J with overlaps of 33%, 50%, and 67%. the IHD data was also confirmed and verified by the ANN technique with a gradient descent learning algorithm. The microhardness, laser energy, overlap, and depth are set as input parameters while the residual stresses are output.

7.1 Introduction

Prevention of implant failures is always a principal concern at the beginning of designing a prosthetic device or the purpose of improving the mechanical properties of the implant by certain surface modification techniques. Failures occur due to various reasons, such as production defects, design deficiencies, or long-term metal fatigue [216, 217]. In the UK National Joint 2019 Report [218], implant fracture accounts for 3.3% (3498) of hip revision surgeries. Although fracture failures caused surgeries may not be high enough amongst all revision surgeries, it is still non-negligible. Mostly, metal implant fractures occur due to tensile residual stress at the implant surface, or near notches (such as drilled holes in intramedullary nails or plates [219-221]). Furthermore, cracking may be encouraged by a corrosive environment, particularly for Stress Corrosion Cracking (SCC) [222]. SCC is a problem for magnesium implant devices [223, 224].

Laser Shock Peening (LSP) is a well-known, advanced surface modification technique [191, 225]that can improve metals' fatigue resistance by introducing deep compressive residual stresses [226]. Residual stresses are internal stresses in a material that is separate from the reaction forces (stresses) required for an engineering component to maintaining its equilibrium with the environment [227]. Tensile residual stress can lead to premature damage so it has a negative effect on the mechanical properties of materials; whilst compressive residual stress

enhances fatigue life by preventing the crack formation and propagation [228]. Based on the length-scale over which they equilibrate, residual stress can be divided into three types: Type 1, Macro-stresses, typically exist over a length scale of several grains in a polycrystalline material. Type 2 micro-stresses are developed in an individual grain. When the scale is around the scale of the atomic spacing in the materials, it is defined as Type 3 micro-stress [229]. Destructive (Sachs Boring, contour method, Slitting and block removal), semi-destructive (hole-drilling), and non-destructive (neutron diffraction, synchrotron X-ray diffraction and laboratory X-ray diffraction) techniques have been developed to experimentally analyse residual stress fields [230] through direct measurement of strain or strain relief.

The incremental hole drilling (IHD) method has been widely employed to determine the depth profile of residual stress in materials. It is quite simple and versatile in application. IHD is a near-surface measurement technique, typically being limited to a small number of millimetres from the surface.

The artificial neural network (ANN) technique is a parallel processing net for nonlinear analysis with features of low cost, high-efficient, and accuracy. Since the last decades, it has been widely employed in complex non-linear problems, correlating input parameters for predicting output variables in different applications. For instance, in laser welding, the welding parameters including laser energy, welding speeding, focal position, shield gas are all set as input variables to predict the cross-sectional shape [231]. Additionally, Rahimi et al. [232], modelled two feed-forward back-propagation neural network to predict the melt-pool geometry and temperature. The prediction outputs were in good agreement (mean square errors of 6.3%-7.9%) with experimental data. Bagchi *et al.* [233], conducted peak temperature predictions based on the ANN method in laser-welded Hastelloy C-276 alloy. In terms of predicting residual stress, Karatas *et al.* [234], determined the shot-peening-induced cross-sectional residual stress fields by a back-propagation learning algorithm with two variables and logistic sigmoid transfer formulas in carbon steel. Maleki *et al.* [235], proposed a new ANN-based method to study the effects of severe shot peening and conventional shot peening on the mechanical properties of cast iron. The results illustrated that ANN is applicable for the prediction of the outcomes of both procedures.

As the manufacturing for the prothesis is costly and expensive, using simulation method for analysing the residual stress distribution in the implant surface is necessary and it will avoid

the damage from the examining method to the implant. From the existing literature [236-238], most works simulating the residual stress following laser peening have used the finite element analysis (FEA) method, typically using ABAQUS® or ANSYS® software. However, the reports regarding the prediction with ANN method are still limited. Compared to FEA, ANN method speeds up the predicting time as the time for meshing the implant and the complicated calculation procedure is saved which is more suitable in the industry. But odd data/trend could be predicted and explained with different equations in FEA. By contrast, ANN couldn`t complete the predicting work as the simulation procedure is accomplished with regular input parameters.

Overall, in this work, IHD characterizes the residual stress field introduced by LSP. In addition, the IHD data is compared to model predictions obtained using the ANN method. To our best knowledge, it is the first time that the ANN technique is used for both validating and predicting laser shock peening introduced residual stress fields in the published literature. This work here is expected to be beneficial to predict the fatigue, wear and other mechanical performance of Ti-6Al-7Nb implants which in turn to be a significant aid to ender-users. In addition, it will also aid in avoiding complex experimental work which not only avoids time consumption and potential errors but also increases the speed of process optimisation and quality control as limited testing can still accommodate a wide range of stress prediction that will aid in improving the process capabilities and advance fundamental understanding.

7.2. Material characterizations and experimental procedures

7.2.1 Incremental hole drilling method

The incremental hole drilling was conducted on a set-up developed by Stresscraft Ltd, UK, following ASTM E837 standard [239] and Measurement Good Practice Guide No. 53 (The National Physical Laboratory) [240]. Firstly, a general 3-element residual strain gauge rosette (Figure 7.1) was glued onto the sample surface. Before milling, the drill bit was placed to the central of the gauge. A total of 16 increments (consisting of four increments of 32μm, four increments of 64μm, and eight increments of 128 μm, to a total hole depth of 1.4 mm) were carried out by an orbital motion with a carbide drill bit. Between each increment, the motion stops and the relaxed strains were measured in order to calculate the residual stress.

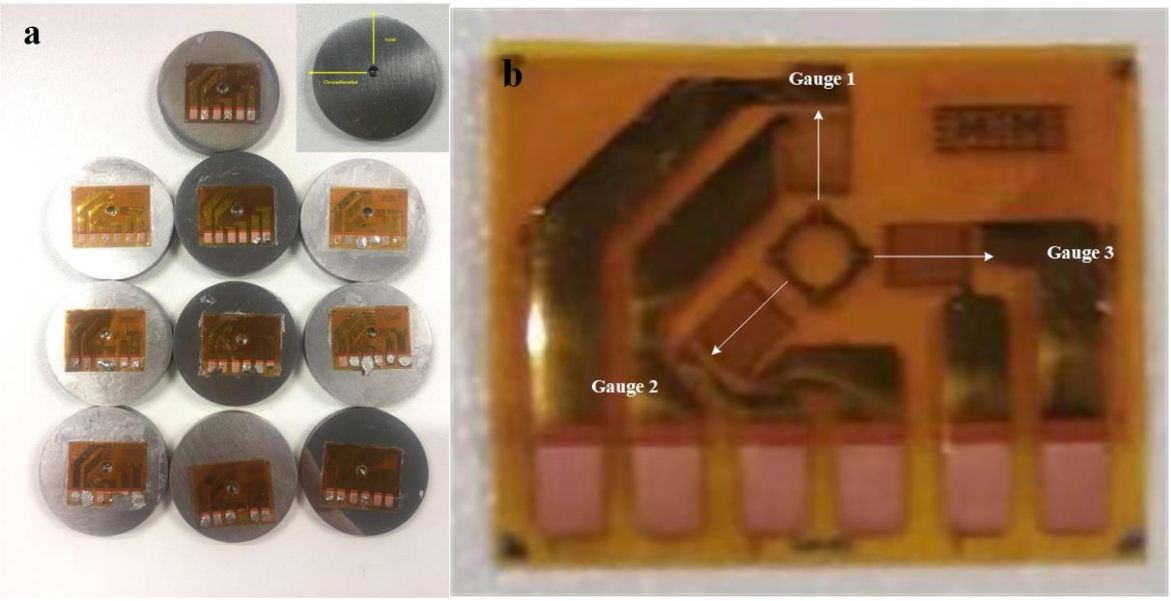

Figure 7.1 Experimental samples after IHD marked with axial and circumferential direction of residual stress (a); a typical 3-element rosette strain gauge (b).

7.2.2 Artificial neural network approach

The Artificial Neural Network technique was inspired by the biological human neural structure [241]. An ANN model can simulate the behaviour of complex variables or systems without prior user assumptions. Such prediction behaviour is based on various independent nodes, which are also called artificial neurons [242]. During the training of the network, these neurons are related to each other in three layers (input layers, output layers, and hidden layers, Figure 7.2). The connections are assigned with numerical values, which are known as weights [243]. These change when different learning algorithms are employed. A feed-forward back-propagation algorithm is employed to train the network: experimentally-determined residual stress from IHD, microhardness, and laser energy and overlap as inputs; and residual stress as the output of the model, as illustrated in Figure 7.2. And the functions and process parameters are given in Table 7.1. SPSS software was employed to develop the ANN model.

The model was developed using data from peening with 3J and 7J laser energy. The results from peening with 5J laser energy were reserved as test samples for validating the trained network.

Firstly, the training process was conducted by pre-set learning rate (0.4) and momentum rate (0.9). By comparing with the target value, the predicted variables were adjusted *via* changing

the weights during training the network. Then the training work was in total, repeated 10 times for the accuracy. Finally, the accuracy of the developed model can be expressed with the mean absolute percentage error (MAPE) listed following Equation 7-1 [244, 245]:

$$\text{MAPE} = \frac{100}{n}\sum_{i=1}^{n}\frac{|T_i - P_i|}{T_i} \quad \text{(7-1)}$$

Where T_i and P_i are the experimental and predicted values, n is the total sample number.

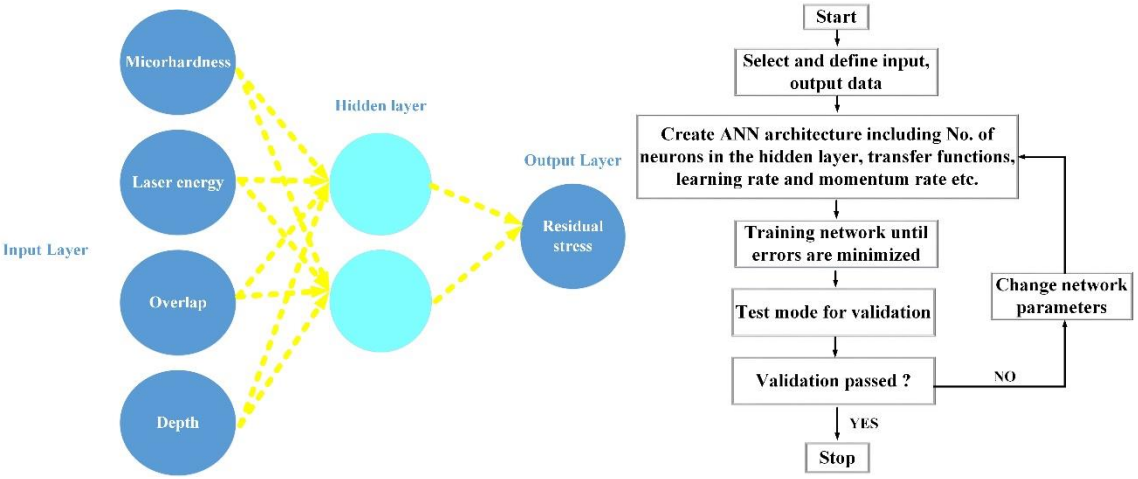

Figure 7.2 ANN architecture applied to RS; flowchart of the algorithm for determining residual stress.

Table 7.1 Network architecture parameters for Residual stress (Circumference and Axial).

Type	Network	
Architecture	Normal feed-forward multi-layer	
Hidden layer number	1	
Number of Neurons	Input - 4 (Surface hardness, Laser Energy, Overlap%, Depth,) Hidden—2 Output—1	Input - 4 (Surface hardness, Laser Energy, Overlap %, Depth,)
Transfer function (hidden layer)	Tan sigmoid	Tan sigmoid

Transfer function (output layer)	Tan sigmoid	Hyberbolic Tangent
Training algorithm	Gradient decedent learning	
Learning rate	0.4	
Momentum rate	0.9	
Error goal	1x10-4	
Epochs	10000	

7.3 Determination of residual stress by IHD

It is well known that laser shock peening can introduce a stable compressive residuals stress layer along with the depth of the metallic material through high pressure shock wave [113, 186]. The drilled samples of images and residual stress directions are shown in Figure 7.1.

Results prior to and after LSP from incremental hole-drilling are shown in Figure 7.3. Due to the surface finish, the tensile stress of 225MPa was introduced in the top surface. Thereafter, it decreases to about 0 MPa at the depth of 180μm, then keeping steady along with the depth. Following peening, depending on the peen parameters the residual stress at the surface ranged from –42 to –516 MPa. The compressive residual stress persisted to a depth of at least 500 μm. The discussion is separately given according to overlap and laser energy in this section.

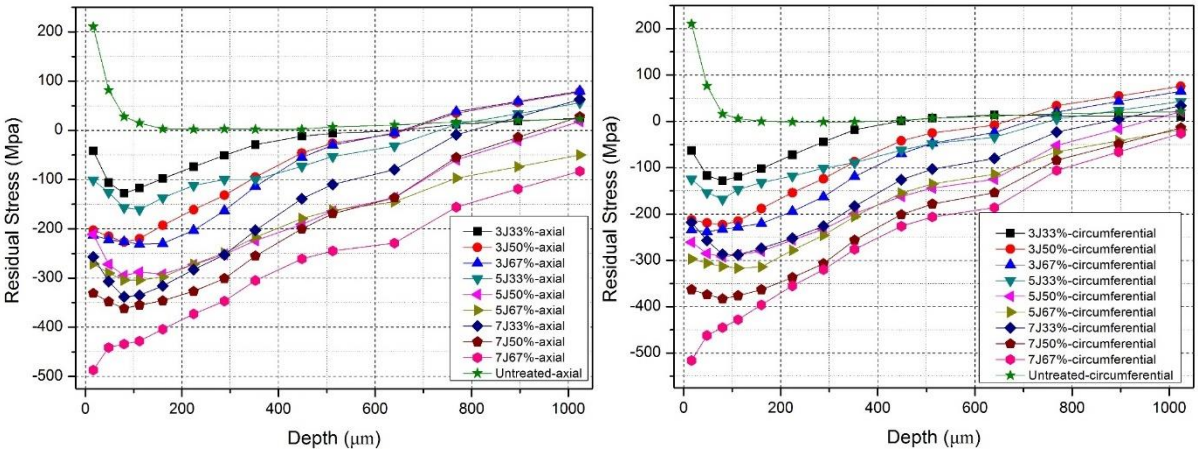

(a) (b)

Figure 7.3 Near-surface measurements of residual stress in Ti-6Al-7Nb before and after LSP: (a) axial direction. (b) Circumferential direction.

Table 7.2 The incremental hole drilling data of Ti-6Al-7Nb before and after laser shock peening

Depth	Residual Stress																			
Unite	MPa																			
	3J						5J						7J						Untreated	
	33%		50%		67%		33%		50%		67%		33%		50%		67%			
	Cir	axial	Cir	axial	Cir	axial	Cir	axial	Cir	axial	Cir	axial	Cir	axial	Cir	axial	Cir	axial	Cir	axial
16	-63	-42	-212	-203	-234	-213	-125	-101	-211	-211	-297	-271	-218	-257	-363	-331	-516	-487	211	211
48	-117	-106	-219	-215	-238	-222	-154	-126	-285	-272	-306	-290	-257	-307	-374	-348	-462	-441	77	82
80	-128	-128	-223	-227	-233	-226	-168	-157	-292	-295	-313	-304	-287	-338	-383	-362	-445	-434	16	28
112	-119	-117	-215	-220	-228	-231	-147	-161	-288	-288	-317	-304	-288	-335	-376	-355	-428	-428	6	15
160	-102	-98	-188	-193	-220	-230	-132	-137	-280	-292	-314	-298	-274	-316	-363	-346	-396	-404	0	3
224	-72	-74	-154	-161	-194	-203	-118	-112	-256	-273	-278	-272	-252	-283	-337	-327	-355	-373	-1	2
288	-44	-51	-124	-132	-163	-163	-101	-100	-233	-252	-246	-249	-226	-253	-307	-301	-320	-347	-1	3
352	-18	-29	-87	-95	-119	-114	-89	-100	-199	-224	-205	-217	-183	-203	-256	-255	-276	-305	-1	2
448	1	-12	-42	-46	-70	-55	-62	-73	-162	-191	-155	-179	-126	-139	-201	-200	-226	-261	2	2
512	7	-6	-25	-26	-47	-30	-48	-53	-144	-164	-135	-162	-103	-110	-178	-169	-206	-245	7	7
640	14	-1	-8	-7	-24	-5	-34	-32	-125	-137	-114	-145	-80	-80	-154	-137	-186	-229	12	11
768	12	12	34	35	20	38	5	12	-52	-60	-66	-97	-23	-9	-84	-55	-106	-156	16	17
896	12	19	55	57	43	59	24	34	-16	-21	-42	-74	5	27	-49	-14	-66	-119	19	20
1024	11	25	76	78	65	80	43	56	21	18	-18	-50	34	63	-14	28	-26	-83	21	23

7.3.1 The effects of laser energy on the cross-section residual stress

Figure 7.4 shows the effect of laser energy on residual stress at constant laser spot overlap. All the curves increase from the near-surface, reaching the highest point at depth of around 100μm, onwards keeping decreasing to final stable value, (excepting the 7J67% curve). What is interesting, after LSP, from the near-surface to the certain depth varying from 430 μm to 1100μm, a compressive residuals stress layer is formed along the cross-section, but the residual stress is transferred to tensile residual stress at the comparative deep depth. Guowei et al [173]used XRD to measure the in-depth residuals stress profile of laser additive manufactured Ti6Al4V alloy after LSP. The affected depth is around 700 μm and onwards 700 μm, it is tensile residual stress. The reason for this transformation is that the thickness of samples is about 3mm. Compared to the drilled depth of 1.4 mm, it is comparatively thin. Therefore, due to this reason, the residuals stress at a deep depth becomes more tensile.

At the 33% overlay in Figure 7.4 (a) and (b), the highest compressive residuals stress is acquired by 7J laser energy with a value of -257MPa (axial) and -217 MPa (circumferential), followed by -101MPa (axial) and -125MPa (circumferential) (5J) and -42MPa (axial) and -63MPa (circumferential) (3J). Additionally, the affected compressive residual stress layer of 3J, 33% is about 448μm, while these values of 5J, 33% and 7J, 33% are 768 μm and 896 μm.

When it comes to 50% overlap, due to the increased overlap, the overall compressive residual stresses were raised to -212MPa & 203 MPa (3J), -211MPa & -261MPa (5J), and -331MPa & -363MPa (7J) for both directions. What is more, the residuals stress affect layer depth of 3J increases to 700μm, while for 5J and 7J, they both reach to 1000 μm.

In the overlay of 67%, the near-surface residual stress still keep increasing, -234MPa & -213MPa (3J), -297MPa & -271 MPa(5J) and -516MPa & -487 MPa(7J). But, not like 33% and 50% trends, the effect layer depth of 3J67% has not been seen as an obvious increase, keeping steady at 700μm to 720 μm in two directions. For the causes of 5J and 7J, due to the high power density, the affecting residual stress is out of measurement, at least higher than 1250 μm according to these two curves trends.

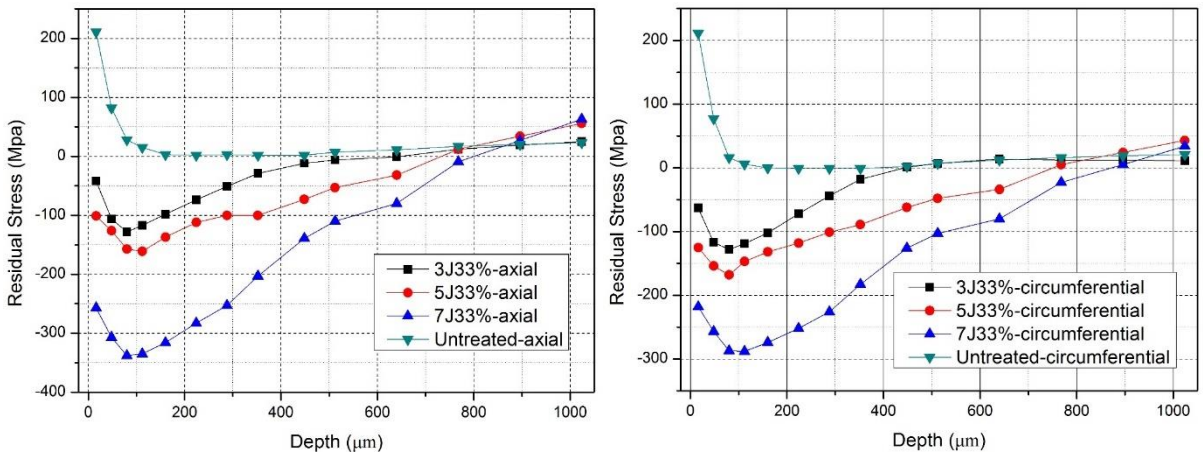

(a)

(b)

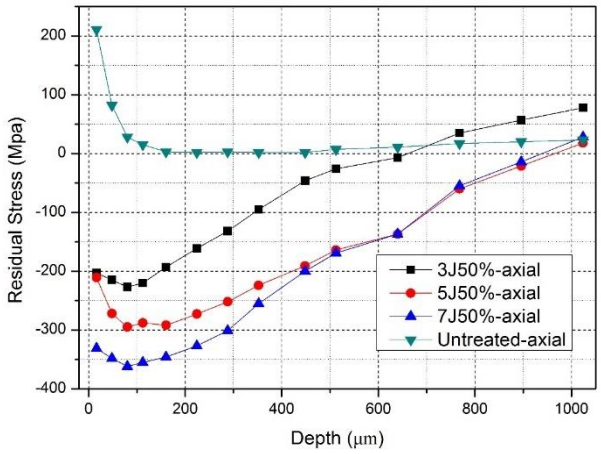

(c)

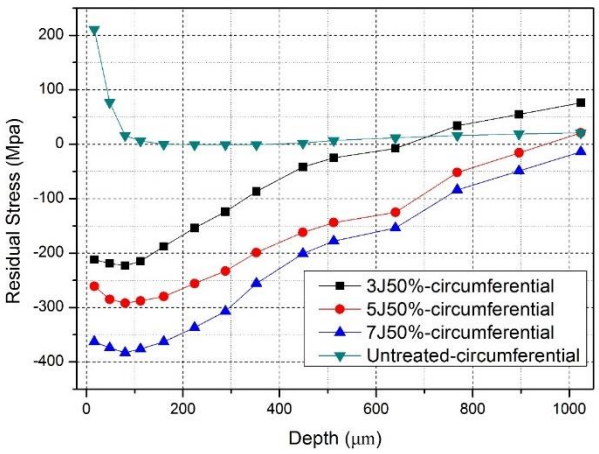

(d)

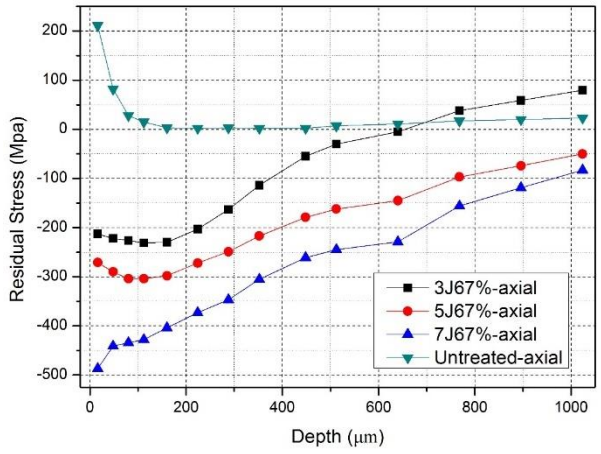

(e)

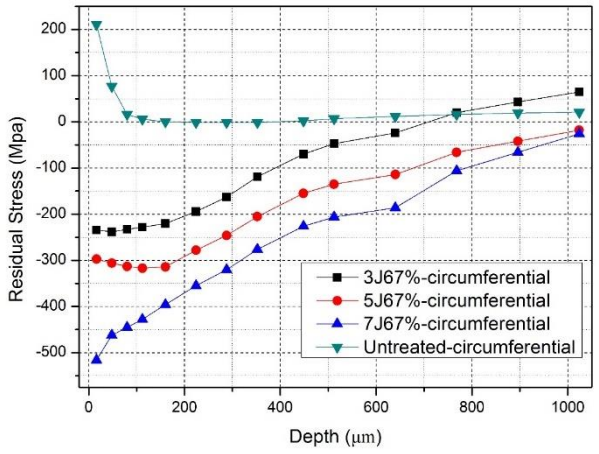

(f)

Figure 7.4 Keeping overlay consistent, cross-sectional residual stress distributions of Ti-6Al-7Nb before and after LSP in both circumferential and axial directions at 3J, 5J and 7J: (a) and (b) 33% overlay, (c) and (d) 50% overly, and (e) (f) 67% overlay.

7.3.2 The effects of overlay on the cross-section residual stress

Figure 7.5 shows the near-surface residual stress before and after LSP for the three spot overlaps. When the laser energy was kept constant, the most interesting phenomenon among these curves is that the residual stress gap between 50% and 67% curves is much lower than the one between 33% and 67% which means curve 50% is very close to curve 67% (Figure 7.5). In the laser energy of 3J (Figure 7.5 (a) and (b)), the near-surface residual stress of 33% is -63/42 MPa, while these values of 50% and 67% are very close to each other which are -212MPa & -203MPa(5J) and -234MPa & -213MPa (7J). The compressive residual stress layer depth of 5J and 7J are higher than 600µm while the one of 33% only has 448 µm.

In the case of 5J (Figure 7.5 c, d), the near-surface residual stress of 33% increases to -125MPa & -101 MPa, while these values of 50% and 67% are -211MPa & -211MPa and -297MPa & -271MPa. In terms of affected depth, the curve of 5J, 33% is 768 µm, followed by 1000µm at 50% overlap and 1200 µm (7J, according to its trend).

When it comes to 7J (Figure 7.5 (e) and (f)), as enough laser-driven power shock-wave, the difference amongt these three overlays distributed more evenly than the one of 3J, and 5J. But, in Figure 7.5(f), curve 50% and curve 67% are still very close to each other. Additionally, the highest top surface residual stress is acquired by 67% with value of -516MPa & -487 MPa, followed by -363MPa & -331MPa (5J) and -218MPa & -257MPa (3J). For the affected residual stress depth of 33% was 896 µm, while 50% and 67% affected residual stress depth were about 1100 to 1400 µm.

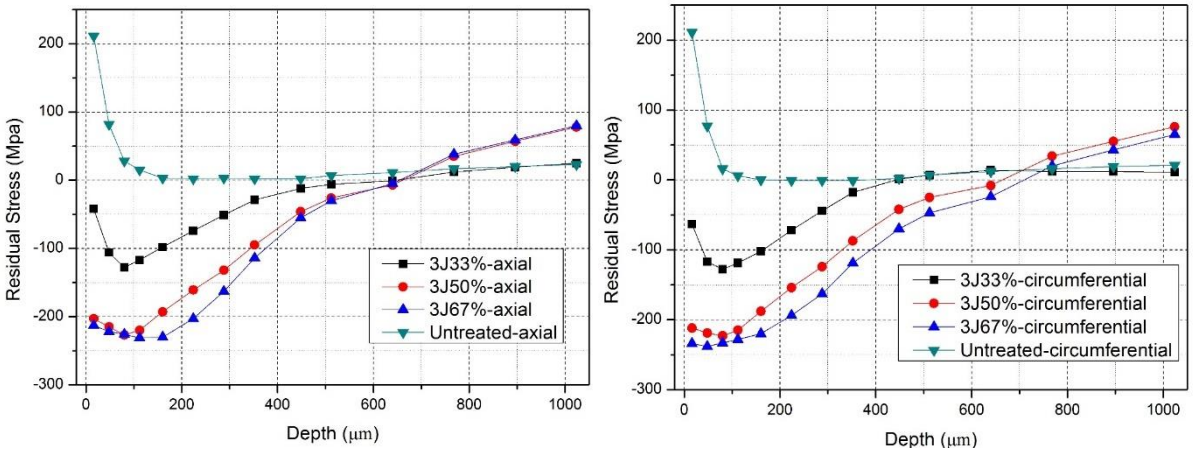

(a) (b)

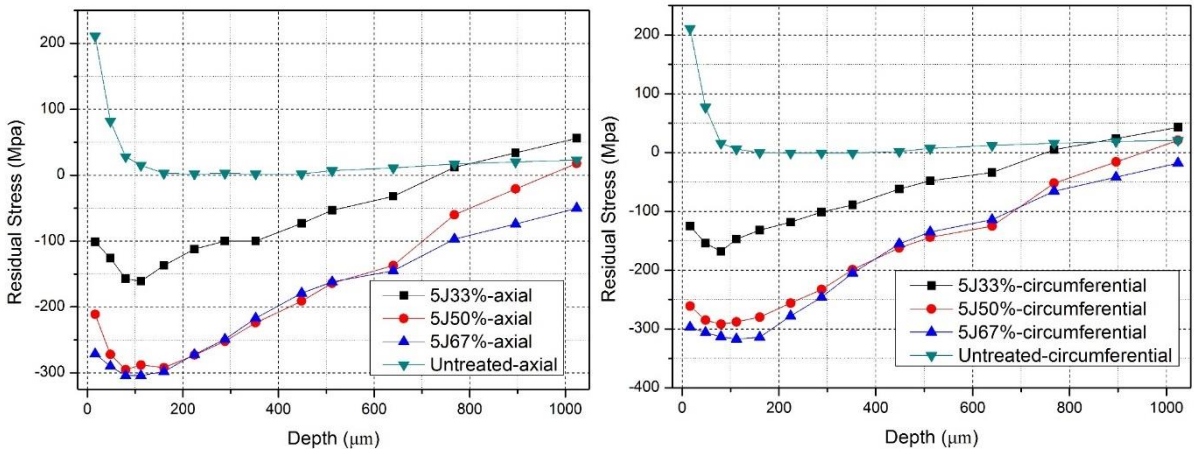

(c) (d)

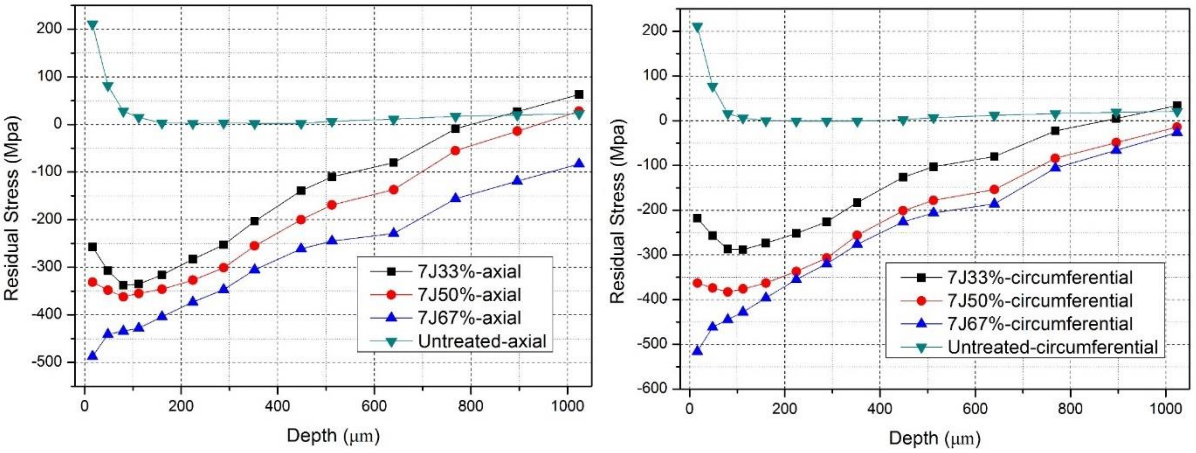

(e) (f)

Figure 7.5 Illustration of the cross-sectional residual stress in both the axial and circumferential directions by keeping the laser energy constant at 33%, 50%, and 67%: (a) and (b) 3J; (c) and (d) at 5J; and (f) 67% at 7J.

7.4 ANN prediction of cross-section residual stress

The most advantage of ANN over other methods is that it is quite useful when the relationships between different parameters in a complex system that are not very clear, thereby, it is applicable in residual stress predicting [246]. In this study, the network training is completed with the residual stress data from 3J and 7J residual stress data and the trained results are satisfactory. From Figure 7.6, we can see that the ANN model form a good correlation to the LSP residual stress prediction as in both two directions (axial and the circumferential), the simulated data has a good fit with the experimental data of 3J and 7J with average MPAE value of 3.84% and 4.84% (the prediction accuracy is 96.16% and 95.16%). Figures 7.7 shows the importance of ranking of input parameters on the output circumference and axial residual stress.

And the important sequence in the simulation is depth > laser pulse energy (LPE) > overlap percentage (OLP)> surface hardness (SH). Therefore, the depth of residual stress is a dominant factor in determining predicted residual stress.

What is more, the testing/validation is performed with 5J laser peening treatment data (Figure 7.8). The mean absolute percentage errors in two directions for 5J residual stress data are 3.1% and 1.59%. The tested residual stress value almost equals experimental data, especially in a circumferential direction.

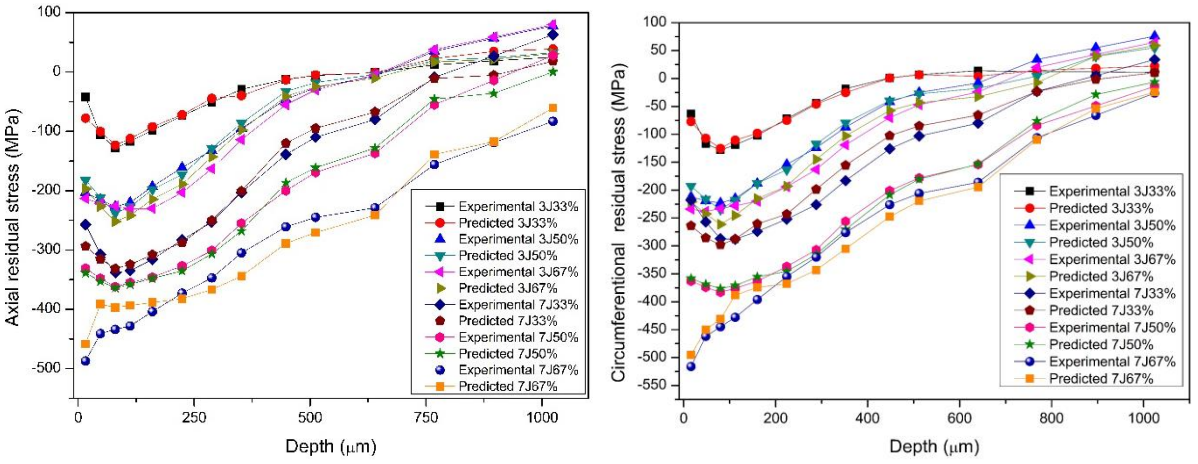

(a) (b)

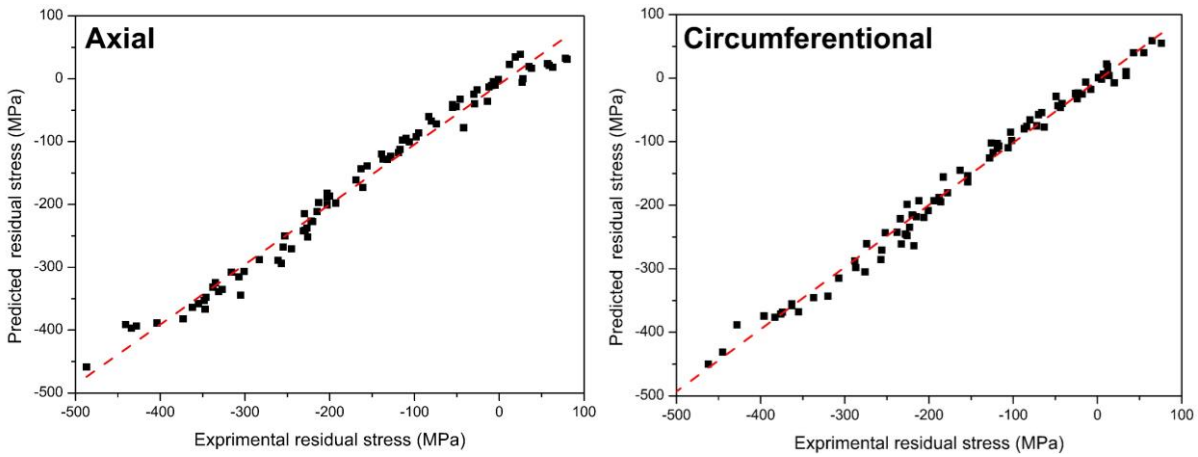

(a) (b)

Figure 7.6 Comparison of experimental *versus* predicted residual stress (axial and circumferentional directions) for trained 3J and 7J data; Goodneess of fitness for trained 3J and 7J data.

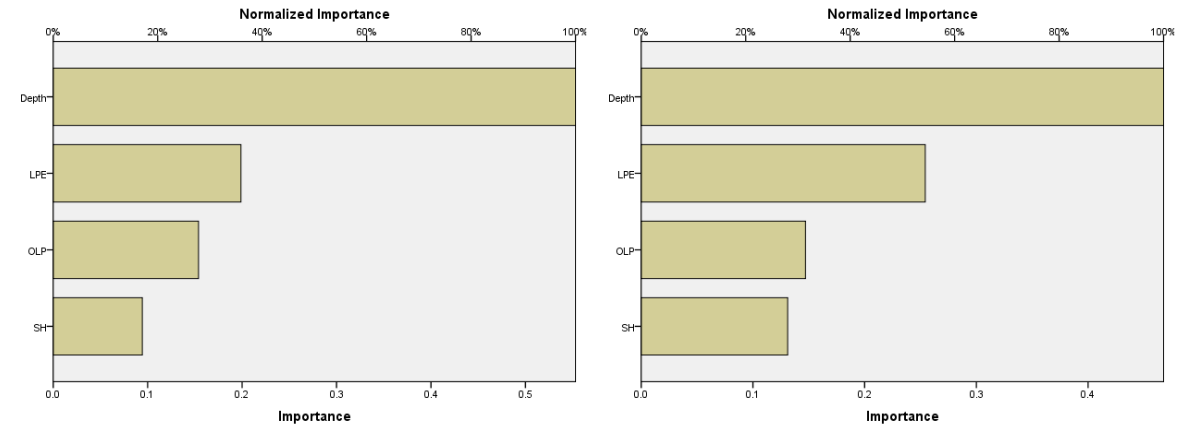

(a) (b)

Figure 7.7: Plot of independent variable importance for circumference and axial RS

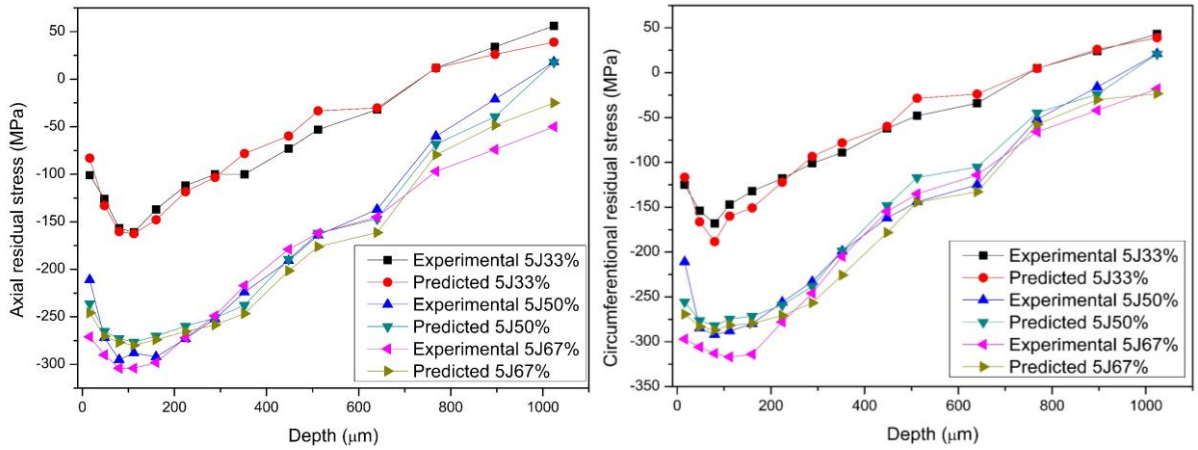

(a) (b)

Figure 7.8 Comparison of experimental *versus* predicted residuals stress(axial and circumferential directions) for tested 5J data

7.5 Summary

In this work, the LSP introduced residual stress field was characterized by incremental hole-drilling. Additionally, the incremental hole drilling data was simulated by an artificial neural network (ANN). As IHD is the macroscopic measurement, it can give a comprehensive evaluation of residual stress fields over the implants. However, due to its measurement features, certain damage will be caused in the implants Therefore, simulation method such as ANN is necessary for not only predicting but validating residual stresses with the prerequisite that the tested data is limited. ANN method avoids specific experimental and numerical experiments, improved effectiveness for residual stress prediction. This work proves a reference for

validation and prediction of residual stresses in Ti-6Al-7Nb alloy implants initial designing or mechanical properties improvement. The conclusions are drawn as follows:

- The near-surface residual stresses along the cross-sectional depth measured by IHD showed that the magnitude of compressive residual stress from -42MPa to -512MPa were observed subjected to different LSP parameters at the depth of 16µm.
- Increasing the laser energy increases the magnitude of the residual stress at the surface and the overall depth of the compressive residual stress; Increasing the amount of overlap increases the magnitude of the near-surface compressive residual stress, with greater difference seen at the highest energy of 7J.
- In ANN results, the predicted data is in good agreement with experimental one with an accuracy value of 96.16% and 95.16% for training 3J and 7J data and 96.9% and 98.41% for testing the data at 5J.

CHAPTER 8 Fretting Wear and Hardness of Ti-6Al-7Nb Alloy Subject to Laser Shock Peening in Simulated Body Fluid

This Chapter is focused on the effect of Laser Shock Peening (LSP) on the micro-hardness and fretting wear of Ti-6Al-7Nb alloy for orthopaedic implant applications in simulated body fluid. LSP surface treatment was conducted at laser energies of 3J, 5J, 7J, and overlap of 33%, 50% and 67% with the laser spot diameter of 3mm. In this study, the samples subject to the variables LSP parameters were investigated on micro-hardness with Vickers indentation, A tribometer was used to measure the wear behaviour of Ti-6Al-7Nb, prior to and after LSP in a simulated body environment (foetal bovine serum, FBS at 37℃). The worn surfaces were characterized by SEM to wear analyzing and 3D-profiler to calculate the wear-loss volume.

8.1 Introduction

Fretting wear is destructive to materials and occurs between two contacting solid bodies when exposed to relatively small amplitude oscillatory motion under a certain load. Such movements would generate fretting fatigue, which may cause material surface damage, thereby, acting as crack initiation sites. Furthermore, micro-cracks will extend from the material surface into the depth direction under the fretting fatigue leading to the reduction of fatigue strength. In a total hip implants system, the fretting wear normally occurs at the junction of head-neck that normally consists of titanium stem and ceramic. The metallic debris was considered to be the main reason for causing osteolysis, and polyethylene debris would even cause implant degradation which further results in aseptic loosening. Therefore, improving the fretting wear resistance of a prosthesis is the main purpose of a surface enhancing technique.

Based on this, the wear resistance of surgical implant biomaterials such as metals, ceramic, and polymers are improved by a variety of surface modifications, namely; shot peening (SP); ultrasonic nanocrystalline surface modification (UNSM); ion implantation and diamond-like carbon (DCL) coating etc. Liu *et al* [247], improved the microhardness and wear resistance by applying SP on the Mg-8Gd-3Y alloy. Compared to the as-received, the average wear volume of the peened regions was decreased by up to 40.7%. Meanwhile, the compressive residual stresses were formed in the deformation layer which contributed to the fatigue resistance[247].

What is more, UNSM was also considered to be an effective technique to enhance the wear resistance of biomaterial in the medical industry. Kheradmandfad *et al* [248], found that the wear resistance of Ti-29Nb-13Ta-4.6Zr (TNTZ) alloy was enhanced more than 7 times than the untreated one after UNSM treatment. Zhang *et al* [249], carried out a reciprocating sliding fretting wear experiment on Ti-6Al-7Nb alloy treated by N-ion implanted and DLC coated respectively. The results showed that DCL coating exhibits better wear resistance than N-ion implantations.

Like SP, Laser shock peening is a cold working method that introduces deep compressive residual stress to enable materials resistance to high cycle fatigue (HCF, high cycle, low stress to failure), low cycle fatigue (LCF, low cycle, high stress to failure), corrosion and wear. It has also been employed to improve the wear resistance of various metallic materials, especially like titanium and magnesium alloys.

As reported in our previous works and others, LSP has presented its capability to not only improve the wear resistance but also altered the surface wettability of Ti-6Al-7Nb alloy by applying surface pattern and surface microstructure refinement. Zhou *et al* [250], investigated the effects of LSP on friction and wear properties of medical Ti-6Al-4V alloy in Hank's solution. The results showed that LSP can reduce debris peeling of Ti-6Al-4V implants. Zhang *et al* [171], demonstrated that LSP not only decreased the coefficient of friction and improved the wear resistance of AZ31B alloy, but also strengthened tensile strength and fatigue performance. What is more, LSP could also be used to strengthen the corrosion resistance. Luo *et al* [251], examined the effects of multiple treatments on electrochemical corrosion properties of Mg-Al-Mn alloy, and obvious improvement of electrochemical corrosion was observed.

It is the first time that medical Ti-6Al-7Nb alloy is surface treated by laser shock peening, and carried out the fretting wear test in simulated body fluid with this material post-laser shock peening. On account of this, laser energy and overlap on the micro-hardness, tribological behaviour and worn surfaces are investigated by means of Vickers microhardness indentation, SEM and 3-D surface profiler.

8.2 Experimental procedures

8.2.1 Microhardness

Vickers hardness tester manufactured by Struer, Germany conducted the microhardness measurements. Each indentation was carried out with a load of 0.05g along the cross-sectional direction. The average value of each point was calculated by three times measurement in the same depth.

8.2.2 Fretting wear experimental settings

A ball-on-flat tribometer (manufactured by Ducom, India) with 6 mm diameter bearing grade ZrO_2 ball, was employed to conduct the reciprocate fretting wear experiment. The Ti-6Al-7Nb samples prior to and after LSP were used as a flat material. Before the test, both counter moving ball and Ti-6Al-7Nb alloy were ultrasonically cleaned with isopropanol and distilled water. The wear test was conducted with a load of 5N running for 18,000 cycles at frequency of 5Hz. The samples were placed in the material rig immersed in 20% foetal bovine serum FBS solution (PH=7.4) at the temperature of 37 ℃. The wear volume (V) of Ti-6Al-7Nb samples before and after LSP were calculated using Klaffke's equation (8.1) as follows:

$$V(mm^3) = \pi R h^2 \left(1 - \frac{h}{4R}\right)^4 \quad (8\text{-}1)$$

Where R is the radius of the counterpart; h is the depth of wear scar.

8.3 Microhardness of Ti-6Al-7Nb

Improving micro-hardness can benefit the wear resistance, which is one of the main failure issues in many surface modification methods, as the main failure mode of orthopaedic implants is wear. The Vickers micro-hardness distributions in the cross-section of the Ti-6Al-7Nb alloy, before and after LSP are shown in Figure 8.1. The cross-sectional microhardness of the untreated scatters from 325HV0.05 to 335 HV0.05. After laser shock peening, it was seen that the Ti-6Al-7Nb alloy are surface hardened and the improvement of microhardness range from 365 $HV_{0.05}$ to 425$HV_{0.05}$. Yin *et al* [187], examined the effects of LSP on microhardness of Ti-6Al-4V. The microhardness was improved from 390 $HV_{0.5}$ to 470$HV_{0.5,}$ due to two factors which separately are a severe plastic layer was generated and the grain refinement according to Hall-Petch formula. The effects of laser energy and overlap will be discussed separately in the following sections.

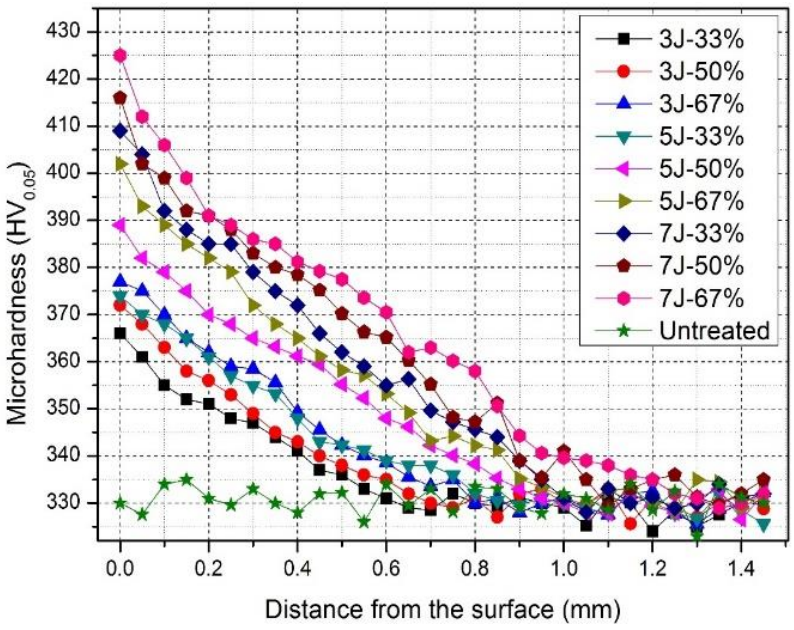

Figure 8.1 The microhardness map showing the cross-section microhardness distribution of Ti-6Al-7Nb alloy before and after multiple laser shock peening.

8.1.1The effects of laser energy on the cross-sectional microhardness

If we keep the overlap constant, looking at the microhardness distribution according to laser energy (as shown in Figure 8.2), we can see that surface hardened layer depth and microhardness are proportional to laser energy. For instance, at 33%, 7J laser-induced around 410 $HV_{0.05}$ at the near-surface followed by 375 $HV_{0.05}$ (5J) and 365$HV_{0.05}$ (3J). The microhardness decreases gradient along the depth direction, eventually, leading to a stable value as same as the untreated means the surface hardened effect are disappeared beyond this point. Ge *et al* [168], laser peened the magnesium with 6.5J, 8.5J and 10.5J laser energy. The plastic deformation layer depths at three different laser energies are 0.6 mm, 0.7 mm and 0.8mm respectively. The surface hardened effect will reduce along the cross-section direction and the affected depth is called plastic deformation layer. A similar trend can also be found in 50% and 67% curves. Among these 3 overlaps, we can see that the gap in the 67% curves are much narrow which means the surface hardened effect is not so obviously improved by 7J laser.

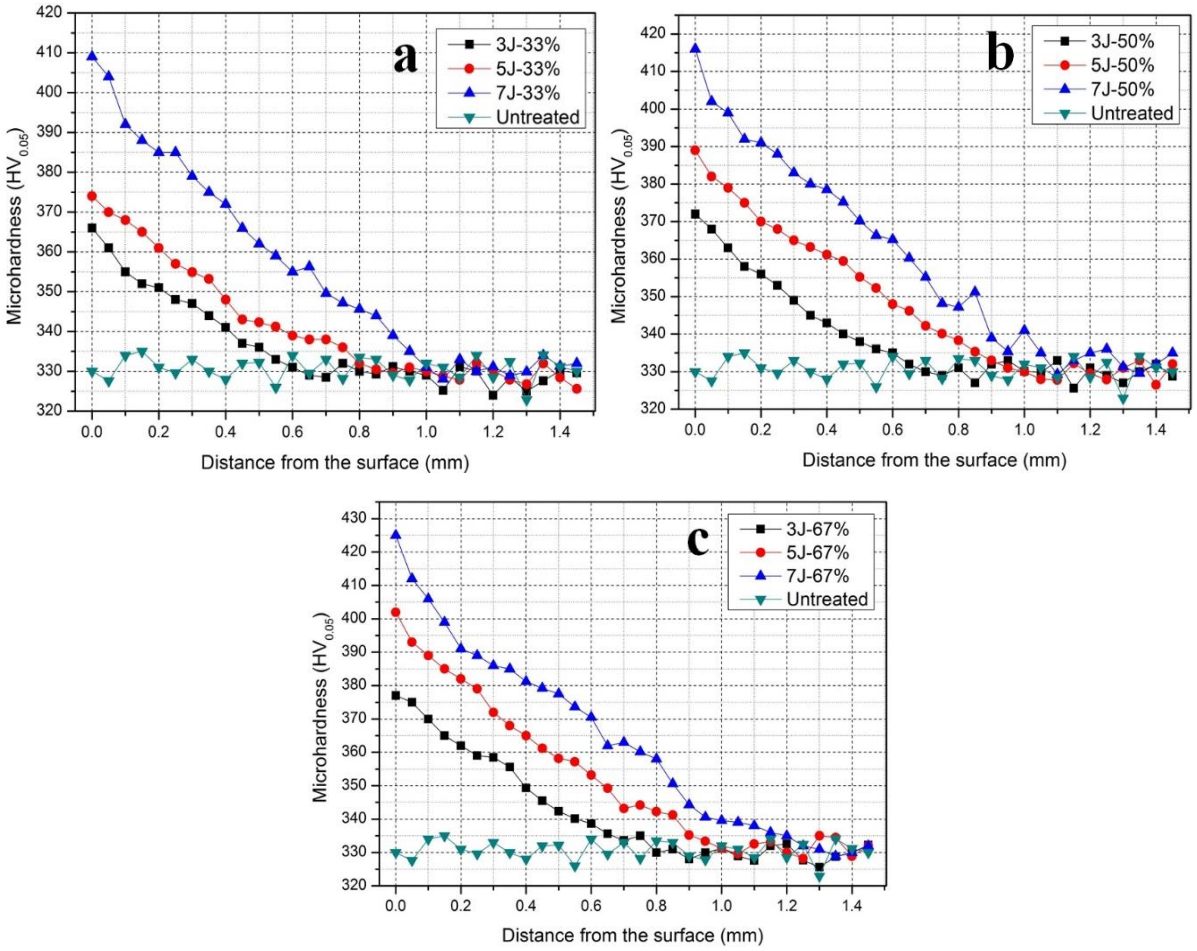

Figure 8.2 Keeping overlay consistent, cross-sectional microhardness distributions of Ti-6Al-7Nb before and after LSP at the overlap of 33% (a), 50% (b) and 67% (c).

8.1.2The effects of the overlay on the cross-section microhardness

By keeping laser energy constant, the microhardness distributions along the cross-section are shown in Figure 8.3. Actually, the curves arranged according to the same laser energy have similar trend like the way that of laser energy has. It can be seen that microhardness and surface harden depth are also proportional to overlap. For example, the micro-hardness of 3J at the near-surface is 365$HV_{0.05}$ (33%), 372$HV_{0.05}$ (50%) and 377$HV_{0.05}$ (67%). In 5J and 7J, the microhardness at the near-surface was improved to 374 $HV_{0.05}$ (5J, 33%), 389 $HV_{0.05}$ (5J, 50%), 402 $HV_{0.05}$(5J, 67%) and 409 $HV_{0.05}$ (7J, 33%), 416 $HV_{0.05}$(7J, 50%) 425 $HV_{0.05}$ (7J, 67%).

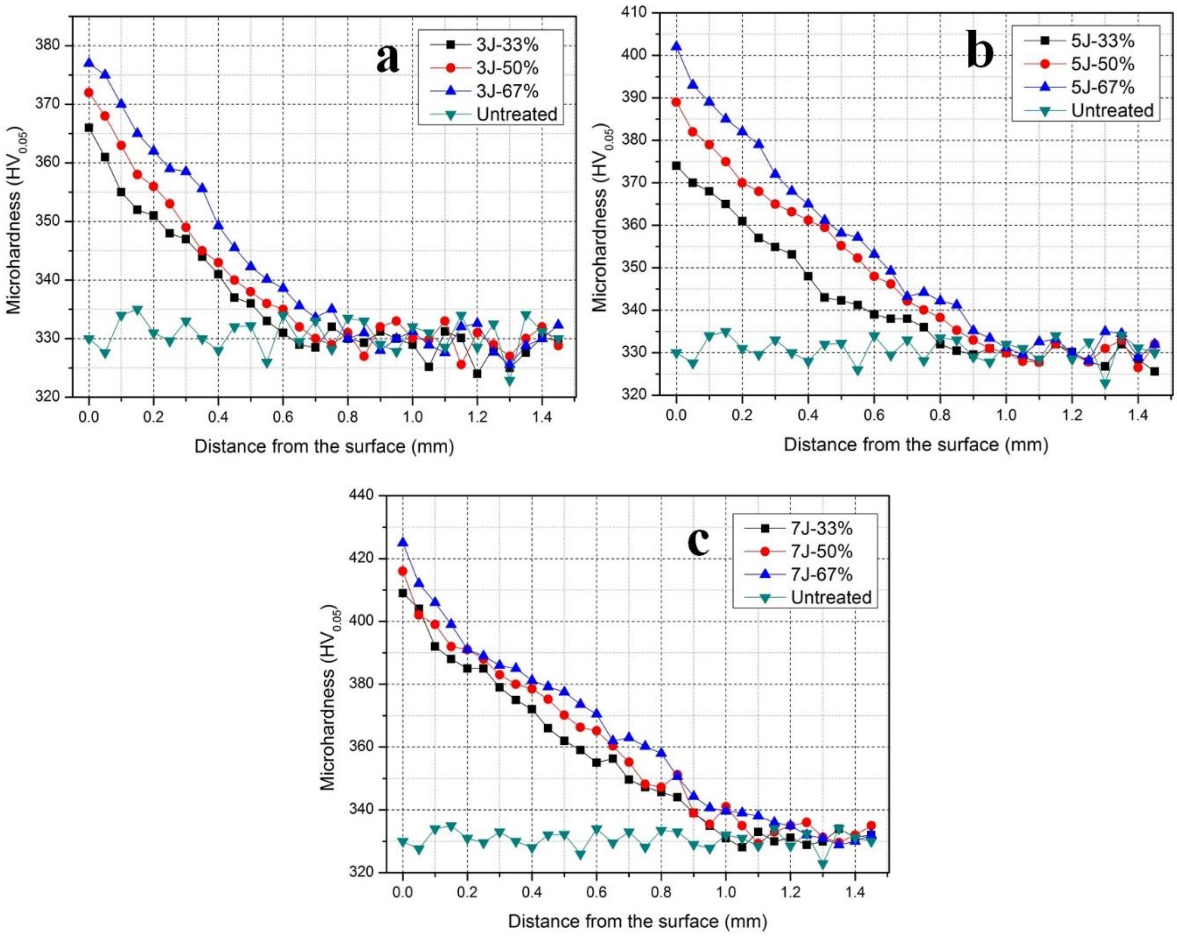

Figure 8.3 Illustration of the cross-sectional microhardness distributions by keeping the laser energy constant at 3J (a), 5J(b) and 7J(c).

8.4 Fretting wear behaviour in simulated body fluid

8.4.1 Fretting wear behaviour

Figure 8.4 to 8.6 shows the COF *versus* number fretting wear cycles of Ti-6Al-7Nb alloy before and after LSP in SBF. All curves (Figure 8.4a, 8.5a and 8.6a) are similar which are characterized by an initial run-in stage with a sharp increase, followed by a steady-state regime. As shown in Figure 8.4b, 8.5b and 8.6b, it was found that in the run-in step, the untreated curve increases faster than that of LSPned curves. This can be attributed to the surface hardness induced by LSP. A low COF indicated an easy sliding of two contacting bodies. However, with the increasing number cycles of fretting wear, there is no obvious difference amongst the untreated and LSPned samples in 3J and 5J groups (Figure 8.4c and 8.5c) when they gradually stabilized in the steady-state step. As present in the microhardness section, the surface harden depth after 3J and 5J LSP is comparatively shorter than that of 7J What is more, although surface harden is induced by LSP, the surface roughness is also increased which is detrimental

to the wear resistance. Once the cycles are more than certain values, the surface harden layer of 3J and 7J samples have already worn out, whereas, the worn surface is the matrix and that is why COFs of the LSPned is very closed to the untreated.

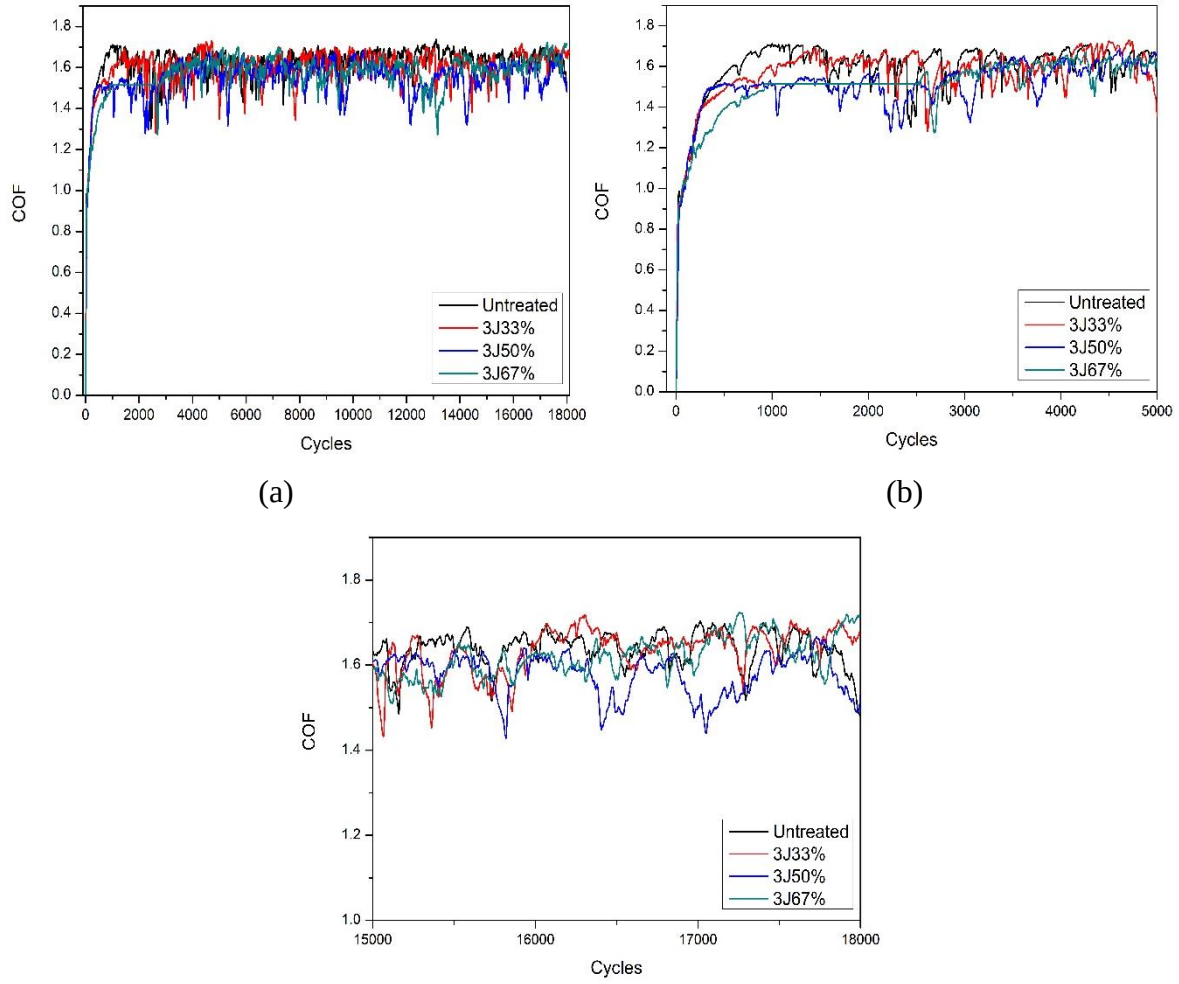

Figure 8.4 Comparative plot showing the friction coefficients (COF) *vs* number of cycles for Ti-6Al-7Nb alloy before and after laser shock peening in 3J,33%; 3J50%; 3J67% (a); the magnified run-in stage in (b); the magnified steady-state step in (c)

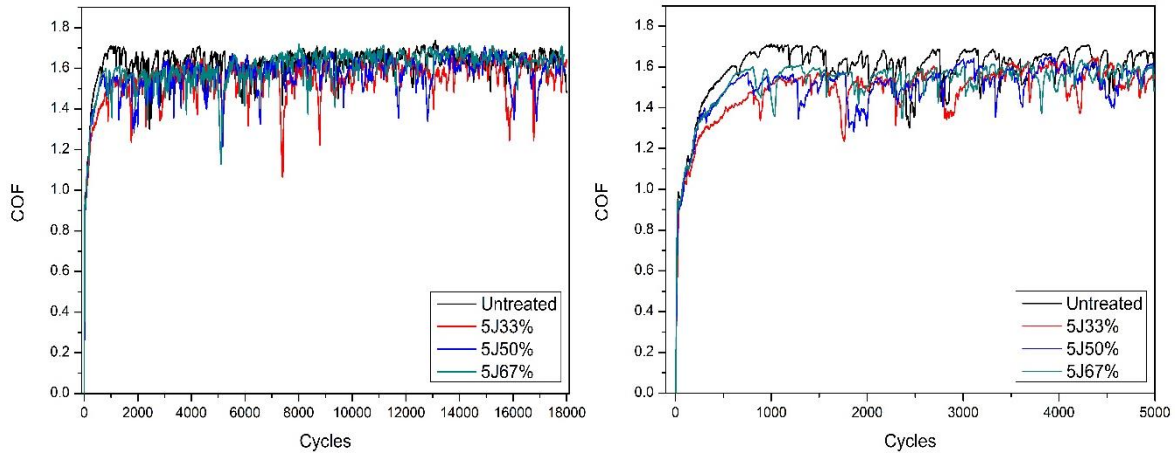

(a) (b)

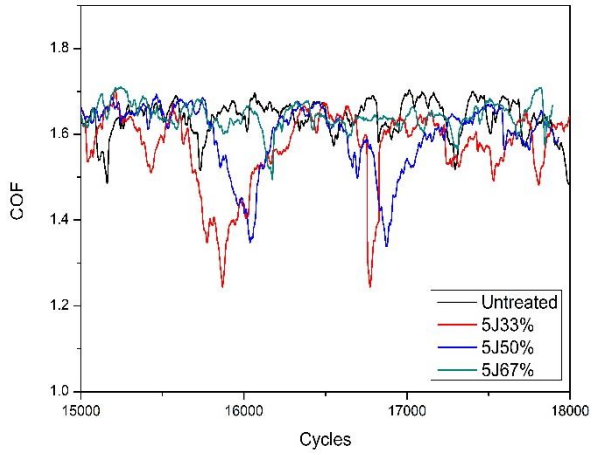

(c)

Figure 8.5 Comparative plot showing the friction coefficients (COF) *vs* number of cycles for Ti-6Al-7Nb alloy before and after laser shock peening in 5J,33%; 5J50%; 5J67% (a); the magnified run-in stage in (b); the magnified steady-state step in (c)

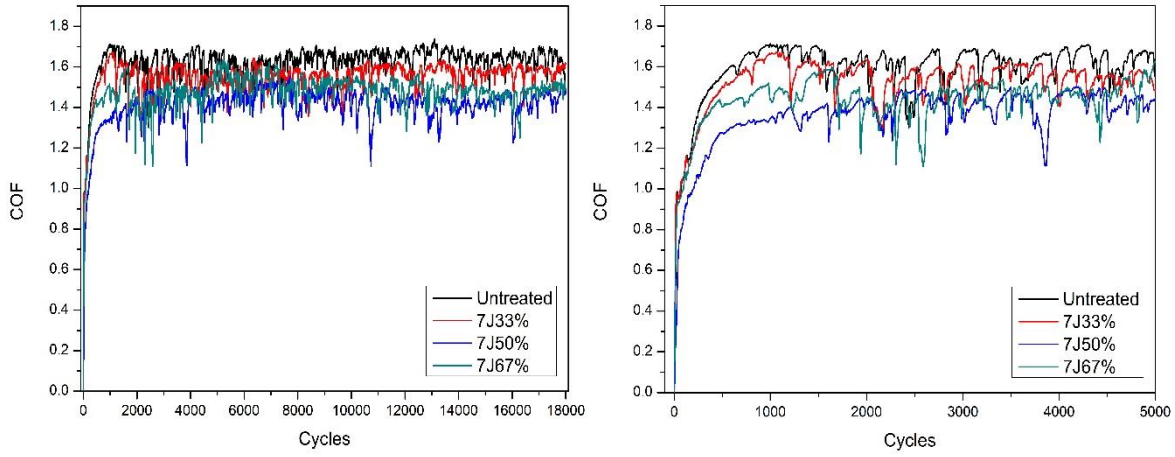

(a) (b)

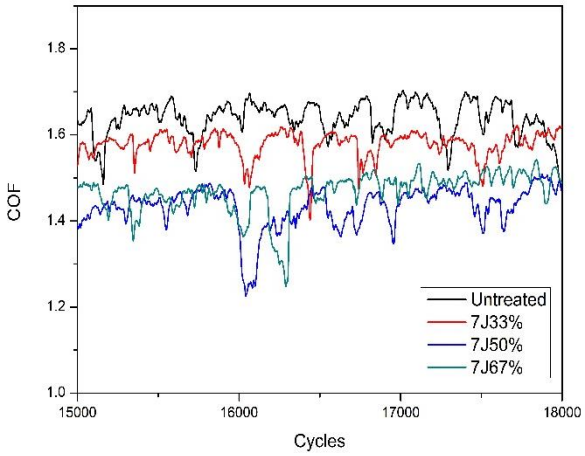

(c)

Figure 8.6 Comparative plot showing the friction coefficients (COF) *vs* number of cycles for Ti-6Al-7Nb alloy before and after laser shock peening in 7J,33%; 7J50%; 7J67% (a); the magnified run-in stage in (b); the magnified steady-state step in (c)

When it comes to 7J groups (Figure 8.6a), at the run-in stage (Figure 8.6b), COFs of untreated also increased higher than that of the LSPned samples. However, in the steady-state step, we can see that the average of COFs of LSPned samples are all lower than that of untreated. In addition, the gradient decreasing sequence can be observed that the sequence is 7J, 33%>7J, 50%≈7J, 67%.

COFs of 7J, 50% and 7J, 67% are comparatively close to each other. What is more, the wear volume loss of Ti-6Al-7Nb samples before and after LSP are calculated with maximum worn depth and presented in Figure 8.7. The wear volume loss of the untreated surface is 5.72×10^{-3} mm^3. In comparison to the untreated surface, 5J, 33% lost the maximum volume amongst all the LSPned samples with a value of 8.23×10^{-3} mm^3, followed by 3J, 50%, (7.01×10^{-3} mm^3), then 3J, 67% (7×10^{-3} mm^3) and finally 3J, 33% (6.89×10^{-3} mm^3) that the wear volume loss are higher than that of the untreated. Once the laser energy and overlap are increased to 5J, 50%, the wear resistance effect of LSP start to show. Marked by blue in the Figure 8.7 which values are lower than that of the untreated surface, 7J, 50% experienced the minimum volume loss (3.2×10^{-3} mm^3), onward is 5J, 67% (3.67×10^{-3} mm^3), 7J, 33% (4.12×10^{-3} mm^3),7J, 67% (4.34×10^{-3} mm^3) and 5J, 50% (5.06×10^{-3} mm^3). It is well-known that beneficial characteristics such as surface hardness and microstructural refinement are induced after LSP surface treatment for improving wear resistance, but the surface roughness is also increased which is detrimental to wear performance. Although, the surfaces are hardness and the average size of

sub-grains are minimised, the wear volume loss is still higher after the LSP. This is because of the increase of surface roughness after LSP. In addition, the wear volume loss of sample 5J, 33% is comparative close to the one of the untreated sample. Therefore, it can be considered as a neutralised result among roughness (negative to the wear resistance), surface hardness and microstructure refinement (positive to the wear resistance).

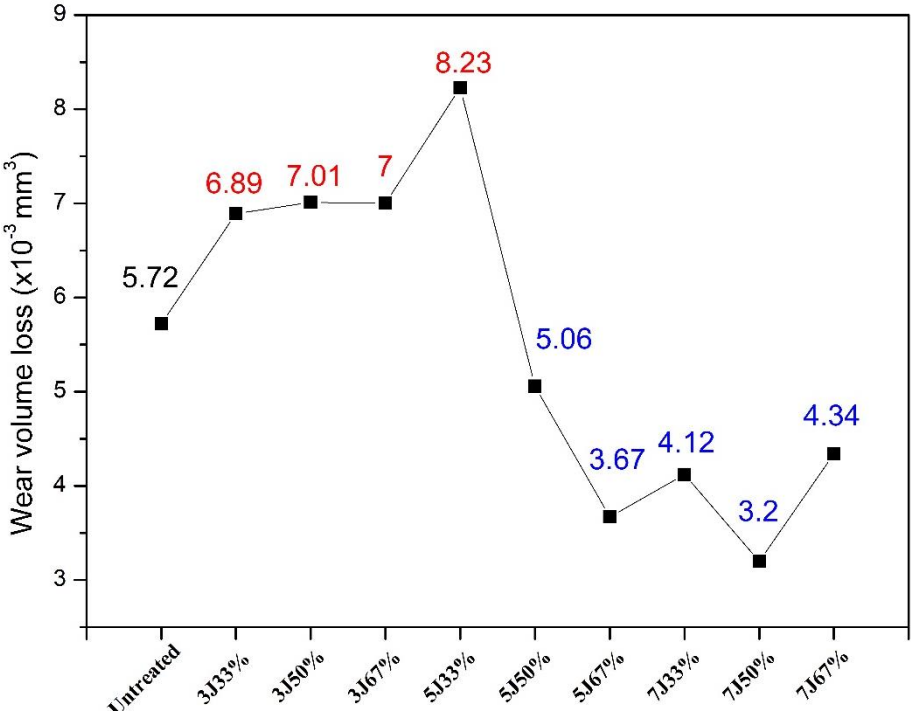

Table 8.7 The plot showing wear volume loss of Ti-6Al-7Nb alloy before and after laser shock peening.

8.4.2. The worn surfaces

Figure 8.8 shows the appearance of fretted scars on Ti-6Al-7Nb before and after LSP. According to the worn surfaces, Ti-6Al-7Nb samples can be divided into 3 categories which are 1) the untreated and treated at 5J, 50%; 2) 3J, 33%, 3J, 50%, 3J, 67% and 5J, 33%; 3) 5J, 67%, 7J, 33%, 7J, 50% and 7J, 67%. This is consistent with the wear volume loss. As shown in Figure 8.8a and 8.8f, the ploughing wear mechanism dominated in the wear process of the untreated and 5J, 50%. In the high magnification images, the micro-ploughing and spalling features on the abraded surfaces can be seen. With respect to the samples 3J, 33%, 3J, 50%, 3J, 67% and 5J, 33%, the worn surfaces exhibited much more severe wear among the others. Extensive debris, grooves, material adhesions and delamination can be found after the adhesive and abrasive wear along the sliding wear direction. Although the hardness surface layer in LSPned samples benefited the wear resistance, the peak-and-valley surface topography

induced by LSP facilitated the removal of the top material off the surface. Compared to that, as shown in Figure 8.8 g-j, 5J, 67%, 7J, 33%, 7J, 50% and 7J, 67% exhibit less wear in the SBF as the surface hardening at least is increased to 400 $HV_{0.05}$ which enable them to get better performance in wear resistance. From the worn SEM images, adhesion and abrasive wear still co-existed on the worn surfaces as the adhesion material, spalling, and delamination can be found. However, the delamination area ratio is proportional to the wear volume loss. Especially in 7J, 50%, from the SEM image, the wear scar consists of most delamination and less adhesion material. Therefore, it can be seen that the delamination wear is the main wear mechanism.

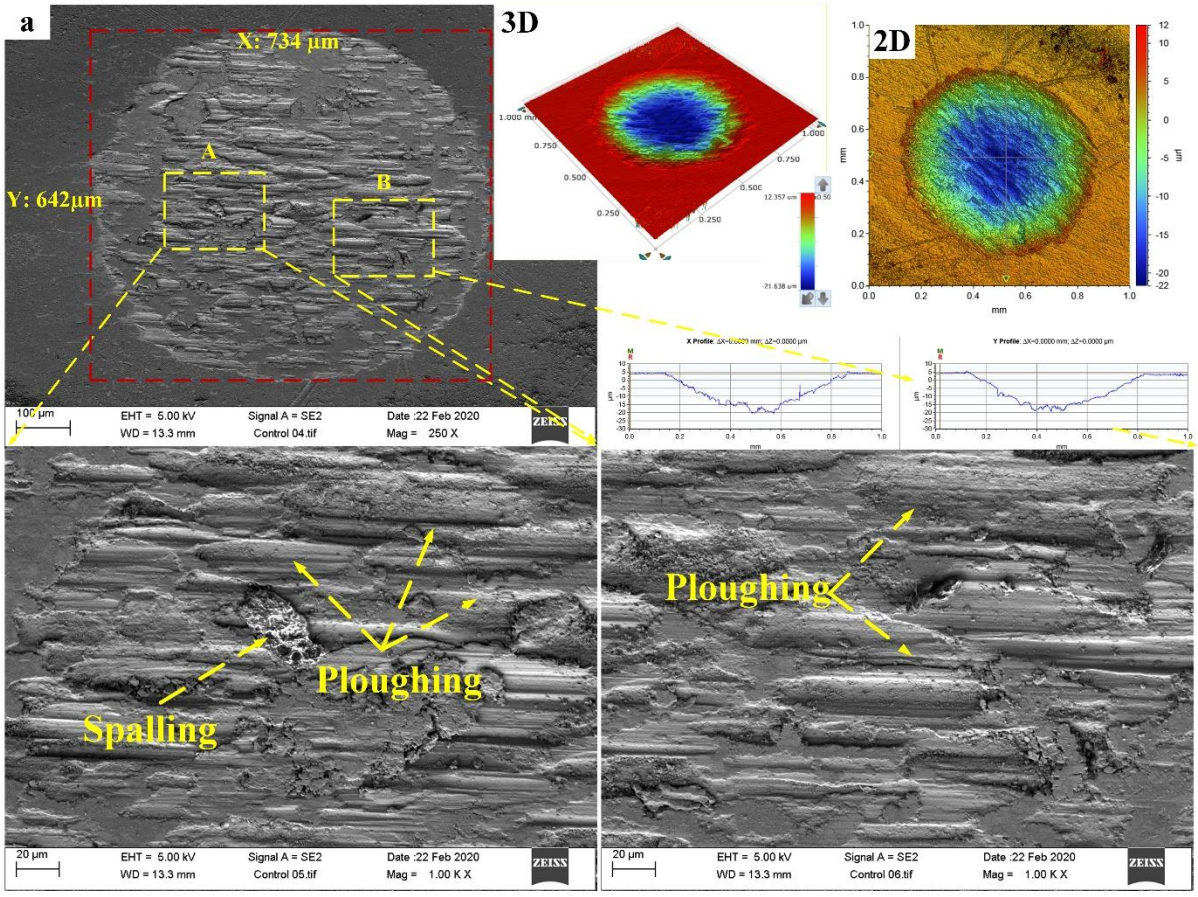

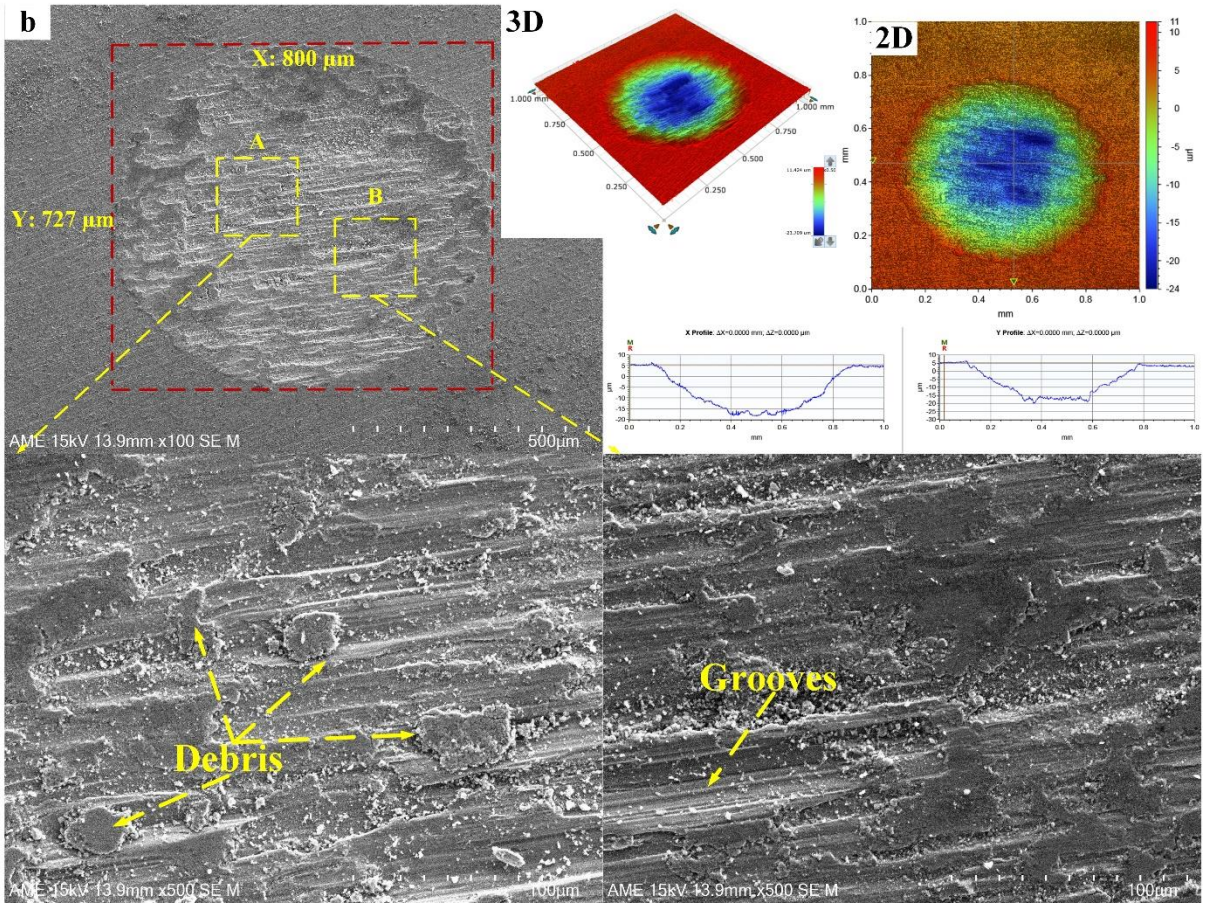
b
X: 800 µm
Y: 727 µm
A
B
3D
2D
AME 15kV 13.9mm x100 SE M
500µm
Debris
Grooves
AME 15kV 13.9mm x500 SE M
100µm

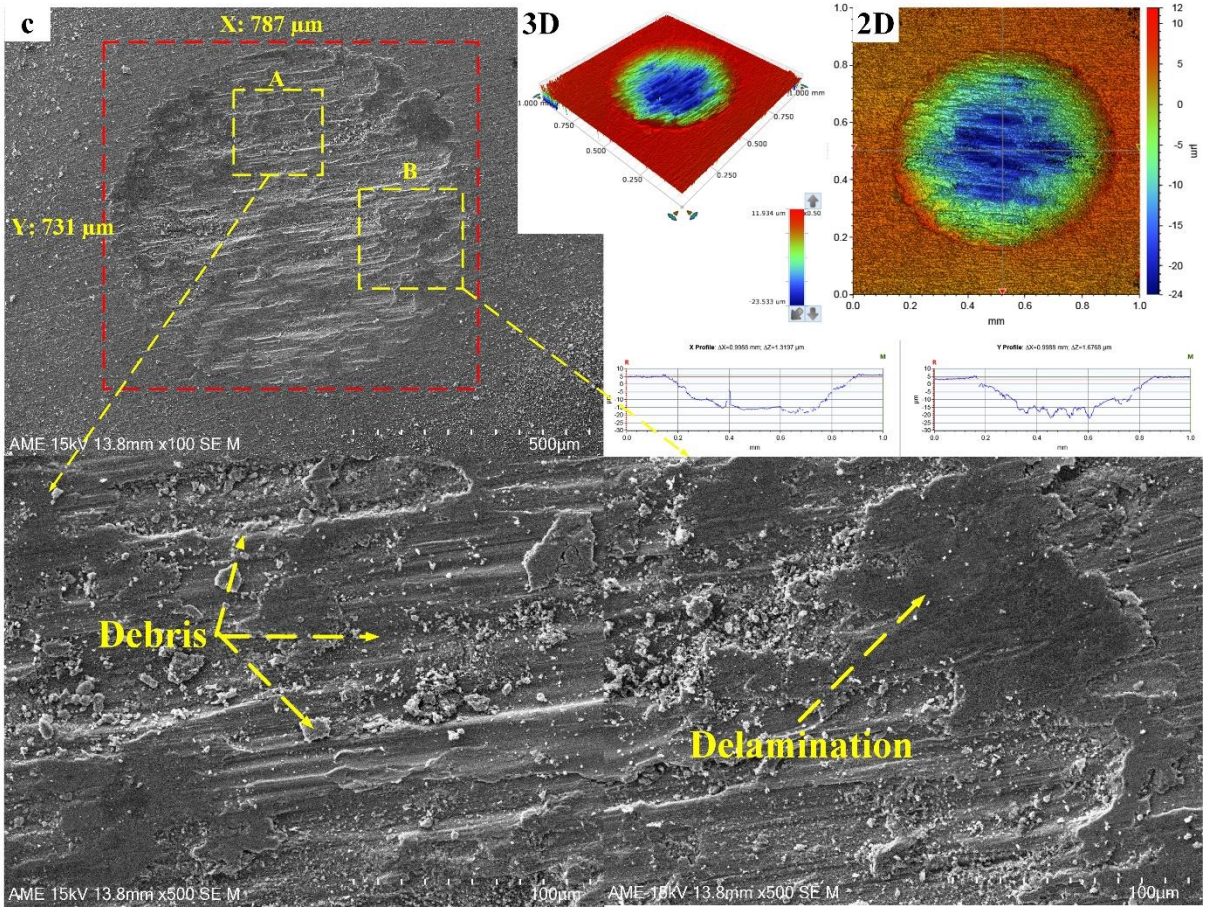
c
X: 787 µm
Y: 731 µm
A
B
3D
2D
AME 15kV 13.8mm x100 SE M
500µm
Debris
Delamination
AME 15kV 13.8mm x500 SE M
100µm

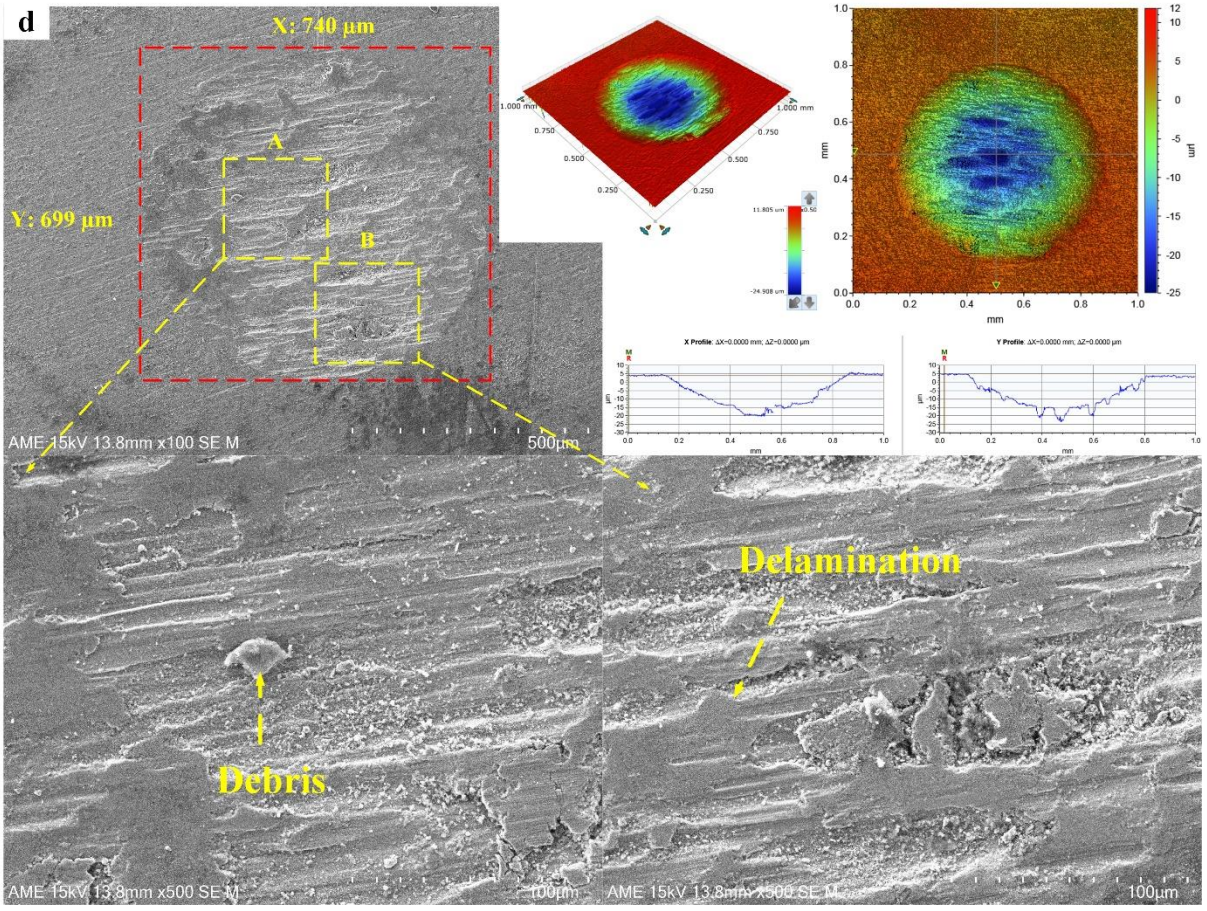
d
X: 740 µm
Y: 699 µm
A
B
AME 15kV 13.8mm x100 SE M
500µm
Debris
Delamination
AME 15kV 13.8mm x500 SE M
100µm
AME 15kV 13.8mm x500 SE M
100µm

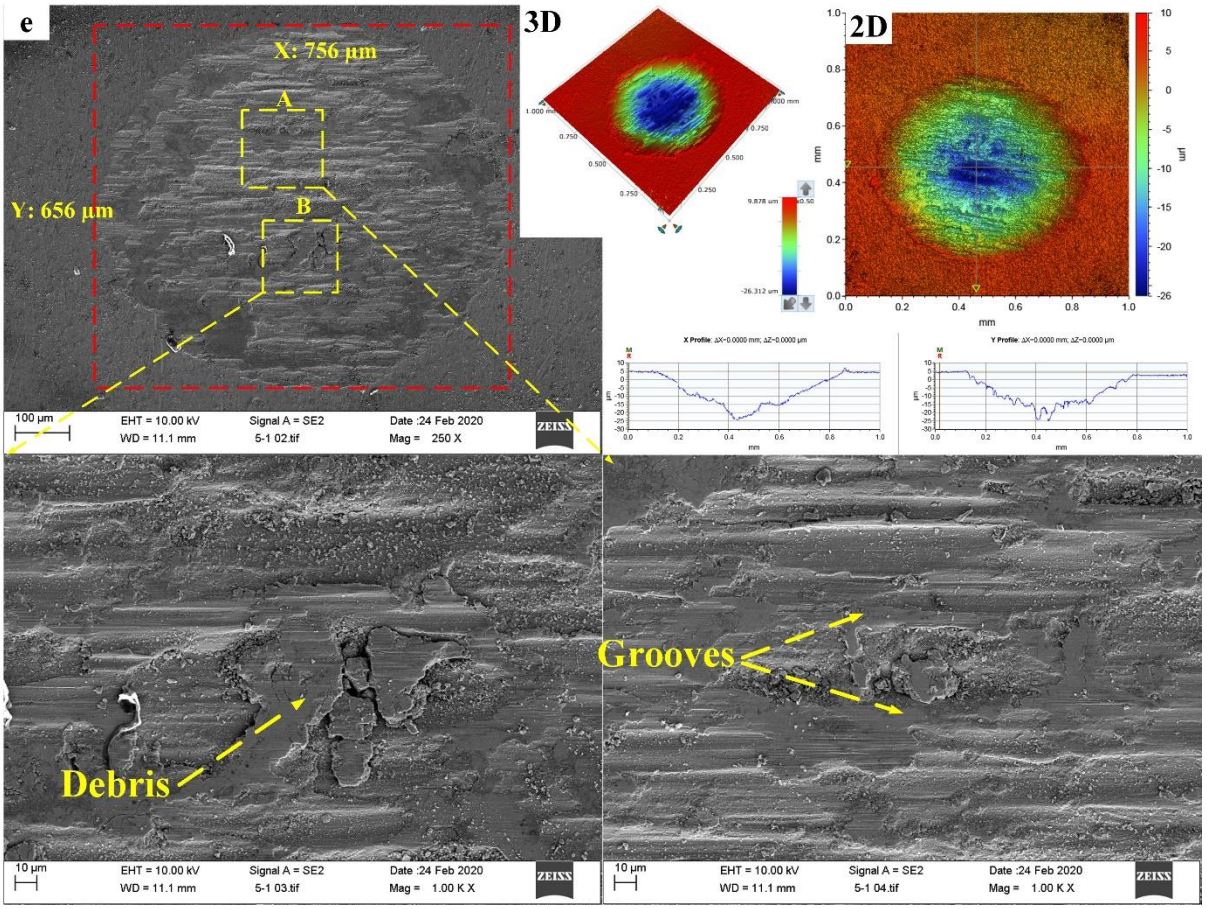
e
X: 756 µm
Y: 656 µm
A
B
3D
2D
100 µm
EHT = 10.00 kV
WD = 11.1 mm
Signal A = SE2
5-1 02.tif
Date :24 Feb 2020
Mag = 250 X
ZEISS
Debris
Grooves
10 µm
EHT = 10.00 kV
WD = 11.1 mm
Signal A = SE2
5-1 03.tif
Date :24 Feb 2020
Mag = 1.00 K X
ZEISS
10 µm
EHT = 10.00 kV
WD = 11.1 mm
Signal A = SE2
5-1 04.tif
Date :24 Feb 2020
Mag = 1.00 K X
ZEISS

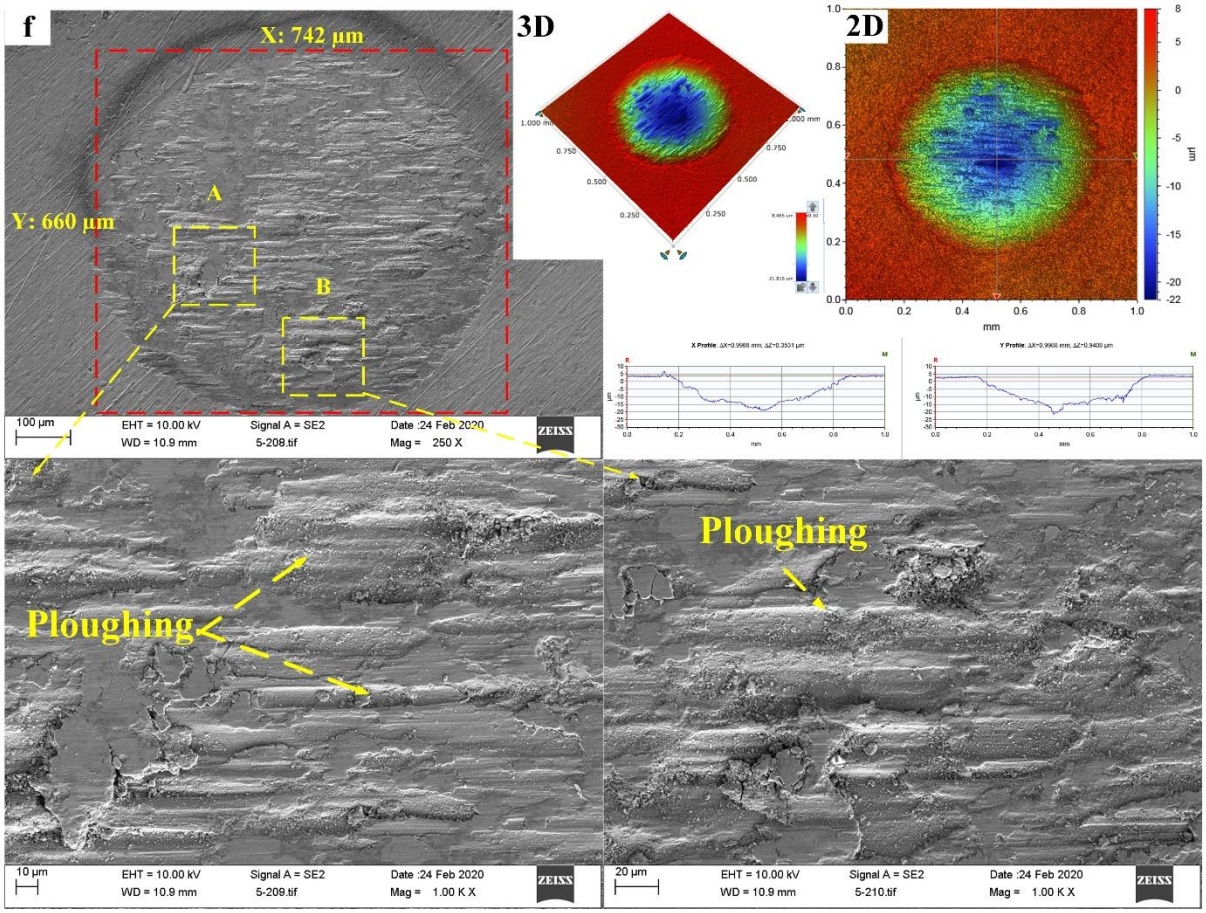
f
X: 742 µm
Y: 660 µm
A
B
3D
2D
mm
µm
Ploughing
Ploughing
100 µm
EHT = 10.00 kV
WD = 10.9 mm
Signal A = SE2
5-208.tif
Date :24 Feb 2020
Mag = 250 X
10 µm
EHT = 10.00 kV
WD = 10.9 mm
Signal A = SE2
5-209.tif
Date :24 Feb 2020
Mag = 1.00 K X
20 µm
EHT = 10.00 kV
WD = 10.9 mm
Signal A = SE2
5-210.tif
Date :24 Feb 2020
Mag = 1.00 K X
ZEISS

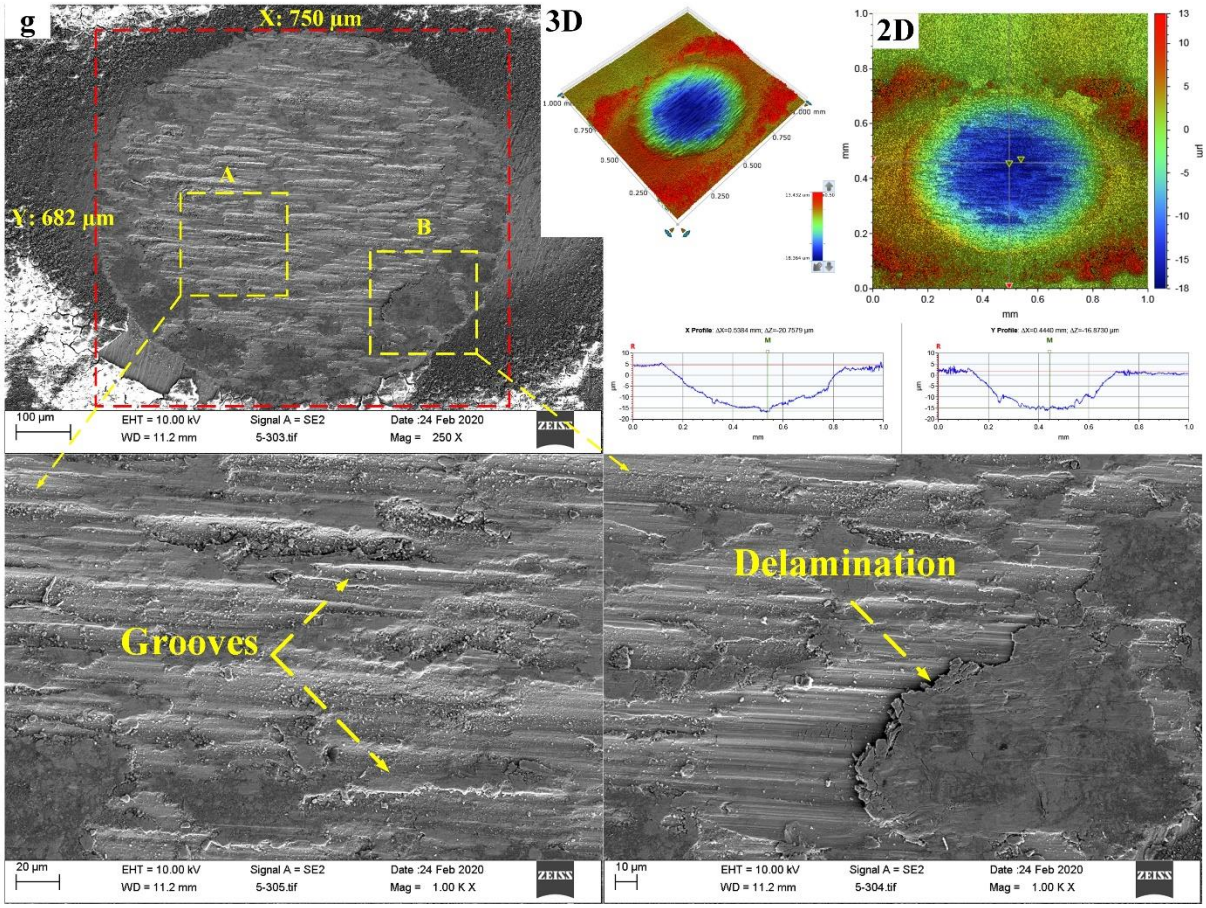
g
X: 750 µm
Y: 682 µm
A
B
3D
2D
mm
µm
Grooves
Delamination
100 µm
EHT = 10.00 kV
WD = 11.2 mm
Signal A = SE2
5-303.tif
Date :24 Feb 2020
Mag = 250 X
20 µm
EHT = 10.00 kV
WD = 11.2 mm
Signal A = SE2
5-305.tif
Date :24 Feb 2020
Mag = 1.00 K X
10 µm
EHT = 10.00 kV
WD = 11.2 mm
Signal A = SE2
5-304.tif
Date :24 Feb 2020
Mag = 1.00 K X
ZEISS

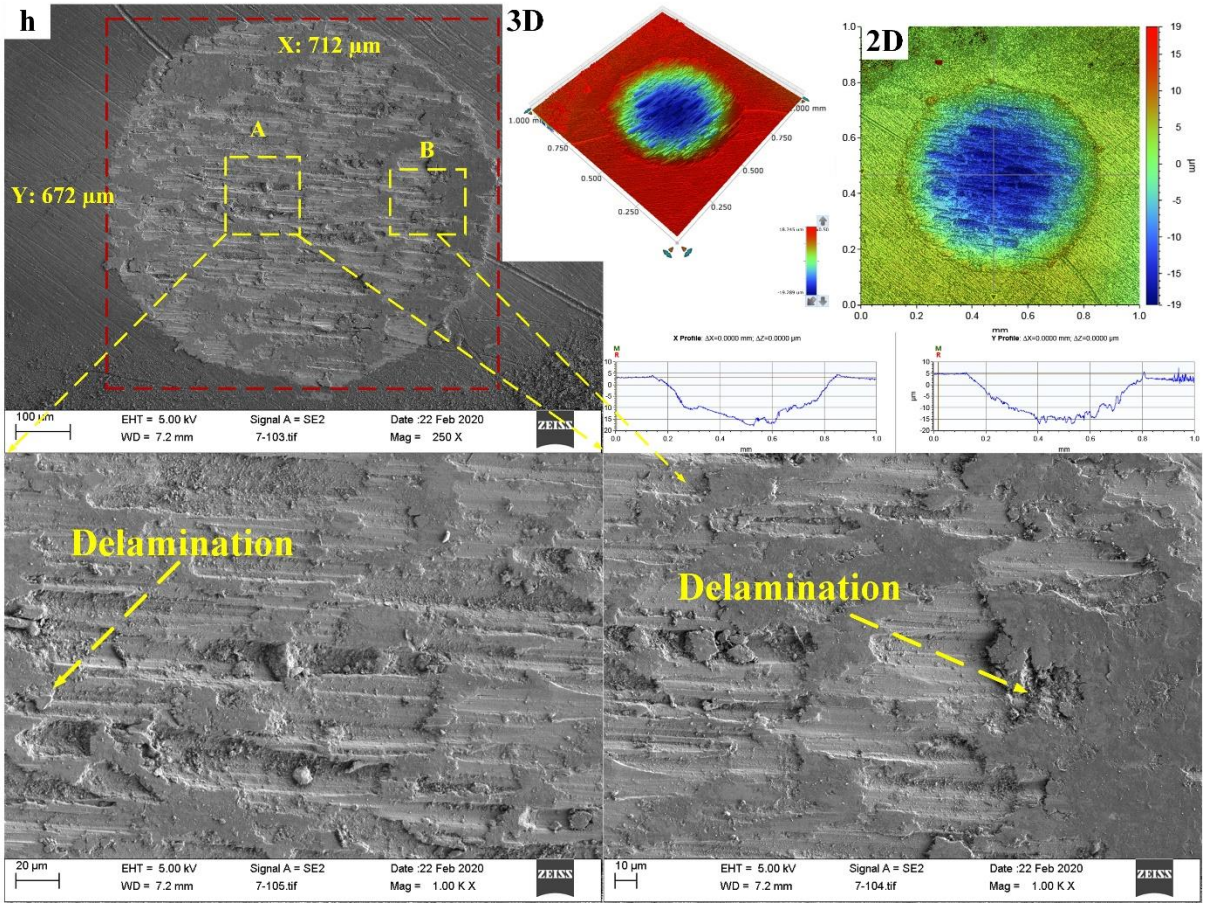
h
X: 712 µm
Y: 672 µm
A
B
3D
2D
Delamination
Delamination
100 µm
EHT = 5.00 kV
WD = 7.2 mm
Signal A = SE2
7-103.tif
Date :22 Feb 2020
Mag = 250 X
20 µm
EHT = 5.00 kV
WD = 7.2 mm
Signal A = SE2
7-105.tif
Date :22 Feb 2020
Mag = 1.00 K X
10 µm
EHT = 5.00 kV
WD = 7.2 mm
Signal A = SE2
7-104.tif
Date :22 Feb 2020
Mag = 1.00 K X

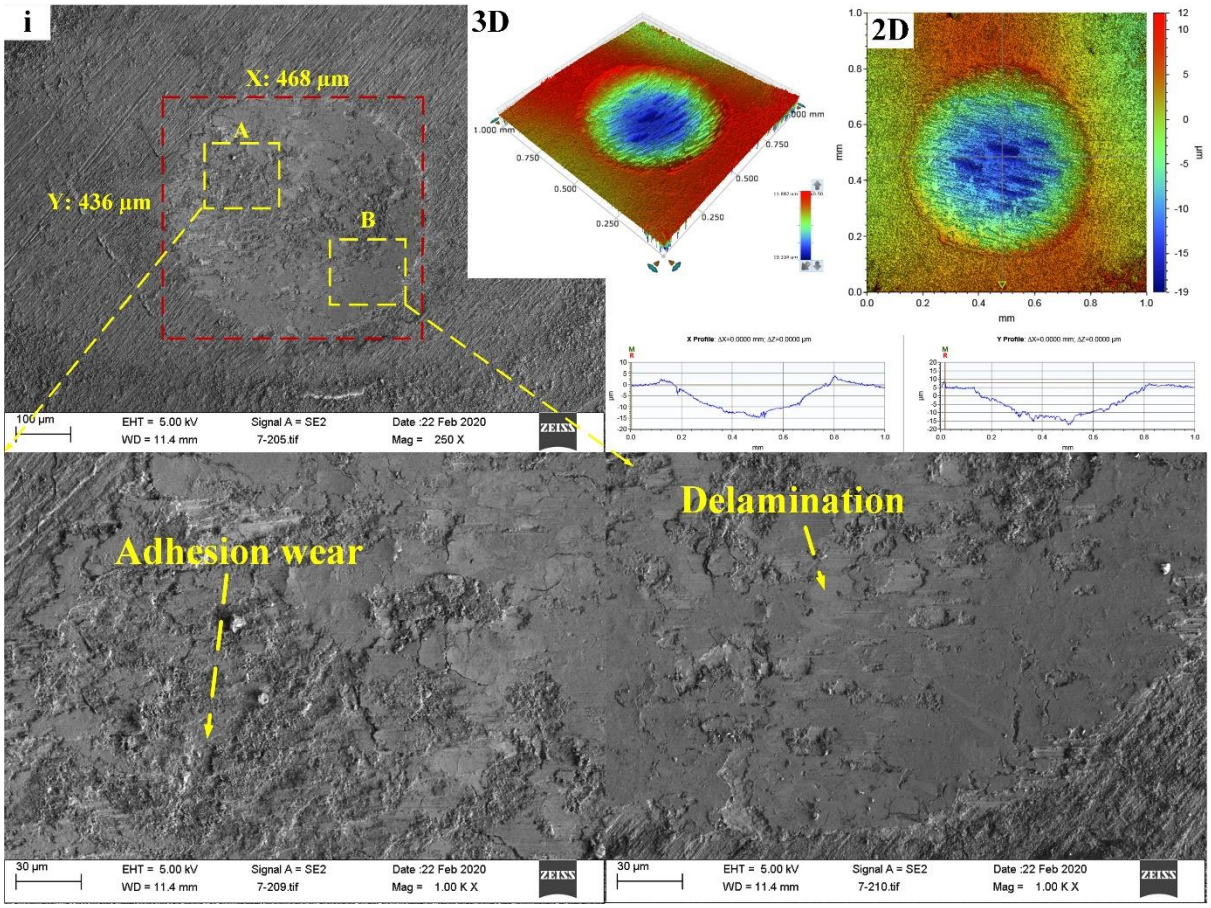
i
X: 468 µm
Y: 436 µm
A
B
3D
2D
Adhesion wear
Delamination
100 µm
EHT = 5.00 kV
WD = 11.4 mm
Signal A = SE2
7-205.tif
Date :22 Feb 2020
Mag = 250 X
30 µm
EHT = 5.00 kV
WD = 11.4 mm
Signal A = SE2
7-209.tif
Date :22 Feb 2020
Mag = 1.00 K X
30 µm
EHT = 5.00 kV
WD = 11.4 mm
Signal A = SE2
7-210.tif
Date :22 Feb 2020
Mag = 1.00 K X

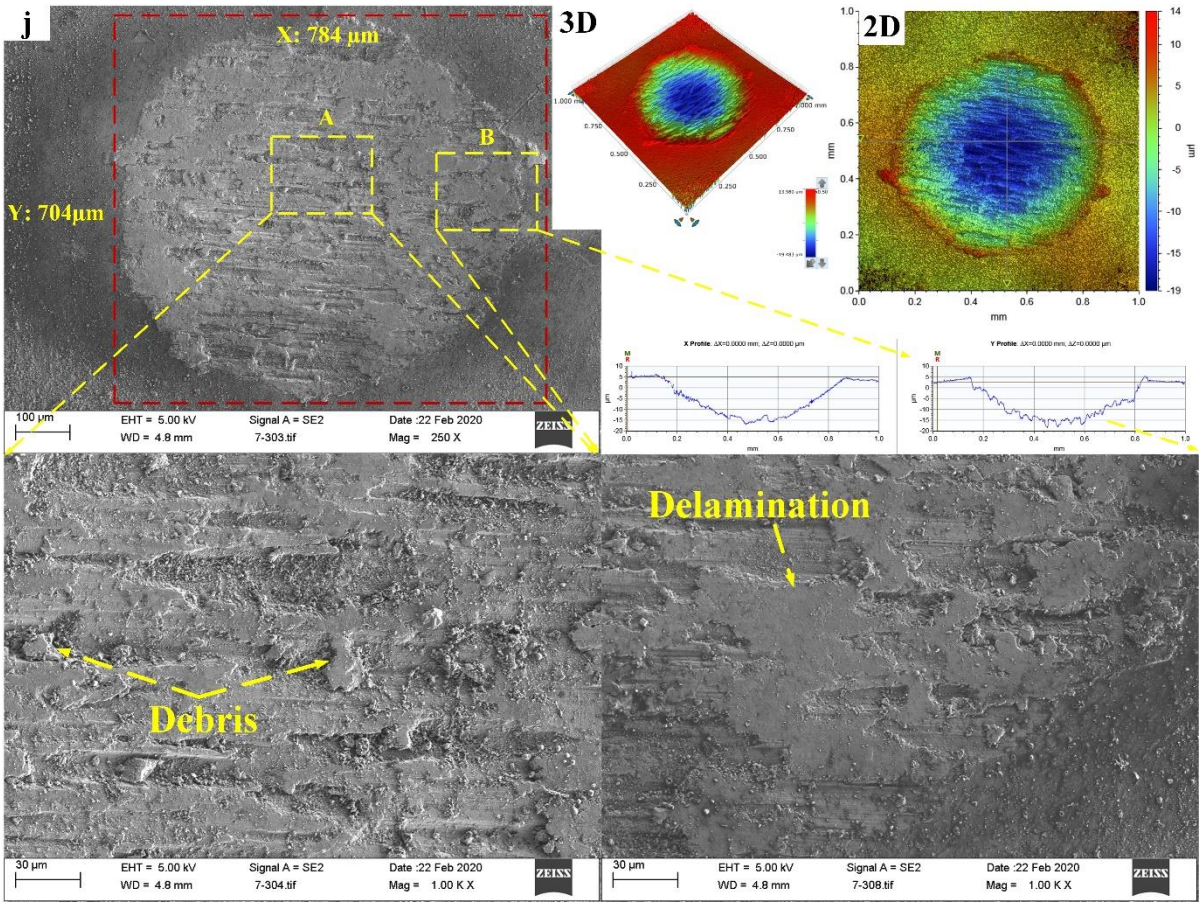

Figure 8.8 SEM and 3-D profiling maps showing the wear scar of Ti-6Al-7Nb alloy prior to and after LSP: (a) the untreated surface; (b) at 3J, 33%; (c) at 3J, 50%; (d) at 3J, 67%; (e) at 5J, 33%; (f) 5J, 50%; (g) 5J, 67%; (h) 7J, 33%; (i) 7J, 50% and (j) 7J, 67%.

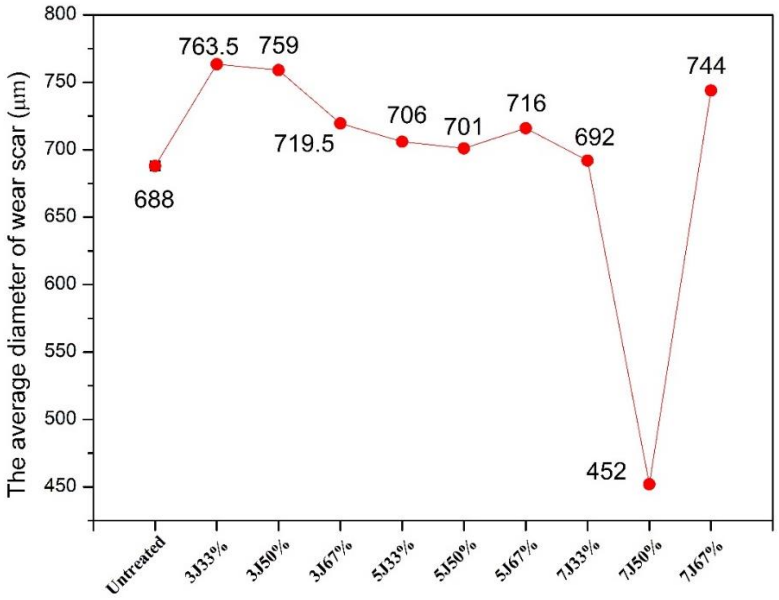

Figure 8.9 The plot showing the average diameter of wear scar for Ti-6Al-7Nb alloy before and after laser shock peening.

In general, the diameter of the wear scar is proportional to the wear scar depth as shown in Figure 8.9. However, some samples such as 3J, 67% and 5J, 33% are not consistent with that trend. This may be due to the FBS environment. The fretting wear is a process that the removal of the passive oxide layer exposing the metallic surfaces, thereby, undergoing anodic dissolution. As such, the wear scar acts as a cathode. The body simulated solution aggravates the anodic dissolution and material removal during the wear process. What is more, in the present study, the wear results is a neutralisation result among surface roughness, surface hardness and the microstructural refinement. In terms of wear scar depth, limited surface hardening with low surface roughness may not be worse than higher surface hardening with higher surface roughness. That is why the two set of parameters in the middle exhibit the maximum wear scar depth.

8.5 Summary

In this chapter, the microhardness and fretting wear tests prior to and after LSP Ti-6Al-7Nb alloy were carried out. The conclusions were summarised as follows:

- The surface was hardened after LSP. Laser energy and overlap were proportional to microhardness at the near-surface.
- LSP parameters of 5J, 67%, 7J, 33%, 7J, 50% and 7J, 67% have effects in improving the wear resistance in SBF while parameters of 3J, 33%, 3J, 50%, 3J, 67% and 5J, 33% could aggravate the implant failure due to wear.
- LSP induced surface roughness is detrimental to the wear resistance of Ti-6Al-7Nb alloy, if the surface hardening effect is not enough.

Chapter 9 Effects of Multiple Laser Shock Peening on the Wear Properties Ti-6Al-7Nb Alloy

This chapter is focused on Laser Shock Peening (LSP) of Titanium alloy (Ti-6Al-7Nb) for the first-time. This was to improve upon the artificial implant failures caused by destitute wear resistance of titanium alloys. As such, millions of patients are suffering from osteoarthritis pain, which costs billions of pounds annually to end-users as they either have to undergo a complete replacement of the particular implants or a second surgery subject to implant failures. Therefore, the effect of multiple impacts on the mechanical properties and sliding wear behaviour of Ti-6Al-7Nb subjected to LSP were investigated. Ti-6Al-7Nb has the advantage of biocompatibility as the material can be applied for orthopaedic implants. It is critical to improve mechanical properties and wear resistance. LSP is one of the most effective methods to improve mechanical properties. Thus, in this study, X-ray Diffraction (XRD); Scanning Electron Microscope (SEM); Surface roughness using 3-D profiling; microhardness using Vickers indentation method; and sliding wear with a tribometer were employed to measure the effect of Ti-6Al-7Nb alloy subjected LSP.

9.1 Introduction

Titanium alloys are widely used as biomedical implant materials for failed hard tissues, due to their favourable properties in corrosion resistance, biocompatibility, microhardness, and strength [7, 46, 252, 253]. Currently, the most applied titanium implant alloy is Ti-6Al-4V (TC4) [164], but elements such as vanadium (V) is found to be released within the body from Ti-6Al-4V. With that said, niobium is un-toxic for human body environment and due to its biocompatibility, V-free Titanium alloy such as Ti-6Al-7Nb alloy [254] was therefore developed for the biomedical implants. Thus, Ti-6Al-7Nb has been widely used due to its advantage biocompatibility, mechanical properties.

As the artificial implants were used to replace the diseased or damaged structures to restore its form and function, Ti-6Al-7Nb alloy was required to comprise of a combination of mechanical strength, corrosion resistance and excellent biological properties. In order to acquire better mechanical and biological properties, several researchers in recent years have adopted surface modification methods to refine the implant materials. Those surface modifications were namely: apatite deposition [255], chemical treatments [256], and severe plastic deformation (SPD). Mhaede *et al.,* [257] evaluated the influence of a surface pre-treatment by shot peening (SP), and SP + coating on the corrosion properties of magnesium alloy AZ31, the result showed that

SP followed by coating improved hardness, surface roughness and corrosion resistance. Ahmed *et al.,* [258]investigated the effects of different shot peening parameters, such as shot size, Almen intensity and percentage of coverage, on the surface micro-hardness, roughness and residual stress of ALSI 316L. Strasky *et al.,* [259] develop a combined treatment including electric discharge machining (EDM), acid etching and SP to create a superimposed microstructure. This provided a better surface for osteoblast proliferation. Kikuchi *et al.,* [260]found that Fine Particle Peening (FPP) using Hydroxyapatite (HAp) shot particles can form a Hap surface layer and improve the fatigue properties of commercially pure (CP) titanium. In order to improve the wear resistance of TC11 alloy, Hong *et al.,* [261]coated TiN/Zr-base amorphous-nanocrystalline composition coating on the metal surface of TC11 alloy with electro-spark deposition (ESD). The results showed that Ti/Zr-base amorphous-nanocrystalline surface coating could effectively improve the wear resistance of TC11 alloy under high loading friction conditions. On the other hand, Sealy *et al.,* [262]found that sequential LSP of a biodegradable Mg-Ca alloy was initiated to create better surface integrity for improving implant's mechanical properties. What is more, Mannava *et al.,* [163]reviewed the fatigue strength of spinal implant made from Ti-6Al-4V ELI using Laser Shock Peening which ultimately to reduced and eased the back pain of the end user.

LSP is an innovative surface modification technique which has been widely used to improve the defects, performance and in turn the quality of mainly aviation components. LSP is able to improve the mechanical properties such as fatigue lives, anti-corrosion, wear resistance and modify the surface metal with using short pulse (nanosecond), high peak power density (GW/cm^2) laser beam, rapidly vaporizing the absorbed layer to generate high-pressure plasma, forming compressive residual stress layer on the metal surface [113]. LSP can be seen as a cold work harden technique as the surface average grain size is reduced to a smaller level than it before. Therefore, surface microhardness can also be strengthened which could benefit the improvement of the wear resistance.

According to the British National Joint 2016 report [14], a total of 20926 of 796636 patients had a first revision (second surgery due to the implant failures—usually up to 10 years). In addition, the adverse soft tissue reaction to particulate debris (3548, a figure may be underestimated) was the third most common reason for a revision. What is more, when people age, the second revision implant surgery risk and the added cost of surgery which the patients endure, will be much more than primary surgery. Some of them cannot even take the risk of

undergoing a second revision surgery due to the patient's poor physical condition. Thus, a solution to this issue is the use of alternative alloy, in particular, Ti-6Al-7Nb which is vanadium-free and is one of the few metals that human bones are able to grow solidly around. Therefore, in order to prolong the operational life of prosthetic implant made from Ti-6Al-7Nb, and ensure the patients endure only one time surgery, it is important to determine techniques that help to prolong the implant service time. And it is the first-time that LSP was employed to improve the mechanical properties of this particular grade of material (Ti-6Al-7Nb) as no previous attempt was made to conduct LSP surface treatment of such a useful grade of titanium alloy. On account of this, we have attempted to investigate the specific effects of LSP on microstructure, micro-hardness, surface roughness and sliding wear behaviours of the orthopaedic Ti-6Al-7Nb. This will develop the understanding of the laser material interaction with a view to providing an advanced surface engineering process for the future generation of titanium based orthopaedic implants made from a biocompatible metal namely Ti-6Al-7Nb.

9.2. Materials and Methods

9.2.1 Details of Ti-6Al-7Nb alloy and sample preparation

The Ti-6Al-7Nb samples were cut into φ25mm x 8mm, polished from 300 to 2000 grit size, SiC abrasive paper in stages until the material comprised of Sa (Arithmetic mean height) 0.16 μm surface finish. It is widely used to the prosthetic implant to relieve patient pain. The Ti-6Al-7Nb titanium alloy belongs to the group of α/β alloys. It is seen that the cross-sectional microstructure consists of globular and acicular α grains within the β-transformed matrix, shown in Fig 1. Regards to the titanium etching methods, due to the toxic and pollution of hydrofluoric acid, Phosphoric acid method was employed for SEM observation samples in this study. The dimensions for SEM and metallographic samples are 10mm × 10mm. These were wet-abraded with 2000 grit SiC abrasive paper and sonicated in deionized water, washed with acetone and dried in room temperature. Thereafter, the surface etching acid etching was carried out by immersion of 100ml beaker in 30ml concentrated phosphoric acid at 80℃ for 20mins in the fume hood. The mechanical properties of Ti-6Al-7Nb alloy were shown in Table 9.1 .

Table 9.1 Showing the mechanical properties of the Ti-6Al-7Nb

Material	Density (gm/cc)	Modulus of Elasticity (GPa)	Ultimate Tensile Strength (Mpa)	Yield Strength 0.2% (Mpa)	Elongation (%)	Hardness HRC
Ti-6Al-7Nb	4.52	105	959	862	17	30

9.2.2 Laser shock Processing Method

The LSP experiments were conducted by a Q-Switched Nd: YAG laser (LPY10J; Litron, Rugby, UK), using a wavelength of 1064nm and 8ns pulse width. The beam parameter product M^2 was >2, with a top hat profile, and a divergence value of 0.5 mrad. The pulse energy was 6.5 J; the laser spot diameter was 3 mm. and the power density was 11.5GW/cm^2, which in turn exhibited a radiance density of 1.44 W.mm^2.Sr^{-1}.µm as determined by methodology from previous work [263-266] as detailed in Table.9.2. The LSP experiment overlap was 65%. The water layer was used as the confinement layer, while coating absorb layer was black tape. Figure 9.1 (a) presents (a) a schematic diagram of the process and (b), the pulse overlapping sequence employed.

Table 9.2 LSP parameters employed for the surface treatment of Ti-6Al-7Nb.

Parameters	Value
Pulse energy (J)	6.5
Laser wavelength (nm)	1064
Spot diameter (mm)	3
Number of laser impacts	1-3
Overlapping rate (%)	65
Pulse duration (ns)	8
Radiance Density per pulse (W.mm^2.Sr^{-1}.µm)	1.44

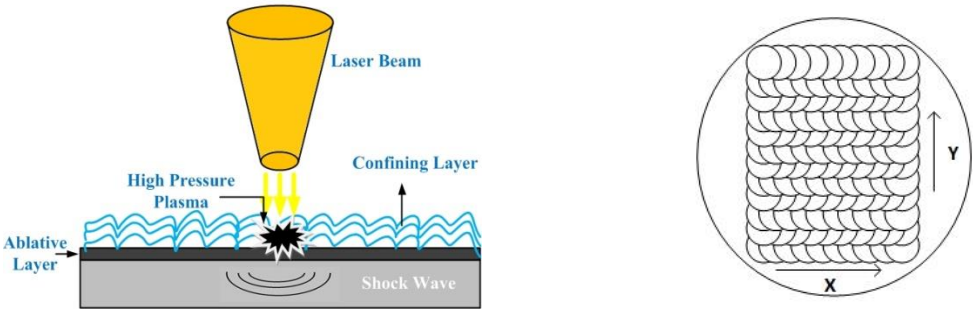

(a) (b)

Figure 9.1 A schematic diagram of the LSP process in (a); (b), the pulse overlapping sequence employed for the LSP surface treatment of Ti-6Al-7Nb.

9.2.3 Characterization Details

9.2.3.1Macro and Microstructural Evaluation

The Optical microscope (x20 Leica, M125, Germany) was employed for Macrostructure observation; The samples were mechanically polished and examined under SEM (TSM3030 Plus, Hitachi, Japan) with an EDS (Energy Dispersive Spectrometer) for Microstructure evaluation at 20kV.

9.2.3.2 Surface roughness

A 3D measuring station motion system (Micromesure2, Polytec, Germany.) was employed to measure surface roughness of Ti-6Al-7Nb alloy treated by x1, x2, x3 LSP impacts and of the as-received surface area. The scan area for surface roughness determination is rectangle 5 × 5 mm^2 and the scan speed is 10μm/s.

9.2.3.3 Hardness Testing

The Edibon hardness tester, with a load of 300gf and a dwell time of 15s, was employed to measure the surface and the cross-sectional Vickers micro-hardness distributions. The measurements were conducted with a spacing of 0.1mm between two successive points using well known methods [267], and *via* Vickers hardness equations (9-1).

$$HV = 0.1891F/D \quad (9\text{-}1)$$

Where HV is the Vickers hardness; F is Loads (N); D is the average value of two indentation diagonals D1 and D2. The indentation footprint made by the diamond indentation was shown in Figure 9.2.

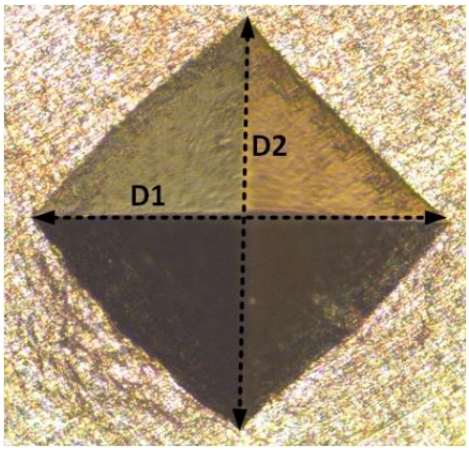

Figure 9.2 A schematic diagram of Vickers micro-hardness.

9.2.3.4 Phase Transformation

The phase evolution analysis of Ti-6Al-7Nb alloy was conducted *via* X-ray diffraction (XRD) equipment (Bruker D8, Germany) with Cu-Kα radiation (wavelength: 0.15418nm) at a scanning speed of 0.01°/s. The generator setting were 40kV and 35mA and the diffraction data were collected over a 2θ range of 20° to 80°, a counting time of 2s/step.

9.2.3.5 Slide Wear Test

The wear tests were performed on the Pin-on-Disk tribometer (CSM, Swiss). The tribometer configurations was Pin-on-flat that the hardened steel ball was employed as a pin on a flat plate rotating in the diameter of 7mm, running for 100m in the room temperature(20℃). There is Load (5 N) on the plate.

9.3 Results

9.3.1 Microstructure observations of Ti-6Al-7Nb

9.3.1.1 Metallographic observations

Figure 9.3 shows the cross-sectional metallographic image of Ti-6Al-7Nb alloy before and after LSP. It can be seen that the untreated globule primary α-phase with average grain size is 30 μm, while the treated grain value is 10μm attributed to the plastic deformation induced by shock waves. As one can see LSP surface treatment led to significant grain refinement and formation of ultrafine-grained (UFG) in the metal alloy. The detailed microstructure evolution will be introduced by XRD and SEM.

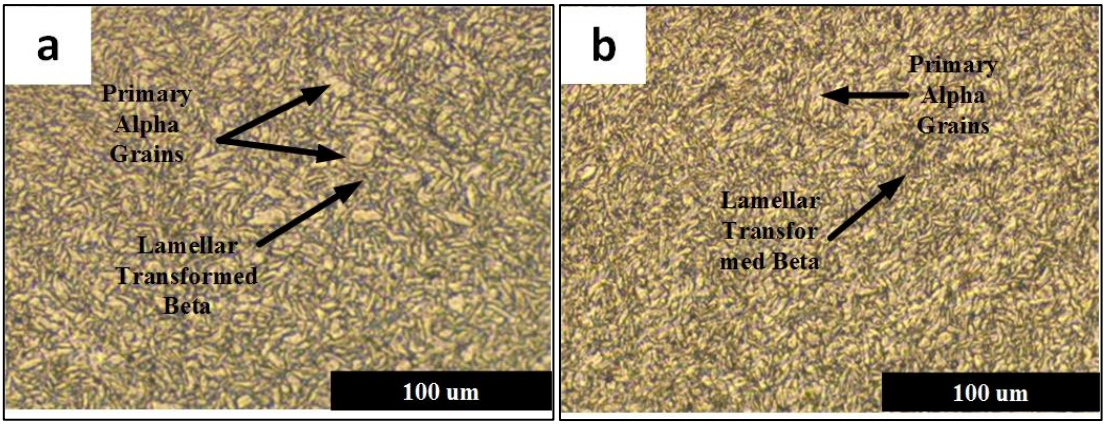

Figure 9.3 Optical image showing the cross-section of the as-received and impacted surface of the Ti-6Al-7Nb in (a) and (b).

9.3.1.2 Microstructure observation

The grain refinement has a significant relationship with the mechanical properties of the metal alloys. In this study, SEM was used to evaluate the microstructure of the Ti-6Al-7Nb alloy. Figure 9.4 presents the SEM observations of the untreated and the surface after LSP. As shown in Figure 9.4, the original microstructure of Ti-6Al-7Nb alloy consists of globular and acicular α and residual β [268-270]. The acicular and globular α distribute non-uniformly that the grains are coarse-grains and have clear phase boundaries. However, the image of the shocked sample shows that the grains were refined to 10 - 15μm due to spontaneous generation of shock-waves, resulting in plastic deformation under high strain rate. The acicular and globular α distribute uniformly and the grain boundary becomes fuzzy.

Figure 9.5 is the cross-sectional SEM image of Ti-6Al-7Nb alloy. The cross-section was divided into two areas by measuring the grain size. As shown in Figure 9.5(b), area A is the top-most of the treated sample that consists of refined globular α-grains and β-grains. Thereinto, β-grains distributed unevenly due to the high shock wave. In Figure 9.5(c), relative acicular α is much bigger than the one in top-most, and the average size was around 20μm. Due to the shock wave propagated damply through the cross direction and dislocations cannot acquire enough energy to refine the coarse grains. While in the top-most, due to the shock wave, plastic deformation occurred in the coarse acicular grains which were refined into much smaller globular. That is why the embed β grains scatter more unevenly than those in the deep substrate.

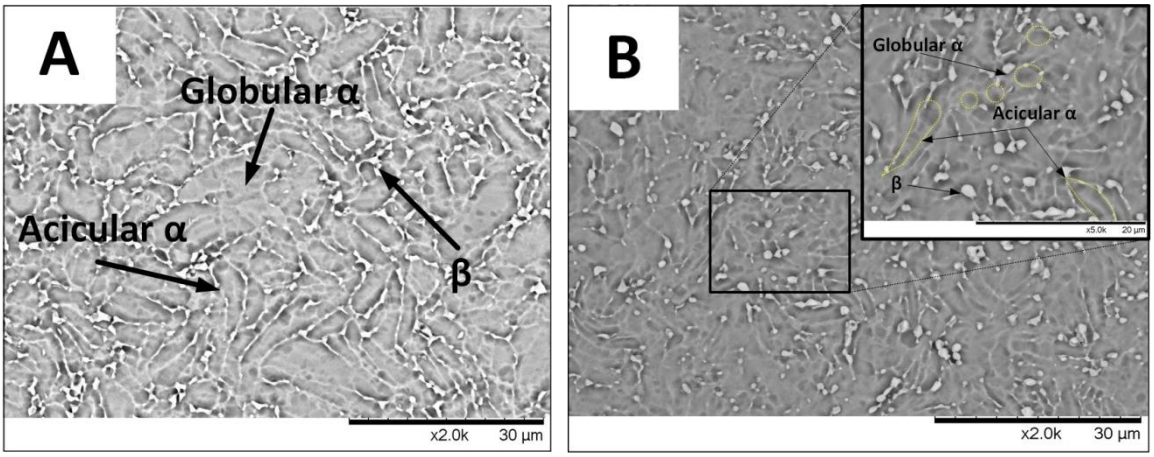

Figure 9.4 SEM image showing the microstructure of the Ti-6Al-7Nb, before and after LSP surface treatment in (a) and (b).

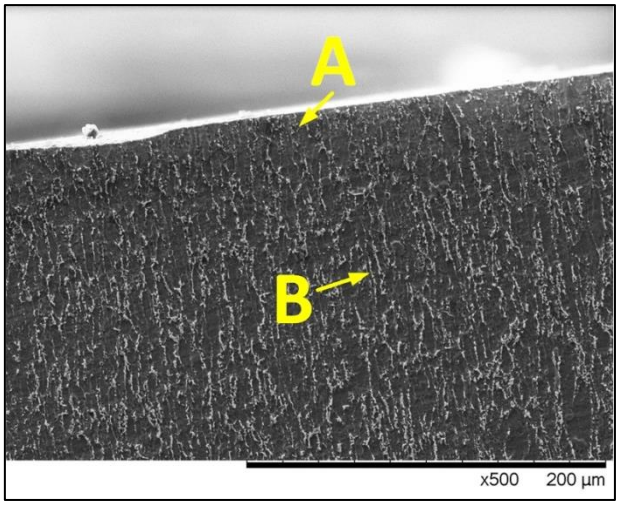

(a)

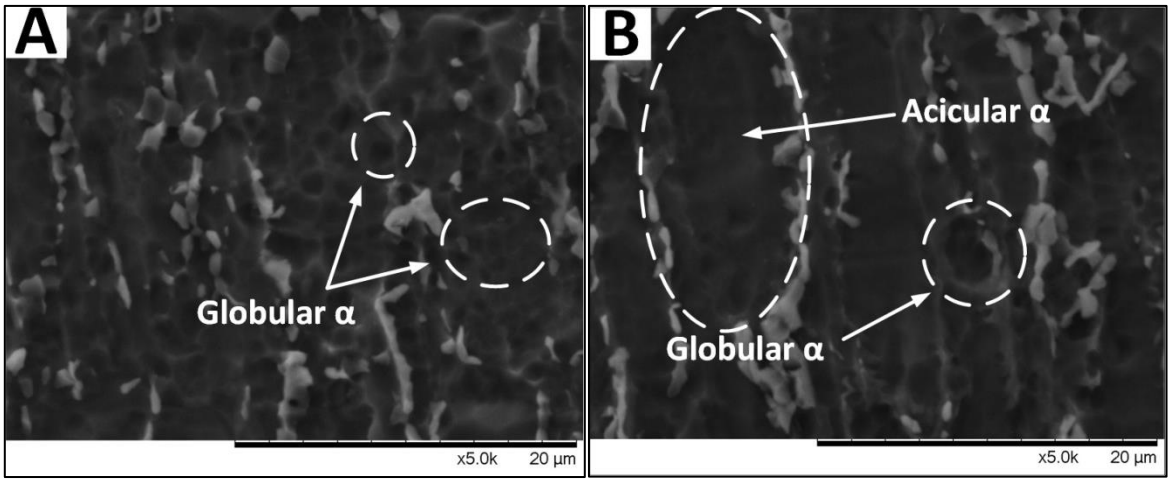

(b) (c)

Figure 9.5 SEM images showing a low resolution cross section of area A and B in (a) and the high resolution image of area A in (b) and the area B shown in (c).

9.3.1.3 Phase Examination

The high pressure shock wave can result in plastic deformation and even grain refinement as evidenced by the microstructure examination. In order to investigate the effect of laser shock processing on the microstructure of Ti-6Al-7Nb, the XRD method was conducted to measure the different diffraction patterns. Therefore, the XRD patterns of multiple laser shock processing samples (2θ from 20° to 80°) was shown in Figure 9.6(a: as-received, b: 1 impact, c: 2 impacts, d: 3 impacts). It can be seen that the main phase of Ti-6Al-7Nb alloy are still peaks of α(100), α(002), α(101), α(102), α(110), α(103), α(200), α(112), α(201) and β(110). There are not any new peaks after multiple LSP impacts. This indicated that there are no phase transformation and no new crystalline phases. The peaks broadening can be found due to dislocations caused by high-strain plastic deformation and micro-strain among the adjacent peaks such as the peaks of α(100), α(002), α(101),and β(110), seen from Figure 9.7 (a) and (b). We find that the peak was broadened with increasing the impact. The main reason for this is that the high strain plastic deformation, caused by the shock wave, resulted in changing atomic distances, which equals to lattice distortion. Besides that, LSP also causes an increase in dislocation density and introduces residual compressive stress.

The average crystallite size can be determined by calculating from full width at half maximum (FWHM) of Bragg diffraction peaks via Scherrer-Wilson [271] equation (2).

$$FW\times \cos\theta = K\times\lambda/D + 4\times\varepsilon\times\sin\theta \quad (2)$$

Where D and K were crystalline sizes and the shape factor of the lattice constant (K=0.89),λ means the wavelength of X ray (λ=0.15418 nm); FW was the full width at half maximum; ε was the micro-strain, and θ was the Bragg angle. Fig 7 shows the grain size and micro-strain. The average crystallite size of the ten peaks decreases with shock impacts, while the micro-strain increases.

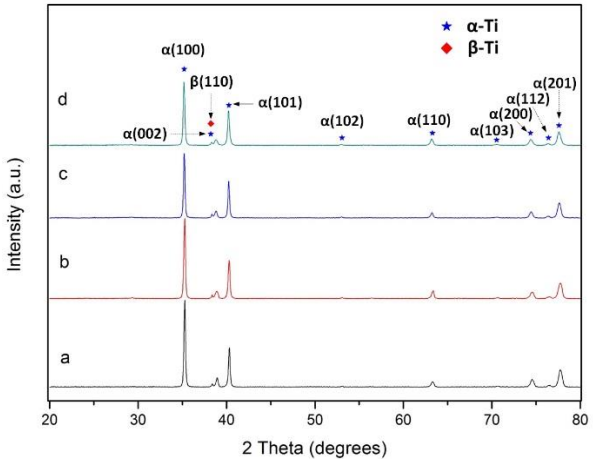

Figure 9.6 XRD patterns of the Ti-6Al-7Nb showing diffraction peaks (20° to 80°); a): 3 impacts, b) 2 impacts, c) 1 impact, d) as-received.

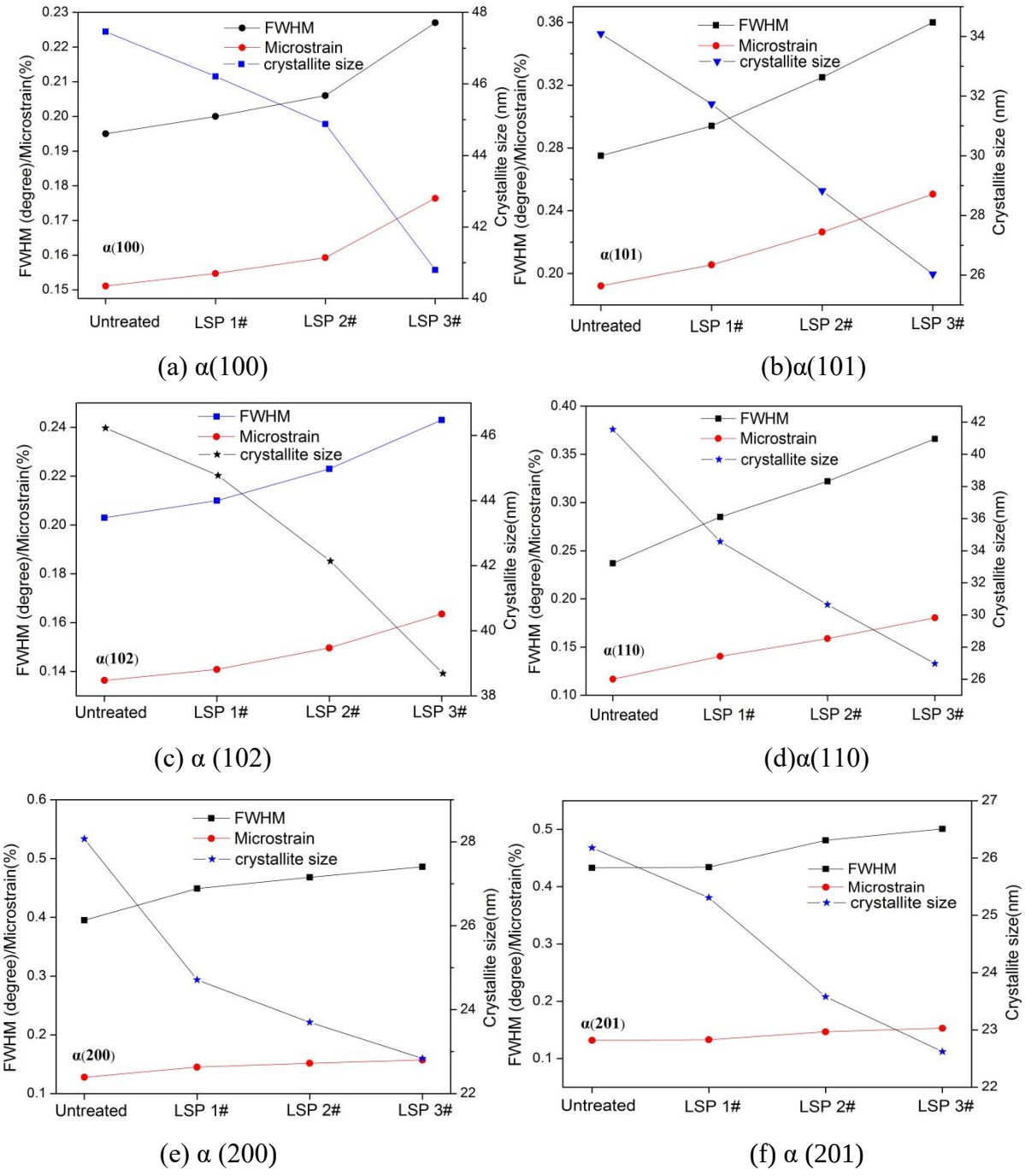

(a) α(100) (b)α(101)

(c) α (102) (d)α(110)

(e) α (200) (f) α (201)

Figure 9.7 FWHM, Micro-strain, Crystallite size of the Ti-6Al-7Nb.

9.3.2 Microhardness of Ti-6AL-7Nb

Examination of the micro-hardness would indicate the resistance of materials to elastic, plastic deformation and fracture [272]. Micro-hardness also influences wear resistance, which is important for this work since the main failure mode of orthopaedic implants is wear. High hardness can effectively improve the wear and fatigue life and in turn, decreasing the risk of

revision surgeries. The Vickers miro-hardness in the cross section of the Ti-6Al-7Nb alloy that were subjected to multiple LSP at the 11.5 GW/cm^2 level is shown in Figure 9.8. The untreated cross-sectional hardness scatters from 293 HV30 to 310 HV30. After one LSP impact, its surface hardness improves to 363.2 HV30, which the maximal hardness locates at the material surface and decreases gradually along the cross direction. With increasing shock pules, x2, x3, the surface micro-hardness is increased to 367.5 HV30 and372.2 HV30. Respectively it represented an improvement of 20.6% and 22.31%. This indicated the surface micro-hardness increases with shock impacts. But further improvement is limited, which was shown by the effect layer with a distance of 0.9 mm. Figure 9.8 indicated that the hardness changed in gradient on the cross-section, decreasing from surface to inner and finally tends to be steady.

The work hardening and structural changes are the main factors of hardness improvement [28-30][273-275]. The work hardened layer can refine surface grains, and inherently, improving the surface micro-hardness. On the one hand, the High pressure plasma generated a severe plastic layer, with the decrease of the shock wave spreading in the material. Further, the plastic deformation gradually decreases until it becomes stable. The plastic deformation layer led to the cold work hardening, which increases the surface micro-hardness. On the other hand, according to the Hall-Petch relationship [276], the grain refinement grain will increase the micro-hardness. As seen in the SEM, the grains were refined by plastic deformation which indicated that the micro-hardness was improved, which is directly favourable to improve the wear resistance.

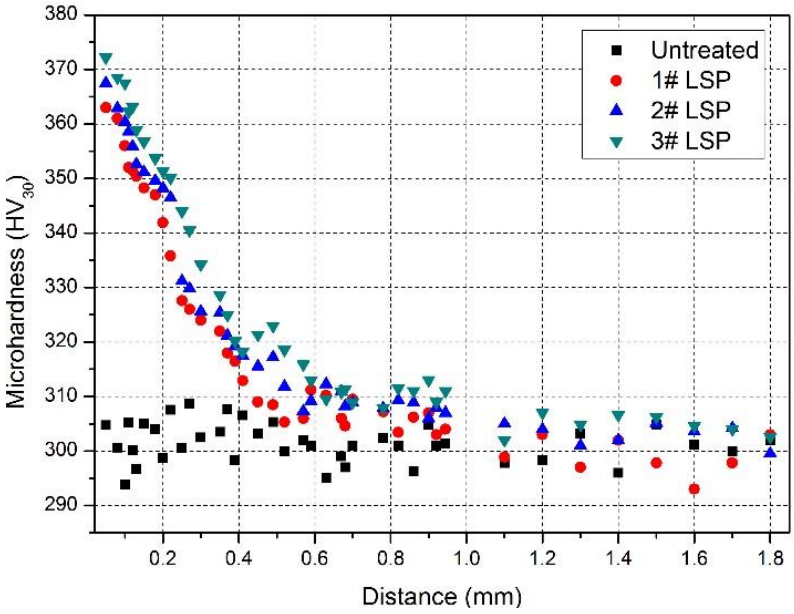

Figure 9.8 Mirohardness distribution on the cross-section with multiple LSP.

9.3.3 Surface roughness of Ti-6Al-7Nb

Figure 9.9 (a) to (d) show the 3-D surface topography of Ti-6Al-7Nb alloy before and after LSP with different multiple shocks impacts (x1, x2 and x3). The untreated samples were polished from 300µm to 2000µm grit size, SiC abrasive paper in stages. Moreover, it can be seen that sharp protrusions distribute non-uniformly on the untreated samples. In Figure 9.9 (b), (c) and (d), the sharp protrusions had vanished after multiple LSP which meant that LSP can blunt the sharp protrusions. In Figure 9.10 (b), subjected to one LSP, the surface sample generated dimples and micro-grooves, resulting in increasing surface roughness from 0.15µm to 0.52µm. Besides that, compared with the untreated samples, sequent micro-dimples can be observed on the metal surface with size of Ø0.2mm. The water employed as confinement layer was known as the main reason for causing the laser bending and self-focus [277, 278], which leads to dimples distribute spatial non-uniformity. Figure 9.9 (c) and (d) is the 3-D topography of the x2 and x3 LSP impacted shots. The surface roughness is decreased to 0.41µm and 0.32µm compared with x1 impacted sample (0.52µm). After multiple LSP, the surface roughness growth tends to be slightly decreased, compared with one impact.

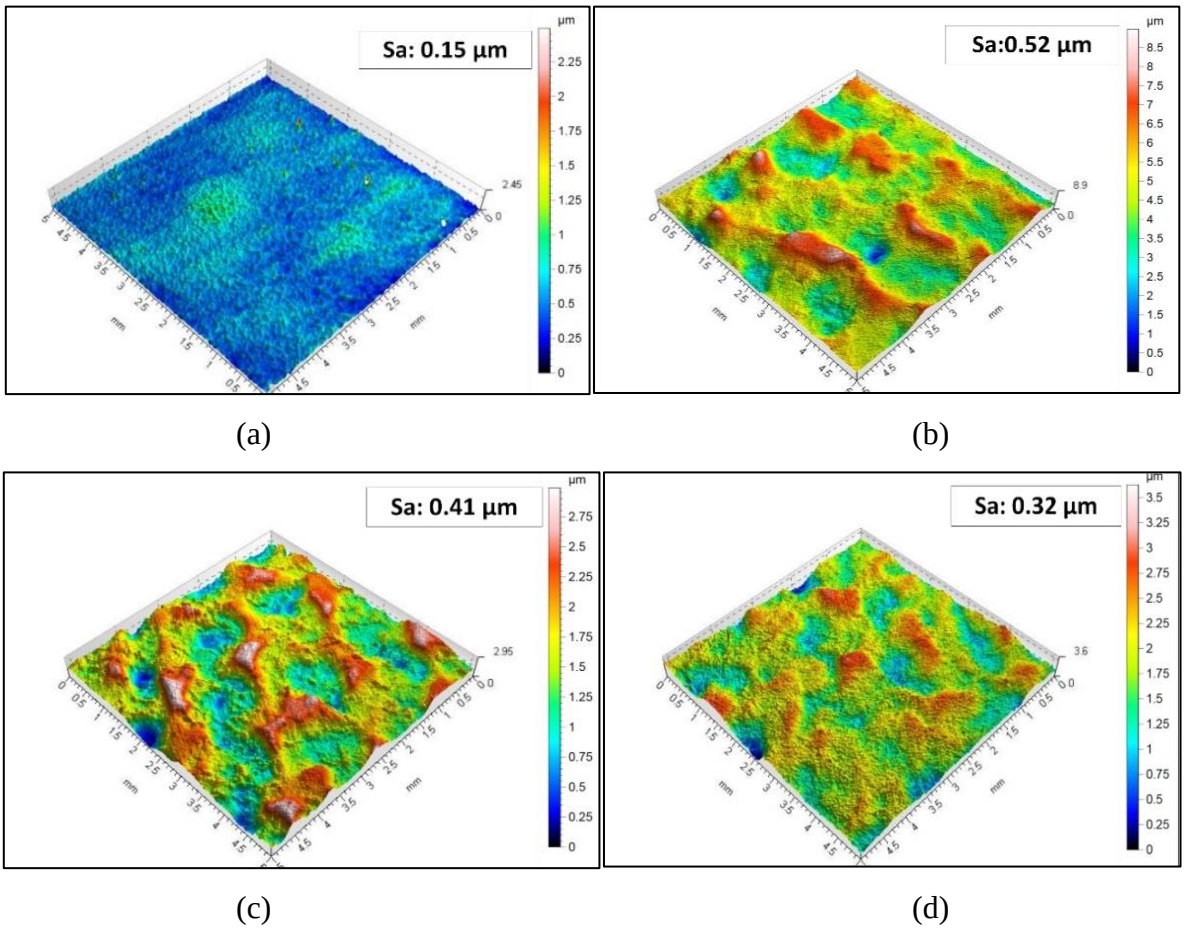

(a) (b)

(c) (d)

Figure 9.9 Surface roughness of the multiple treated and untreated Ti-6Al-7Nb alloy (a) 2000 µm SiC untreated (b) x 1 LSP, (c) x2 LSP, (d) x3 LSP.

What is more, Figure 9.10 is the cross-sectional profile of Ti-6Al-7Nb alloy. Figure 10(a) shows the surface height of 2000µm untreated sample scattered from 0.2µm to -0.2µm, which is very smooth, but after one impact, the surface roughness scattered from -2.5 µm to 2.5 µm. When subjected to two or three impacts, it ranged from 0.6µm to -0.6 µm. We can find that through the cross section, the deepest kink is 2.5µm and with the increase of impacts, the deepest depth of dimples changed into 0.6µm. In addition, as the number of impacts increased, the growth of roughness tends to increase to a certain level and then becomes saturated. This was evident from the work of Dai *et. al.* [277], based on multiple impacts of LSP on stainless steel.

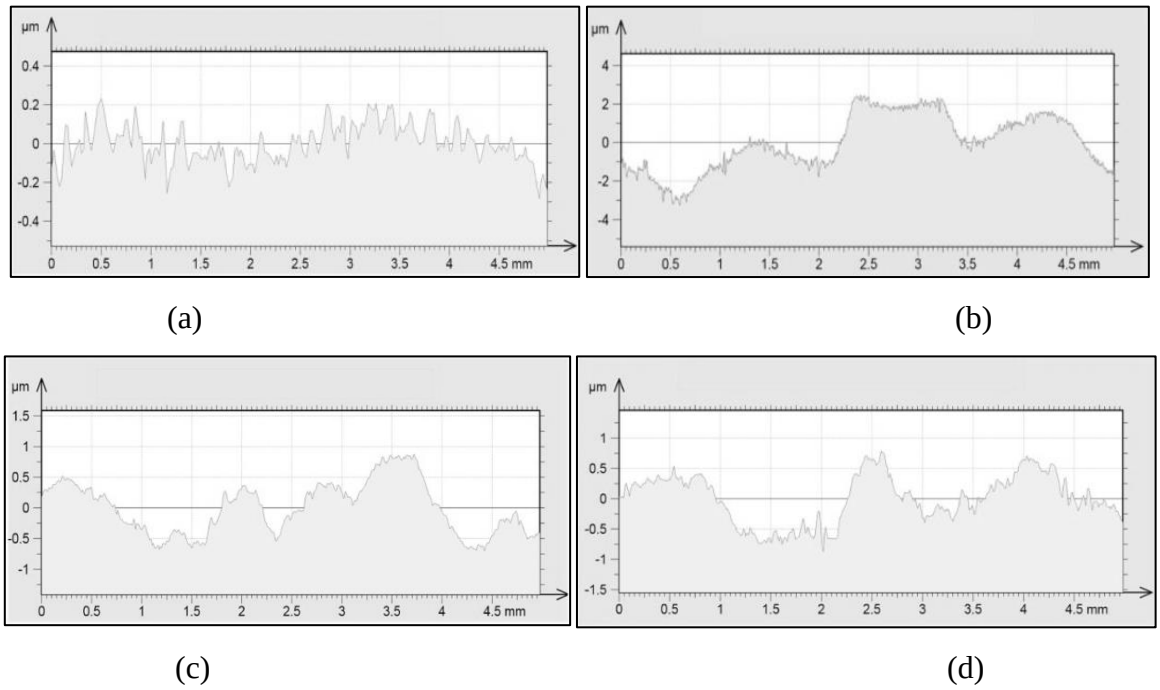

Figure 9.10. Cross-sectional profile of Ti-6Al-7Nb alloy before and after LSP: (a) as-received (b) 1 impact, (c) 2 impacts, (d) 3 impacts.

9.3.4 Sliding Wear Behaviours

Wear resistant is one of the most important implant mechanical properties that wear failure contributes 13.6% from all implants failure reasons [279]. Recently, Lu *et al.*, [280]found the LSP to be effective on wear resistance of AISI 8620 Stainless steel. Despite that, the sliding wear data subject to LSP of Titanium alloy is still scared. Figure 9.11 (a) shows the friction co-efficient variation with different multiple impacts at the power density of 11.5 Gw/cm^2. It can

be seen that treated samples have a similar trend. When the tests were conducted, the friction coefficients took a stable value very quickly that the stability continued for long time, until the end of the experiments. Figure 9.11 (b) is the manifested image of friction coefficient-time curve between 0 s to 200 s. Compared with the friction coefficient curve of the as-received samples, these impacted curves increased more slowly at the initial stage (0-25s). After that, as-received coupon rapidly reached a high stable value of 0.48. At the same time, the friction coefficient of impacted Ti-6Al-7Nb decreased with shock impacts. What is more, those coupons reached a stable value when it was after 120s. Generally, the friction coefficient of the as-received or impacted samples increased during dry sliding wear experiments. Amongst impacted samples, with increasing the impacts - the friction coefficient became lower at the initial stage. Figure 9.12 presents the wear mass loss comparison of Ti-6Al-7Nb alloy coupons after dry sliding wear experiments. It can be obviously inferred that the wear mass loss of impacted coupons (16, 15, 12 ×10-4g) were much lighter than as-received (25×10-4g). This decreased with the increasing impacts. Hence, multiple LSP can effectively improve the sliding wear property of Ti-6Al-7Nb.

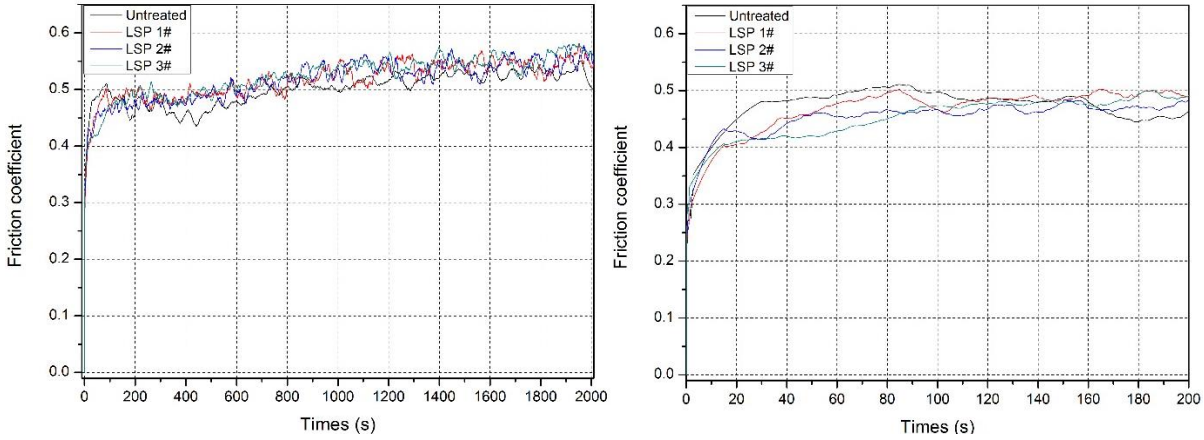

Figure 9.11 Friction coefficients of different impacts of Ti-6al-7nb alloy vary with time: a) 0s to 2000s b) Magnified image of 0s to 200s.

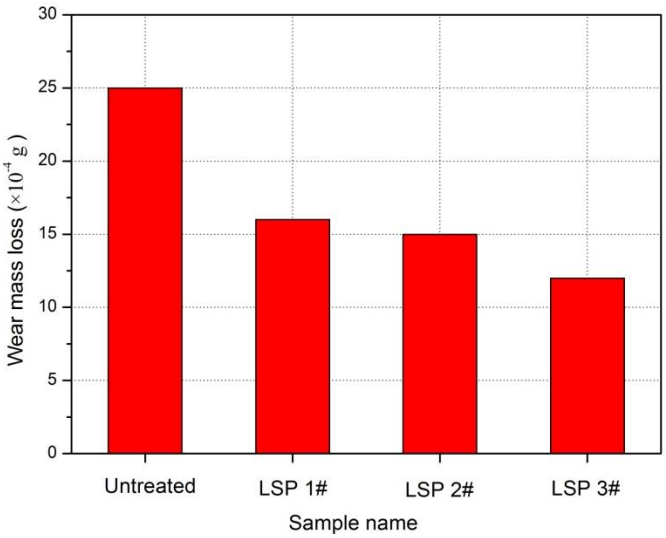

Figure 9.12 Wear mass loss of Ti-6Al-7Nb alloy.

9.3.5 Worn surface observation and Analyses

Figure 9.13 presents the SEM of worn surfaces before and after x3 impacts at 11.5 GW/cm^2. Examination of low magnificent SEM impacted coupon not only had smoother wear tracks than as-received surfaces. The width of the sliding abrasion track of impacted coupon was nearly as same as the as-received surfaces. However, although the presence of abrasion can be evident in both worn surfaces, impacted surfaces exhibit a much smoother track, indicating that impacted coupon experienced less wear damage in comparison to the as-received. In addition, the atomic concentration is a good evidence of the comprising of Ti, O, C, Nb and Al (see Table 3).

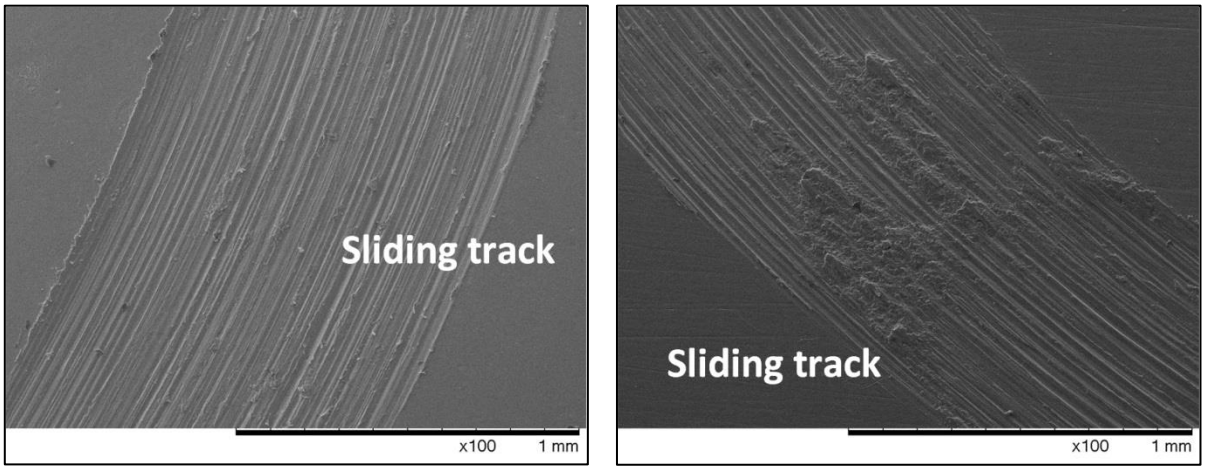

(a) (b)

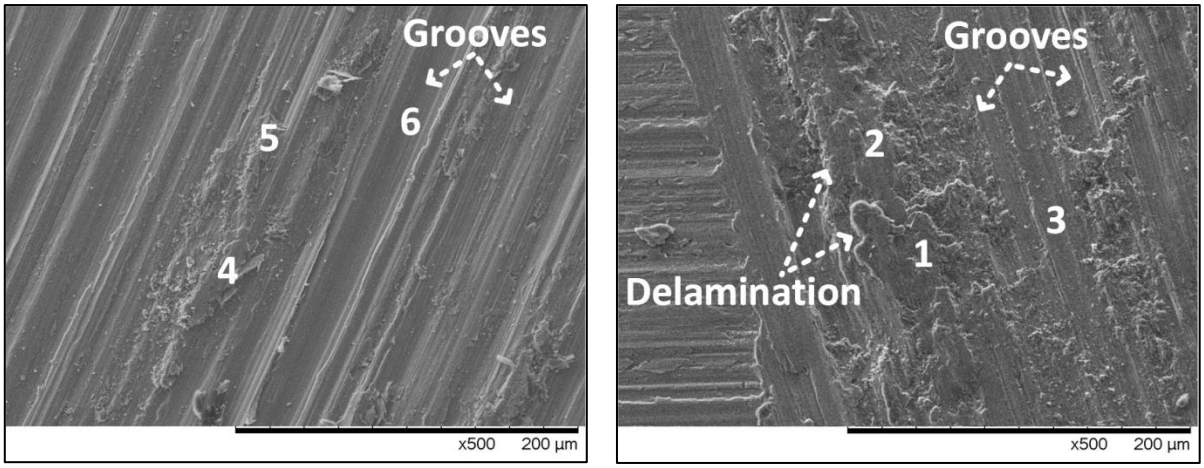

(c) (d)

Figure 9.13 SEM micrograph of a) the LSP impact track; b) the as-received track, c) the SEM of Impacted coupons, d) SEM of as-received coupons.

9.4 Discussion

Grain size, surface roughness and micro-hardness are important factors affecting the wear property. Section 9.3.1 (SEM and XRD) respectively observed and analyzed the refinement of Ti-6AL-7Nb by LSP that refine the grain size from 30 µm to 10 µm. Section 9.3.2 (Surface Micro-hardness) shows that LSP can improve the micro-hardness of Ti-6Al-7Nb alloy. Section 9.3.3 (Surface roughness) presents that LSP can greatly increase the surface roughness when the as-received is very smooth. The sliding wear property of Ti-6Al-7Nb before and after multiple LSP was strongly effected by all the above experimental results. Moreover, wear resistance has a direct connection with metal grain size. Generally, according to Hall-Petch equation, decreasing the grain size will lead in increasing the microhardness, which is the substantial harden of metal materials. And multiple LSP can obviously refine the surface microstructure of as-received coupons as shown in Fig 9.3. What is more, XRD calculation shows that multiple LSP also can refine the crystalline of Ti-6Al-7Nb. Previously works found that LSP has effective on straining initiation and propagation of surface micro crack that can improve the sliding wear property of Ti-6Al-7Nb.

As we know that, under the same conditions the higher surface roughness the coupons have, the worse destitute wear resistance they perform. Therefore, among impacted coupons, the surface roughness of samples decreases with shock impacts, Meanwhile, the microhardness of impacted coupons are on the contrary. Thus, we can say that within impacted coupons multiple laser shock peening is prior than single impact. But compared with the as-received coupons the

surface roughness is increased nearly by 100%. However, the microhardness were improved by 22%. Valuing from those two factors, the wear resistance (wear mass loss) is improved by 44% which means the increment of surface roughness is acceptable.

Measuring the O wt% from the worn surfaces of impacted and as-received coupons shown in Table 9.3. Each of the coupons was selected out of three areas. From Table.9.3, the O atom wt% of as-received coupons scatters from 7.7% to 19.8% while this volume of impact is 8.3% to 27%. Compared with different depth from one coupon, O atom wt% decreased through the depth that means oxidative wear is one of the wear mechanisms at least. Besides that, in both as-received and impacted coupons, there are many grooves and wear debris on the worn surface of Ti-6Al-7Nb, which means the wear mechanism is abrasive wear. Therefore, the sliding wear mechanism of Ti-6Al-7Nb alloy is the composition of oxidative wear and abrasive wear.

Table 9.3 Atomic concentration (wt%) of the worn surfaces of Ti-6Al-7Nb alloy before and after LSP: Area 1, 2, 3 of Fig 13(d): the as-received coupons; Area 4, 5, 6 of Fig 13(c): the impacted coupons.

Element (wt%)		Ti	O	Al	Nb	C
Untreated	1	64	19.8	6.3	4.5	5.4
	2	71.5	12.4	4.7	5.6	5.8
	3	82.6	7.7	4	3.5	2.2
Impacted by LSP	4	57.1	27	5.5	4.5	5.9
	5	52.9	21.3	16	4	5.8
	6	77.3	8.3	6.4	5.5	2.5

9.5 Summary

This chapter presents a first-time and a first-step study demonstrating modifications of mechanical properties of orthopaedic Ti-6Al-7Nb subject to multiple LSP impacts. The results in this chapter have shown some promise with regards to generating strengthening of vanadium-free Titanium based alloys (Ti-6Al-7Nb), suitable for implant applications. By applying such technique to strengthen implant materials would directly influence the end user's quality of life by modification of suitable mechanical properties as shown in this chapter. The main conclusions obtained were as follows:

- Grain refinement was assessed by SEM observations and XRD analysis. This in turn showed grain reduction from around 30 μm to 10 μm. Surface XRD patterns showed that the phases were not affected as peaks were shifting and broadening was evident after the LSP.
- The microhardness of Ti-6Al-7Nb alloy can be effectively improved by the LSP surface treatment. With one impact, the surface microhardness was 363HV_{30}, which increased by just under 20%. After 3 impacts the microhardness was increased to over 22%.
- LSP will increased the surface roughness, from 0.15μm to 0.52μm. However, with increasing impacts, the growth of roughness tends to be steady.
- The sliding wear improved by 44% subject to 3 multiple impacts. In addition, for both impacted and as-received samples, the sliding wear mechanism was the composition of oxidation wear and abrasive wear, which was confirmed from the EDS data and worn SEM images.

PART 4 TOPOGRAPHY, WETTABILITY AND BIOLOGICAL ASPECTS

CHAPTER 10 Examination of Topography Modifications Subject to Laser Shock Peening in Ti-6Al-7Nb Alloy

Implants surfaces with macroscopic and microscopic features such as dimples and grooves play an significant role in cell adhesion, differentiation and proliferation osseointegration. Therefore, it is critical for surface modification method to form such features on the surfaces of the implant. However, effective methods for changing the surface characteristics are still limited. Thus, this chapter is focused on investigating the effect of laser shock peening on surface topographies of Ti-6Al-7Nb alloy. The topographies prior to and after LSP were characterized by non-contact white-light interferometer (WLI). What is more, LSP induced surface topography was examined in nanoscale by using Atomic Force Microscopy (AFM).

10.1 Introduction

As we discussed in Chapter 7 (Mechanical part), LSP can introduce a stable compressive residual stress layer which benefits the mechanical properties. However, apart from the compressive residual stress factor, as a by-product, the component surface has also been roughened due to the plastic deformation. Considering the surface roughness as an independent factor, increasing surface roughness is detrimental to fatigue performance as stress concentration could be easily formed, thereby, leading to the crack initiation and nucleation under fatigue loading. Haghshenas *et al* [281], investigated the evolution of the surface roughness parameters from starting to ending stages in both low and high cycle fatigue. It has been found that the increasing rate of surface roughness parameters has rendered a positive relationship with the applied stress. Additionally, surface roughness can represent damage accumulation as the surface roughness parameters show a linear increase relationship with the damage accumulation.

After LSP treatments, the surface roughness of components was also greatly increased [282]. Unlike the surface morphology caused by laser ablation that removes the material from a solid surface by irradiating with laser beam[283], LSPned surface finishing is formed by plastic movements induced by plasma shock waves. Lu *et al* [284] characterized the surface topography and morphology after LSP in a Ni-based single crystal superalloy. After LSP, surface features such as pit, dimples and pile-up region were observed. These could lead to

non-uniformity of micromechanical properties, thereby, leading to the failure of materials during service. Therefore, Dai *et al* [285], proposed two methods separately called elastic contact laser shock peening (ECLSP) and laser shock-wave planishing (LSPWP) to decrease the surface roughness introduced by LSP. For ECLSP, compared to conventional LSP treated sample surface, the piled-up region height after ECLSP treatment is much lower than the one of LSPned (0.78 μm *vs* 1.3 μm). Also, in terms of LSPWP, the surface roughness after CNC milling can be decreased from 3.07 μm to 0.977 μm or 0.577 μm by applying one or two LSPWP impacts.

Nevertheless, when it comes to medical applications, rough surface finishing contributes to improving the osseointegration of the implant, which benefits to the patients' recovering. Literatures showed that different topography relates to the cell/protein adhesion, proliferation and differentiation [286, 287]. Normally, the rougher the surface, the higher the osseointegration performance of the implant. Due to that reason, certain surface modification methods such as sandblasting, aid-etching, and shot peening were employed to enhance the biocompatibility of the implants. These techniques would introduce some surface features such as pits, dimples, and grooves which are needed for osteoblast cells to settle down on the implant surface and start to survive. Wang *et al* [288], employed multiple surface modification methods (diamond shot peening, acid etching and Al_2O_3 blasting) to get different surface topography of titanium alloy and examined the proliferation stability of bone marrow mesenchymal stem cells (BMSCs) on these modified surfaces. By comparing the plane grinding group (as control), all modified surfaces have been improved in terms of cell proliferation.

Apart from the mechanical and biological applications, the surface topography also has a great influence on the wettability. The detailed discussed will be conducted in Chapter 11. Therefore, the characterizations of the surface topography after to LSP is critical In this chapter, atomic force microscopy (AFM), laser confocal scanning microscopy are used to characterize the surface features.

10.2 Characterization methods

A 3-D white light interferometer (Contour GT-K, Bruker, Germany, shown in Figure 10.1) was employed to measure surface topography of Ti-6Al-7Nb alloy. The mapping was carried with 5x lens at 2x magnification. Scanning strategy starts from the left corner on the LSPned

surfaces then taking zig-zags routine for acquiring finally a rectangle map with the size of 10 × 10 mm^2.

The 3-D surface topography was determined by an atomic force microscope (Nanosurf EasyScan 2, Switzterland) with a scanned area of 20 μm× 20 μm (shown in Figure 10.1). The Setpoint is 20nN and the scanning points are 256.

Figure 10.1 Contour GTK, Bruker white-light interferometer and Atomic Force Microscopy (Nanosurf EasyScan 2, Switzerland)

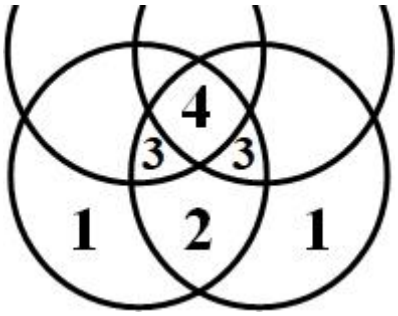

Figure 10.2 A schematic of the impacts zone layout z on the LSP surface.

Upon applying LSP surface treatment on the sample surface is normally fulfilled by changing laser energy and overlay etc. Actually, there are various regions subjected to 1 to 4 impacts on the LSPned surfaces shown in Figure 10.2. Therefore, the micro surface features subject to LSPned will be characterized by AFM by measuring single impact 1 to 4 times with 3J, 5J and 7J.

10.3 Characterization of micro features surface morphology by Atomic Force Microscopy Mapping

In Figure 10.3 the average surface roughness of the untreated sample is 22.9nm. Compared to the untreated surface, the surface roughness has been increased due to LSP (maximum up to 43nm and minimum of 23nm). Amongst the samples subjected to 3J LSP and 5J (exclude 4 impacts), there are no obvious differences between LSPned and untreated surfaces. However, the surface reliefs start to form when the impact increases to 4 at the laser energy of 5J. This may due to enough high plastic movements are driven by comparatively high laser energy and impact numbers. According to the statement from [38], surface relief is a typical morphological representation of the free (semi-constrained) plastic flow of metallic surfaces during non-contact plastic deformation, characterizing a unique local microscale reverse deformation phenomenon. In 7J-1 impact and 7J, 2 impacts, the number of surface reliefs reach its peak as well as the surface roughness (42.7nm and 43.4nm). What is interesting is that the surface reliefs and surface roughness begin to decrease with the impact increasing to 3 and 4 impacts. It is postulated that these surface reliefs can be used as anchorages for the cell adhesion.

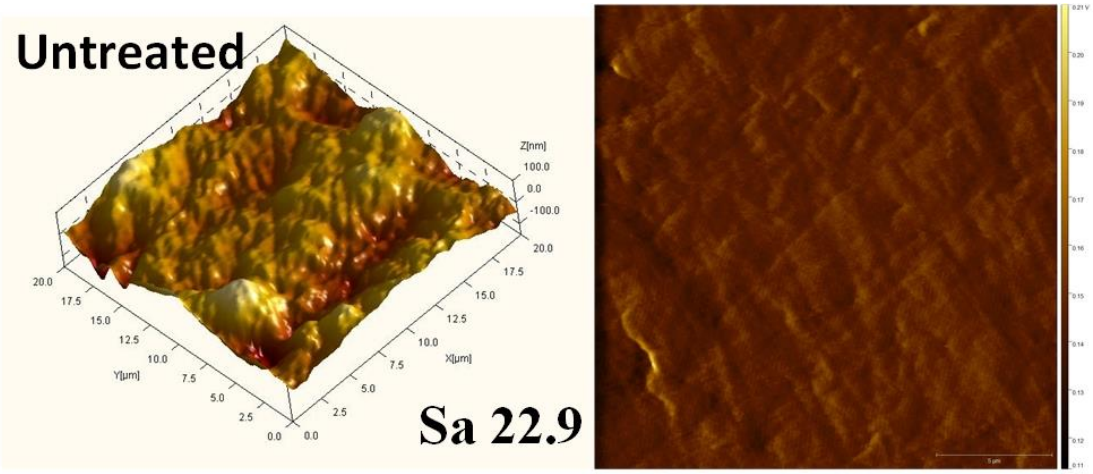

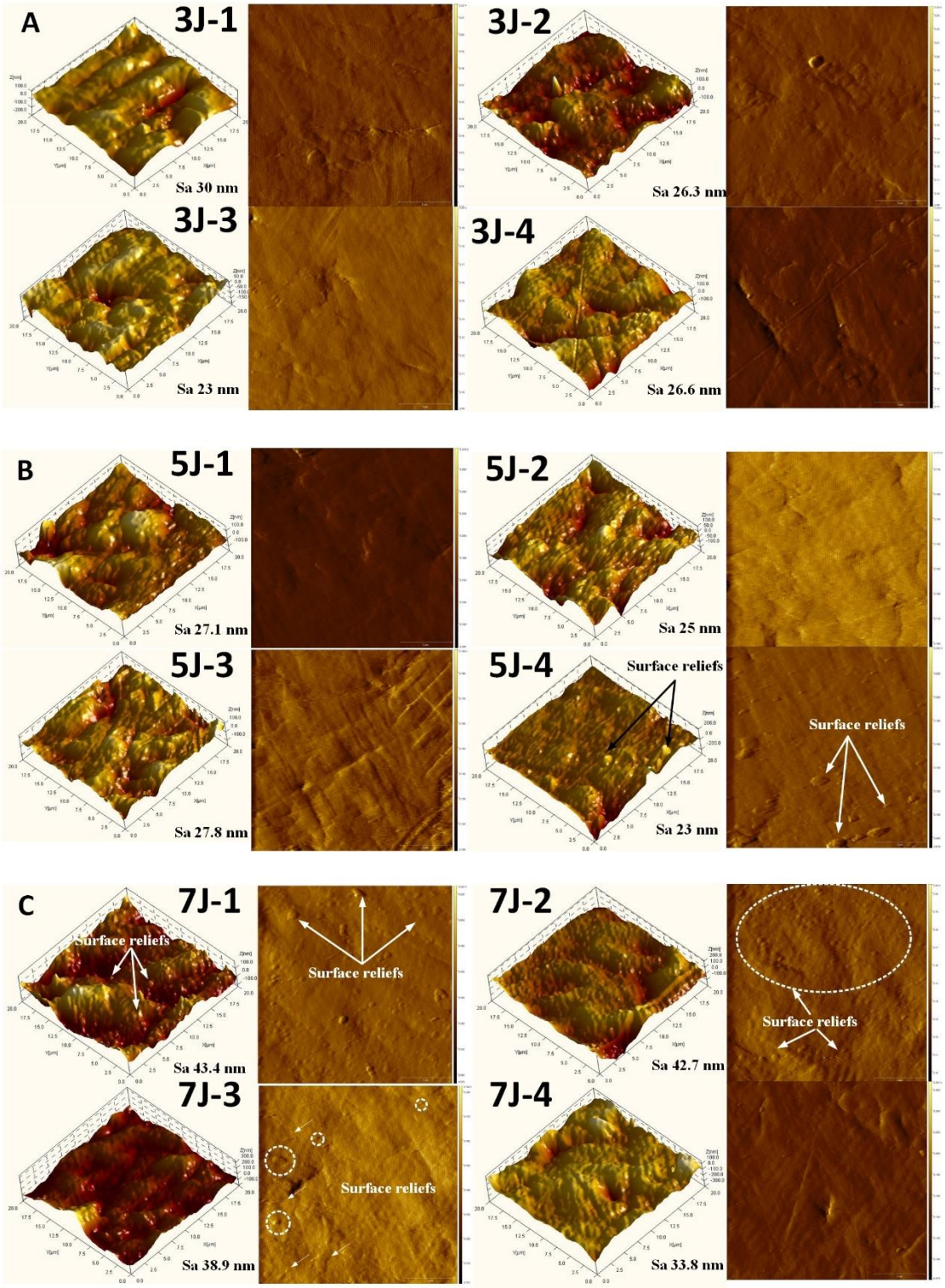

Figure 10.3 AFM image showing the micro topographies of Ti-6Al-7Nb alloy before and after LSP: Untreated; in A) at 3J, including 1-4 impacts; B) at 5J, including 1-4 impacts; C) at 7J, including 1-4 impacts.

10.4 3-Dimensional topography and surface roughness of LSPned Ti-6Al-7Nb alloy

In many previous literatures [278, 289, 290], it has been observed that LSP can increase the surface roughness with increasing laser energy and multiple impacts. In the meanwhile, surface topography and surface chemistry determine the wettability of materials. Therefore, studying the effect of LSP on the surface roughness is very pertinent. Both 2-D and 3-D topographies of LSPned samples were mapped, and the cross-section profile along the X-and-Y directions was presented in Figure 10.4.

Upon changing, LSP parameters such as laser energy, overlap, spot size, surface characteristics, namely, grooves and dimples can be acquired. According to grooves direction, each sample was placed along the longitudinal way (Y direction). At the same overlap, the surface topographies of 3J 5J 7J laser energy are fundamentally same.

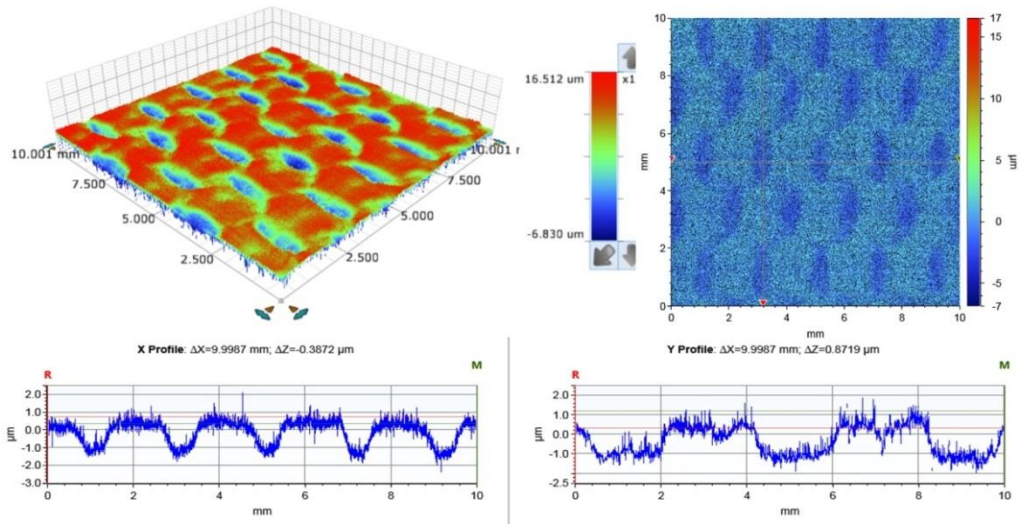

3J33%

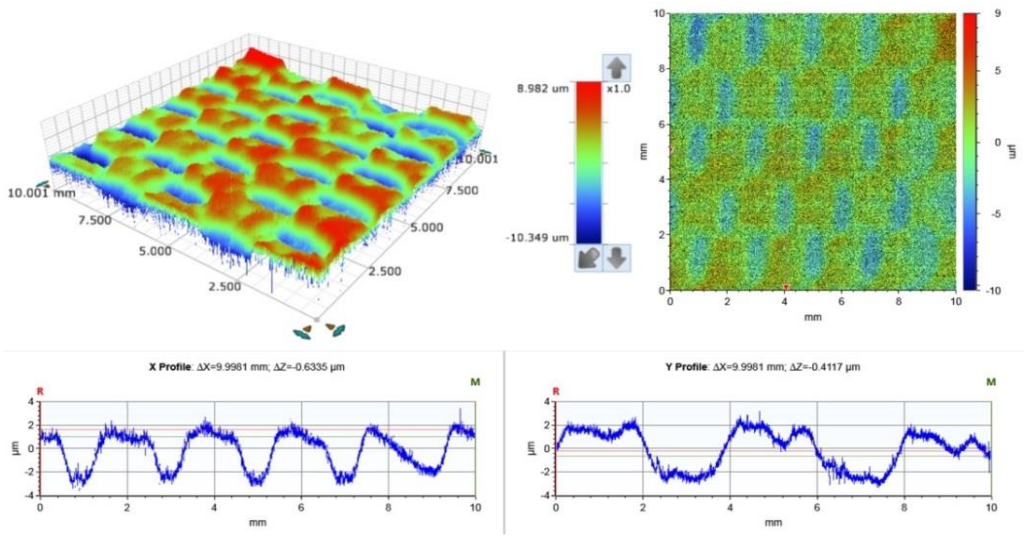

5J 33%

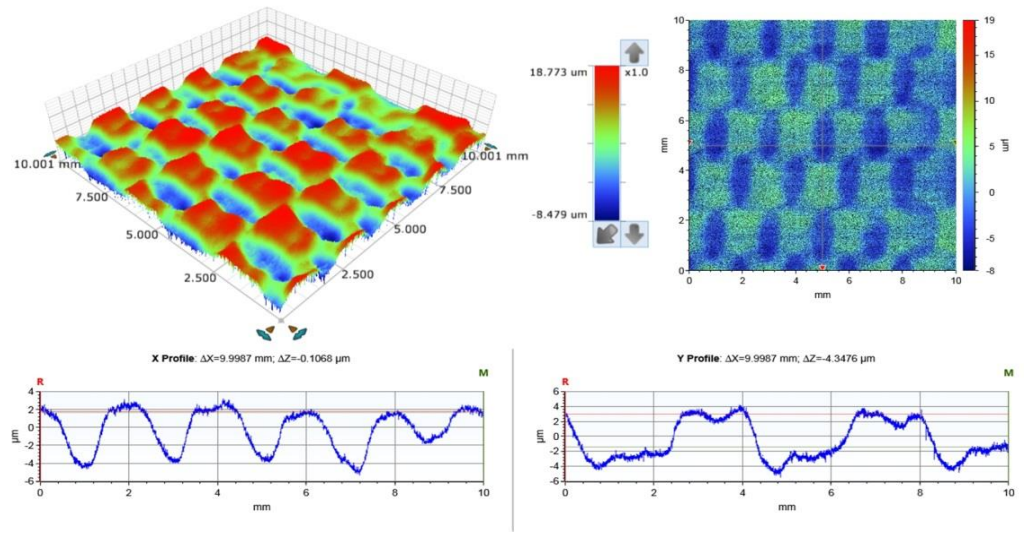

7J 33%

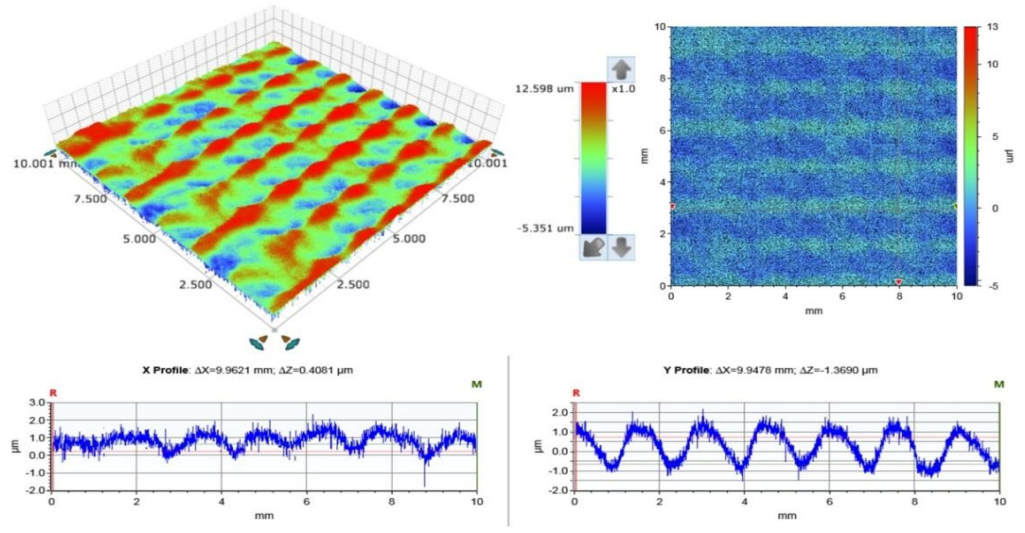

3J, 50%

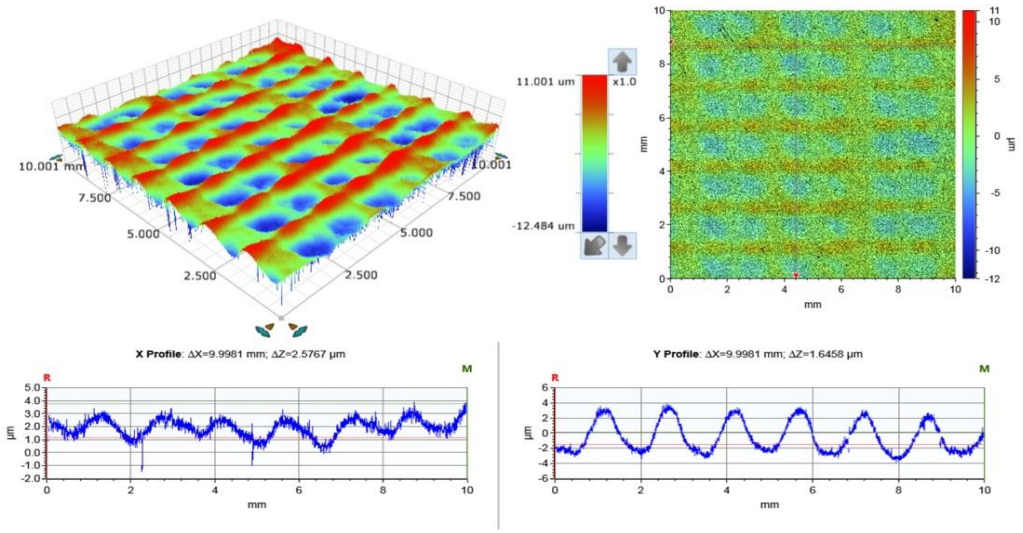

5J, 50%

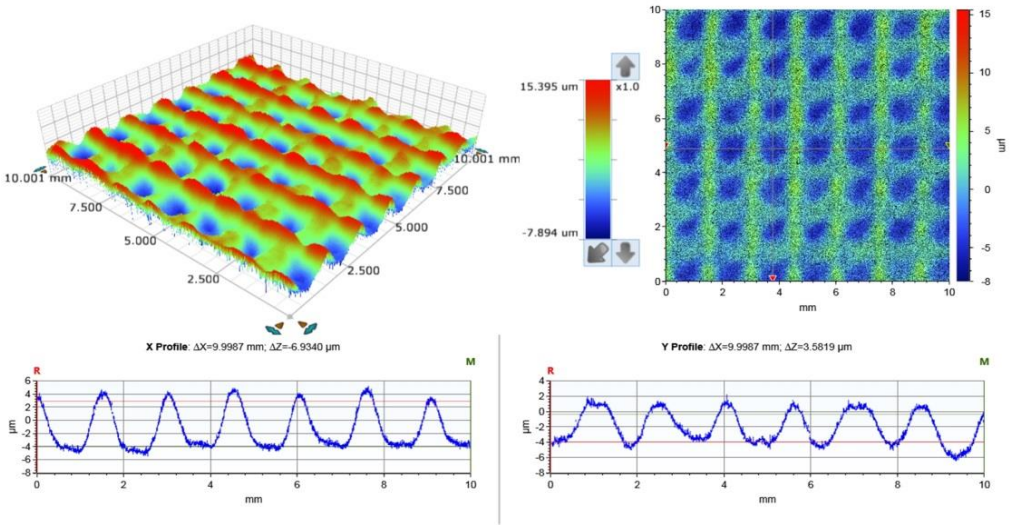

7J, 50%

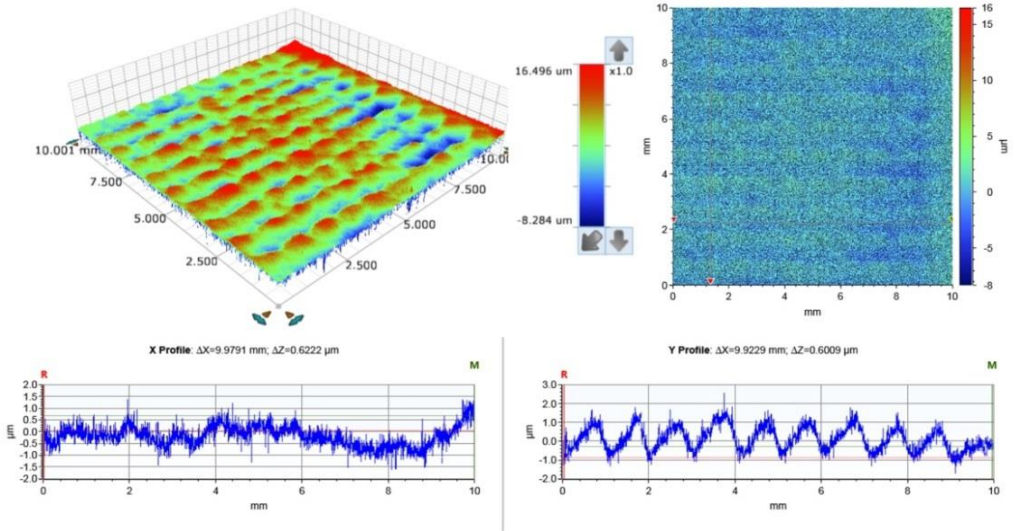

3J, 67%

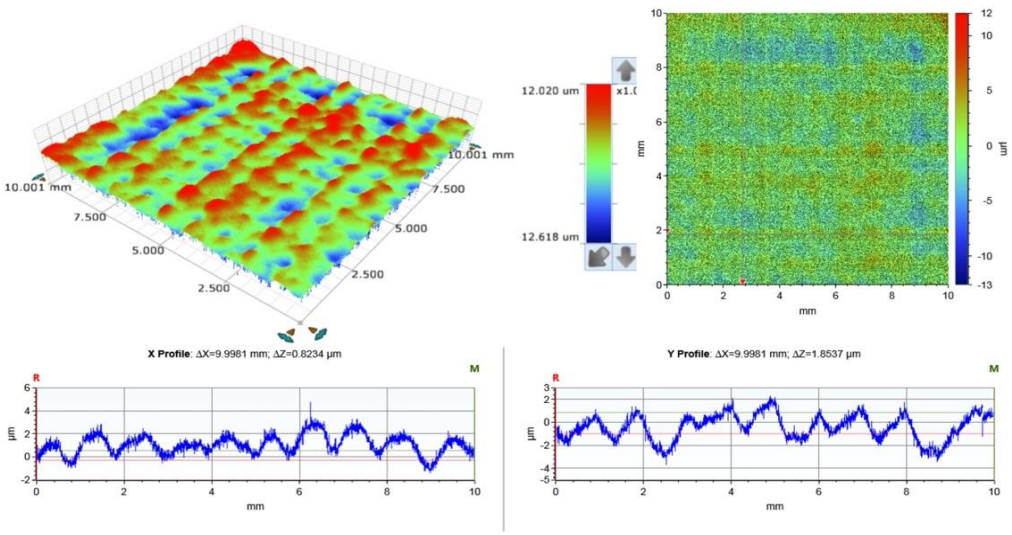

5J, 67%

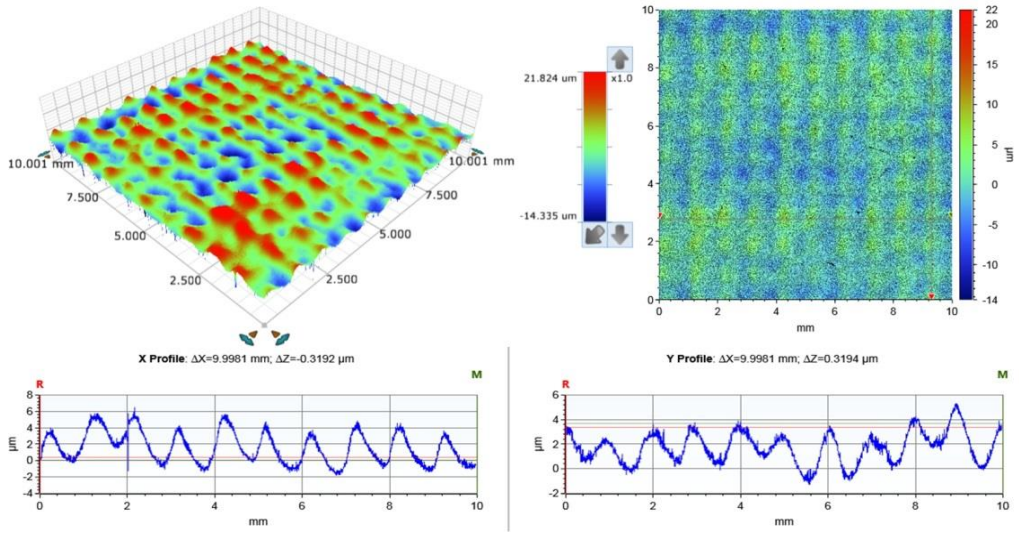

7J, 67%

Figure 10.4 Surface topography of laser shock peened Ti-6Al-7Nb alloy 3J, 33%, 3J, 50%, 3J, 67%; 5J, 67% 50% 33%; 7J 67% 50% 33%.

In terms of 33%, due to the 1/3 step movement (33% overlap), the comparative large dimples are formed after LSP while grooves are not observed. As shown in Figure 10.5, in the 3J X profile, the most top is at 1µm and the depth reaches to -0.5 µm, while the values of 5J and 7J are 2 µm /-3µm and 2.2µm/-4µm. Also, for Y profile, the top is 1µm and bottom is at -1.5µm, while the values of 5J and 7J are 2µm/-3µm and 4µm/-4.2 µm. Therefore, it can be concluded that the depth of these dimples is proportional to laser energy at the 33% overlap.

Compared to 33% overlap, a square-grid topography was formed on 50% overlap samples subject to LSP due to the 1/2 step movement during the LSP. Additionally, grooves are formed

upon the surfaces. In terms of amplitude of the curves in the X profile, the highest among three samples was 4 μm /-4.5 μm (7J), followed by 3 μm /-0.5 μm (5J), 2 μm /-0.5 μm (3J) in Y direction, while the sequence in X direction is 1.8 μm /-4.5 μm (7J), 3 μm /-2.5 μm (5J) 1.8 μm /-1 μm (3J).

In the overlap of 67%, due to the larger step movement step (2/3), the width of the groove is much smaller than one of 33% (2μm) overlap and 50% (1.54μm) overlap with average distance of 1μm in X-direction while in Y-direction the values are 1 μm (7J), 1.54 μm (5J), 2.8 μm (3J). Regarding to the amplitude, in X-direction, they are 0.5 μm /-1 μm (3J), 2 μm /0 μm (5J), 4.5 μm /-1 μm (7J); and in Y direction, they are 1.2 μm /-1 μm (3J), 1 μm /-3 μm (5J), 3.8 μm /0 μm (7J).

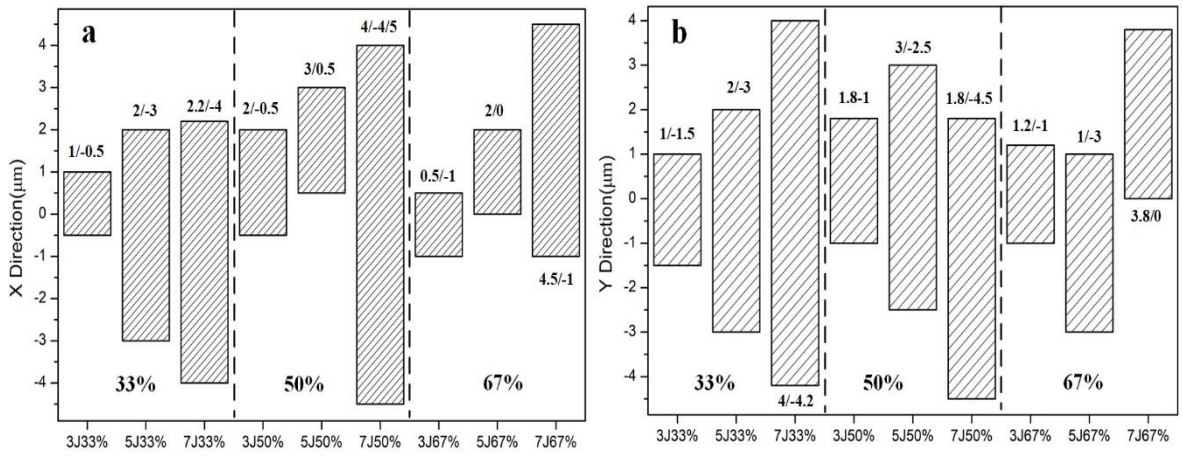

Figure 10.5 The comparative plot showing the amplitude of laser shock peening induced dimples at X direction (a) and Y direction (b).

10.5 Discussion

At the microscopic level, as reviewed by Lu *et al.* [291], a surface relief structure related by LSP impacts and spot size has been the most crucial feature of the microscale surface topography after laser shock peening. Such surfaces features as shown in Figure 10.3, the surface relief has a relative height of tens to hundreds compared to the base surface. It is the surface relief that facilitate the cell adhesion when the implant is inset to the human body at the very beginning.

By contrast, at the macroscopic level, the surface roughness works as a main influence factor to characterize the surface morphology after LSP.The average surface roughness Sa (arithmetic mean of the absolute values of the surface departures from the mean plane) and Ra (arithmetical mean roughness value over the entire measured length) along the LSP parameters distributions are given in Figure 10.6. Overall, in the longitudinal direction, it can be seen, that increasing the laser energy will lead to the rise of surface roughness. At the same laser energy level, all three curves decrease along the transverse way. But, in particular, at the laser energy of 3J, the values of both Sa and Ra of the overlaps are nearly same around 0.5-0.52μm. Excluding the lowest energy, 5J and 7J curves decline more significantly from 50% to 67% overlap with a reduction of 1.9μm (1.65μm) to 1.4μm (1.38μm), while in the range of 33% to 50%, the reduction of surface roughness was much lower. This is because, compared to 7J, the power density of 3J is comparatively lower than that of 5J and 7J. Therefore, from the normal direction of laser process, the depth of the dimples are also more shallow. The depth would somehow affect the wettability of the LSPned determing which wetting regime is more suitable. This will be discussed in detail in Chapter 11.

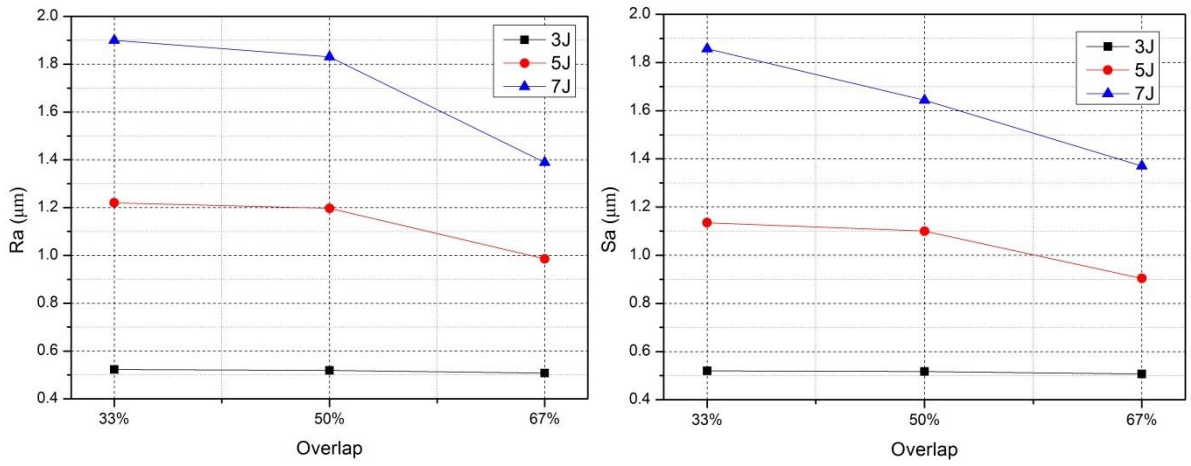

Figure 10.6 The distribution of Ra and Sa with overlap and laser energy.

10.6 Summary

This investigation was focused on the effects of LSP on the surface topography. The work addresses the required parameters for cell response on LSP modified titanium alloys The specific conclusions can be drawn as follows：

- At the microscopic level, surface reliefs were formed when the laser energy and impact number was enough (in this chapter, starting from 5J, 4 impacts). The number

of reliefs increased with laser energy and impacts number reaching its peaks at 7J, 2 impacts and decreasing in 7J, 3 impacts and 7J, 4 impacts.

- By multiple energy and overlap of Laser Shock Peening, different surface morphologies are formed. The surface roughness rises with the increase of laser energy when the overlap was kept constant. In addition, when applying the constant laser energy, the higher overlap leads to lower surface roughness.

CHAPTER-11 Effects of Laser Shock Peening on the Wetting Characteristics of Ti-6Al-7Nb Alloy

Wettability of biomaterial surfaces integrated with surface characteristics play an important role in cell/ protein adhesion and osseointegration. However, effective methods for changing the wetting characteristics of surfaces are still limited. Therefore, this chapter is focused on the modification of wetting characteristics using laser shock peening (LSP). In particular, the effects of laser energy and beam footprint overlap of LSP were explored on Ti-6Al-7Nb alloy, quantified by using the measurement of dynamic contact angle, followed by determination of the surface free energy and work of adhesion. Surface modification by LSP was conducted at laser energies of 3J, 5J, 7J, & overlap of 33%, 50%, 67%. In this work, the effects of the above variables on contact angle, surface free energy and adhesion. The contact angle was measured using the needle-in method with sessile drops profile filled separately by two different liquids (distilled water, ethylene glycol) to acquire surface-free energy including dispersion and polar components, with subsequent calculation of the work of adhesion.

11.1 Introduction

Ti-6Al-7Nb titanium alloy has been widely employed in clinical application due to its excellent biocompatible and outstanding mechanical properties [292-294]. However, due to variety reasons such as aseptic loosen[295], fracture[296], wear and corrosion[297], the implants could failure inside human body after the first clinical surgery, resulting in another replacement surgery which is highly risks and money costly. To avoid or delay such secondary surgery, it is necessary to prolong the service life of implants which requires not only improve the mechanical properties, but also biocompatibility of titanium alloy. After implantation, titanium and its alloys initially react with the host tissue that the reaction determines the healing speed or long-term performance of the implants. This performance depends on the physicochemical parameters of implant surfaces including surface free energy, wettability, and surface roughness. These surface properties, especially wetting characteristics, have a great influence on the cell/protein adhesion, growth, proliferation and differentiations after being inserted into the human body in the early stage. Therefore, it is crucial to acquire a suitable surface wettability for the success of a clinical implantation. And these wetting characteristics are mainly determined by the material itself. But, by means of surface modification methods, the surface wettability could be changed within some extend range, even from hydrophilic to

super-hydrophobic[298-300]. In terms of medical implants biomaterial, Gentelmen *et al* [301] and Groth *et al* [302]reported that 60º-70º contact angle of material surfaces benefits cell the integration of cell/implants and 65º contact angle is thought to be an ideal levels of cell attachment and spreading.

Moreover, another factor which is the by-product of surface modification-----roughness also have association with the surface wettability. De Silva *et al* [303]found that roughening surfaces could introduce physico-chemical changes thereby affecting the wettability and surface free energy. Comparative high surface roughness may lead to an increase of stress concentration. Therefore, acquiring biocompatible surface topography is quite important as a modification method purpose.

Laser shock peening (LSP), as an effective surface improvement method for metal, has been continuously been applied in aerospace industry for over 60 years since it was firstly invented [113, 304] in the 1960s. It has been successfully applied in improve the metallic mechanical properties such as wear-resistance, corrosion resistance and fatigue life [168, 305-307]. In recent years, researchers start to seek an application for LSP namely medical industry. Mannava et al. [163] applied LSP on the spinal implant rod to increase fatigue strength in order to decrease the back pain of end-user. Caralapatti et al. [124]and Guo et all.[166] found that the corrosion resistance performance of biodegradable magnesium and magnesium-calcium alloys could be enhanced by LSP. Additionally, the fatigue performance of MgCa alloy subject to LSP was also improved, observed by Sealy et al [262]. Zhang et al [171] also demonstrated the tensile and fatigue strength of AZ31B magnesium alloy was significantly increased. Furthermore, in our previous work[186], the mechanical properties of Ti-6Al-7Nb alloy such as wear resistance were improved by multiple laser shock peening.

More recently, most research of medical metals (magnesium and titanium) subject to LSP are focusing on the improvement of mechanical properties. However, in terms of the effect of LSP on the wettability of titanium alloy, the research is still blurry. As the metallic manufactured implants would integrate with cells/proteins in *vivo*, the surface wettability of LSPned metals must be also evaluated. Thus, In this work, it is the first time to evaluate the effect of two LSP parameters------laser energy and overlap on the wettability of Ti-6Al-7Nb titanium alloy. On account of this, our research group have attempted to study on the effect of LSP on the topography, microstructure, wetting characteristics, and calculated the surface free energy and work of adhesion of orthopaedic titanium specimens subject to LSP. This work will develop

optimum LSP processing parameters for acquiring suitable surface wetting characteristics which further will be seen as a fundamental factor of cell adhesions.

11.2 Analysis of Wettability

11.2.1 Wetting characterization

The wetting circumstance is normally characterized by Contact Angle (CA) which describes the surface tension at the interface among the three-phase (liquid/gas/solid) system, shown in Figure 11.1. And this interaction can be described by using Young`s equation (11-1)

$$\gamma_{SG} = \gamma_{SL} + \gamma_{LG} \cos\theta \tag{11-1}$$

Where $\cos\theta$ is a single-valued equilibrium contact angle; γ_{SG}, γ_{SL}, γ_{LG} are the solid/gas, solid/liquid, liquid/ gas interfacial tensions.

However, Young`s equation can only be applied at the assumption that the surface is homogenous, physically and chemically inert to the liquid [308]. Whereas, in real surfaces, due to the surface roughness, there are more than one equilibrium contact angle on the surface. Therefore, in terms of real surfaces which are higher than 0.5 um, the dynamic contact angle including advancing and receding contact angle are employed as the equilibrium contact angle.

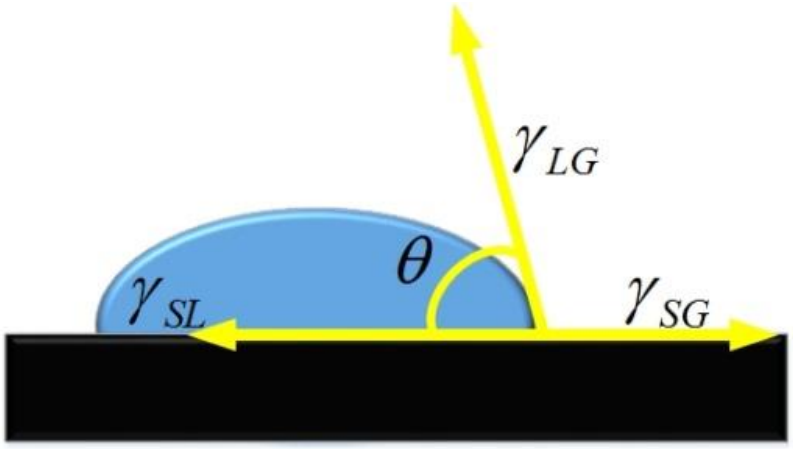

Figure 11.1 A schematic of a liquid drop showing the quantities in Young`s equation.

2.3.1 Hysteresis measurement

The dynamic contact angle is produced in the course of wetting or de-wetting, which represented as advancing angle and receding angle separately which results in the contact angle Hysteresis (11-2) [309].

$$H = \theta_{Ad} - \theta_{Re} \quad (11\text{-}2)$$

Where θ_{Ad} is advancing contact angle and θ_{Re} is receding contact angle. The contact angle hysteresis H is also defined as the arithmetic difference which describes the wetting ability of the surface.

It should be noted that the advancing angle has been commonly used for calculated the surface interfacial tensions as the surface roughness has less influence on the advancing contact angle, compared to the receding contact angle.

In order to acquire the advancing contact angle, sessile drop goniometric method was used via a instrument OSCA20 developed by Dataphysiscs, Germany (Figure 11.2), which the measurement was conducted automatically, by filming in the course of wetting(advance angle) from de-wetting(receding angle) at the room temperature (22±2℃). At first, a liquid droplet of 0.5μl was dosed onto the surface by a syringe pump. But the syringe needle was still inserting inside the drop. Then, the amount of 10μl liquid with the inserting velocity of 0.5μl/s was continuously pumped onto the surface, expanding the volume of the original drop lasting for 20s. After that, the drop would keep stable as the syringe stops pumping in liquid for 10s. By the end, all liquid would be preceded by the syringe with the same velocity. In every second of the course, the images were recorded and analysis by the Software namely SCA 20 for dynamic contact angle. A typical Advancing and receding angle data are shown in Figure 11.3. The advancing and receding angle are separately the mean value of the contact angle during the wetting and de-wetting course. The schematic images of the advancing angle and receding angle are shown in Figure 11.4.

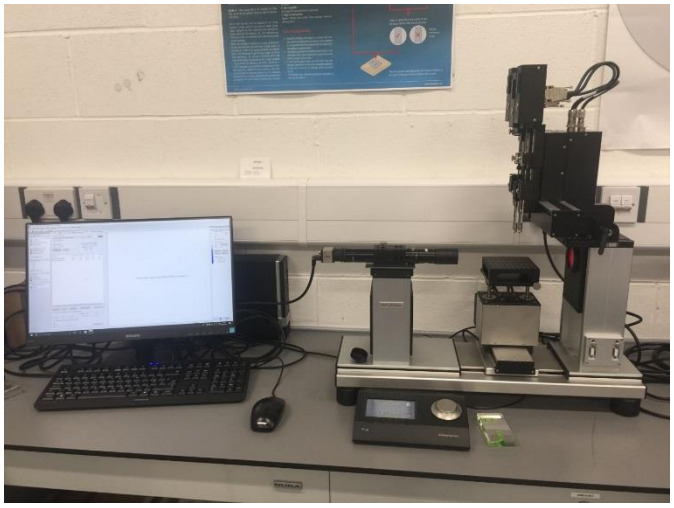

Figure 11.2 Image of Goniometry instrument (OSCA 20, from Coventry University)

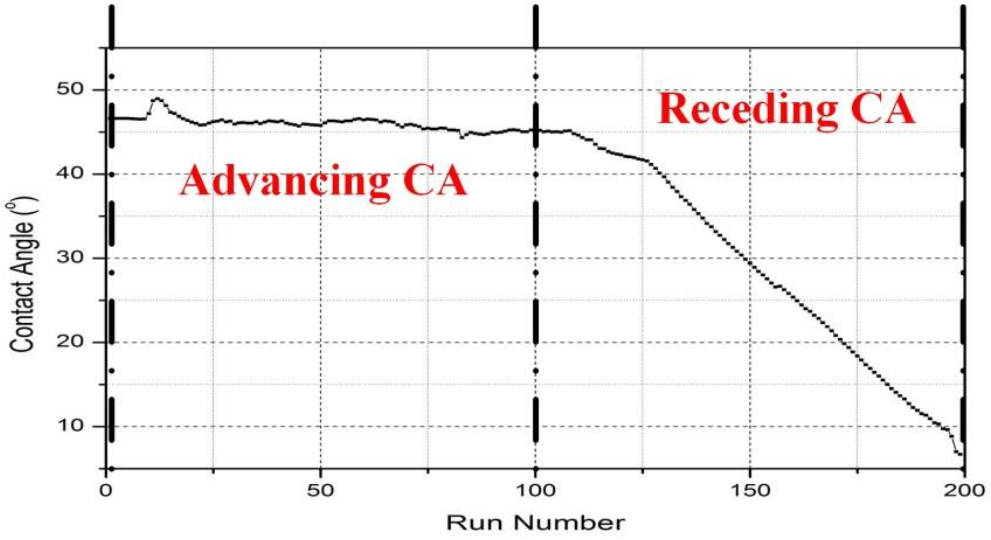

Figure 11.3 The typical advancing angle and receding angle collected from the contact angle plot diagram.

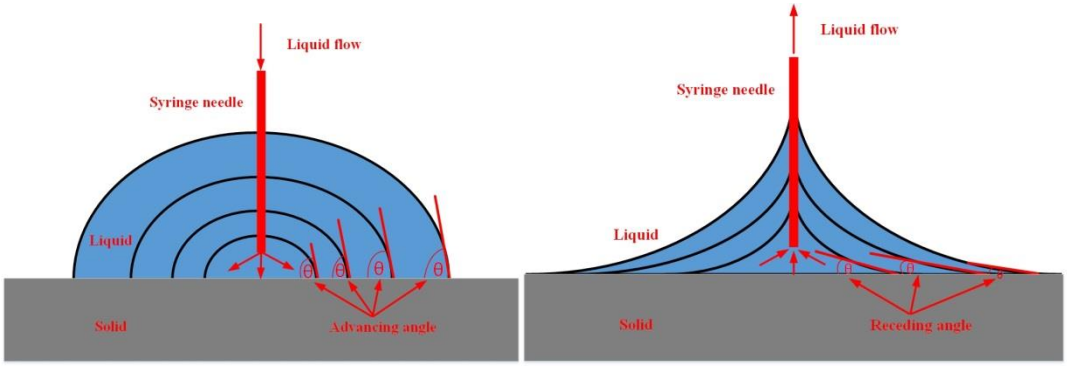

(a)

Figure 11.4 Schematic of advance angle(a) and receding angle(b)

2.3.4 Surface free energy

By dropping different test liquid onto the solid surface, the surface free energy (SFE) of a solid can be calculated using several theoretical models such as Fowkes method [310], Owen-Wendt method [311] and Van Oss-Chaudhury-Good method [312] etc. In this work, Owens-Wendt-Rabel-Kaeble(OWRK) model was selected to quantitate the surface free energy[313]. The equation is shown in the following:

$$\gamma_{SL} = \gamma_S + \gamma_L - 2\sqrt{\gamma_S^d \gamma_L^d} - 2\sqrt{\gamma_S^p \gamma_L^p} \tag{11-3}$$

Where γ_{SL} is the interfacial tension of solid/liquid tension, γ_S is the solid free energy, γ_S^d is the dispersive part and γ_S^p is polar of the solid surface free energy. γ_L^d is dispersive part of test liquid and γ_L^p is a polar part of test liquid. Combined with Young`s equation, equation (1) is acquired below:

$$\frac{\gamma_L(1+\cos\theta)}{2\sqrt{\gamma_L^d}} = \sqrt{\gamma_S^p} \times \sqrt{\frac{\gamma_L^p}{\gamma_L^d}} + \sqrt{\gamma_S^d} \tag{11-4}$$

The total surface free energy γ^T is consist of the polar components γ^p and the γ^ddispersive components are shown in the equation (11-5):

$$\gamma^T = \gamma^p + \gamma^d \tag{11-5}$$

Therefore, to quantitate the surface free energy of a solid surface including polar part and dispersive part, at least two kinds of test liquid are needed. In this work, distilled water and ethylene glycol was employed for calculating the total surface free energy. The values of surface-free energy, and its components of distilled and ethylene glycol are shown in table 11.1.

Table 11.1 the surface free energy γ^T, polar part γ^p and dispersive part γ^d of distilled water and ethylene glycol.

	Total surface energy mN/m	Dispersive part mN/m	Polar part mN/m
Distilled water	72.8	21.8	51
Ethylene glycol	48	29	19

2.3.3 Work of adhesion

The work of adhesion is defined as the work which is needed to separate the interface from the equilibrium state of two phase(liquid/solid) to a separation distance of infinity [314]. The work of adhesion is described as following equation (11-6):

$$W_a = \gamma_L + \gamma_S - \gamma_{SL} \tag{11-6}$$

According to OWRK equation (3). The work of adhesion can also be expressed below (11-7):

$$W_a = 2(\sqrt{\gamma_l^d \gamma_s^d} + \sqrt{\gamma_l^p \gamma_s^p}) \tag{11-7}$$

The above equation is based on the known components and parameters of liquid and solid. If not, the work of ahesion can also be calculated by Young-Dupree equation(11-8) [315]

$$W_a = \gamma_L(1 + \cos\theta) \tag{11-8}$$

11.3 Wetting characterization

11.3.1 Contact angle and surface free energy

The advancing contact angle of Ti-6Al-7Nb titanium before and after LSP with distilled water and ethylene glycol is presented in Figure 11.5. For both Figures 11.5(a) (b), the contact angle curves are similar. As a baseline, the contact angle of untreated samples with two liquids are separately 53.96(distilled water) and 41.87(ethylene glycol). Comparing this, all LSPned contact angles are higher than the untreated which Prbhakaran *et al* [133] and Caralapatti *et al* [128], in their works have found the same conclusion. The highest water contact angle is 79.94, and the ethylene glycol contact angle is 58.8, which is 3J33%. Meanwhile, the lowest water one is 64.09, and ethylene glycol one is 47.12, which is 7J67%. What is more, observing the two figures form longitudinal direction, contact angle values rise with the increase of laser energy at the same overlap. However, in the transverse way, the contact angles decreased with the increase of overlap at the same laser energy level.

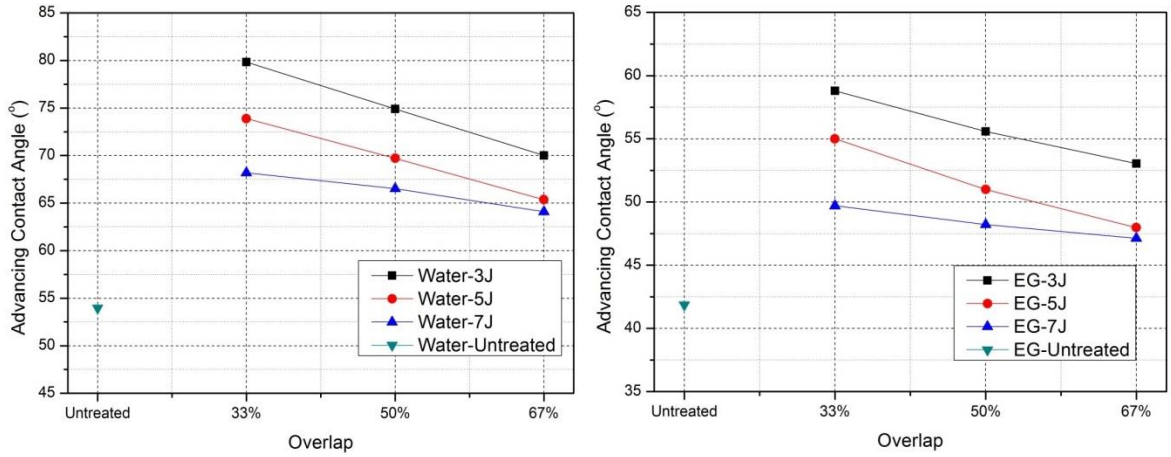

Figure 11.5 Advancing contact angle on both untreated and LSPned specimens for distilled water (a) and ethylene glycol (b).

Table 11.2 Advance contact angle for Ti-6Al-7Nb titanium alloy after LSP.

	Distilled water			Ethylene glycol		
Overlap	3J	5J	7J	3J	5J	7J
33%	79.84	73.89	68.18	58.8	55	49.7
50%	74.91	69.71	66.52	55.58	50.99	48.22
67%	70.01	65.36	64.09	53.04	47.98	47.12208

Calculated by using ORWK model with two different liquids (distilled water and ethylene glycol), the surface free energy and its components is given in table 11.3 and Figure 11.6

Table 11.3 The surface free energy and its components of Ti-6Al-7Nb post laser shock peening and untreated.

	$\gamma^T/(\gamma^p:\gamma^d)$					
Overlap	3J		5J		7J	
33%	27.65		30.44		34.44	
	16.49	11.16	13.7	16.74	12.73	21.7
50%	29.89		33.34		35.68	
	14.23	15.67	13.13	20.21	12.38	23.3
67%	32.87		36.55		37.58	
	11.55	21.32	11.47	25.08	10.99	26.59
Untreated	47.68					

	6.74	40.94

In terms of SFE, the highest value is obtained in untreated specimen with the value of 47.68mN/m. Among the LSPned samples, specimen 7J67% reaches the highest surface energy (37.58 mN/m) while the lowest is specimen 3J33% (27.65mN/m). According to the Wenzl`s theory [316], if the surface roughness is increased, the contact angle should be decreased. However, in the real application, the contact angle of specimen after LSP get raised. This is because the surface free energy of the LSPned specimen are decreased due to laser ablation. (Normally, SFE is inversely proportional to CA). In the same column (overlap), the SFE of 7J specimen are always the highest among there different laser energy, while the one of 3J is the lowest. Additionally, at the same laser energy level, SFE has a positive correlation with the overlap. What is interesting, the SFE difference among three laser energy becomes smaller when the overlap increased from 33% to 67%.

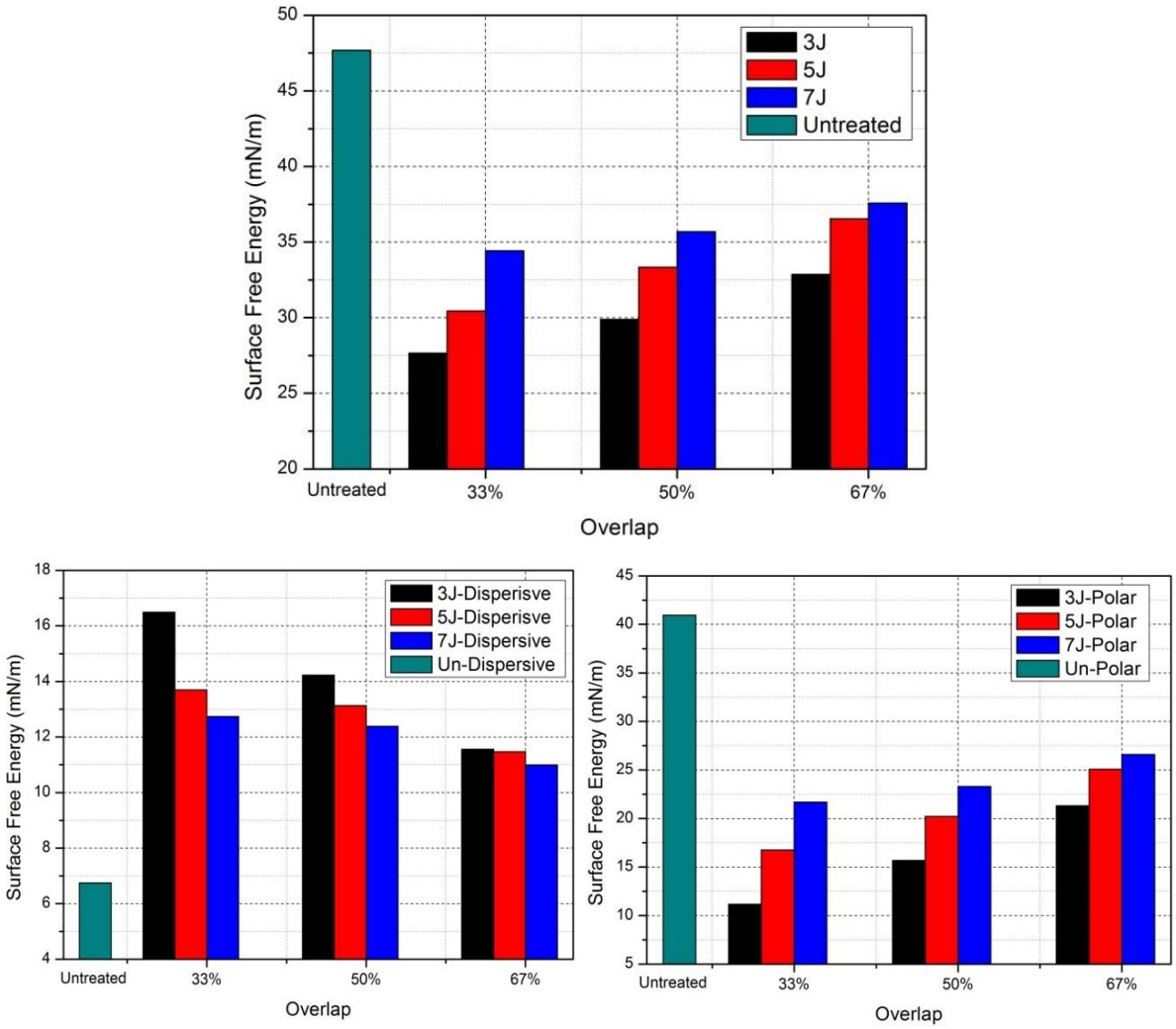

Figure 11.6 SFE in (a); its components dispersive in (b); and polar (c).

In Figure 11.6 (b) and (c) exhibit the distribution of dispersive component and the polar component of Ti-6Al-7Nb alloy. It can be seen that the 40.94mN/m out of 47.68mN/m is polar component, and dispersive part is 6.74mN/m. The polar part accounts for 85.78% in the total SFE. However, after LSPned, the ratio has been dramatically changed. In Figure 11.6(c), the dispersive columns have a similar tendency as well as the SFE columns. But, with regard to dispersive component distribution, all dispersive parts of LSPned are higher than the one of untreated. Especially, specimen 3J33% get the highest with the value of 16.49mN/m, onward decreasing with the increase of overlap and the laser energy separately.

11.3.1 Work of adhesion

The adhesion work of Ti-6Al-7Nb specimens for wetting liquids (distilled water and ethylene glycol), calculated from equation (ORWK), is given in Figure 11.7 (a)(b) and Table 11.4. For both liquids, the highest Wa is produced in the untreated specimen (Distilled water:115.63mN/m; Ethylene glycol:83.743mN/m). The adhesion work of 7J is higher than others laser peening processed titanium alloy in the same overlap. And in the same laser energy, the adhesion work rises with the increase of overlap for both wetting liquids. What is more, when the application is distilled water, in the 7J specimens, the difference is quite small with the value of 4.75º, while one of the 3J specimens is 12.05º. Using ethylene glycol, such values are 1.62 º(7J) and 4 º(3J).

Table 11.4 The work of adhesion of distilled water and ethylene glycol on the LSPned specimens.

	Distilled water			Ethylene glycol		
	3J	5J	7J	3J	5J	7J
30%	85.64175	93.00071	99.85917	72.8653	75.53167	79.04591
50%	91.75246	98.045	101.80563	75.12855	78.21389	79.98107
67%	97.68713	103.15145	104.6106	76.86006	80.13072	80.66105
Untreated	115.63187			83.74373		

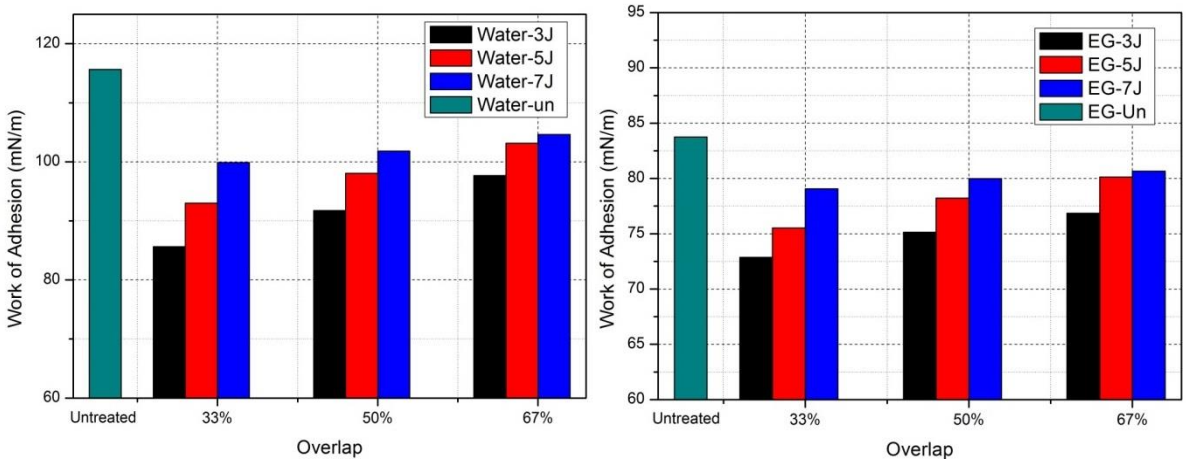

(a) (b)

Figure 11.7 Work of adhesion of distilled water(a) and ethylene glycol (b) onto the laser shock peened and untreated specimen surface.

11.4 Discussion

As mentioned in the previous paragraph, the wettability is determined by surface topography and surface physic-chemistry properties [317]. In terms of chemical changes, laser shock peening has been proved that no new chemical substance will be introduced on the material surface after LSP. The real results which could affect wettability of material are surface topography and surface grain refinement from the aspect of Laser shock peening. However, due to high affinity to oxygen, a thin composition oxide layer mainly consisted of TiO_2, Ti_2O_3, and TiO is immediately formed when titanium is exposed to air. The thickness of the film will increase with time according to environmental conditions. With the isolation from the substrate by TiO_x, the contact angle of wetting liquid is determined by both the oxide layer and the refined surfaces. Researches [318, 319] have confirmed that the surface free energy of ultrafine surface is higher than the one of coarse grain material in titanium alloys with thin TiOx layer. In previous section 3.3, the surface microstructure before and after LSP show that average surface sub-grain is refined from 266.5nm to 150nm which is one of the evidences of the improvement of the surface-free energy post LSP.

What is more, surface roughness and surf ace topography also play an fundamental role in the wetting behaviour. As mentioned above, Wenzel introduces a surface roughness factor r into to Young`s equation showing in the following equation.

$$\cos\theta_W = \frac{r(\gamma_{SG}+\gamma_{SL})}{\gamma_{LG}} = r\cos\theta_Y \quad (11\text{-}9)$$

Where r is the surface roughness factor; the equation describes the mechanism that roughen can enhance the wetting behaviour of the solid surface. In another case, Cassie-Baxter further considered the material surface randomly consists of n sorts of materials. And every piece of materials is characterized by the factor of surface characteristics namely surface tension or surface energy i.e. The Cassie-Baxter equation is expressed as follow

$$\cos\theta_{CB} = \sum_i^n f_i(\gamma_{i,SV} - \gamma_{i,SL})/\gamma_{LV} = \sum_i^n f_i \cos\theta_{i,Y} \quad (11\text{-}10)$$

Where $\gamma_{i,SV}$ and $\gamma_{i,SL}$ is the surface energy/tension of each piece material. And f_i is the respective material fraction with $f_1 + f_2 + \cdots + f_n = 1$. It should be noted that in some specific application, both regimes can coexist on the same surface. The schematic diagram of Wenzel`s model and Cassie-Baxter Model is shown in Figure 11.8.

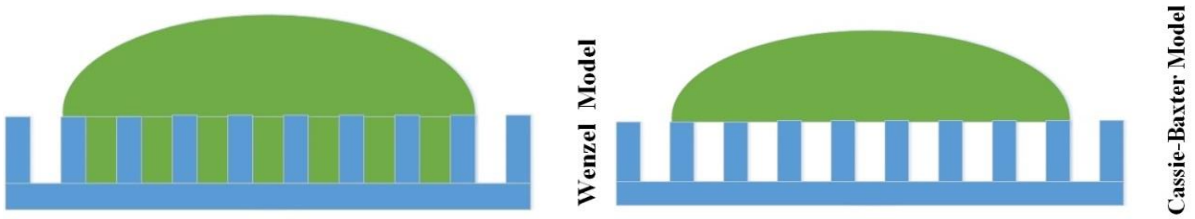

Figure 11.8 Schematic of Wenzel Model and Cassie-Baxter Model.

In the case of LSPned specimens, obviously, the mechanism is not determined by Wenzel regime, while it should be the Cassie-Baxter or the combination model. In Figure 11.9, the relationship between surface roughness and surface free energy is shown. At the same laser energy level, surface roughness has a negative correlation with Surface free energy. Additionally, compared to 7J specimens, the curve of 3J is steeper, nearly vertical to the surface axis.

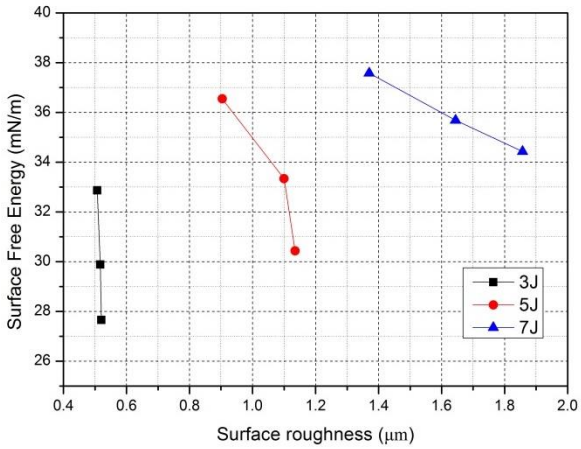

Figure 11.9 Distribution of Surface Free Energy with average surface roughness (Sa).

To explain why the contact angle of 7J specimen is higher than the ones of 3J and 5J specimens in the same overlap, the following statement is addressed. When the overlay keeps consistent, laser energy as a variable, the surface morphology also keeps consistent showed in the 3D and 2D images in Chapter 10. In particular, the shape of surface characteristics namely grooves and dimples are the same. The difference among the surface morphologies is the topography of the groove and dimple introduced by variable laser energy. Compared to an ideal surface, when a liquid drop sits onto such grooves and dimples, according to Wenzel, The defects (grooves and dimples) on the surfaces will be filled by the wetting liquid. Thus, the amount volume of liquid is lower than same amount liquid onto the flat surface. The mechanism of the above case can be explained by Wenzel`s Model. The higher the surface roughness is, the lower contact angles are. However, it can be only applied among the specimens subject to laser shock peening.
Furthermore, when the laser energy keeps consistent, overlap as a variable, the contact angle is proportional to overlap (surface roughness). Therefore, in this case, the Wenzel`s Model is not suitable while the Cassie-Baxter Model or the combination of both is.

11.5 Summary

To summarise this work, laser shock peening can be used as a method to modify the wettability of the solid surface. One of its advantages is that LSP does not introduce new chemical substance onto the solid surface with accurate controlled processing course. Overall, LSP is used to reduce the surface free energy by applying variable laser energy. Furthermore, adjusting the ratio of dispersive and polar components can be fulfilled by changing the overlapping during the LSP course. Based on the wetting characteristics, further cell culturing work could

keep going on which will introduce in the next chapter. The specific conclusions can be made below：

- It was observed that an increase in overlap leads to an inversely proportional increase in contact angle at the same laser energy level, and increasing the laser energy will lead to the decrease of contact angle when apply in the same overlap. Due to the negative correlation to contact angle, the surface free energy, and work of adhesion have an opposite correlation with laser energy and the overlap. It should be noted that with the increasing overlap, overall, dispersive component decreases while the polar part of surface free energy increases.
- In untreated and LSPned specimens, the reduction of surface free energy is used to address why the contact angle is improved after LSP. Comparing the contact angle of variable laser energy at the same overlap, the main mechanism can be explained by Wenzel`s model. Additionally, the effect of overlap at the same laser energy can be explained with the Cassies-Baxter model as the increase surface roughness leads to an inversely proportional increase in Contact angle.

CHAPTER 12 In-v*itro* Biological Examination of Laser Shock Peened Ti-6Al-7Nb Alloy

This chapter consists of a biological evaluation on Ti-6Al-7Nb, subject to LSP treatment. The osteoblast-like MG63 cells were employed to measure the cell viability using MTT assay. The cells were seeded and cultured on the culture plate as the positive control, LSP treated surfaces and untreated surface for 24hrs and 72hrs. The cell morphologies were characterized by fluorescence microscope. The fluorescence images indicated that the cells can be attached onto the surface subjected LSP which in other words also suggested that LSP is not cytotoxic to MG 63 cells. The MTT results show that the cell viability on the LSPned surfaces is comparatively lower than that of the untreated after 24hrs. However, after 72hrs, the cell viability on LSPend surfaces was dramatically improved. Based on 24hrs and 72hrs results amongst the laser shock peening Ti-6Al-7Nb, the 5J,33% was the best LSP parameters for improving the cell viability in all LSP parameters.

12.1 Introduction

Osseointegration refers to “functional ankylosis (bone adherence)”, where new bone is laid down directly on the implant surface and the implant exhibits mechanical stability defined by Schroeder [320]. This is considered as a prerequisite for load bearing implant and for the long-term clinical success for orthopaedic implants. In particular, cell adhesion, proliferation, differentiation and migration influence the osseointegration performance. Therefore, the osseointegration of biomaterials is a crucial factor for implantation surgeries [321]. The implants could failure in the early stage due to the lack of osseointegration between the bone and the implant, or after a long- service time then the implant factures due to the metal fatigue problem. The former leads to the implant loosening which accounted the largest percentage in the failure reason for the second surgeries. The later could be resolved by applied suitable surface modification techniques on the biomaterials.

Long-term osteointegration of implants with bones has always been one of the most crucial aims for considering the recovering of patients after implantations [322]. Once an implant was inserted into the human body, it would initially react with host issue, involving a series of physiochemical changes, ranging from the molecular level to the cellular level [323]. The reaction determines the healing speed and long-term performance of implants, affected by the surface physicochemical properties of biomedical materials such as surface topography,

wettability electricity properties, the pore size of biomaterials and bioactive molecules. Therefore, surface modifications to improve the biocompatibility of biomaterials are considered to be crucial to enhance the integration of interface where cell/protein adheres.

In particular, to acquire a certain surface roughness and enhance osseointegration, Flamant *et al* [324] , applied hydrofluoric acid (HF) to a dental ZrO_2 to increase roughness. It was found that a concentration 40% HF gives a uniform surface morphology with the shortest etching time. Blasting techniques including sandblasting, alumina blasted, and micro-abrasive blasting are also useful methods to roughen surfaces to promote, bio-compatibility. Gunay-Bulutsuz *et al* [325] investigated the cell response of sandblasted on ultrafine and coarse titanium surfaces. Ultrafine and blasted surfaces are more biocompatible for human gingival fibroblast cells. What is more, Granato *et al* [326], evaluated the effect of micro-abrasive blasting and alumina-blasted/acid-etched on pure Ti surfaces. In comparison to as-machined surface, both surface treatments in terms of roughness lead to the improvement of osseointegration in pure Ti substrates. Additionally, compared to conventional chemical methods, laser texturing enabled a wide variety of structures at the nano and the micro-scale, and the process is fast, reproducible, controllable and contactless.

Therefore, as discussed in the above literature reviews, a variety of surface modification methodologies or fabricated techniques, especially, laser-based techniques, were employed to improve the osseointegration of implants. It is reported that laser introduces surface features such as grooves, dimples, lines are beneficial in strengthening the bonding of implants and human bones [327]. Raimbault *et al* [111], the cell behaviour on a femtosecond laser-fabricated titanium surface at nanoscale and microscale. Cells are showing more sensitivity to the nanoscale structures which will be potential for titanium modification in orthopaedic or dental applications. Batal *et al* [328] employed a nanosecond pulse laser for surface texturing on CoCrMo alloy and compared the cell viability of Saos-2 osteoblast like cells on an as-received and various laser textured surfaces. A laser textured surface presented a better performance in terms of cell viability. What is more, a CO_2 laser was used to modified the surface of nylon 6,6 and the mesenchymal stem cell was employed for evaluation. The viable cell counting was increased to 60,000 cells/ml due to CO2 laser surface treatment. What is more, by applying 3D printing technique, the young`s module of orthopaedic scaffolds can be maintained close to that of bones with interconnected porous network which favouring the osseointegration and

relieving the stress shielding effect [329]. It is also a new promising direction for achieving long-term osseointegration of implants.

Laser based technique namely: Laser shock peening, is a very useful method to for surface modification [186] It has been widely used in aerospace and auto industry for decades [330]. It is promising that LSP could also be employed in extending implant service life by not only improving mechanical properties but also enhancing the biocompatibility. LSP has its own advantages in medical applications, compared to conventionally employed surface modification techniques such as sandblasting, shot peening, laser texturing and so on. In comparison to sandblasting, no contaminations will be left after LSP. This is because LSP is a cold working method and laser would not contact metal surfaces directly rather than exploding the absorptive layer generating plasma-driven shock-waves, which causes material deformations. With the same capability like LSP, shot peening could also introduce a stable compressive residual layer in the treated materials [331]. However, when it comes to the complex medical implants, components such as acetabular, trabecular and proximal tibial, the focused laser beam was able to precisely process the corner of the complex components, where conventional shot peening cannot reach. Besides that, due to the microstructural deformation caused by high plasma pressure during the peening processing, surface morphologies were generated by applying laser energy and foot-print overlap, which means LSP also could benefit orthopaedic or dental implant osseointegration due to introducing certain surface roughness. The features of topographies after LSP, namely: grooves and dimples, are contributed to the cells/proteins adhesion and proliferation on the implant surfaces. This in turn strengthens the mechanical interlock between the implant and the bones. More than that, the stable compressive residual stress layer which benefits fatigue will be formed after LSP that is what other laser treatments (such as laser texture) are not capable of.

As a surface modification technique, the first and foremost point is that this surface technique should not be any cytotoxic to any biomaterials. Based on that prerequisite, an in vitro biological evaluation was carried with determining the cell viability of LSPned surfaces by using MTT assay for 24hrs and 73hrs. The cell morphology was characterized by fluorescence microscope. In this work, the evaluation of the cell viability on the LSPned is conducted for the first time. No such paper hitherto has shown investigations in relation to any parameters of laser shock peening discussed herein at any depth. Moreover, the work in this chapter could directly benefit the end-users who will be suffering the pain caused by implant failures.

12.2 In vitro biological evaluations

The osteoblast-like MG63 cell was employed in this biological evaluation. MG63 cells have been widely used in evaluating the biocompatibility of bio-materials as they have lots of characteristic in common with osteoblasts [332]. The MG63 cells were cultured in tissue culture flasks in Dulbecco's modified Eagle's medium (DMEM), supplemented with 10% foetal bovine serum (FBS), 100 U/mL penicillin and 100 mg/ml streptomycin. Then incubated at 3˚C CO_2 humidified incubator. Once confluent they were split, cells were treated with 0.05% trypsin/0.02% EDTA, obtained by centrifugation and resuspended in DMEM. Cell counting was performed visually by using a haemocytometer, following seed 1×10^4 cells/ml cells onto the surfaces. The MG63 cultured on the plate was used as the positive control. This is a known technique implemented by Nayak *et al* [333].

12.2.1 Methyl-tetrazolium (MTT) assay

In order to check the biocompatibility against live cells, the metal samples were sterilized by washing with sterile water, ethanol and PBS and immersed in DMEM media for about 15 days. The spent media with immersed samples and leachate if any, was used to carry out the study. Biocompatibility of the metal samples was evaluated using osteosarcoma cells (MG63). The cells were grown in DMEM supplemented with 10% FBS, penicillin (100 I.U/ml) and streptomycin (0.1 mg/ml) all obtained from HiMedia Laboratories, India. The cells were maintained in a humidified incubator (ESCO Cellmate Biotech, Singapore) at 37℃ with 5% CO_2 environment. The cells (Mg63) were seeded onto the 24 well plates at $1x\ 10^4$ cells per well and allowed to attach overnight with complete media. Thereafter, 24 hours the complete media was aspirated and the immersed media of the metal samples was replaced and the study was done for 24 hours and 72 hours after the change.

After the first day and third day the (3-(4,5-Dimethylthiazol-2-yl)-2,5-Diphenyltetrazolium Bromide) MTT reagent was added (1mg/ml) and incubated for 1 hour after which DMSO was added to dissolve the formed formazan crystals. The dissolved solution was transferred to 96 well plates and the absorbance was measured using a spectrophotometer (Read well touch, Robonik, India) at a wavelength of 570 nm. Reported values are the mean of 3 replicates and expressed as percentages of the control values.

12.2.2 Fluorescence imaging

The metal samples were sterilized with ethanol followed by washing with PBS and remained in UV light overnight. An equal number of osteosarcoma cells (MG-63) (1 x 10^4 cells) were seeded on the surface of the metal samples. The cells were grown in DMEM supplemented with 10% FBS, penicillin (100 I.U/ml) and streptomycin (0.1 mg/ml). The cells were maintained in a humidified incubator (ESCO Cellmate Biotech, Singapore) at 37 ℃ with 5% CO2 environment. A very minimal amount of media was added initially to prevent the runaway of cells directly on to the surface treated well plate. After 4 hours more media was added to the cells and allowed to culture. The imaging was done on the third day after 20 mins of incubation of cells with nuclear staining dye 4',6-diamidino-2-phenylindole (DAPI from HiMedia).

12.2.3 Statistical Analysis

The whole experiment was repeated there times as mean values with standard deviation. The data were statistically analysed using analysis of variance (ANOVA) for assessing the significance level of the differences between the groups. The possibility P less than 0.05 was considered significant differences.

12.3 Cell Viability using MTT assay and Cell morphology

Figure 12.1 presents the fluorescence images of the attached cells on the titanium surfaces prior to and after LSP after 72hrs. It can be seen that the morphology of cells exhibits spread structure on both surfaces prior to and after LSP in Figure 12. 1A. In the Figure 12.1B, C, D (3J group from 33% to 67% overlap), the cell numbers are increased with the respective laser overlap. However, compare to the untreated, the cell numbers are quite lower after 3J laser energy processing. In 5J groups, the cell numbers are not increased with overlap as cells on the 50% and 67% are comparatively lower than that of 5J, 33% overlap. In comparison to the untreated, the numbers in 5J, 33% and 5J, 67% are higher than that of untreated. In terms of 7J groups (7J, 33%, 7J, 50% and 7J, 67%), only the cell numbers in 7J, 33% is lower than that of the untreated and the lowest among the three variables. 7J, 50% and 7J, 67% are comparatively close to each other.

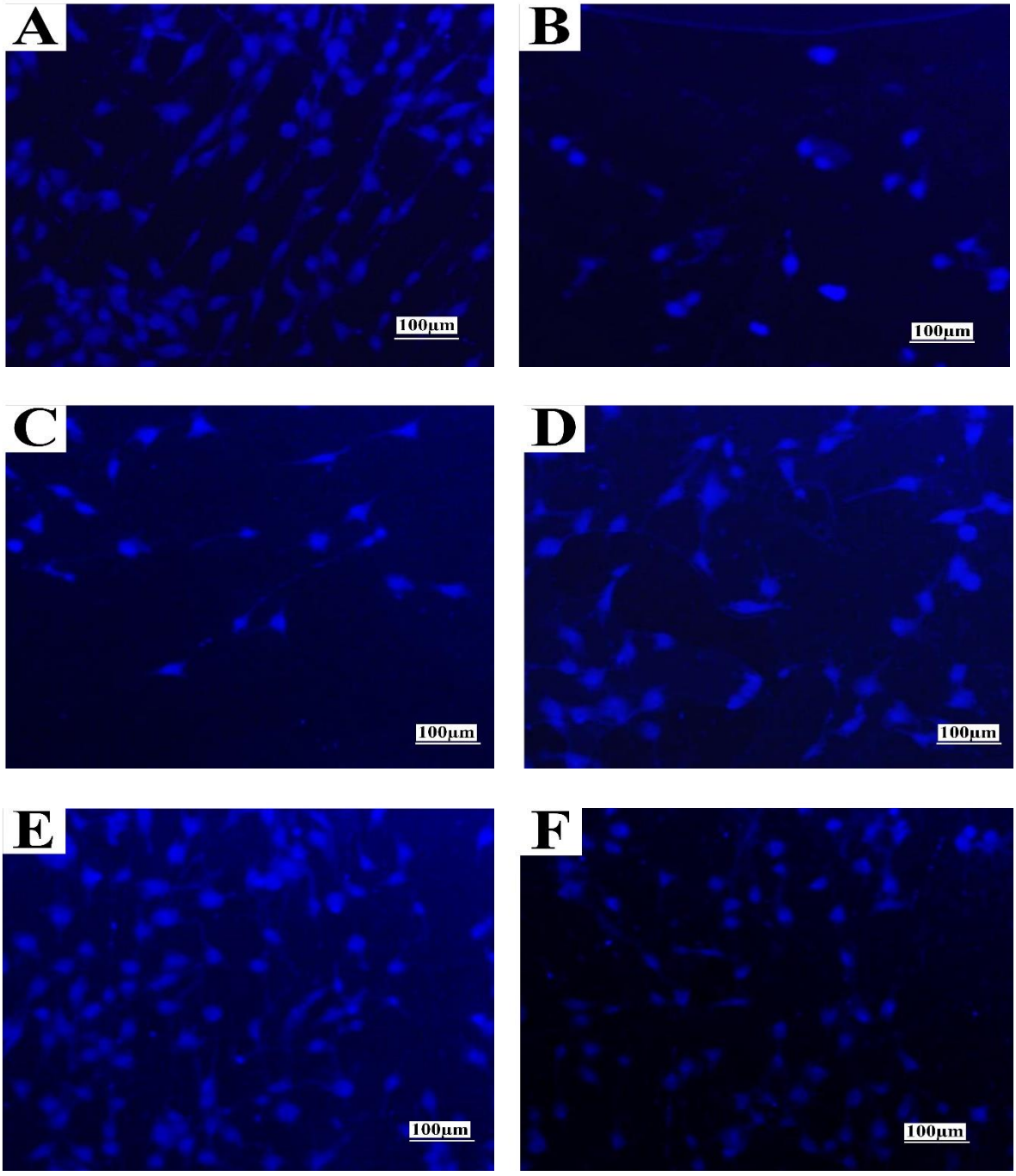
A
100µm
B
100µm
C
100µm
D
100µm
E
100µm
F
100µm

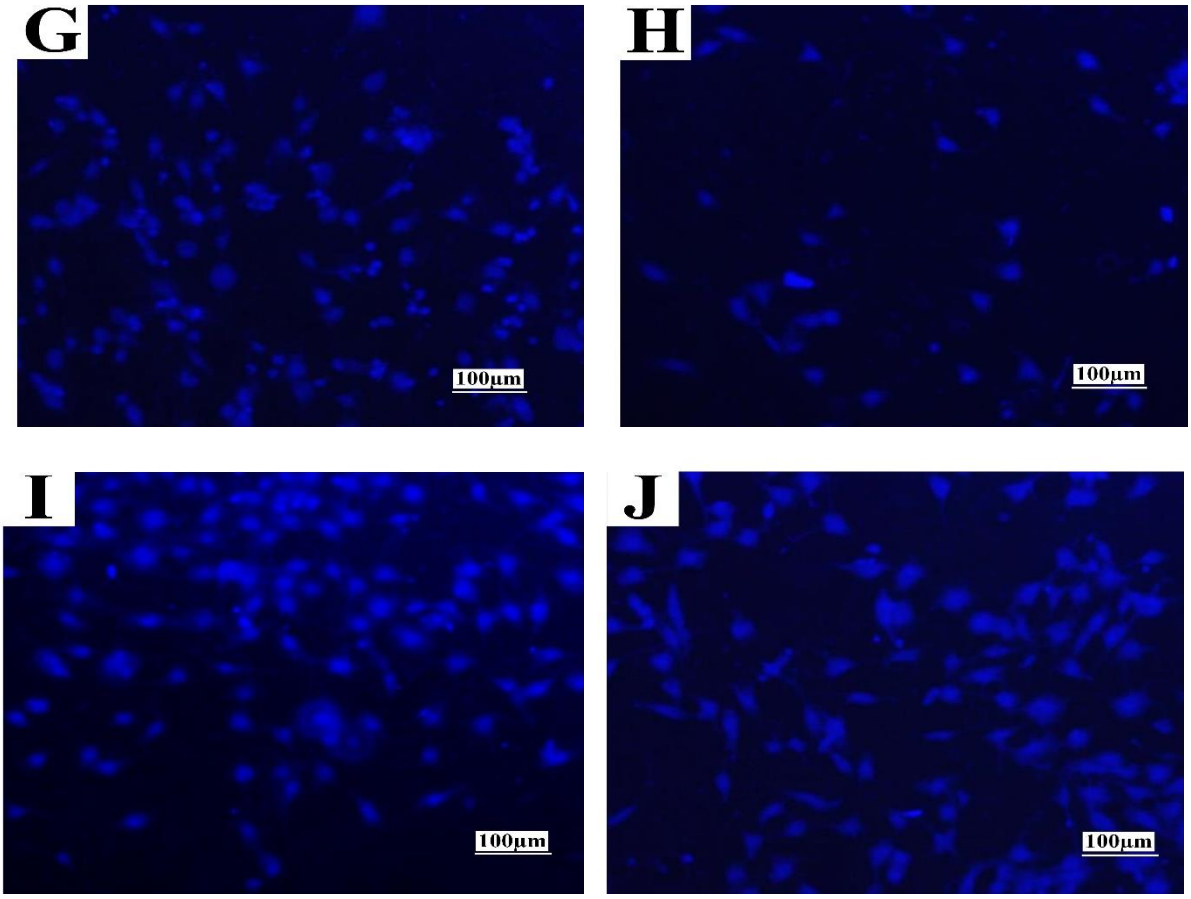

Figure 12.1 Fluorescence image showing cell morphology prior to and after Ti-6Al-7Nb alloy after 72hrs: (A) Untreated; (B) 3J, 33% overlapping; (C) 3J, 50%; (D)3J, 67%; (E) 5J, 33%; (F) 5J, 50%; (G) 5J, 67%; (H) 7J, 33%; (I) 7J, 50%; (J) 7J, 67%.

Figure 12.2 presents the cell viability of MG63 cells after 24hrs and 72hrs on the as-control and the LSPned with MTT assay. Overall, it was seen that the MG63 cells can attach onto both surfaces of untreated and the LSPned, which means LSP is not cytotoxic to Ti-6Al-7Nb alloy. Then, in the data for 24hours group, except 5J, 33% and 7J, 67%; the optical density value of the rest of the LSPned are all lower than untreated. This means the cell viability in the above samples are not higher than that of untreated. There is no signs indicating that laser overlap is correlated with the cell viability of the LSPned.

After 72hours, it can be seen that all optical density value of the LSPned are comparative to or higher than that of untreated. 5J, 50% reached the highest cell with a mean value of 0.82, followed by 5J, 33% (0.79), 3J, 67% (0.73) and 7J, 50% (0.712).

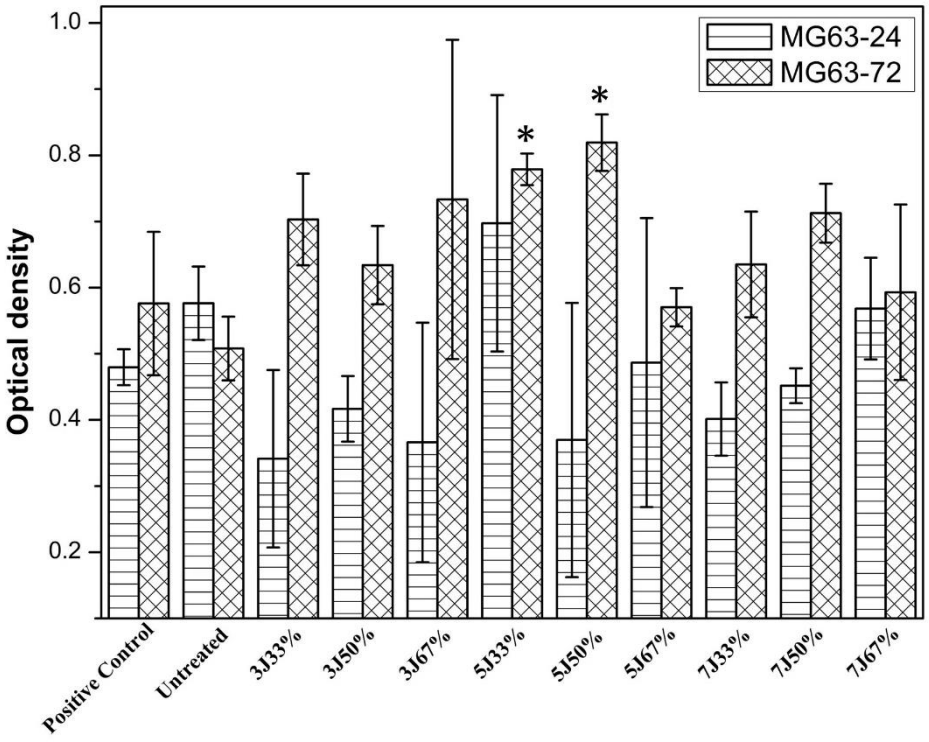

Figure 12.2 showing the absorbance of MG63 cells on the surfaces of positive control, untreated and the LSPned for 24hrs and 72hrs (Data=mean±St. Dev; N=3, *p<.05 compared to the positive control at the same time point).

12.4 Discussion

The confocal images suggest that not all LSP parameters are beneficial to the osseointegration of implant materials despite having a high level of compressive residual stress. It can be seen that cell numbers after some LSP are much lower than that of untreated in the confocal images. These LSP parameters are: 3J, 33%, 3J, 50%, 3J, 67%, 5J, 50%, 7J 33%. Furthermore, in the 1 days MTT result, cell viability of 3J groups, 5J, 50%, 7J, 33% and 7J, 50% are comparatively close to or lower than that of the untreated. This is postulated due to the differences amongst the surface morphologies after LSP. From another point of view, LSP surface treatment can works as a filter function that LSP selects high viability cell and eliminates the unhealthy cells and in turn, could render greater benefits. This meant in the early stages, certain LSP parameters are detrimental to the cell number, and somehow, the cell on the LSPned surfaces will decrease. These results are also in agreement with the work of Bagherifard *et al* [334], who seeded osteoblast cells on shot peened and untreated surfaces for 1,3 and 7 days. It was found that after 1 and 3 days, the viability of the cells of shot peened was lower than that of the untreated. Even after 7 days culture, there were still no significant improvements after shot peened surfaces. However, in our study, compared to 1-day result, the cell viabilities of all LSPned surfaces

were dramatically increased after 72hrs, while the untreated surfaces of Ti-6Al-7Nb, were slightly decreased. This is because the rough surface will be beneficial to the bone-implant interface ossoeintegration. It is the micro features such as dimples, grooves and nano features (reliefs) induced by LSP (Chapter 10) that improved the cell viability on the treated surfaces. What is more, the increased value was found to be comparatively large in 3J group, and sample 5J, 50%.

Overall, amongst 9 LSP parameters, 3 of them: 5J, 33%, 5J, 67% and 7J,6%, exhibited consistent performance in both 1 day and 3 days experiments. Compared to the untreated; the increase of 5J, 67% and 7J, 67%, are not obvious. In addition, after considering the performance in 24hours experiments, although, 5J, 50% was the highest (0.82) in 72hrs experiment, 5J, 33% was the optimal LSP parameters for cell viability as it rendered high cell viability from evaluating all the experiments.

It has been reported by literatures that the biocompatibility of the implant is affected by surface finishing, and the corresponding surface wettability. Surface topographies were characterized by parameters such as root mean squared, maximum valley depth, maximum peak height and skewness *etc*. With that said, the parameters of 3-D mean average roughness Sa was the most used parameter to present implant surface finishing. However, such parameters are not suitable to stand for the periodic surface structures after surface modification as different surface morphologies may have the same surface roughness with totally different wetting properties. Therefore, in this study, considering the relationship between the cell viability and the overlap is not appropriate as the surface morphologies induced by overlap vary from each other at the same laser energy. Keeping the overlap consistent and laser energy variable is because in Chapter 10, the surface morphologies are nearly with varying in the depth of the valley and the height of the peak. It is more reasonable to analysis the relationship by keeping the overlap consistent. Figure 12.3 showed the scatter distribution of the contact angle (water) *vs* the optic density. It can be seen that the highest cell viability exhibits in the range between contact angle of 70°-75°. In 33%, 50% and 67% groups, 5J, 33%, 5J, 50% and 3J, 67% present the highest cell viability which are closed or in the range. If the contact angle is lower than 70° or higher than 75°, the cell viability will comparative lower than that in this range. The fitted third-degree polynomials equation indicated that the optimal contact angle should be located at 71.56°. Tamada *et al* [335], found that the optimal water contact angle for cell adhesion was approximately 70° which is in good agreement from this work. From above discussion, surface wetting properties is the directly influential factor while the surface roughness is also

determining the cell viability by indirectly affects. It should be noted that surface roughness is also an important factor that determines the surface wettability.

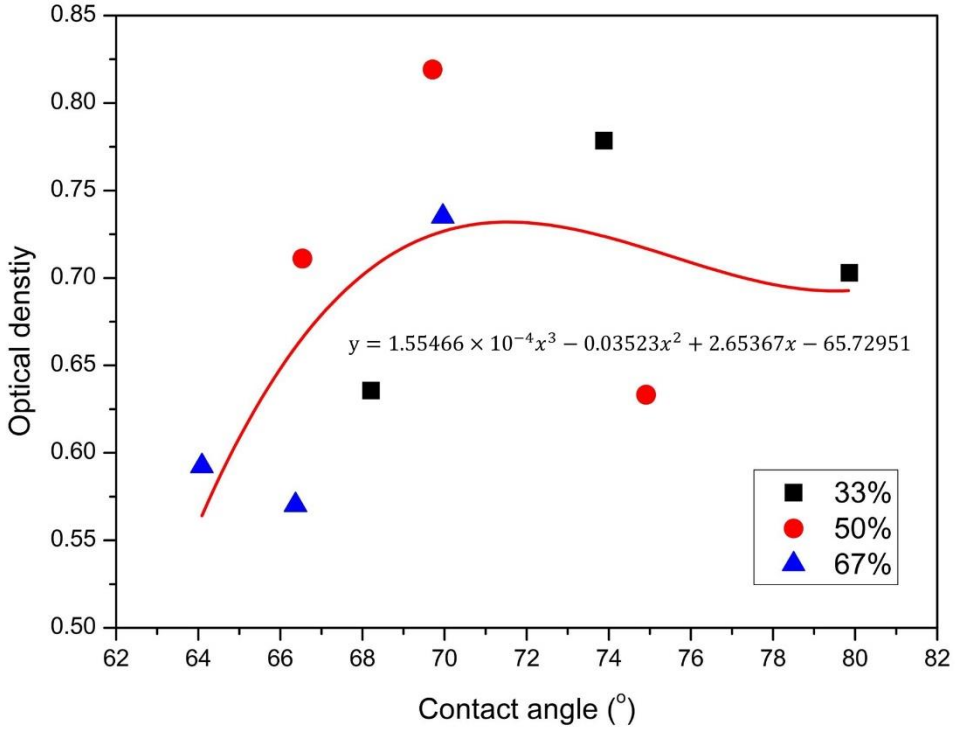

Figure 12.3 plot of contact angle *vs* optical density with the fitting equation.

Combining with the mechanical, interfacial results, properties such as biocompatibility, mechanics, and wettability cannot be all benefited by only one simple LSP parameter. For example, with respect to residual stress and microhardness, 7J, 67% is the optimal LSP parameter leading to maximum compressive residual stress and surface hardening. However, such benefits may be an issue with the corresponding surface morphology. The morphology may also affect the wettability - increasing the contract angle. Therefore, the evaluations of the performance post different LSP conditions need to be considered comprehensively, with a particular requirement and or a specification. It has to be compromised between mechanical and biological properties.

Regarding the LSP parameters of 3J, although, the cell viability after 72hrs was higher than that of 7J treated surfaces, the wear resistance was worser after LSP. This is not acceptable for the medical industry application as wear debris may be worn out inside the human body, leading to early failure of the implant. Thus, low laser energy is not applicable for improving the wear resistance.

In the 5J LSP group, regarding cell viability performance, 5J, 33% and 5J, 50% are comparatively better than 5J, 67%. But the wear loss volumes are higher due to the lower surface hardening. Especially, the wear volume loss of 5J, 33% is the highest amongst all LSP samples. In other way, compared to the untreated, 5J, 67% improved the wear resistance, but did not enhance the cell viability. 5J, 50% compromises the wear volume loss and the cell viability. As for 72hrs culture, the cell viability is the highest amongst samples post all LSP parameters with the comparative low wear loss volume. For further improvement, multiple LSP impacts can be applied to the 5J, 50% for the deeper surface hardening layer, thereby, enhancing the wear resistance.

As mentioned above, 7J samples received the deepest surface hardening and exhibited the best performance in wear resistance. However, the improvements of the cell viability are comparatively lower than that of others LSP parameters. This is due to the decrease of contact angle leading to contact angle value lower than 70°. The pros and cons of LSP on cell viability and wear resistance are summarized in Table 12.1. It can be seen that compromising the results of the cell viability and wear resistance, 7J, 50% is the optimal LSP parameter for improving the comprehensive properties of Ti-6Al-7Nb alloy.

Table 12.1 The pros and cons of laser shock peening on cell viability and wear resistance

×: Worse than the untreated

-: Comparatively closed to the untreated

√: Better than the untreated

	Wear Resistance	Cell Viability
3J, 33%	×	√ √
3J, 50%	×	√
3J, 67%	×	√ √
5J, 33%	× ×	√ √
5J, 50%	-	√√
5J, 67%	√ √	√
7J, 33%	√ √	√
7J, 50%	√ √ √	√ √
7J, 67%	√ √	-

12.5 Summary

In-vitro biological assessment was carried to evaluate the biological effects of LSP on the cell viability of laser shock peened Ti-6Al-7Nb alloy surfaces. The following conclusions were drawn from the above experiments.

- From the fluoresce images after 72hrs, it was seen that LSP was not toxic to MG63 cell adhesion. There is not a dramatic increase in the cell numbers on both surfaces before and after LSP. By contrast, the cell numbers of non-optimal LSP parameters are even quite lower than that untreated.
- The MTT assay results show that some LSP parameters are detrimental to cell viability after 24hrs cell culture. However, after 72hrs the cell viability of LSPned samples are all higher than that of untreated. The optimal LSP parameter is 5J, 33% overlapping, as it keeps high in both 24hrs and 72hrs culture experiment. Considering with both mechanical and biological performance, 7J, 50% is the optimal LSP processing parameters for improve the implant properties.
- Laser shock peening is potential to be used to improve the implant osseointegration as it not only improves the mechanical properties but also the cell viability. The cell viability is directly related to the surface wetting properties as the more the contact angle is close to 71.5, the higher cell viability it presents. But it needs to be proved with further biological experiments such as cell proliferation, adhesion, and differentiation.

Conclusions

The research in this thesis focuses on the evaluation of both the mechanical and biological properties of a first-time laser shock peened orthopaedic Ti-6Al-7Nb alloy. The results are separated in to four aspects (microstructural, mechanical, interfacial and biological):

Microstructural Aspects

- The average sub-grain sizes of alpha-phase after LSP were reduced by 12.5% to 39%. The XRD patterns indicated that no new phase was formed after LSP, and the peaks were broadened. In addition, high density dislocation features were observed which contribute to the improvement of the mechanical properties in-line with Hall-Petch theory.
- Furnace cooling post solution treatment at either 900 ℃ and 950℃ leads to a globular microstructure of Ti-6Al-7Nb alloy. Longer thermal preservation time at the same temperature decreased the local sub-grain misorientation. According to KAM maps, 950℃ for 4hrs is the optimal parameters for acquiring globular microstructure.
- The average sub-grains size post heat treatment were reduced by 20.4% and 26.5%, by LSP parameters of 7J, 50% and 7J, 67% overlap. The α and β of low angle misorientation of Ti-6Al-7Nb alloy subject to 7J, 50% and 7J, 67% were increased by 3%, 14.4% and 51.9%, and 42.3% respectively. The saturated local misorientation was located in the depth of 200 to 400 μm rather than the top surface. Twin {10-12} and {11-21} can be found in the sub-surface after 10 LSP impacts. The α (100) peaks were broadened and shifted toward high diffraction angles due to changes in crystal size and microstrain. As calculated by Williamson-hull plot, the micro-strain of 7J, 67% was compressive, while that of the rest of the LSP parameters were tensile. In addition, crystal received refinement with 7J LSP parameters.

Mechanical Aspects

- Incremental Hole Drilling (IHD) results showed that the magnitude of CRS from -42MPa to -512MPa were formed after LSP at the depth of 16μm. Comparatively, the ANN predicted results is in good agreement with experimental one, with accuracy of 96.16% and 95.16% for training the 3J and 7J data and 96.9% and 98.41% for experimental results at 5J.

- The surface micorhardness were improved by 14% to 26.5% after LSP. From the comparison of the plots (Figure 8.1), it can be seen that laser energy and overlap were proportional to microhardness at the near-surface. The wear scar and wear volume loss showed that LSP parameters of 5J, 67%; 7J, 33%; 7J, 50% and 7J, 67% have beneficial effects of wear resistance in SBF, while parameters of 3J, 33%; 3J, 50%; 3J, 67% and 5J, 33% could be detrimental as LSP also increased the surface roughness.
- The SEM images showed grain reduction from around 30μm to 10μm after multiple LSP. With increasing impacts, the growth of roughness tends to be steady. Furthermore, the sliding wear property was improved by 44% subject to 3 impacts LSP. For all samples, the sliding wear mechanism was the combination of oxidation wear and abrasive wear.

Interfacial and Biological Aspects

- At the microscopic level, surface reliefs are formed when the laser energy and impacts are higher than 5J at 4 impacts. Moreover, the surface roughness was proportional to the laser energy when the overlap was kept constant. On the other hand, roughness is lower when increase the overlap with consistent laser energy.
- The overlap and laser energy were are inversely proportional to dynamic contact angles. The effect of overlap at the same laser energy can be explained with the Cassies-Baxter model as the increase surface roughness leads to a proportional increase in contact angle. Furthermore, at the same overlapping LSP treatment, the contact angles have a negative correlation with the laser energy. This can be explained by Wenzel's model.
- The MTT assay results showed that some LSP parameters are detrimental to cell viability for 24hrs. However, after 72hrs, the cell viability of laser shock peened samples were all higher than that of the untreated. For cell viability, 5J, 33% was the best LSP parameters in both 24hrs and 72 hrs culture experiment. In addition, cell viability is directly related with contact angle and the optimal contact angle after LSP is 71.5°.
- The evaluation of different LSP parameters cannot be completed by only one property. All aspects have to be considered and compromised. Therefore, combing with the wear resistance and the cell viability data, 7J, 50% is the optimal LSP parameter for improving the comprehensive properties of the implant.

Future Study

LSP has several advantages over the conventional surface modification techniques previously used for processing implant biomaterials and the application of LSP in the medical sector is still new topic that requires broad and in-depth research. Further studies are suggested to further advance the field.

Laser Shock Peening Process Related Aspects

In this thesis, conventional laser shock peening including multiple LSP were carried out. With the development LSPwC, WLSP, HRLSP, future experiments could entail LSPwC at high energy to particular surface topographies that support biocompatibility. This will allow LSP more applicable in the industry as the coating time is saved which means the processing efficiency is improved. What is more, another process related purpose is to induce deeper residual stress and avoid using large power density laser. This can be achieved in cryogenic environment. However, the healthy and safety during the process need to be extra cared of.

Microstructural Aspects

In the microstructure post heat treatment, the misorientation of the LSPned surface was successfully characterized by KAM map. However, detailed slip system and twining deformation were not covered in the cross-section microstructure. In the future study, multiple LSP is employed to form twining deformation, slip system in the hexagonal closed pack structure. What is more, in terms of characterization methods, it would add more insight into the HCP structure deformation mechanism under the plasma shock-waves induced by LSP.

Mechanical Aspect

Although LSP benefits the fatigue resistance of metallic materials, fatigue measurement needs to carried out not only for the standard fatigue samples but also on the specific implants. What is more, such as corrosion (especially stress corrosion cracking), nano-indentations, tensile tests could be also carried out in the future.

Biological evaluation Aspect

In particular, cell viability could be evaluated by live/dead staining assay and DNA quantification assay. Assessment of cell differentiation can be carried out by alkaline phosphatas assay. What is more, regarding the cell numbers, flow cytometry method can be employed to account the numbers on the surfaces. SEM can be employed to observed the morphology of cells on the LSPned illustrating how the cells are attached on the surfaces.

Technology Transfer

The scientific methodologies and findings in this research could be used for future studies. These can be applied to an industrial problem. Such understanding can now be transferred to an experiment in *vivo* such as implanting an LSPned screw into a rabbit or using LSP to processing a 3D hip implant for in *vitro* experiment. Corresspoding LSP experiment will be applied to these 3D implants, and then biological test such as cell adhesion, proliferation and viability can be carried out to evaluate the biocompatibility the LSPned 3D implant. If these experiments are successful, it would dramatically speed up the application of LSP in the medical sector and relief the pain of the patients.

Reference

1. Ronald Lakatos, M.A.H., *General Principles of Internal Fixation*, in *Medscape* 2018.
2. Ortiz, A.J., et al., *Metallic ions released from stainless steel, nickel-free, and titanium orthodontic alloys: toxicity and DNA damage.* American Journal of Orthodontics and Dentofacial Orthopedics, 2011. **140**(3): p. e115-e122.
3. Walley, K.C., et al., *The chronicle of a stainless steel orthopaedic implant.* The Orthopaedic Journal at Harvard Medical School, 2016. **17**: p. 68-74.
4. Ferraris, S. and S.J.M.S. Spriano, *Antibacterial titanium surfaces for medical implants.* Materials Science and Engineering: C, 2016. **61**: p. 965-978.
5. Bekmurzayeva, A., et al., *Surface modification of stainless steel for biomedical applications: Revisiting a century-old material*. Materials Science and Engineering: C, 2018.
6. Chojnacka, A., et al., *Corrosion anisotropy of titanium deformed by the hydrostatic extrusion.* Applied Surface Science, 2017. **426**: p. 987-994.
7. Geetha, M., et al., *Ti based biomaterials, the ultimate choice for orthopaedic implants – A review.* Progress in Materials Science, 2009. **54**(3): p. 397-425.
8. Aherwar, A., A.K. Singh, and A. Patnaik, *Current and future biocompatibility aspects of biomaterials for hip prosthesis.* AIMS Bioeng, 2015. **3**(1): p. 23-43.
9. Aherwar, A., A.K. Singh, and A. Patnaik, *Cobalt Based Alloy: A Better Choice Biomaterial for Hip Implants.* Trends in Biomaterials, 2016. **30**(1).
10. *The state of musculoskeletal health 2019*. Versus Arthritis
11. Tracey Loftis, B.E., Tom Margham, *Musculoskeletal conditions and multimorbidity* 2016.
12. Curtis, E.M., et al., *Epidemiology of fractures in the United Kingdom 1988–2012: variation with age, sex, geography, ethnicity and socioeconomic status.* Bone, 2016. **87**: p. 19-26.
13. Sözen, T., L. Özışık, and N.Ç. Başaran, *An overview and management of osteoporosis.* European journal of rheumatology, 2017. **4**(1): p. 46.
14. HQIP, *National joint registry 13th annual report*. 2016: UK.
15. Research, B. *Global Orthopedics Devices Market to Reach $61.02 Billion by 2023, Reports BIS Research*. 2017; Available from: https://www.prnewswire.com/news-releases/global-orthopedics-devices-market-to-reach-6102-billion-by-2023-reports-bis-research-636723973.html.
16. Havelin, L.I., et al., *The Norwegian arthroplasty register: a survey of 17,444 hip replacements 1987–1990.* Acta Orthopaedica Scandinavica, 1993. **64**(3): p. 245-251
17. Malchau, H., P. Herberts, and L. Ahnfelt, *Prognosis of total hip replacement in Sweden: follow-up of 92,675 operations performed 1978–1990.* Acta Orthopaedica Scandinavica, 1993. **64**(5): p. 497-506.
18. Malchau, H. and P. Herberts, *Prognosis of total hip replacement: revision and re-revision rate in THR: a revision-risk study of 148,359 primary operations*. 1998.
19. Ridzwan, M.I.Z., et al., *Problem of stress shielding and improvement to the hip implant designs: a review*. J. Med. Sci, 2007. **7**(3): p. 460-467.
20. Denard, P.J., et al., *Stress shielding of the humerus in press-fit anatomic shoulder arthroplasty: review and recommendations for evaluation.* Journal of shoulder and elbow surgery, 2018. **27**(6): p. 1139-1147
21. Teles, A.R., et al., *Fractures After Removal of Spinal Instrumentation: Revisiting the Stress-Shielding Effect of Instrumentation in Spine Fusion.* World neurosurgery, 2018. **116**: p. e1137-e1143

22. Joshi, M.G., et al., *Analysis of a femoral hip prosthesis designed to reduce stress shielding.* Journal of biomechanics, 2000. **33**(12): p. 1655-1662
23. Weinans, H., et al., *Sensitivity of periprosthetic stress-shielding to load and the bone density–modulus relationship in subject-specific finite element models.* Journal of Biomechanics, 2000. **33**(7): p. 809-817.
24. Schierholz, J.M. and J. Beuth, *Implant infections: a haven for opportunistic bacteria.* Journal of Hospital Infection, 2001. **49**(2): p. 87-93
25. Kaiser, A.B., *Antimicrobial Prophylaxis in Surgery.* New England Journal of Medicine, 1986. **315**(18): p. 1129-1138.
26. Campoccia, D., L. Montanaro, and C.R. Arciola, *The significance of infection related to orthopedic devices and issues of antibiotic resistance.* Biomaterials, 2006. **27**(11): p. 2331-2339.
27. Raphel, J., et al., *Multifunctional coatings to simultaneously promote osseointegration and prevent infection of orthopaedic implants.* Biomaterials, 2016. **84**: p. 301-314.
28. Zhu, Y.H., K.Y. Chiu, and W.M. Tang, *Polyethylene wear and osteolysis in total hip arthroplasty.* Journal of orthopaedic surgery, 2001. **9**(1): p. 91-99
29. Broomfield, J.A.J., et al., *The Relationship Between Polyethylene Wear and Periprosthetic Osteolysis in Total Hip Arthroplasty at 12 Years in a Randomized Controlled Trial Cohort.* The Journal of Arthroplasty, 2017. **32**(4): p. 1186-1191.
30. Fukuzumi, Y., T. Wada, and H. Kato, *Surface improvement for biocompatibility of Ti-6Al-4V by dealloying in metallic melt*, in *Interface Oral Health Science 2014*. 2015, Springer, Tokyo. p. 93-101.
31. Ku, C.-H., et al., *Effect of different Ti–6Al–4V surface treatments on osteoblasts behaviour.* Biomaterials, 2002. **23**(6): p. 1447-1454.
32. Bothe, R.T., *Reaction of bone to multiple metallic implants.* Surg Gynecol Obstet, 1940. **71**: p. 598-602.
33. Okabe, T. and H. Hero, *The use of titanium in dentistry.* Cells and Materials, 1995. **5**(2): p. 9.
34. Sidambe, A., *Biocompatibility of advanced manufactured titanium implants- A review.* Materials, 2014. **7**(12): p. 8168-8188.
35. Long, M. and H.J. Rack, *Titanium alloys in total joint replacement—a materials science perspective.* Biomaterials, 1998. **19**(18): p. 1621-1639.
36. Choi, K., et al., *The elastic moduli of human subchondral, trabecular, and cortical bone tissue and the size-dependency of cortical bone modulus.* Journal of Biomechanics, 1990. **23**(11): p. 1103-1113.
37. Song, Y., et al., *Theoretical study of the effects of alloying elements on the strength and modulus of β-type bio-titanium alloys.* Materials Science and Engineering: A, 1999. **260**(1): p. 269-274.
38. Cvijović-Alagić, I., et al., *Wear and corrosion behaviour of Ti–13Nb–13Zr and Ti–6Al–4V alloys in simulated physiological solution.* Corrosion Science, 2011. **53**(2): p. 796-808.
39. Yang, X. and C.R. Hutchinson, *Corrosion-wear of β-Ti alloy TMZF (Ti-12Mo-6Zr-2Fe) in simulated body fluid.* Acta Biomaterialia, 2016. **42**: p. 429-439.
40. Koizumi, H., et al., *Castability and mechanical properties of Ti-15Mo-5Zr-3Al alloy in dental casting.* Journal of Oral Science, 2018. **60**(2): p. 285-292.
41. Najdahmadi, A., A. Zarei-Hanzaki, and E. Farghadani, *Mechanical properties enhancement in Ti–29Nb–13Ta–4.6Zr alloy via heat treatment with no detrimental effect on its biocompatibility.* Materials & Design (1980-2015), 2014. **54**: p. 786-791.
42. Ferrandini, P.L., et al., *Aging response of the Ti–35Nb–7Zr–5Ta and Ti–35Nb–7Ta alloys.* Journal of Alloys and Compounds, 2007. **433**(1): p. 207-210.

43. Saini, M., et al., *Implant biomaterials: A comprehensive review.* World journal of clinical cases, 2015. **3**(1): p. 52-57.
44. Veiga, C., J.P. Davim, and A.J.R. Loureiro, *Properties and applications of titanium alloys: a brief review.* Rev. Adv. Mater. Sci, 2012. **32**(2): p. 133-148.
45. Niinomi, M., *Recent research and development in titanium alloys for biomedical applications and healthcare goods.* Science and technology of advanced Materials, 2003. **4**(5): p. 445
46. Li, Y., et al., *New Developments of Ti-Based Alloys for Biomedical Applications.* Materials, 2014. **7**(3).
47. Kwasniak, P., et al., *Influence of oxygen content on the mechanical properties of hexagonal Ti—First principles calculations.* Materials Science and Engineering: A, 2014. **590**: p. 74-79.
48. Kawałko, J., et al., *Microstructure of titanium on complex deformation paths: Comparison of ECAP, KOBO and HE techniques.* Materials Characterization, 2018. **141**: p. 19-31.
49. Gu, K., et al., *Microstructure evolution in metastable β titanium alloy subjected to deep cryogenic treatment.* Materials Science and Engineering: A, 2018. **723**: p. 157-164.
50. Vert, M., et al., *Terminology for biorelated polymers and applications (IUPAC Recommendations 2012).* Pure and Applied Chemistry, 2012. **84**(2): p. 377-410
51. Mavrogenis, A.F., et al., *Biology of implant osseointegration.* J Musculoskelet Neuronal Interact, 2009. **9**(2): p. 61-71.
52. Parithimarkalaignan, S. and T.V. Padmanabhan, *Osseointegration: An Update.* The Journal of Indian Prosthodontic Society, 2013. **13**(1): p. 2-6.
53. Singhatanadgit, W., *Biological Responses to New Advanced Surface Modifications of Endosseous Medical Implants.* Bone and Tissue Regeneration Insights, 2009. **2**: p. BTRI.S3150.
54. Carlsson, L., et al., *Osseointegration of titanium implants.* Acta Orthopaedica Scandinavica, 1986. **57**(4): p. 285-289.
55. Chug, A., et al., *Osseointegration—Molecular events at the bone–implant interface: A review.* Journal of Oral and Maxillofacial Surgery, Medicine, and Pathology, 2013. **25**(1): p. 1-4.
56. Fraker, A.C. and C.D. Griffin, *Corrosion and Degradation of Implant Materials: Second Symposium: a Symposium.* 1985: ASTM International.
57. Wang, G., et al., *Corrosion Behavior of Titanium Implant with different Surface Morphologies.* Procedia Manufacturing, 2017. **10**: p. 363-370.
58. Harada, R., et al., *Corrosion behavior of titanium in response to sulfides produced by Porphyromonas gingivalis.* Dental Materials, 2018. **34**(2): p. 183-191.
59. Lukina, E., et al., *Fretting corrosion behavior of nitinol spinal rods in conjunction with titanium pedicle screws.* Materials Science and Engineering: C, 2017. **72**: p. 601-610.
60. Pouilleau, J., et al., *Structure and composition of passive titanium oxide films.* Materials Science and Engineering: B, 1997. **47**(3): p. 235-243.
61. Budimir, A., *Metal ions, Alzheimer's disease and chelation therapy.* Acta Pharmaceutica, 2011. **61**(1): p. 1-14.
62. Chenghao, L., et al., *Crevice Corrosion Behavior of CP Ti, Ti-6Al-4V Alloy and Ti-Ni Shape Memory Alloy in Artificial Body Fluids.* Rare Metal Materials and Engineering, 2015. **44**(4): p. 781-785.
63. Yu, J., Z.J. Zhao, and L.X. Li, *Corrosion fatigue resistances of surgical implant stainless steels and titanium alloy.* Corrosion Science, 1993. **35**(1): p. 587-597.

64. Sivakumar, B., L.C. Pathak, and R. Singh, *Role of surface roughness on corrosion and fretting corrosion behaviour of commercially pure titanium in Ringer's solution for bio-implant application.* Applied Surface Science, 2017. **401**: p. 385-398.
65. Oliveira, C.A., et al., *Metallosis: A diagnosis not only in patients with metal-on-metal prostheses.* European Journal of Radiology Open, 2015. **2**: p. 3-6.
66. Ho, J., et al., *Metallosis in cemented titanium alloy total knee arthroplasty without apparent metal-on-metal articulation.* The Knee, 2018. **25**(4): p. 728-731.
67. Anderson, J.M., A. Rodriguez, and D.T. Chang, *Foreign body reaction to biomaterials.* Seminars in Immunology, 2008. **20**(2): p. 86-100.
68. de Viteri, V.S.í. and E. Fuentes, *Titanium and titanium alloys as biomaterials*. Tribology - Fundamentals and Advancements. 2013. 155-181.
69. McGee, M.A., et al., *Implant retrieval studies of the wear and loosening of prosthetic joints: a review.* Wear, 2000. **241**(2): p. 158-165.
70. AZoM. *Titanium alloys in medical applicaitons*. 2003; Available from: https://www.azom.com/article.aspx?ArticleID=1794.
71. Koizumi, H., et al., *Application of titanium and titanium alloys to fixed dental prostheses.* Journal of Prosthodontic Research, 2019. **63**(3): p. 266-270.
72. McKay, M. *Why understanding dental implant abutments can save u an extra trip (and money) to Mexico?* 2013; Available from: https://www.dayodental.com/why-understanding-dental-implant-abutments-can-save-you-an-extra-trip-and-money-to-mexico-2/.
73. Kim, K.T., et al., *General review of titanium toxicity.* International journal of implant dentistry, 2019. **5**(1): p. 10-10.
74. Cluett, J. *What Type of Hip Replacement Implant Is Best?* 2019; Available from: https://www.verywellhealth.com/what-type-of-hip-replacement-implant-is-best-2549558.
75. Care, M.H. *Hip Parts and Materials*. Available from: https://www.muhealth.org/conditions-treatments/orthopaedics/hip-pain/hip-replacement-surgery/hip-parts-and-materials.
76. Asri, R.I.M., et al., *Corrosion and surface modification on biocompatible metals: A review.* Materials Science and Engineering: C, 2017. **77**: p. 1261-1274.
77. Liu, X., P.K. Chu, and C. Ding, *Surface modification of titanium, titanium alloys, and related materials for biomedical applications.* Materials Science and Engineering: R: Reports, 2004. **47**(3): p. 49-121.
78. Citeau, A., et al., *In vitro biological effects of titanium rough surface obtained by calcium phosphate grid blasting.* Biomaterials, 2005. **26**(2): p. 157-165.
79. Gbureck, U., et al., *Tribochemical structuring and coating of implant metal surfaces with titanium oxide and hydroxyapatite layers.* Materials Science and Engineering: C, 2003. **23**(3): p. 461-465.
80. Fini, M., et al., *Biomechanical and histomorphometric investigations on two morphologically differing titanium surfaces with and without fluorohydroxyapatite coating: an experimental study in sheep tibiae.* Biomaterials, 2003. **24**(19): p. 3183-3192.
81. *Standard Guide for Descaling and Cleaning Titanium and Titanium Alloy Surfaces*. 2017.
82. Sittig, C., et al., *Surface characterization.* Journal of Materials Science: Materials in Medicine, 1999. **10**(1): p. 35-46.
83. Pan, C., et al., *Corrosion resistance and biocompatibility of magnesium alloy modified by alkali heating treatment followed by the immobilization of poly (ethylene glycol), fibronectin and heparin.* Materials Science and Engineering: C, 2017. **70**: p. 438-449.

84. Kim, H.M., et al., *Preparation of bioactive Ti and its alloys via simple chemical surface treatment.* Journal of Biomedical Materials Research: An Official Journal of The Society for Biomaterials and The Japanese Society for Biomaterials, 1996. **32**(3): p. 409-417
85. Wang, C.X., X. Zhou, and M. Wang, *Mechanism of apatite formation on pure titanium treated with alkaline solution.* Bio-medical materials and engineering, 2004. **14**(1): p. 5-11
86. Rautray, T.R., R. Narayanan, and K.-H. Kim, *Ion implantation of titanium based biomaterials.* Progress in Materials Science, 2011. **56**(8): p. 1137-1177.
87. Bagaria, A.N. *Doping by diffusion and implantation* 2006; Available from: https://docplayer.net/63738985-Doping-by-diffusion-implantation-by-ashutosh-nandan-bagaria-iit-kharagpur.html.
88. Li, J., et al., *Microstructure and properties of Ag/N dual ions implanted titanium.* Surface and Coatings Technology, 2011. **205**(23): p. 5430-5436.
89. Yu, Y., et al., *Multifunctions of dual Zn/Mg ion co-implanted titanium on osteogenesis, angiogenesis and bacteria inhibition for dental implants.* Acta Biomaterialia, 2017. **49**: p. 590-603.
90. Fauchais, P. and G. Montavon, *Plasma Spraying: From Plasma Generation to Coating Structure*, in *Advances in Heat Transfer*, A. Fridman, et al., Editors. 2007, Elsevier. p. 205-344.
91. Amin, S. and H. Panchal, *A review on thermal spray coating processes.* transfer, 2016. **2**(4).
92. Vardelle, A., et al., *A Perspective on Plasma Spray Technology.* Plasma Chemistry and Plasma Processing, 2015. **35**(3): p. 491-509.
93. Matejka, D. and B. Benko, *Plasma spraying of metallic and ceramic materials.* John Wiley and Sons, Baffins Lane, Chichester, West Sussex, PO 19 1 UD, UK, 1989. 280, 1989.
94. Utu, I.D., et al., *Properties of the thermally sprayed Al2O3–TiO2 coatings deposited on titanium substrate.* International Journal of Refractory Metals and Hard Materials, 2015. **51**: p. 118-123.
95. Abraham, C.M., *A brief historical perspective on dental implants, their surface coatings and treatments.* The open dentistry journal, 2014. **8**: p. 50-55.
96. Chu, C., et al., *Fabrication and characterization of titanium-matrix composite with 20 vol% hydroxyapatite for use as heavy load-bearing hard tissue replacement.* Journal of Materials Science: Materials in Medicine, 2006. **17**(3): p. 245-251.
97. Chen, H., et al., *Construction of surface HA/TiO2 coating on porous titanium scaffolds and its preliminary biological evaluation.* Materials Science and Engineering: C, 2017. **70**: p. 1047-1056.
98. Zhang, L., et al., *Enhanced in vitro bioactivity of porous NiTi–HA composites with interconnected pore characteristics prepared by spark plasma sintering.* Materials & Design, 2016. **101**: p. 170-180.
99. Singh, G., H. Singh, and B.S. Sidhu, *Characterization and corrosion resistance of plasma sprayed HA and HA–SiO2 coatings on Ti–6Al–4V.* Surface and Coatings Technology, 2013. **228**: p. 242-247.
100. Singh, G., H. Singh, and B.S. Sidhu, *Corrosion behavior of plasma sprayed hydroxyapatite and hydroxyapatite-silicon oxide coatings on AISI 304 for biomedical application.* Applied Surface Science, 2013. **284**: p. 811-818.
101. He, Y.H., et al., *Effect of HA (Hydroxyapatite) content on the microstructure, mechanical and corrosion properties of (Ti13Nb13Zr)-xHA biocomposites synthesized by sparkle plasma sintering.* Vacuum, 2016. **131**: p. 176-180.

102. Kweh, S.W.K., K.A. Khor, and P. Cheang, *An in vitro investigation of plasma sprayed hydroxyapatite (HA) coatings produced with flame-spheroidized feedstock.* Biomaterials, 2002. **23**(3): p. 775-785.
103. Fazan, F. and P.M. Marquis, *Dissolution behavior of plasma-sprayed hydroxyapatite coatings.* Journal of Materials Science: Materials in Medicine, 2000. **11**(12): p. 787-792.
104. Riveiro, A., et al., *Laser Surface Texturing of Polymers for Biomedical Applications.* 2018. **6**(6).
105. Udaya Kumar, G., et al., *A review on the role of laser textured surfaces on boiling heat transfer.* Applied Thermal Engineering, 2020. **174**: p. 115274.
106. Riveiro, A., et al., *Laser surface modification of PEEK.* Applied Surface Science, 2012. **258**(23): p. 9437-9442.
107. Riveiro, A., et al., *Influence of laser texturing on the wettability of PTFE.* Applied Surface Science, 2020. **515**: p. 145984.
108. Chen, L., et al., *Load-bearing capacity research in wet clutches with surface texture.* Measurement, 2019. **142**: p. 96-104.
109. Li, X., et al., *Enhanced lubrication effect of gallium-based liquid metal with laser textured surface.* Tribology International, 2019. **129**: p. 407-415.
110. Kümmel, D., et al., *Tribological behavior of nanosecond-laser surface textured Ti6Al4V.* Wear, 2019. **422-423**: p. 261-268.
111. Raimbault, O., et al., *The effects of femtosecond laser-textured Ti-6Al-4V on wettability and cell response.* Materials Science and Engineering: C, 2016. **69**: p. 311-320.
112. Xu, Y., et al., *Friction stability and cellular behaviors on laser textured Ti–6Al–4V alloy implants with bioinspired micro-overlapping structures.* Journal of the Mechanical Behavior of Biomedical Materials, 2020. **109**: p. 103823.
113. Wang, C., et al., *Effects of laser shock processing on microstructure and mechanical properties of K403 nickel-alloy.* Materials & Design, 2016. **89**: p. 582-588.
114. Ding, K. and L. Ye, *Simulation of multiple laser shock peening of a 35CD4 steel alloy.* Journal of Materials Processing Technology, 2006. **178**(1): p. 162-169.
115. Fabbro, R., et al., *Physical study of laser‐produced plasma in confined geometry.* Journal of applied physics, 1990. **68**(2): p. 775-784
116. Meyers, M.A., et al., *Constitutive description of dynamic deformation: physically-based mechanisms.* Materials Science and Engineering: A, 2002. **322**(1): p. 194-216.
117. Berthe, L., et al., *The generation of laser shock waves in a water-confinement regime with 50 ns and 150 ns XeCl excimer laser pulses.* Journal of Physics D: Applied Physics, 2000. **33**(17): p. 2142-2145.
118. Curtiss-Wright. *Laser peening* Available from: https://cwst.com/laser-peening/overview/#.
119. Mallozzi, P. and B. Fairand, *Altering material properties*. 1974, Google Patents.
120. Hill, M.R., et al., *Laser Peening Technology.* Advanced materials & processes, 2003. **161**(8): p. 65-67
121. LSPT. *Our Story* Available from: https://www.lsptechnologies.com/our-story/.
122. MacGillivray, K., et al. *F-22 laser shock peening depot transition and risk reduction*. 2010.
123. Hong, X., et al., *Confining medium and absorptive overlay: Their effects on a laser-induced shock wave.* Optics and Lasers in Engineering, 1998. **29**(6): p. 447-455.
124. Caralapatti, V.K. and S. Narayanswamy, *Effect of high repetition laser shock peening on biocompatibility and corrosion resistance of magnesium.* Optics & Laser Technology, 2017. **88**: p. 75-84.

125. Gill, A.S., A. Telang, and V.K. Vasudevan, *Characteristics of surface layers formed on inconel 718 by laser shock peening with and without a protective coating.* Journal of Materials Processing Technology, 2015. **225**: p. 463-472.
126. Liao, Y., C. Ye, and G.J. Cheng, *[INVITED] A review: Warm laser shock peening and related laser processing technique.* Optics & Laser Technology, 2016. **78**: p. 15-24.
127. Ye, C., et al., *Microstructure and mechanical properties of copper subjected to cryogenic laser shock peening.* Journal of Applied Physics, 2011. **110**(8): p. 083504.
128. Caralapatti, V.K. and S. Narayanswamy, *Analyzing the effect of high repetition laser shock peening on dynamic corrosion rate of magnesium.* Optics & Laser Technology, 2017. **93**: p. 165-174.
129. Kamkarrad, H., *High Repetition Rate Laser Shock Peening on Biodegradable Magnesium Alloys*. 2016, Concordia University.
130. Mukai, N., et al. *Laser processing for underwater maintenance in nuclear plants*. 1995.
131. Trdan, U., et al., *Laser shock peening without absorbent coating (LSPwC) effect on 3D surface topography and mechanical properties of 6082-T651 Al alloy.* Surface and Coatings Technology, 2012. **208**: p. 109-116.
132. Kulkarni, A., et al., *Effect of laser shock peening without coating on surface morphology and mechanical properties of nickel-200.* Mechanics, Materials Science & Engineering MMSE Journal. Open Access, 2017. **9**.
133. Prabhakaran, S., et al., *Laser shock peening without coating induced residual stress distribution, wettability characteristics and enhanced pitting corrosion resistance of austenitic stainless steel.* Applied Surface Science, 2018. **428**: p. 17-30.
134. Karthik, D. and S. Swaroop, *Laser peening without coating—an advanced surface treatment: A review.* Materials and Manufacturing Processes, 2017. **32**(14): p. 1565-1572.
135. Sano, Y., N. Mukai, and M. Obata. *Laser peening without coating: process, effects and applications*. 2008.
136. Masaki, K., et al., *Effects of laser peening treatment on high cycle fatigue properties of degassing-processed cast aluminum alloy.* Materials Science and Engineering: A, 2007. **468-470**: p. 171-175.
137. Karthik, D. and S. Swaroop, *Laser peening without coating induced phase transformation and thermal relaxation of residual stresses in AISI 321 steel.* Surface and Coatings Technology, 2016. **291**: p. 161-171.
138. Sano, Y., et al., *Improvement in fatigue performance of friction stir welded A6061-T6 aluminum alloy by laser peening without coating.* Materials & Design (1980-2015), 2012. **36**: p. 809-814.
139. Ye, C., Y. Liao, and G.J. Cheng, *Warm laser shock peening driven nanostructures and their effects on fatigue performance in aluminum alloy 6160.* Advanced Engineering Materials, 2010. **12**(4): p. 291-297
140. Meng, X.-k., et al., *Residual stress relaxation and its effects on the fatigue properties of Ti6Al4V alloy strengthened by warm laser peening.* Materials Science and Engineering: A, 2017. **680**: p. 297-304.
141. Lu, J.Z., et al., *Tensile properties and surface nanocrystallization analyses of H62 brass subjected to room-temperature and warm laser shock peening.* Journal of Alloys and Compounds, 2017. **698**: p. 633-642.
142. Ye, C., et al., *Fatigue performance improvement in AISI 4140 steel by dynamic strain aging and dynamic precipitation during warm laser shock peening.* Acta Materialia, 2011. **59**(3): p. 1014-1025.

143. Zhou, J., et al., *Improvement in fatigue properties of 2024-T351 aluminum alloy subjected to cryogenic treatment and laser peening.* Surface and Coatings Technology, 2018. **345**: p. 31-39.
144. Novelli, M., et al., *On the effectiveness of surface severe plastic deformation by shot peening at cryogenic temperature.* Applied Surface Science, 2016. **389**: p. 1169-1174.
145. Ye, C., et al., *Cryogenic ultrahigh strain rate deformation induced hybrid nanotwinned microstructure for high strength and high ductility.* Journal of Applied Physics, 2014. **115**(21): p. 213519.
146. Li, J., et al., *Simultaneously enhancing mechanical properties and damping capacity of pure titanium subjected to cryogenic laser peening.* Materials Letters, 2019. **254**: p. 423-427.
147. Li, J., et al., *Analysis of microstructure and tensile properties produced by cryogenic laser peening on 2024-T351 aluminum alloy.* Vacuum, 2018. **158**: p. 141-145.
148. Li, J., et al., *High-temperature wear properties and microstructural characterization of 40CrNiMo structural steel treated by cryogenic laser peening.* Vacuum, 2018. **157**: p. 320-323.
149. Li, J., et al., *Twin formation and its strengthening mechanism of pure titanium processed by cryogenic laser peening.* Optics & Laser Technology, 2019. **120**: p. 105763.
150. Garrison, B., *High cycle fatigue (HCF) science and technology program 2000 annual report*. 2000, UNIVERSAL TECHNOLOGY CORP DAYTON OH.
151. Thompson, S.D., et al., *Laser shock peening vs. shot peening--a damage tolerance investigation.* Minerals, Metals and Materials Society/AIME(USA), 1996: p. 239-251.
152. Davis, B., et al., *Performance of Gen IV LSP for Thick Section Airfoil Damage Tolerance*, in *45th AIAA/ASME/ASCE/AHS/ASC Structures, Structural Dynamics & Materials Conference*. 2004, American Institute of Aeronautics and Astronautics.
153. Sokol, D.W., et al. *Applications of laser peening to titanium alloys*. in *Conference on Lasers and Electro-Optics/Quantum Electronics and Laser Science and Photonic Applications, Systems and Technologies*. 2005. Baltimore, Maryland: Optical Society of America.
154. Philip Withers, M.P. *Laser peening extends the lifetime of Rolls-Royce fan blades* 2007; Available from: https://www.materials.manchester.ac.uk/research/impact/laser-peening/.
155. Ganesh, P., et al., *Studies on laser peening of spring steel for automotive applications.* Optics and Lasers in Engineering, 2012. **50**(5): p. 678-686.
156. Stan Bovid, P.E. *Laser Peening Application Review* 2014; Available from: https://www.lsptechnologies.com/resources/laser-peening-application-review-automotive-engines/.
157. Sano, Y., et al., *Laser peening without coating as a surface enhancement technology.* Journal of Laser Micro/Nanoengineering, 2006. **1**(40): p. 161-166.
158. Yoda, M. and B. Newton. *Underwater laser peening*. in *Welding and Repair Technology for Power Plants Eighth International EPRI Conference*. 2008. Florida.
159. Zhu, J., et al., *Applications of Underwater Laser Peening in Nuclear Power Plant Maintenance.* Energy Procedia, 2012. **16**: p. 153-158.
160. Vasudevan, V.K., et al., *Investigation of the Use of Laser Shock Peening for Enhancing Fatigue and Stress Corrosion Cracking Resistance of Nuclear Energy Materials*, U.S.D.o. Energy, Editor. 2017, University of Cincinnati, OH United States.
161. Kashaev, N., et al., *Effects of laser shock peening on the microstructure and fatigue crack propagation behaviour of thin AA2024 specimens.* International Journal of Fatigue, 2017. **98**: p. 223-233.

162. Spanrad, S.K., *Fatigue crack growth in laser shock peened aerofoils subjected to foreign object damage*. 2011, University of Portsmouth.
163. Mannava, S.R., *Application of laser shock peening for spinal implant rods.* International Journal of Structural Integrity, 2011. **2**(1): p. 101-113.
164. Correa, C., et al., *Eigenstrain simulation of residual stresses induced by laser shock processing in a Ti6Al4V hip replacement.* Materials & Design, 2015. **79**: p. 106-114.
165. Zhang, Y., et al., *Effects of laser shock processing on stress corrosion cracking susceptibility of AZ31B magnesium alloy.* Surface and Coatings Technology, 2010. **204**(24): p. 3947-3953.
166. Guo, Y., M.P. Sealy, and C. Guo, *Significant improvement of corrosion resistance of biodegradable metallic implants processed by laser shock peening.* CIRP Annals, 2012. **61**(1): p. 583-586.
167. Guo, Y., et al., *Effect of laser shock peening on tribological properties of magnesium alloy ZK60.* Tribology International, 2020. **144**: p. 106138.
168. Ge, M.-Z., et al., *Wear behavior of Mg-3Al-1Zn alloy subjected to laser shock peening.* Surface and Coatings Technology, 2018. **337**: p. 501-509.
169. Trdan, U., et al., *Application of massive laser shock processing for improvement of mechanical and tribological properties.* Surface and Coatings Technology, 2018. **342**: p. 1-11.
170. Parry, V., G. Berthomé, and J.-C. Joud, *Wetting properties of gas diffusion layers: Application of the Cassie–Baxter and Wenzel equations.* Applied Surface Science, 2012. **258**(15): p. 5619-5627.
171. Zhang, R., et al., *The effects of laser shock peening on the mechanical properties and biomedical behavior of AZ31B magnesium alloy.* Surface and Coatings Technology, 2018. **339**: p. 48-56.
172. Khandaker, M., et al., *Peen treatment on a titanium implant: effect of roughness, osteoblast cell functions, and bonding with bone cement.* Int J Nanomedicine, 2016. **11**: p. 585-94.
173. Guo, W., et al., *Laser shock peening of laser additive manufactured Ti6Al4V titanium alloy.* Surface and Coatings Technology, 2018. **349**: p. 503-510.
174. Li, J., et al., *Influence of multiple laser peening on vibration fatigue properties of TC6 titanium alloy.* Optics & Laser Technology, 2019. **118**: p. 183-191.
175. Boyer, R.R., *An overview on the use of titanium in the aerospace industry.* Materials Science and Engineering: A, 1996. **213**(1): p. 103-114.
176. Lu, X., *In-situ transmission electron microscopy study of dislocation in TI-6AL-4V*. 2017, University of Birmingham.
177. Takata, T., et al., *Effect of Confinement Layer on Laser Ablation and Cavitation Bubble during Laser Shock Peening.* MATERIALS TRANSACTIONS, 2016. **57**(10): p. 1776-1783.
178. Polese, C., D. Glaser, and R. Bedekar, *Water Confinement Influences on the Laser Shock Peening process*. 2012.
179. Qian, X.Y., et al., *Grain refinement mechanism and improved mechanical properties in Mg–Sn alloy with trace Y addition.* Journal of Alloys and Compounds, 2020. **820**: p. 153122.
180. Yang, Y., K. Zhou, and G. Li, *Surface gradient microstructural characteristics and evolution mechanism of 2195 aluminum lithium alloy induced by laser shock peening.* Optics & Laser Technology, 2019. **109**: p. 1-7.
181. Yang, Y., et al., *Effects of laser shock peening on microstructures and properties of 2195 Al-Li alloy*. Journal of Alloys and Compounds, 2019. **781**: p. 330-336.

182. Zhou, L., et al., *Laser shock peening induced surface nanocrystallization and martensite transformation in austenitic stainless steel.* Journal of Alloys and Compounds, 2016. **655**: p. 66-70.
183. Bartha, K., et al., *Lattice defects in severely deformed biomedical Ti-6Al-7Nb alloy and thermal stability of its ultra-fine grained microstructure.* Journal of Alloys and Compounds, 2019. **788**: p. 881-890.
184. Ashida, M., et al., *Microstructures and Mechanical Properties of Ti-6Al-7Nb Processed by High-pressure Torsion.* Procedia Engineering, 2014. **81**: p. 1523-1528.
185. Basiaga, M., et al., *Evaluation of physicochemical properties of surface modified Ti6Al4V and Ti6Al7Nb alloys used for orthopedic implants.* Materials Science and Engineering: C, 2016. **68**: p. 851-860.
186. Shen, X., et al., *Improvement in mechanical properties of titanium alloy (Ti-6Al-7Nb) subject to multiple laser shock peening.* Surface and Coatings Technology, 2017. **327**: p. 101-109.
187. Yin, M.-g., et al., *Improving impact wear resistance of Ti-6Al-4V alloy treated by laser shock peening.* Transactions of Nonferrous Metals Society of China, 2019. **29**(7): p. 1439-1448.
188. Geng, Y., et al., *Effect of microstructure evolution and phase precipitations on hot corrosion behavior of IN718 alloy subjected to multiple laser shock peening.* Surface and Coatings Technology, 2019. **370**: p. 244-254.
189. Szymczyk, P., et al., *Application of Ti6Al7Nb Alloy for the Manufacture of Biomechanical Functional Structures (BFS) for Custom-Made Bone Implants.* Materials, 2018. **11**(6).
190. Yella, P., et al., *Effect of laser shock peening on high cycle fatigue characteristics of 316LN stainless steel.* International Journal of Pressure Vessels and Piping, 2019. **176**: p. 103972.
191. Pavan, M., et al., *Fatigue crack growth in a laser shock peened residual stress field.* International Journal of Fatigue, 2019. **123**: p. 157-167.
192. Soyama, H., *Comparison between the improvements made to the fatigue strength of stainless steel by cavitation peening, water jet peening, shot peening and laser peening.* Journal of Materials Processing Technology, 2019. **269**: p. 65-78.
193. Shen, X., et al., *Altering the wetting properties of orthopaedic titanium alloy (Ti–6Al–7Nb) using laser shock peening.* Journal of Alloys and Compounds, 2019. **801**: p. 327-342.
194. Ullrich, H.J.R.W.C., P. Haasen., *Materials science and technology A comprehensive treatment. Volume 2B: Characterization of Materials (Part II) VCH Weinheim; New York; Basel; Cambridge; Tokyo 1994, 775 pages, 491 figures, 32 tables, DM 450,– ISBN 3-527-28265-3 (VCH Weinheim), ISBN 1-56081-128-5 (VCH, New York)*. Crystal Research and Technology, ed. E. Lifshin. Vol. 29. 1994: John Wiley & Sons, Ltd. 786-786.
195. Sercombe, T., *Heat treatment of Ti ‐6Al ‐7Nb components produced by selective laser melting.* Rapid Prototyping Journal, 2008. **14**(5): p. 300-304.
196. Dąbrowski, R., *The phase transformations during continuous cooling of Ti6Al7Nb alloy from the two-phase α+ β range.* Journal of Achievements in Materials and Manufacturing Engineering, 2013. **59**(1): p. 7-12.
197. Wang, K., et al., *Hot working of Ti-17 titanium alloy with lamellar starting structure using 3-D processing maps.* Journal of Materials Science, 2010. **45**(21): p. 5883-5891.
198. Yang, C., et al., *Equiaxed grained structure: A structure in titanium alloys with higher compressive mechanical properties.* Materials Science and Engineering: A, 2013. **580**: p. 397-405.

199. Kang, L.M., et al., *Bimodal eutectic titanium alloys: Microstructure evolution, mechanical behavior and strengthening mechanism.* Materials Science and Engineering: A, 2017. **700**: p. 10-18.
200. Geetha, M., et al., *Effect of thermomechanical processing on evolution of various phases in Ti–Nb–Zr alloys.* Journal of Alloys and Compounds, 2004. **384**(1): p. 131-144.
201. Sabban, R., et al., *Globularization using heat treatment in additively manufactured Ti-6Al-4V for high strength and toughness.* Acta Materialia, 2019. **162**: p. 239-254.
202. Xu, J., et al., *Prediction of static globularization of Ti-17 alloy with starting lamellar microstructure during heat treatment.* Computational Materials Science, 2014. **92**: p. 224-230.
203. Wang, K., et al., *Dynamic globularization kinetics during hot working of Ti-17 alloy with initial lamellar microstructure.* Materials Science and Engineering: A, 2010. **527**(10): p. 2559-2566.
204. Gallego, J., et al., *Microstructural characterization of Ti-6Al-7Nb alloy after severe plastic deformation* Materials Research, 2012. **15**: p. 786-791.
205. Lu, J.Z., et al., *Microstructural response and grain refinement mechanism of commercially pure titanium subjected to multiple laser shock peening impacts.* Acta Materialia, 2017. **127**: p. 252-266.
206. Lainé, S.J., et al., *Microstructural characterisation of metallic shot peened and laser shock peened Ti–6Al–4V.* Acta Materialia, 2017. **123**: p. 350-361.
207. Gill, A.S., et al., *Localized plastic deformation and hardening in laser shock peened Inconel alloy 718SPF.* Materials Characterization, 2018. **142**: p. 15-26.
208. Lu, J.Z., et al., *Surface EBSD analysis and strengthening mechanism of AISI304 stainless steel subjected to massive LSP treatment with different pulse energies.* Materials Characterization, 2017. **125**: p. 99-107.
209. Mao, B., Y. Liao, and B. Li, *Abnormal twin-twin interaction in an Mg-3Al-1Zn magnesium alloy processed by laser shock peening.* Scripta Materialia, 2019. **165**: p. 89-93.
210. Xu, S., et al., *Sequential {101¯2} twinning stimulated by other twins in titanium.* Acta Materialia, 2017. **132**: p. 57-68.
211. Polyakova, V.V., et al., *Influence of grain boundary misorientations on the mechanical behavior of a near-α Ti-6Al-7Nb alloy processed by ECAP.* Materials Letters, 2017. **190**: p. 256-259.
212. Bisht, A., et al., *Observation of ex-situ microstructure relaxation of non-conventional misorientations post femtosecond laser shock exposure in cp-Ti.* Acta Materialia, 2018. **150**: p. 161-172.
213. McCabe, R.J., et al., *Quantitative analysis of deformation twinning in zirconium.* International Journal of Plasticity, 2009. **25**(3): p. 454-472.
214. Rai, A.K., et al., *Study on the effect of multiple laser shock peening on residual stress and microstructural changes in modified 9Cr-1Mo (P91) steel.* Surface and Coatings Technology, 2019. **358**: p. 125-135.
215. Jayasankar, K., et al., *Evaluation of microstructural parameters of nanocrystalline Y2O3 by X-ray diffraction peak broadening analysis.* Materials Chemistry and Physics, 2016. **171**: p. 195-200.
216. Gupta, S., H. Gupta, and A. Tandan, *Technical complications of implant-causes and management: A comprehensive review.* National journal of maxillofacial surgery, 2015. **6**(1): p. 3-8.
217. Sonntag, R., et al., *Fatigue Performance of Medical Ti6Al4V Alloy after Mechanical Surface Treatments.* PLOS ONE, 2015. **10**(3): p. e0121963.

218. HQIP, *National joint registry 16th annual report*. 2019: UK.
219. Aggerwal, S., et al., *Failure of intramedullary femoral nail with segmental breakage of distal locking bolts: a case report and review of the literature.* Chinese Journal of Traumatology (English Edition), 2011. **14**(3): p. 188-192.
220. Okazaki, Y., E. Gotoh, and J. Mori, *Strength–Durability Correlation of Osteosynthesis Devices Made by 3D Layer Manufacturing.* Materials, 2019. **12**(3).
221. Korhonen, L., et al., *Intramedullary nailing of forearm shaft fractures by biodegradable compared with titanium nails: Results of a prospective randomized trial in children with at least two years of follow-up.* Biomaterials, 2018. **185**: p. 383-392.
222. Shi, C., et al., *Peridynamic investigation of stress corrosion cracking in carbon steel pipes.* Engineering Fracture Mechanics, 2019. **219**: p. 106604.
223. Choudhary, L. and R.K. Singh Raman, *Magnesium alloys as body implants: Fracture mechanism under dynamic and static loadings in a physiological environment.* Acta Biomaterialia, 2012. **8**(2): p. 916-923.
224. Ritchie, R.O., et al., *High-cycle fatigue of Ti-6Al-4V*. Fatigue and Fracture of Engineering Materials and Structures, 1999. **22**(7): p. 621-632.
225. Sun, R., et al., *Fatigue of Ti-17 titanium alloy with hole drilled prior and post to laser shock peening.* Optics & Laser Technology, 2019. **115**: p. 166-170.
226. Chahardehi, A., F.P. Brennan, and A. Steuwer, *The effect of residual stresses arising from laser shock peening on fatigue crack growth.* Engineering Fracture Mechanics, 2010. **77**(11): p. 2033-2039.
227. Skouras, A., et al., *Residual stress measurements in a ferritic steel/In625 superalloy dissimilar metal weldment using neutron diffraction and deep-hole drilling.* International Journal of Pressure Vessels and Piping, 2013. **101**: p. 143-153.
228. Luo, K.Y., et al., *Investigation and microstructural analyses of massive LSP impacts with coverage area on crack initiation location and tensile properties of AM50 magnesium alloy.* Materials Science and Engineering: A, 2016. **650**: p. 110-118.
229. Everaerts, J., et al., *Evaluation of macro- and microscopic residual stresses in laser shock-peened titanium alloy by FIB-DIC ring-core milling with different core diameters.* Surface and Coatings Technology, 2018. **349**: p. 719-724.
230. Ahmed, R., M.E. Fitzpatrick, and N.H. Faisal, *A comparison of neutron diffraction and hole-drilling residual strain measurements in thermally sprayed coatings.* Surface and Coatings Technology, 2012. **206**(19): p. 4180-4185.
231. Sathiya, P., K. Panneerselvam, and R. Soundararajan, *Optimal design for laser beam butt welding process parameter using artificial neural networks and genetic algorithm for super austenitic stainless steel.* Optics & Laser Technology, 2012. **44**(6): p. 1905-1914.
232. Rahimi, M.H., et al., *Modelling and optimization of laser engraving qualitative characteristics of Al-SiC composite using response surface methodology and artificial neural networks.* Optics & Laser Technology, 2019. **112**: p. 65-76.
233. Bagchi, A., et al., *Numerical simulation and optimization in pulsed Nd: YAG laser welding of Hastelloy C-276 through Taguchi method and artificial neural network.* Optik, 2017. **146**: p. 80-89.
234. Karataş, C., A. Sozen, and E. Dulek, *Modelling of residual stresses in the shot peened material C-1020 by artificial neural network.* Expert Systems with Applications, 2009. **36**(2, Part 2): p. 3514-3521.
235. Maleki, E., *Modeling of Severe Shot Peening Effects to Obtain Nanocrystalline Surface on Cast Iron Using Artificial Neural Network.* Materials Today: Proceedings, 2016. **3**(6): p. 2197-2206.

236. Hfaiedh, N., et al., *Finite element analysis of laser shock peening of 2050-T8 aluminum alloy.* International Journal of Fatigue, 2015. **70**: p. 480-489.
237. Zhang, X., et al., *Investigation on residual stress distribution in thin plate subjected to two sided laser shock processing.* Optics & Laser Technology, 2019. **111**: p. 146-155.
238. Wei, X.L. and X. Ling, *Numerical modeling of residual stress induced by laser shock processing.* Applied Surface Science, 2014. **301**: p. 557-563.
239. Astm, S.E. *Standard test method for determining residual stresses by the hole-drilling strain-gage method*. 2008.
240. Grant, P.V., J.D. Lord, and P.S. Whitehead, *Measurement good practice guide no. 53.* UK, National Physical Laboratory, 2002.
241. Durodola, J.F., et al., *Artificial neural network for random fatigue loading analysis including the effect of mean stress.* International Journal of Fatigue, 2018. **111**: p. 321-332.
242. Mousavi Anijdan, S.H., H.R. Madaah-Hosseini, and A. Bahrami, *Flow stress optimization for 304 stainless steel under cold and warm compression by artificial neural network and genetic algorithm.* Materials & Design, 2007. **28**(2): p. 609-615.
243. Zhu, Y., et al., *Artificial neural network approach to predict the flow stress in the isothermal compression of as-cast TC21 titanium alloy.* Computational Materials Science, 2011. **50**(5): p. 1785-1790.
244. Anand Kumar, S., et al., *Prediction of fretting wear behavior of surface mechanical attrition treated Ti–6Al–4V using artificial neural network.* Materials & Design, 2013. **49**: p. 992-999.
245. Kaunda, R., *New artificial neural networks for true triaxial stress state analysis and demonstration of intermediate principal stress effects on intact rock strength.* Journal of Rock Mechanics and Geotechnical Engineering, 2014. **6**(4): p. 338-347.
246. Sheikh, H. and S. Serajzadeh, *Estimation of flow stress behavior of AA5083 using artificial neural networks with regard to dynamic strain ageing effect.* Journal of Materials Processing Technology, 2008. **196**(1): p. 115-119.
247. Liu, H., et al., *Surface layer microstructures and wear properties modifications of Mg-8Gd-3Y alloy treated by shot peening.* Materials Characterization, 2019. **158**: p. 109952.
248. Kheradmandfard, M., et al., *Significant improvement in cell adhesion and wear resistance of biomedical β-type titanium alloy through ultrasonic nanocrystal surface modification.* Journal of Alloys and Compounds, 2018. **762**: p. 941-949.
249. Zheng, X.-y., Y.-r. Zhang, and B.-r. Zhang, *Effect of N-ion implantation and diamond-like carbon coating on fretting wear behaviors of Ti6Al7Nb in artificial saliva.* Transactions of Nonferrous Metals Society of China, 2017. **27**(5): p. 1071-1080.
250. Zhou, J., et al., *Effect of laser peening on friction and wear behavior of medical Ti6Al4V alloy.* Optics & Laser Technology, 2019. **109**: p. 263-269.
251. Luo, K.Y., et al., *Effects of coverage layer on the electrochemical corrosion behaviour of Mg-Al-Mn alloy subjected to massive laser shock peening treatment.* Journal of Alloys and Compounds, 2019. **782**: p. 1058-1075.
252. Matykina, E., et al., *Electrochemical Anisotropy of Nanostructured Titanium for Biomedical Implants.* Electrochimica Acta, 2015. **176**: p. 1221-1232.
253. Han, A., et al., *The effect of titanium implant surface modification on the dynamic process of initial microbial adhesion and biofilm formation.* International Journal of Adhesion and Adhesives, 2016. **69**: p. 125-132.
254. Rafieerad, A.R., et al., *Mechanical properties, corrosion behavior and in-vitro bioactivity of nanostructured Pd/PdO coating on Ti–6Al–7Nb implant.* Materials & Design, 2016. **103**: p. 10-24.

255. Fatehi, K., et al., *In vitro biomimetic deposition of apatite on alkaline and heat treated Ti6A14V alloy surface.* Bulletin of Materials Science, 2008. **31**(2): p. 101.
256. Le Guéhennec, L., et al., *Surface treatments of titanium dental implants for rapid osseointegration.* Dental Materials, 2007. **23**(7): p. 844-854.
257. Mhaede, M., F. Pastorek, and B. Hadzima, *Influence of shot peening on corrosion properties of biocompatible magnesium alloy AZ31 coated by dicalcium phosphate dihydrate (DCPD).* Materials Science and Engineering: C, 2014. **39**: p. 330-335.
258. Ahmed, A.A., et al., *The effect of shot peening parameters and hydroxyapatite coating on surface properties and corrosion behavior of medical grade AISI 316L stainless steel.* Surface and Coatings Technology, 2015. **280**: p. 347-358.
259. Stráský, J., et al., *Characterization of electric discharge machining, subsequent etching and shot-peening as a surface treatment for orthopedic implants.* Applied Surface Science, 2013. **281**: p. 73-78.
260. Kikuchi, S., et al., *Characterization of the hydroxyapatite layer formed by fine hydroxyapatite particle peening and its effect on the fatigue properties of commercially pure titanium under four-point bending.* Surface and Coatings Technology, 2016. **288**: p. 196-202.
261. Hong, X., et al., *Microstructure and wear resistant performance of TiN/Zr-base amorphous-nanocrystalline composite coatings on titanium alloy by electrospark deposition.* Surface and Coatings Technology, 2016. **305**: p. 67-75.
262. Sealy, M.P., et al., *Fatigue performance of biodegradable magnesium–calcium alloy processed by laser shock peening for orthopedic implants.* International Journal of Fatigue, 2016. **82**: p. 428-436.
263. Shukla, P.P. and J. Lawrence, *The influence of brightness during laser surface treatment of Si3N4 engineering ceramics.* Optics and Lasers in Engineering, 2012. **50**(12): p. 1746-1751.
264. Shukla, P. and J. Lawrence, *Role of laser beam radiance in different ceramic processing: A two wavelengths comparison.* Optics & Laser Technology, 2013. **54**: p. 380-388.
265. Shukla, P., J. Lawrence, and Y. Zhang, *Understanding laser beam brightness: A review and new prospective in material processing.* Optics & Laser Technology, 2015. **75**: p. 40-51.
266. Shukla, P.P. and J. Lawrence, *Identification of optical parameters for determination of radiance.* Journal of Optics, 2015. **44**(1): p. 12-19.
267. Fischer-Cripps, A.C., *The measurement of hardness of very hard materials.* Surface and Coatings Technology, 2016. **291**: p. 314-317.
268. Rafieerad, A.R., et al., *Self-organized TiO2 nanotube layer on Ti–6Al–7Nb for biomedical application.* Surface and Coatings Technology, 2015. **265**: p. 24-31.
269. Oliveira, D.P., et al., *Surface chemical treatment of ultrafine-grained Ti–6Al–7Nb alloy processed by severe plastic deformation.* Journal of Alloys and Compounds, 2015. **643**: p. S241-S245.
270. Chlebus, E., et al., *Microstructure and mechanical behaviour of Ti—6Al—7Nb alloy produced by selective laser melting.* Materials Characterization, 2011. **62**(5): p. 488-495.
271. Liu, Y.G., M.Q. Li, and H.J. Liu, *Surface nanocrystallization and gradient structure developed in the bulk TC4 alloy processed by shot peening.* Journal of Alloys and Compounds, 2016. **685**: p. 186-193.
272. Fu, J., et al., *Effect of laser shock peening on mechanical properties of Zr-based bulk metallic glass.* Applied Surface Science, 2014. **313**: p. 692-697.

273. Chai, L., et al., *Microstructural, textural and hardness evolution of commercially pure Zr surface-treated by high current pulsed electron beam.* Applied Surface Science, 2016. **390**: p. 430-434.
274. Tan, X.-R., et al., *Effects of milling on the microstructure and hardness of Al2NbTi3V2Zr high-entropy alloy.* Materials & Design, 2016. **109**: p. 27-36.
275. Costa, T.A., et al., *Effect of solution time in T6 heat treatment on microstructure and hardness of a directionally solidified Al–Si–Cu alloy.* Journal of Alloys and Compounds, 2016. **683**: p. 485-494.
276. Roa, J.J., et al., *Hall-Petch strengthening of the constrained metallic binder in WC–Co cemented carbides: Experimental assessment by means of massive nanoindentation and statistical analysis.* Materials Science and Engineering: A, 2016. **676**: p. 487-491.
277. Dai, F.Z., et al., *A method to decrease surface roughness in laser shock processing.* Surface and Coatings Technology, 2015. **261**: p. 35-40.
278. Dai, F., et al., *A technique to decrease surface roughness in overlapping laser shock peening.* Applied Surface Science, 2016. **370**: p. 501-507.
279. Duong, X., J.R.R. Mayer, and M. Balazinski, *Initial tool wear behavior during machining of titanium metal matrix composite (TiMMCs).* International Journal of Refractory Metals and Hard Materials, 2016. **60**: p. 169-176.
280. Lu, J.Z., et al., *Effects of multiple laser shock processing (LSP) impacts on mechanical properties and wear behaviors of AISI 8620 steel.* Materials Science and Engineering: A, 2012. **536**: p. 57-63.
281. Haghshenas, A. and M.M. Khonsari, *Damage accumulation and crack initiation detection based on the evolution of surface roughness parameters.* International Journal of Fatigue, 2018. **107**: p. 130-144.
282. Trdan, U., et al., *Surface modification of laser ‐ and shot ‐peened 6082 aluminium alloy: Laser peening effect to pitting corrosion.* International Journal of Structural Integrity, 2011. **2**(1): p. 9-21.
283. Rao, M.C., *PULSED LASER DEPOSITION — ABLATION MECHANISM AND APPLICATIONS.* International Journal of Modern Physics: Conference Series, 2013. **22**: p. 355-360.
284. Lu, G.X., et al., *Nonuniformity of morphology and mechanical properties on the surface of single crystal superalloy subjected to laser shock peening.* Journal of Alloys and Compounds, 2016. **658**: p. 721-725.
285. Dai, F., et al., *Surface roughness control of LY2 aluminum alloy milled surface subjected to laser shock wave planishing processing.* Applied Surface Science, 2019. **486**: p. 121-127.
286. Bacakova, L., et al., *Modulation of cell adhesion, proliferation and differentiation on materials designed for body implants.* Biotechnol Adv, 2011. **29**(6): p. 739-67.
287. Shukla, P., et al., *10 - Laser surface structuring of ceramics, metals and polymers for biomedical applications: A review,* in *Laser Surface Modification of Biomaterials*, R. Vilar, Editor. 2016, Woodhead Publishing. p. 281-299.
288. Wang, Y., et al., *Surface morphology of modified titanium alloy affects proliferation stability of bone marrow mesenchymal stem cells.* Surface and Coatings Technology, 2019. **366**: p. 156-163.
289. Petan, L., J.L. Ocaña, and J. Grum, *Influence of laser shock peening pulse density and spot size on the surface integrity of X2NiCoMo18-9-5 maraging steel.* Surface and Coatings Technology, 2016. **307**: p. 262-270.
290. Ran, Z., et al., *Finite Element Analysis of Surface Roughness Generated by Multiple Laser Shock Peening.* Rare Metal Materials and Engineering, 2018. **47**(1): p. 33-38.

291. Lu, G., et al., *Nanosecond pulsed laser-generated stress effect inducing macro-micro-nano structures and surface topography evolution.* Applied Materials Today, 2019. **15**: p. 171-184.
292. Ye, Q. and G. He, *In-situ formed graded microporous structure in titanium alloys and its effect on the mechanical properties.* Materials & Design, 2015. **83**: p. 295-300.
293. Hammann, C.P.W., et al., *Direct submicron patterning of titanium for bone implants.* Microelectronic Engineering, 2018. **195**: p. 13-20.
294. Torres, Y., et al., *Design, processing and characterization of titanium with radial graded porosity for bone implants.* Materials & Design, 2016. **110**: p. 179-187.
295. Long, W.J., et al., *Early aseptic loosening of the Tritanium primary acetabular component with screw fixation.* Arthroplasty Today, 2018. **4**(2): p. 169-174.
296. Igarashi, K. and K.I. Afrashtehfar, *Clinical assessment of fractured implant abutment screws: The Bernese silicone replica technique.* The Journal of Prosthetic Dentistry, 2018. **119**(5): p. 717-719.
297. Çomaklı, O., et al., *Effect of Ti amount on wear and corrosion properties of Ti-doped Al2O3 nanocomposite ceramic coated CP titanium implant material.* Ceramics International, 2018. **44**(7): p. 7421-7428.
298. Kwon, M.H., H.S. Shin, and C.N. Chu, *Fabrication of a super-hydrophobic surface on metal using laser ablation and electrodeposition.* Applied Surface Science, 2014. **288**: p. 222-228.
299. Edalatpour, M., et al., *Managing water on heat transfer surfaces: A critical review of techniques to modify surface wettability for applications with condensation or evaporation.* Applied Energy, 2018. **222**: p. 967-992.
300. Du, Q., et al., *Tailoring the surface wettability of polyimide by UV laser direct texturing in different gas atmospheres.* Materials & Design, 2016. **104**: p. 134-140.
301. Gentleman, M.M. and E. Gentleman, *The role of surface free energy in osteoblast–biomaterial interactions.* International Materials Reviews, 2014. **59**(8): p. 417-429.
302. Groth, T. and G. Altankov, *Studies on cell-biomaterial interaction: role of tyrosine phosphorylation during fibroblast spreading on surfaces varying in wettability.* Biomaterials, 1996. **17**(12): p. 1227-1234.
303. da Silva, L.F.M., et al., *Effect of grooves on the strength of adhesively bonded joints.* International Journal of Adhesion and Adhesives, 2010. **30**(8): p. 735-743.
304. Shukla, P., et al., *Surface property modifications of silicon carbide ceramic following laser shock peening.* Journal of the European Ceramic Society, 2017. **37**(9): p. 3027-3038.
305. Shukla, P., et al., *Surface engineering alumina armour ceramics with laser shock peening.* Materials & Design, 2017. **134**: p. 523-538.
306. Luo, S., et al., *Regain the fatigue strength of laser additive manufactured Ti alloy via laser shock peening.* Journal of Alloys and Compounds, 2018. **750**: p. 626-635.
307. Wang, J.T., et al., *Effects of laser shock peening on stress corrosion behavior of 7075 aluminum alloy laser welded joints.* Materials Science and Engineering: A, 2015. **647**: p. 7-14.
308. Orlova, E.G., et al., *Spreading of a distilled water droplet over polished and laser-treated aluminum surfaces.* European Journal of Mechanics - B/Fluids, 2018. **68**: p. 118-127.
309. Shi, Z., et al., *Dynamic contact angle hysteresis in liquid bridges.* Colloids and Surfaces A: Physicochemical and Engineering Aspects, 2018. **555**: p. 365-371.
310. Żenkiewicz, M., *Methods for the calculation of surface free energy of solids.* Journal of Achievements in Materials and Manufacturing Engineering, 2007. **24**(1): p. 137-145

311. Rudawska, A. and E. Jacniacka, *Analysis for determining surface free energy uncertainty by the Owen–Wendt method.* International Journal of Adhesion and Adhesives, 2009. **29**(4): p. 451-457.
312. Rieke, P.C., *Application of Van Oss-Chaudhury-Good theory of wettability to interpretation of interfacial free energies of heterogeneous nucleation.* Journal of Crystal Growth, 1997. **182**(3): p. 472-484.
313. Waugh, D.G. and J. Lawrence, *On the use of CO2 laser induced surface patterns to modify the wettability of poly(methyl methacrylate) (PMMA).* Optics and Lasers in Engineering, 2010. **48**(6): p. 707-715.
314. Ebnesajjad, S. and C. Ebnesajjad, *Surface treatment of materials for adhesive bonding*. 2013: William Andrew.
315. Schrader, M.E., *Young-Dupre Revisited.* Langmuir, 1995. **11**(9): p. 3585-3589.
316. Whyman, G., E. Bormashenko, and T. Stein, *The rigorous derivation of Young, Cassie–Baxter and Wenzel equations and the analysis of the contact angle hysteresis phenomenon.* Chemical Physics Letters, 2008. **450**(4): p. 355-359.
317. Rudawska, A., et al., *The effect of sandblasting on surface properties for adhesion.* International Journal of Adhesion and Adhesives, 2016. **70**: p. 176-190.
318. Baek, S.M., et al., *Superior Pre-Osteoblast Cell Response of Etched Ultrafine-Grained Titanium with a Controlled Crystallographic Orientation.* Scientific Reports, 2017. **7**(1): p. 44213.
319. Jin, W., et al., *Improvement of corrosion resistance and biocompatibility of rare-earth WE43 magnesium alloy by neodymium self-ion implantation.* Corrosion Science, 2015. **94**: p. 142-155.
320. Schroeder, A., O. Pohler, and F. Sutter, *Tissue reaction to an implant of a titanium hollow cylinder with a titanium surface spray layer.* 1976. **86**(7): p. 713-727.
321. Agarwal, R. and A.J. García, *Biomaterial strategies for engineering implants for enhanced osseointegration and bone repair.* Advanced drug delivery reviews, 2015. **94**: p. 53-62.
322. Hudecki, A., G. Kiryczyński, and M.J. Łos, *Chapter 7 - Biomaterials, Definition, Overview*, in *Stem Cells and Biomaterials for Regenerative Medicine*, M.J. Łos, A. Hudecki, and E. Wiecheć, Editors. 2019, Academic Press. p. 85-98.
323. Chen, S., et al., *Tuning surface properties of bone biomaterials to manipulate osteoblastic cell adhesion and the signaling pathways for the enhancement of early osseointegration.* Colloids and Surfaces B: Biointerfaces, 2018. **164**: p. 58-69.
324. Flamant, Q., et al., *Hydrofluoric acid etching of dental zirconia. Part 1: etching mechanism and surface characterization.* Journal of the European Ceramic Society, 2016. **36**(1): p. 121-134.
325. Günay-Bulutsuz, A., et al., *Biological responses of ultrafine grained pure titanium and their sand blasted surfaces.* Materials Science and Engineering: C, 2018. **91**: p. 382-388.
326. Granato, R., et al., *Osteointegrative and microgeometric comparison between micro-blasted and alumina blasting/acid etching on grade II and V titanium alloys (Ti-6Al-4V).* Journal of the Mechanical Behavior of Biomedical Materials, 2019. **97**: p. 288-295.
327. Mukherjee, S., S. Dhara, and P. Saha, *Enhancing the biocompatibility of Ti6Al4V implants by laser surface microtexturing: an in vitro study.* The International Journal of Advanced Manufacturing Technology, 2015. **76**(1): p. 5-15.
328. Batal, A., R. Sammons, and S. Dimov, *Response of Saos-2 osteoblast-like cells to laser surface texturing, sandblasting and hydroxyapatite coating on CoCrMo alloy surfaces.* Materials Science and Engineering: C, 2019. **98**: p. 1005-1013.

329. Xiong, Y.-Z., et al., *Rationally designed functionally graded porous Ti6Al4V scaffolds with high strength and toughness built via selective laser melting for load-bearing orthopedic applications.* Journal of the Mechanical Behavior of Biomedical Materials, 2020. **104**: p. 103673.
330. Clauer, H.A., *Laser Shock Peening, the Path to Production.* Metals, 2019. **9**(6).
331. Gujba, K.A. and M. Medraj, *Laser Peening Process and Its Impact on Materials Properties in Comparison with Shot Peening and Ultrasonic Impact Peening.* Materials, 2014. **7**(12).
332. Song, Y., et al., *Effect of the nanostructure of porous alumina on growth behavior of MG63 osteoblast-like cells.* Journal of Bioscience and Bioengineering, 2013. **116**(4): p. 509-515.
333. Nayak, S., et al., *The promotion of osseointegration of titanium surfaces by coating with silk protein sericin.* Biomaterials, 2013. **34**(12): p. 2855-2864.
334. Bagherifard, S., et al., *Effects of nanofeatures induced by severe shot peening (SSP) on mechanical, corrosion and cytocompatibility properties of magnesium alloy AZ31.* Acta Biomaterialia, 2018. **66**: p. 93-108.
335. Tamada, Y. and Y. Ikada, *Cell adhesion to plasma-treated polymer surfaces.* Polymer, 1993. **34**(10): p. 2208-2212.